GHENT UNIVERSITY

FACULTY OF SCIENCES

FORMATION AND TEXTURE OF THIN FILM SILICIDES

FILIP GEENEN

Promotor:
Prof. Dr. Christophe Detavernier

This research was supported by the Research Foundation-Flanders (FWO-Vlaanderen).

Dissertation presented in partial fulfillment for the degree of
Doctor in Sciences: Physics
May 2017

MEMBERS OF THE EXAMINATION COMMITTEE:

Prof. Dr. Maarten Baes	UGent, chairman
Dr. Davy Deduytsche	UGent
Prof. Dr. Christian Lavoie	IBM
Dr. Cristian Mocuta	Synchrotron SOLEIL
Prof. Dr. André Vantomme	KU Leuven
Prof. Dr. Henk Vrielinck	UGent

CLOSED DEFENSE	April 28, 2017
PUBLIC DEFENSE	May 22, 2017

Putting it on paper lets you start fixing it.
If it stays in your head, a perfect idea,
you'll never share it with anyone.

— Emma Coats, *Pixar rules for storytelling*

NEDERLANDSTALIGE SAMENVATTING - SUMMARY IN DUTCH

De technologische vooruitgang in de micro-elektronica heeft een indrukwekkende evolutie doorgaan tijdens de laatste decennia. Zo heeft men de verschillende elektronische componenten kunnen herschalen naar uitzonderlijk kleine afmetingen, waardoor een hedendaagse computer niet alleen meer, maar ook goedkopere en snellere rekenkracht bezit in vergelijking met oudere modellen.

Deze miniaturisatie is enkel mogelijk gemaakt door technologische innovatie en onderzoek dat de verschillende onderdelen in zo'n computerchip optimaliseerden voor deze kleinere afmetingen. Binnen deze context bestuderen we in deze thesis het materiaal dat verantwoordelijk is voor het elektrische contact met de op silicium gebaseerde halfgeleider in de *source* en *drain* gebieden van veldeffecttransistoren. De elektrische weerstand van dit contact kan worden verminderd door gebruik te maken van een *silicide*, i.e. een materiaal dat gebaseerd is op een chemische verbinding tussen een metaal (b.v. kobalt, nikkel of titaan) en silicium. De voortdurende miniaturisatie in de micro-elektronica gaat gepaard met dunnere en smallere silicidegebieden in de transistor. Deze verkleining zorgt ervoor dat silicides die gebruikt worden in een bepaalde technologische generatie mogelijks niet meer gebruikt kunnen worden in een toekomstige generatie. Deze thesis bestudeert daarom het effect van de diktevermindering op de vorming en stabiliteit van silicides.

NIKKEL SILICIDES

Het eerste deel van dit werk bestudeert nikkel-gebaseerde silicides. Hedendaagse, planaire veldeffecttransistoren maken gebruik van nikkel monosilicide (NiSi) contacten. Dit contact wordt gevormd door een dunne Ni laag te deponeren op het Si substraat en vervolgens op te warmen. Hierdoor zorgt de thermische energie ervoor zorgt dat Ni diffundeert in het Si, waarna een chemische verbinding tussen Ni en Si tot stand kan komen. Helaas is NiSi morfologisch onstabiel bij opwarming, hetgeen een onoverkomelijke stap is tijdens het productieproces van de transistor. Dusdanig evolueert een dunne NiSi laag naar gescheiden NiSi eilandjes, zodat er geen continue en elektrisch geleidende laag meer is in de transistor. Meer nog, de temperatuur waarbij dat dit agglomeratieproces plaatsvindt, ver-

laagt wanneer de silicidelaag dunner wordt. Deze morfologische instabiliteit zorgt voor een dramatische verhoging van de elektrische weerstand in de transistor. Het is dus zeer belangrijk om dit te vermijden. Een veelvoorkomende strategie om agglomeratie te vertragen is door het silicidecontact te vormen tussen Ni en Si in aanwezigheid van een gecontroleerde hoeveelheid van een legeringselement. Zodoende wordt Pt gebruikt om de stabiliteit van NiSi drastisch te verhogen. Deze oplossing zorgt slechts voor een vertraagde agglomeratie, en dus niet voor een permanente oplossing. Daarom is het cruciaal om alternatieve strategieën te overwegen en te onderzoeken.

Epitaxiale silicides zijn interessante kandidaten voor de vorming van elektrische contacten op halfgeleiders, aangezien ze worden gerapporteerd met lagere contactweerstanden en een hogere stabiliteit. De vorming van nikkel silicides beperkt zich niet alleen tot nikkel monosilicide. Wanneer men een NiSi laag opwarmt naar hogere temperaturen ($> 800\,^{\circ}C$), dan kan deze laag transformeren naar $NiSi_2$. Deze kristallijne fase heeft een opmerkelijke gelijkenis met het silicium substraat. Beide kristalroosters zijn kubisch, en verschillen slechts 0.42% in de roosterafstand van hun eenheidscel. Deze geometrische gelijkenis zorgt ervoor dat $NiSi_2$ epitaxiaal kan groeien op het substraat. De groei van een gecontroleerde, epitaxiale $NiSi_2$ laag is echter zeer uitdagend. Het is bijvoorbeeld gekend dat er twee verschillende epitaxiale oriëntaties mogelijk zijn van $NiSi_2$ op Si, en de aanwezigheid van beide epitaxiën gaat gepaard met een verhoogde contactweerstand. Bijkomend vormt $NiSi_2$ zich slechts bij relatief hoge temperaturen (b.v. $800\,^{\circ}C$), zodat de voorgaande silicidelaag reeds geagglomereerd kan zijn of waardoor de Ni atomen de thermische energie hebben om ongecontroleerd te diffunderen in de transistor.

Invloed van Al als legeringselement op de fasevolgorde

Er werd recent aangetoond dat de vormingstemperatuur van epitaxiale $NiSi_2$ sterk wordt verlaagd door de toevoeging van Al als legeringselement. De invloed van dit legeringselement is tot op heden onderzocht met klassieke *cook and look* methodieken, hetgeen als gevolg heeft dat er enkel data beschikbaar is voor het ternaire Ni-Al-Si systeem bij een beperkt aantal aluminiumconcentraties of opwarmtemperaturen. In dit werk bestudeerden we deze fasevorming systematisch met behulp van *in situ* meettechnieken tijdens opwarming en Al-concentratiegradiënten. We vonden dat er vier verschillende fase-sequenties bestaan die onderscheiden kunnen worden volgens de initiële aluminiumconcentratie. Voor aluminiumconcentraties hoger dan 32 at.% in de initiële laag, reduceerde

de vormingstemperatuur van $NiSi_2$ zelfs tot onder 400 °C. Bijkomend hebben we de epitaxiale oriëntatie onderzocht van $NiSi_2$, en gevonden dat deze de hoogste kwaliteit had in het concentratie-venster tussen 30 en 50 at.%. Aluminium concentraties lager dan 30 at.% resulteren slechts bij hogere temperaturen in de vorming van $NiSi_2$ en dit in twee epitaxiale orientaties. Aluminium concentraties hoger dan 50 at.%. resulteren in de vorming van een axiotaxiale $NiSi_2$ orientatie. Deze resultaten kunnen als leidraad gebruikt worden om de gewenste aluminium concentratie en opwarmtemperatuur te selecteren voor het vormen van een epitaxiale $NiSi_2$ laag.

Invloed van initiële nikkeldikte op de fasevolgorde

Naast het gebruik van legeringselementen, kan men ook een tweede strategie overwegen om epitaxiale $NiSi_2$ films te groeien bij relatief lage temperaturen. De vastestofreactie tussen nikkel en silicium verandert abrupt wanneer de initiële nikkeldikte daalt onder ca. 5 nm, een dikte die soms de *kritische dikte* wordt genoemd. Het opwarmen van dikkere films resulteert in de gekende fasevorming, waarbij poly-kristallijn NiSi gevormd wordt bij temperaturen tussen 300 en 450 °C. Dunnere nikkel films vormen bij deze temperaturen echter $NiSi_2$ in plaats van NiSi. Deze fase vormt dan met een epitaxiale orientatie ten opzichte van het silicium substraat. De gevormde epitaxiale films blijken niet te agglomereren en zijn thermodynamisch stabiel tot 900 °C, een opmerkelijke verbetering in vergelijking met NiSi-lagen.

Deze abrupte verandering in vastestofreactie vindt plaats bij een dikteregime dat in dezelfde grootte-orde ligt van de silicides gebruikt in de transistoren van de nabije toekomst. Vandaar dat men dit *ultradunne* regime probeert te begrijpen en zoekt naar manieren om de dikte waarbij deze verandering in fasesequentie plaatsvindt, te sturen naar hogere of lagere waarden. In deze thesis hebben we twee aspecten van deze kritische dikte bestudeerd. Ten eerste onderzochten we de specifieke fasevolgorde boven en onder de kritische dikte, en hoe het toevoegen van legeringselementen (zoals aluminium, cobalt of platinum) deze fases kunnen beïnvloeden. Als tweede onderzochten we met behulp van diktegradiënten hoe legeringselementen de *waarde* van de kritische dikte kunnen beïnvloeden.

Invloed van legeringselementen op de fasevolgorde

Allereerst werd de vastestofreactie bestudeerd boven en onder de kritische dikte door het opwarmen van een dunne nikkellaag gedeponeerd op

een siliciumsubstraat, met een initiële nikkeldikte van 9 nm of 3 nm, gedeponeerd op een Si substraat. De nikkellagen werden optioneel gelegeerd met 10 at.% Al, Co of Pt. Deze lagen werden bestudeerd en de volgorde waarbij de verschillende silicides worden gevormd, alsook hun stabiliteit als functie van temperatuur en hun kristallijne oriëntatie ten opzichte van het siliciumsubstraat werden opgemeten. Deze metingen tonen aan dat de silicides over een breder temperatuursvenster worden waargenomen wanneer het legeringselement oplosbaar is in de fase (e.g. Co in δ-Ni_2Si). Daarentegen, wanneer een legeringselement niet oplosbaar is in een silicidefase (e.g. Pt in δ-Ni_2Si), dan is de vorming van deze fase uitgesteld, zodat deze over een minder groot temperatuursvenster observeerbaar is. Daarnaast tonen X-stralendiffractie poolfiguurmetingen aan dat de kristallijne orientatie van de verschillende silicides beïnvloed kan worden door de legeringselementen. Bijkomend wijzen de metingen erop dat de preferentiële orientatie van de kristalkorrels kan worden overgeërfd van één silicide fase naar de andere. Deze overerving kan verklaard worden door de vergelijkbare silicide kristalroosters. De atomaire posities in de kristalroosters hoeven slechts een klein beetje te veranderen om de fasetransitie door te voeren. Bijgevolg kan een eventuele preferentiële orientatie met het substraat behouden worden, ook al wordt een nieuwe silicide gevormd met een andere kristalrooster. Dit kan ook energetisch een voordeel hebben, aangezien deze overerving geen drastische verhoging van de oppervlakteenergie zal teweeg brengen.

Invloed van legeringselementen op de kritische dikte

De vastestofreactie van nikkellagen tot een dikte van 15 nm met het silicium substraat werd bestudeerd met als doel om de kritische dikte precies waar te nemen. De nikkellagen werden optioneel gelegeerd met Al, Co, Ge, Pd of Pt, hetgeen de kritische dikte naar hogere (Al) en lagere (Pt, Ge, Pd) waarden kon gestuurd worden. Deze waarneming kan geinterpreteerd worden aan de hand van de oplosbaarheid van het legeringselement in ofwel NiSi of $NiSi_2$ via klassieke nucleatietheorie. Alsdusdanig zullen Pt, Ge en Pd, die niet oplosbaar zijn in $NiSi_2$, eerst moeten diffunderen naar korrelgrenzen of het oppervlak van de dunne film alvorens de ultradunne en epitaxiale $NiSi_2$ fase kan gevormd worden. Dit is niet nodig voor de vorming van NiSi, gezien deze legeringselementen Ni lokaal kunnen vervangen. De vorming van NiSi wordt geobserveerd voor dunnere films bij het toevoegen van Pt, Ge en Pd en dus kan men vaststellen dat de kritische dikte verlaagt. Het omgekeerde is waargenomen voor Al, een element dat Si kan vervangen in de $NiSi_2$ structuur maar niet in de NiSi

structuur, zodat $NiSi_2$ gevormd wordt bij lagere temperaturen en voor dikkere nikkellagen. Co kan in NiSi en $NiSi_2$ een Ni atoom substitueren, en beïnvloedt de kritische dikte bijgevolg niet. Zodoende besluiten we het eerste deel van deze thesis door een overzicht te geven van de verschillende mechanismes die voor een onstabiele nikkelsilicide kunnen zorgen. Bijkomend overlopen we welke legeringselementen de stabiliteit van nikkelsilicides beïnvloeden als functie van dikte en temperatuur.

TITAAN SILICIDES

In het tweede deel van deze thesis wordt een recente ontwikkeling uitgediept voor silicides als contactmateriaal. De nieuwe architectuur van veldeffecttransistoren heeft ervoor gezorgd dat titaan-gebaseerde silicides weer worden gebruikt voor het contacteren van de silicium-gebaseerde halfgeleider. Dit geeft aanleiding om de C54-$TiSi_2$ fase opnieuw te onderzoeken. Deze fase werd vroeger gebruikt voor het contacteren van transistoren in de vroege jaren 90. Hoewel deze fase niet gemakkelijk gevormd kan worden in de huidige transistoren, is hij nog steeds te vinden in hedendaagse toepassingen die een hoge betrouwbaarheid vereisen, zoals de wagenindustriesector. De vernieuwde interesse in titaan-gebaseerde silicides inspireerde ons om deze fase opnieuw te onderzoeken met behulp van de hedendaags beschikbare apparatuur, die een sterk verhoogde meetkwaliteit vertonen in vergelijking met 25 jaar geleden. Daarom onderzochten we de preferentiële orientatie van de C54-$TiSi_2$ korrels ten opzichte van Si(100) en Si(111) substraten. De metingen tonen voor het eerst een axiotaxische orientatie aan van de $TiSi_2$ fase, samen met enkele epitaxiale orientaties die reeds gekend waren. De metingen tonen duidelijk de link aan tussen de reeds gekende epitaxiale orientaties en de axiotaxische textuur. Deze correlatie bespreken we als functie van het aligneren van de kristalvlakken tussen het titaansilicide en het silicium substraat. Door het dunner maken van de initiële titaanlaag is de epitaxiale alignatie dominanter in vergelijking met de axiotaxische orientatie. De oppervlakte-energie speelt, net zoals bij dunnere nikkelsilicides, een belangrijke rol bij de verklaring van deze verandering in preferentiële orientatie.

CONTENTS

ACRONYMS

BF-TEM	bright-field transmission electron microscopy
BNL	Brookhaven national lab
CTE	coefficient of thermal expansion
DDS	dominant diffusing species
EDS	energy dispersive spectroscopy
EHF	effective heat of formation
FET	field effect transistor
HKMG	high-k metal gate
JCPDS	joint committee on powder diffraction standards
LURE	Laboratoire pour l'utilisation du rayonnement électromagnétique
MOSFET	metal-oxide field effect transistor
NSLS	national synchrotron light source
OME	oxide mediated epitaxy
PEEK	polyether ether ketone
PVD	physical vapour deposition
RBS	Rutherford backscattering spectrometry
RBS-C	Rutherford backscattering spectrometric channelling
RCA	Radio corporation of America
SALICIDE	self-aligned silicide
SBH	Schottky barrier height
SEM	scanning electron microscopy
SG	Space Group
SOLEIL	source optimisée de lumiére d'énergie intermédiaire du LURE
SOI	semiconductor on insulator
SR	sheet resistance
SSR	solid-state reaction
STI	shallow trench isolation
STEM	scanning transmission electron microscopy

TEM	transmission electron microscopy
TIME	titanium mediated epitaxy
UHV	ultra-high vacuum
XPS	X-ray photoelectron spectroscopy
XRD	X-ray diffraction
XRF	X-ray fluorescence
XRR	X-ray reflectivity

Part I

INTRODUCTION

1

INTRODUCTION

Over the past decades, the micro-electronics industry has achieved impressive advances in both increasing the performance and reducing the cost of transistor-based processors, as described by *Moore's Law*. In 1965, Gordon Moore was invited to submit an article concerning future trends in semiconductor technology [1]. At that point in time, the second generation of integrated circuits contained roughly double the number of transistors of the first generation, i.e. from eight to about sixteen. Laboratory devices were already exploring chips with roughly 30 elements and proof-of-concepts were created that would contain more than 60 elements. As a rough estimate how this trend would evolve for the near future, Moore extrapolated the available data and stated that this increase in the number of transistors follows an exponential rate and that a similar increase in performance of the computer chip could be expected as a function of time.

Five decades later, in 2015, we celebrated the 50th anniversary of this still-ongoing trend, though it has slightly decelerated. Needless to say, this achievement is the result of remarkable innovations and fine-tuning in transistor technology. The material under consideration of this thesis, metal silicides, was as such introduced in the metal-oxide-semiconductor field-effect transistor (MOSFET) technology as an intermediate layer between the Si-based semiconductor regions (e.g. Si, Si_xGe_{1-x}, SiC) and the electrical wiring (also denoted as the via's) to resolve issues in the electrical contact. As such, PtSi and Pd_2Si were introduced in the 1970's as contact pads between Al via's and the Si substrate [2–4].

As transistors scaled down, the silicide contacts had to scale accordingly, offering a lower contact resistance or better resilience to degradation. By consequence, silicides used in one technology node proved unable to be maintained in more advanced nodes, and therefore a sequence of different silicides, such as WSi_2, $TiSi_2$, $CoSi_2$ and NiSi, has been used in state-of-the-art devices. However, there is a certain inertia within the micro-electronics industry to shift from one silicide to another, as the introduction of a new silicide often goes hand in hand with new and unexpected challenges that need to be resolved. To make it so, researchers engaged innovative ways to improve the properties of the formed silicide phases, for example by adding alloying elements to the silicide.

This introduction chapter first provides an overview of the models on silicide formation (section 1.1). The theoretical concepts introduced therein will prove useful for the full scope of this work, and will reveal some of the key mechanisms in silicide research such as classical nucleation theory, discussed in 1.2 and the formation of the first silicide as discussed in section 1.3. Moreover, as silicides are often formed when in contact with a single-crystal Si substrate, they often exhibit a peculiar preferential orientation, or texture, with respect to the substrate. Section 1.4 provides an introduction to texture research and some of the implications on the silicides' properties. As such, this chapter allows us to introduce some of the major challenges for silicides in the micro-electronics industry, and section 1.5 briefly describes some of the reasons to change from one silicide to another. Section 1.6 concludes this introduction with an overview of the key results that were obtained in this work.

1.1 CONCERNING THE FORMATION OF SILICIDE PHASES

The first silicide appeared in the transistor technology during the 1980's in order to replace highly-doped poly-crystalline Si as a contact material. Since then, small and large changes have been introduced that altered the formation and properties of the formed silicide contacts, which have been discussed in several reviews and book chapters [2–7]. The implementation of the self-aligned silicide process (SALICIDE), which was introduced in the MOSFET fabrication process at the beginning of the 1990's, is a benchmark which resulted in the success of silicide materials in the micro-electronics industry. In this process, schematically represented in figure 1.1, a metallic layer (e.g. Ti, Co, Ni) is deposited on top of the patterned wafer, which contains the three characteristic terminals of the MOSFET (source, drain and gate) and the intermediate spacers. A subsequent rapid-thermal anneal (RTA) allows the metal to form a silicide in the regions where it is in direct contact with Si (e.g. source, drain and gate). In other regions, no chemical reaction is expected to occur and the metal remains as deposited. Thereafter, a chemical selective etch can be used to remove the unreacted metal, resulting in silicide formation restricted to the desired regions[1]. The formation process thus has the advantage that no additional patterning step is needed to remove silicide material from regions of the wafer where it is not desired.

1 The SALICIDE process often requires a two-step thermal treatment, separated by the chemical etch step, in order to avoid large atomic migration of either the metal or silicon atoms. Such atomic drift would initiate uncontrolled silicide formation with the risk of accidental short-circuiting.

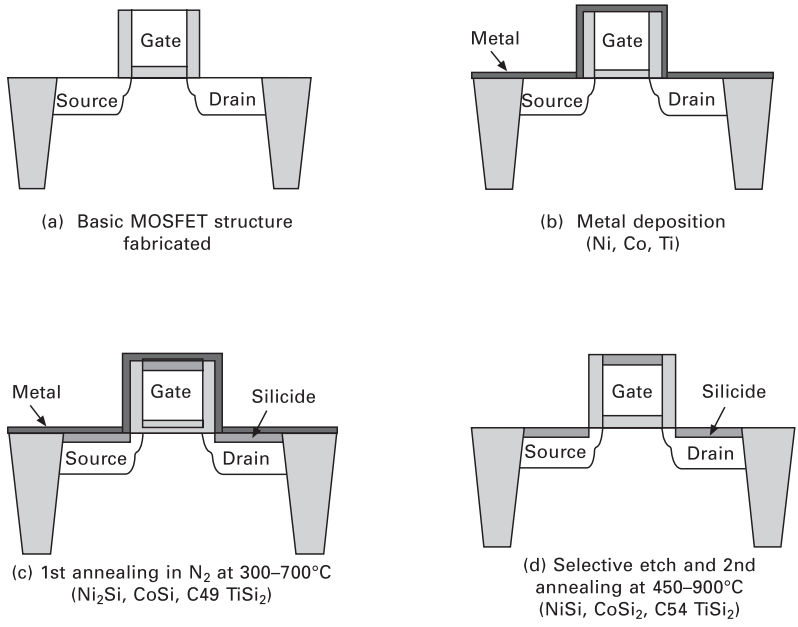

Figure 1.1: Schematic representation of the self-aligned silicide formation process. **(a)** prior to the metal deposition, the different terminals (source, drain and gate) and insulating spacers (gray) are prepared on the substrate. **(b)** A metal layer is deposited on top of the entire wafer. **(c)** A subsequent thermal treatment induces silicide formation in the regions where the metal is in direct contact with Si, where after **(d)** unreacted metal is removed through a chemical etching process. Adapted from [7].

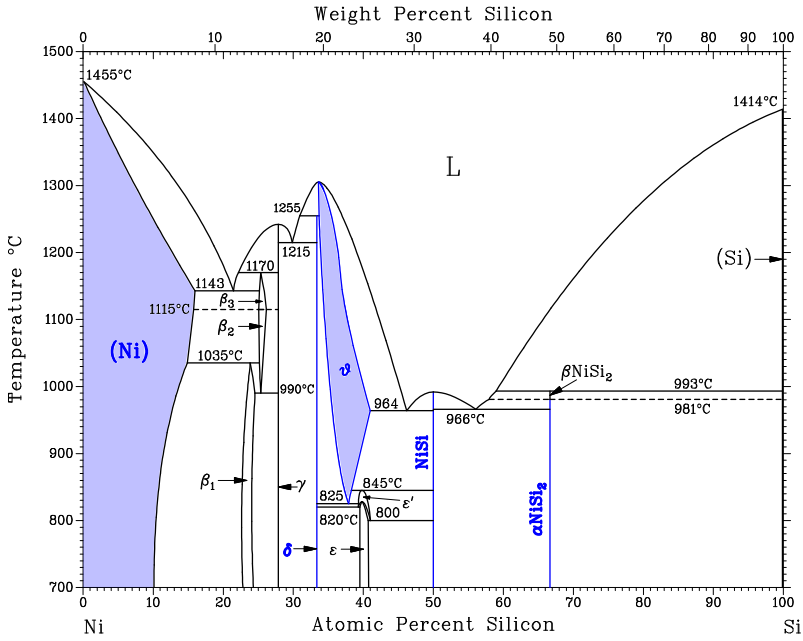

Figure 1.2: The binary phase diagram for the bulk Ni-Si system. Phases with bold phase identifications appear also in thin-film silicide phase sequence. Adapted from [8].

The self-aligned silicide formation significantly simplified the silicide integration in the MOSFET-fabrication process. However, there is no guarantee that an established silicide formation process is transferable from one technology node to another smaller node. Several effects during the silicide formation influence the properties and usability of the finally formed material. For example, the reduction of the contact's line width and thickness combined with a nucleation-driven process are known to significantly influence the formation process or the stability of the used silicide.

A different set of models is therefore needed to describe this thin-film formation process in comparison with bulk-diffusion couples. This is illustrated by comparing the equilibrium Ni-Si phase diagram displayed in figure 1.2 with the set of observed nickel silicide phases in thin-film research. According to the phase diagram, a total of 7 phases are stable in the typically used SALICIDE temperature range (i.e. up to around 800 °C): $NiSi_2$, NiSi, ϵ-Ni_3Si_2, δ-Ni_2Si, γ-$Ni_{31}Si_{12}$, β_1-Ni_3Si and Ni, which can accommodate up to 10 % of Si. Only a selection of these phases are observed when annealing a thin (e.g. 10 nm) film on a Si substrate (i.e. δ-Ni_2Si,

NiSi, $NiSi_2$). More intriguingly, the θ-Ni_2Si phase is also observed during the solid-phase reaction at low temperatures around 300 °C whereas this phase should only be stable at much higher temperatures according to the bulk phase diagram [9].

The initial formation of a specific silicide phase during a thin-film anneal is a process that, for simplicity reasons, can be ascribed to two main mechanisms. Firstly, an initial grain of the specific phase needs to nucleate from a reaction involving the metal atoms (M) and silicon atoms (Si) to form M_xSi_y. The thermodynamic parameters that govern this nucleation process are described in section 1.2. Secondly, the initially-small silicide grains then need to grow, a process that requires the migration of M and/or Si atoms towards the formation interface. A brief overview of the most important factors that can influence this diffusion are given in section 1.3. In general, one can state that the crystallisation of a silicide will be limited by one of these two mechanisms, and the reaction is thus either *nucleation-limited* or *diffusion-limited*.

A complete picture of the silicide phase sequence, however, requires taking into account all phases that are in competition with one-another during the thermal anneal. Therefore, the prediction of silicide formation is a challenging exercise.

1.2 CLASSICAL NUCLEATION THEORY

The initial nucleation process of a silicide grain can be understood through classical nucleation theory. This framework for silicide films is clarified with elaborate discussion in several review papers, such as the overview given by d'Heurle et al. [10], who was one of the pioneers in silicide research.

Classical nucleation theory is a thermodynamic model focusing on the change in energy due to the nucleation of a phase AB from two neighbouring regions A and B, as illustrated in figure 1.3a. When a specific volume of A and B is replaced by the AB grain, this will result in a change in free energy, as a difference in free energy per volume Δg_V will exist between the original volumes of A and B grains, and the novel AB grain. As the phase change should occur spontaneously at elevated temperatures, one may assume that the change in Gibbs free energy per unit volume Δg_V is negative. As such, larger volumes of the new AB phase will lower the total energy of the system. However, in addition to these volume energetic parameters, one should also take into account that the creation of a new phase requires the introduction of a new interface, and thus changes the total surface energy. Indeed, the nucleation of the new AB grain will elim-

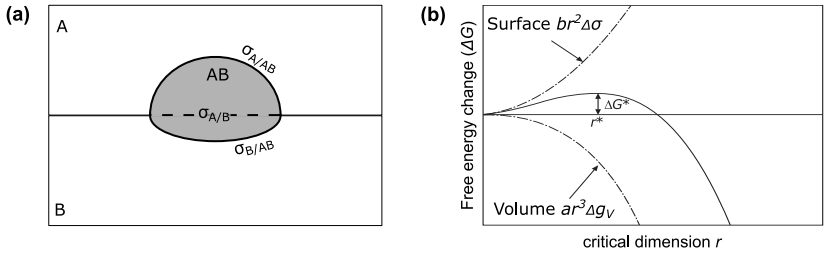

Figure 1.3: **(a)** schematic representation of the nucleation of a new crystal grain AB from two neighbouring A and B regions, **(b)** resulting in a change in total Gibbs free energy. This can be separated in Gibbs free energy per unit volume Δg_V and surface energy per unit area $\Delta\sigma$ as a function of critical dimension r. Adapted from [7, 10].

inate part of the interface between A and B ($\sigma_{A/B}$ in Fig. 1.3 a), which is replaced through the creation of new interfaces between A and B regions and the novel AB grain ($\sigma_{A/AB}$ and $\sigma_{B/AB}$ in Fig. 1.3a). The formation of this interface is then energetically represented through $\Delta\sigma$, the energy *cost* per unit area.

So, in order to nucleate a particle whose critical dimension scales with radius r, one may assume that the volume energy will scale with r^3, whereas the surface energy will scale with r^2. The net change in the total free energy ΔG of the system is then described by the equation:

$$\Delta G = -ar^3\Delta g_V + br^2\Delta\sigma \tag{1.1}$$

where a and b represent geometrical factors, dependent on the geometrical shape of the nucleating grain. The final energy balance is therefore a trade-off between volume and surface-energy, and is dependent on the critical dimension r, as depicted in figure 1.3b. The growth of a small grain, with a relatively large surface- to volume-energy ratio, will require an increase in energy ΔG. However, it is also clear from 1.3b that the growth of a bigger grain with a smaller surface- to volume-energy ratio will eventually result in a *decrease* of the total free energy ΔG upon growth. The switch-over between these regimes is thus a critical dimension r^*, which can be calculated through the first derivative of eq. 1.1:

$$r^* = \frac{2b\Delta\sigma}{3a\Delta g_V} \tag{1.2}$$

The corresponding total free energy ΔG^*, associated with a nucleus of size r^*, therefore represents the energy barrier that the system needs to overcome for the spontaneous formation of a stable AB grain:

$$\Delta G^* = \frac{4b^3 \Delta\sigma^3}{27a^2 {\Delta g_V}^2} \tag{1.3}$$

A higher energy barrier will therefore result in a more difficult nucleation of the silicide phase. When phase-formation is limited by the nucleation of the initial grains, it is considered a *nucleation-controlled* growth. In the following section we will consider the situation when nucleation is not a limiting factor, as only a small energy barrier is present.

The individual thermodynamic parameters Δg_V and $\Delta\sigma$ are not always available in the literature with satisfying precision to allow quantitative calculations. For the specific case of nickel silicides considered in this thesis, the enthalpy of formation are known for most phases, but their values are comparable (see Section 2.1), thus again hindering a quantitative approach. Therefore the classical nucleation theory is often used as a framework in order to qualitatively explain observed changes in the silicide formation with respect to the change in interface alignment or in entropy. The success of this model is illustrated by providing a successful framework to understand, for example, the influence of impurities on solid-phase reaction of Ni-silicides (see Chapter 3) or the thickness dependence of phase formation in the Ni-silicide system (see section 2.4).

1.3 FIRST PHASE SELECTION

As the pioneer of the classical theory of nucleation, d'Heurle also investigated the kinetics of silicide formation, with the emphasis on the first-phase formation [11]. In the initial situation of an as-deposited film on a Si substrate, the change in energy Δg_V through the formation of a silicide is considered sufficiently high for most silicides. As such, this would exclude nucleation as a selection criterion for the formation of the first silicide due to a low energy-barrier (eq. 1.3).

Instead, d'Heurle stated that here, *'One gets that which grows'* [11], as such proposing a diffusion-controlled growth of the first silicide. Through this simple rule, d'Heurle implies that the initial nucleation of different silicides should occur more-or-less simultaneously. Subsequently, it is proposed that the first *observed* silicide phase is that phase which can grow the fastest, potentially consuming other nucleated phases. The concept relies on the fact that high differences exist between atomic diffusion coefficients, which can differ by several orders of magnitude for different

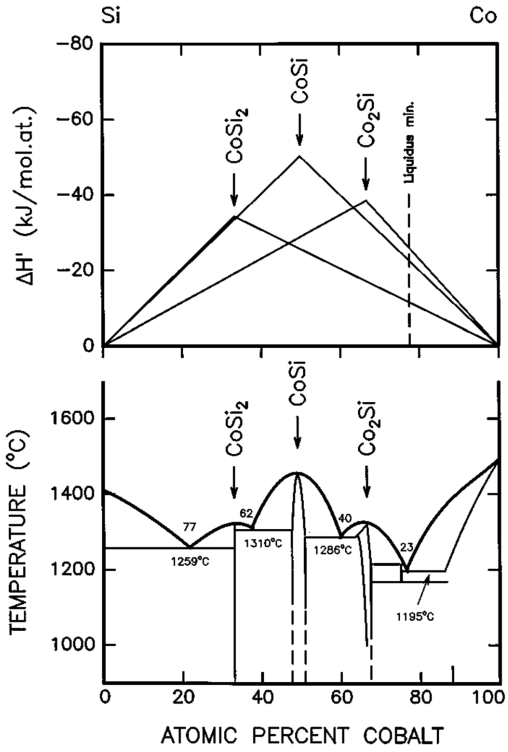

Figure 1.4: The effective heat of formation $\Delta H'$ diagram for compound phase formation (top) and the phase diagram (bottom) for the Co-Si system. Each triangle represents the evolution of the effective heat of formation as a function of effective concentration. Figure from [13].

silicide phases of the same binary compounds. However, the experimental determination of diffusion coefficients is a challenging task. This is due to the significant difference between these thin-film systems and the diffusivity derived from bulk materials, as the diffusion-rate in thin films at low temperatures is largely facilitated through grain boundaries instead of bulk-diffusion through the individual silicide grains. For example, Barge *et al.* [12] found that the diffusion in the Co-Si system is much faster in thin films than in bulk materials.

Alternatively, Pretorius *et al.* developed a model for determining the first formed phase based on the *effective* heat of formation (EHF) [13, 14], which was based on the preceding work of Walser and Bené [15]. According to Pretorius *et al.*, a model concerning the first phase formation

should take into account the effective concentration of the different participating elements at this reaction interface, given that a silicide is required to form between neighbouring atoms. Therefore, the EHF model considers a modified heat of formation $\Delta H'$, which is calculated as a function of the concentration at the reaction interface:

$$\Delta H' = \Delta H^0 \frac{\text{effective concentration of limiting element}}{\text{compound concentration limiting element}} \tag{1.4}$$

ΔH^0 represents the standard heat of formation of the forming silicide compound. The limiting element is that element which has a lower concentration at the reaction interface than the required concentration of the forming silicide. As an example, figure 1.4 represents the different $\Delta H'$ for the Co-Si binary system as a function of effective concentration. The enthalpy gain for a specific silicide is thus the highest when the effective concentrations of the reacting elements exactly match that of the silicide compound.

In order to predict the first phase formation, one should therefore know the effective concentration at the reaction interface. It is proposed that the effective concentration of two elements at the interface can be estimated to be the composition of the *liquidus minimum*, i.e. the concentration which has the lowest eutectic point in the phase diagram [16]. For the case of Co-Si phase formation, this model thus correctly predicts that Co_2Si is expected to form first upon annealing (Fig. 1.4).

The EHF theory is reported to predict most of the tested silicide systems. However, a quantitative application of the theory requires the thermodynamic data on ΔH^0, similar to the application of classical nucleation theory. These values are sometimes, as is the case of nickel silicdes, very comparable between the different phases. As such, the differences in ΔH^0 are not always sufficiently high in order to obtain a reliable prediction. For other phases, these thermodynamic values are not known at all. In addition, the first phase to form in silicides is not always straightforwardly detected. For example, recent investigation on the formation of nickel silicides reports on a yet unobserved epitaxial phase [9], formed simultaneously or prior to δ-Ni_2Si.

1.4 CONCERNING THE TEXTURE OF SILICIDE PHASES

The single-crystalline Si substrate can have a significant impact on the alignment of the individual silicide grains during the nucleation of silicide films. Indeed, the interface energy between substrate and silicide will be significantly different when the orientation of the silicide with respect

to the Si substrate is changed. Therefore, one can expect that silicides will orient preferentially to the substrate in order to reduce the interface energy. The statistical distribution of the orientation of the grains with respect to the substrate is also referred to as crystallographic *texture*. Several different types of texture can be identified: *epitaxial*, *fiber*, *axiotaxial* and *random* alignment. These alignment types identify the degree of order of the individual silicide grains' orientation, going from highly-ordered (epitaxial) to completely random. The alignment of an individual grain with the Si substrate will significantly influence the properties of that grain boundary such as diffusion, and the contact resistance between the semiconductor and the silicide.

The different types of texture can be explained in relation to the degrees of freedom available to the individual grains (Fig. 1.5). An *epitaxial* texture fixes the orientation of each grain, resulting in zero rotational degrees of freedom. The *fiber* and the *axiotaxial* textures allow a single degree of rotational freedom for each grain (e.g. one out of the three Euler angles). These textures pin the orientation of one specific crystalline direction of the grain (e.g. a crystal's plane normal). As this pinning eliminates two degrees of freedom, the fixed crystal normal acts as a rotational axis of symmetry. These two textures differ from one another in terms of the driving force causing them. Fiber texture originates from a minimisation of the surface energy by stacking closed-pack planes on top of the host substrate. The axiotaxial texture occurs due to a continuation of crystal planes through the interface between a grain and the underlying substrate. As a consequence, the rotational axis of symmetry is always observed perpendicular to the substrate for a fiber texture, whereas the axiotaxial texture does not have this limitation. Finally, for *random* oriented grains, no limitations are present and each grain has three rotational degrees of freedom.

The investigation of the silicides' preferential orientation with the underlying Si substrate is of significant importance for this work. Here, we have mainly employed X-ray diffraction pole-figure measurements in order to identify the different texture types and to determine which planes are periodically matching at the interface. In summary, a pole figure displays the diffracted intensity of a crystalline plane as a function of orientation with respect to the substrates' normal. To accomplish this, the sample is rotated around both *in-plane* and *out-of-plane* angles (ϕ and χ, respectively) and the measured intensities are presented using a stereographical projection. The resulting patterns are then dependent on the ensemble of alignments of the crystal grains in the sample, as illustrated in figure 1.6. A recent review of De Schutter *et al.* [18] provides a concise overview of

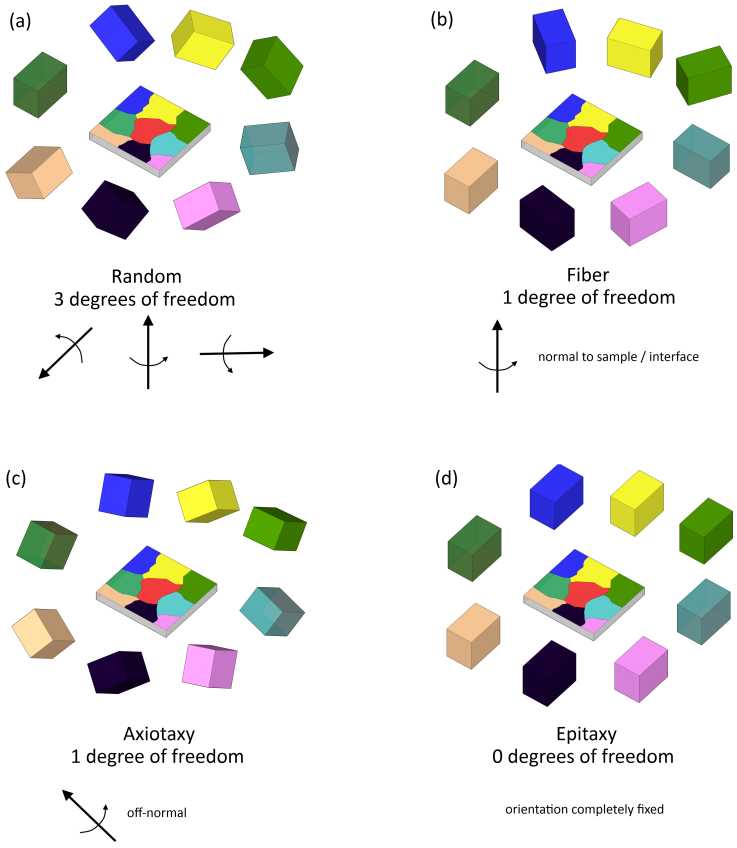

Figure 1.5: Different top views of a silicide films with multiple grains, each represented by a different color. The possible variation in the grain alignments are represented by the orientation of the crystal unit cell for different textures: **(a)** random, **(b)** fiber, **(c)** axiotaxy and **(d)** epitaxy. Figure from [17].

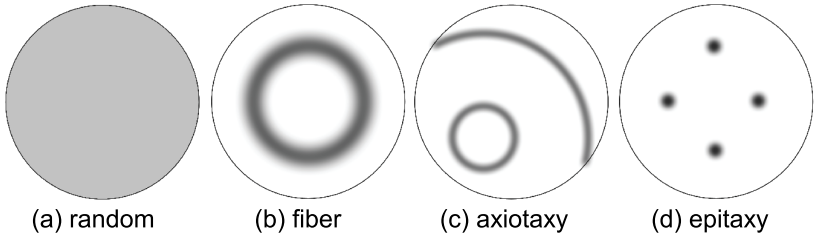

Figure 1.6: Schematic representation of different diffraction features as seen in a pole figure, indicative for the different textures. Figures from [17].

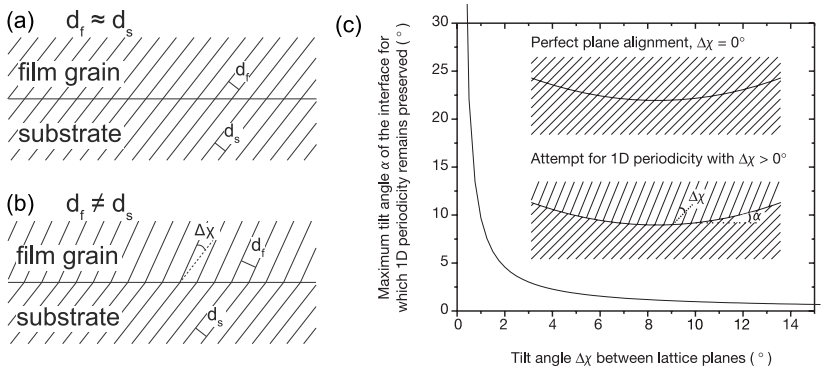

Figure 1.7: **(a)** An axiotaxial alignment between planes with a perfect match in d-spacing will result in repetitive matching of crystal planes along the interface. **(b)** If there is no perfect match in d-spacing, then a plane-to-plane match can still be maintained by introducing a small tilt $\Delta\chi$ to compensate the difference in plane matching. **(c)** However, the match will be sensitive to the curvature of the interface, breaking the periodic matching when a tilt angle α exceeds a specific angle. Thus a smaller $\Delta\chi$, or better matching d-spacings, will be more stable with respect to interfacial roughness. Figures from [18] and [19].

the many publications concerning preferential orientations of silicides and germanides. Readers who are interested in the measurement of XRD pole figures and how they can be easily identified are referred to Appendix B.

The physical origin of the axiotaxial alignment [19] is explained when a pair of low-index planes can be found between film and substrate which have reasonably similar crystalline d-spacings (e.g. the Si (220) and NiSi (211) planes both have a d-spacing of 1.92 Å). If those planes are aligned parallel across the silicide-silicon interface, then their similar d-spacing ensures a periodic match along the interface (Fig. 1.7a). Slight deviations from the perfect match in d-spacing does not necessarily imply that the periodicity is destroyed. Indeed, one can also try to align a pair of nearly-matching planes (e.g. the Si (220) and NiSi (112) planes have a d-spacing of 1.92 and 1.98 Å, respectively) by applying a small tilt $\Delta\chi$ (Fig. 1.7b). This compensation-mechanism can, in theory, also work for planes which significantly differ in d-spacing by introducing a relatively large $\Delta\chi$ angle. However, relatively high values of $\Delta\chi$ will only maintain periodicity for a perfectly flat interface, whereas a real physical interface will contain roughness. Figure 1.7c illustrates the match across the interface when interfacial roughness is present. A perfect alignment, $\Delta\chi = 0$, will be stable when the interface is drastically rough. For higher angles $\Delta\chi$,

matching can only be maintained for low interfacial roughness, which is parametrised through the inclination angle α. This is corroborated by experimental observations, where only axiotaxial alignments with $\Delta\chi < 5°$ are reported, in confirmation with these geometrical arguments.

Geometrical matching was also employed to understand, or even predict, epitaxial alignments between the silicide and the substrate. The epitaxial alignment requires at least two sets of plane-to-plane matches along the interface, in contrast to only one pair of planes required by axiotaxial alignment. For example, such alignment with the substrate can be found rather straightforwardly for $NiSi_2$, as $NiSi_2$ and Si share a cubic structure and only have a lattice mismatch of 0.46 %. The cubic unit cells can therefore form an epitaxial alignment through the trivial orientation defined by $NiSi_2(001)//Si(001)$ and $NiSi_2(100)//Si(100)$. Theoretical calculations by Zur *et al.* [20, 21] showed that the epitaxial alignment of $NiSi_2$ results in one of the lowest lattice mismatches and highest matching frequencies from the collection of then-known epitaxial silicides. However, silicide films with only a single epitaxial alignment are rare. More often, the silicide film tends to form a number of different orientations with respect to the substrate. For example, $NiSi_2$ will often form in two orientations, where the A-type orientation is a continuation of the Si lattice, as described previously, and the B-type results from a stacking fault caused by a 180° rotation of the $NiSi_2$ grain with respect to the Si(111) direction.

One can argue that the presence of an epitaxial interface will significantly lower the interface energy $\Delta\sigma$, and increase the adhesion and stability of the interface due to periodic chemical bonding [22]. Tung *et al.* [23–25] reported that an epitaxial $NiSi_2$ phase with only the type-A alignment and no type-B alignment has a lower contact resistance than a silicide film which contains both type-A and B epitaxies. Therefore, epitaxial silicides prove highly interesting in the search for low contact-resistance.

1.5 SILICIDES AND THEIR APPLICATION IN MOSFET DEVICES

Historically, the silicide was introduced in the MOSFET during the 1980's, more than two decades later than the initial development of the MOSFET by Kahng and Atalla at Bell labs in 1959 [26]. In the original design of the MOSFET, the local interconnections between devices were facilitated through highly-doped poly-crystalline Si. The reduction of the line width within the MOSFET, a trend driven by Moore's law, resulted in an increase in resistance of these poly-Si interconnects, and materials with a lower electrical resistance were required [4, 7]. As such, WSi_2 was first introduced for enhancing the electrical conductivity of the MOSFET, through the so-called

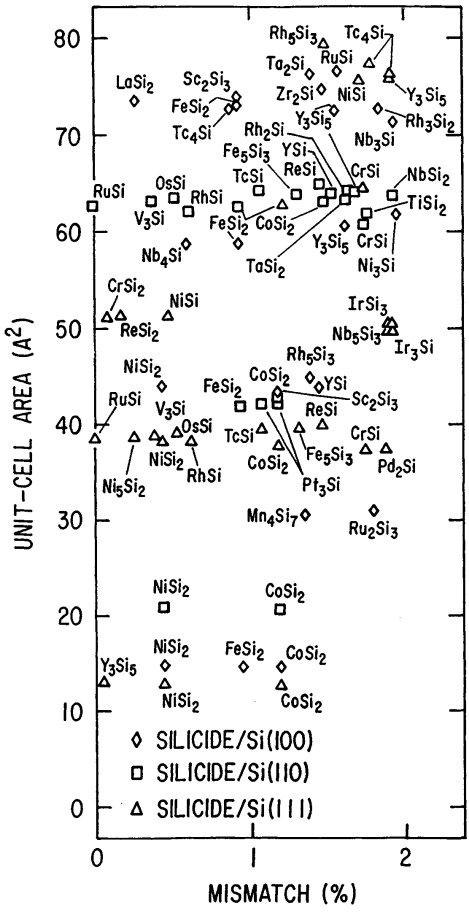

Figure 1.8: Lattice matching of metal silicides on silicon (100), (110) and (111) substrates at room temperatures. A lower lattice mismatch will result in a periodicity which is stable for over a large area of the silicide-silicon interfaces. A smaller unit-cell area will result in a higher frequency of matching per unit area. Figure from [20].

polycide process. This process, however, was limited to contact the gate with silicides that were stable during high temperatures anneals, which was required for the subsequent dopant activation in the semiconductor. The polycide process was then replaced by the salicide process described earlier for large scale integration, as it enabled to also address parasitic resistance in the source and drain regions.

Table 1.1: Properties of the silicide phases involved in salicide processes, including phases introduced through alloying or during the phase formation process. The first two columns indicate those parameters important to achieve a low parasitic resistance of the silicide contact: the Schottky barrier height Φ and bulk sheet-resistivity ρ. T_m represent the melting temperature of the silicide phase, according to the bulk equilibrium phase diagrams which are displayed in Appendix C. The formation temperature T_f, the dominant diffusing species (DDS) and kinetics provide information on the formation of the silicide during a SALICIDE formation process. Data from [7, 27] and references therein.

SILICIDE	Φ (eV)	ρ ($\mu\Omega$ cm)	T_f (°C)	T_m (°C)	DDS	KINETICS
C49-$TiSi_2$	n.a.	60-80	350-700	n.a.	Si	n.a.
C54-$TiSi_2$	**0.60**	**15-20**	**750**	**1500**	**Si**	**nucl.**
Co_2Si	n.a.	110	350	1334	Co	diff.
CoSi	0.68	147	375	1460	Si	diff.
$CoSi_2$	**0.64**	**15**	**500**	**1326**	**Co**	**mixed**
δ-Ni_2Si	0.65	24	250-400	1255	Ni	diff.
θ-Ni_2Si	n.a.	n.a.	250-825	1306	Ni	n.a.
NiSi	**0.65**	**10.5**	**250-400**	**992**	**Ni**	**diff.**
$NiSi_2$	0.65	34	700-800	981	Ni	nucl.
Pt_2Si	0.88	14-16	200-300	1100	Pt, Si	diff.
PtSi	0.85	28-35	300-500	1229	Pt, Si	diff.

Although most of the transition metals are able to form a silicide compound, and therefore more than a hundred silicide phases exist, only a fraction of these silicide materials were ever considered for contacts in the micro-electronics industry. Specific properties are required by the MOSFET technology, and therefore the silicide must, at least:

- exhibit a low sheet-resistivity ρ
- exhibit a low contact resistance with the semiconductor
- be compatible with other processing steps such as etching
- have limited metal diffusion as to avoid formation of accidental conduction paths

The industry has been using, in chronological order, C54-$TiSi_2$, $CoSi_2$ en NiSi as self-aligned silicide contact. Their characteristic properties are summarized in Table 1.1, together with other phases which are important for the overall solid-phase formation. A major advantage of these three silicides lies in their relatively low sheet resistivity and contact resistance. However, their formation properties differ significantly. For example, the formation of C54-$TiSi_2$ is limited by nucleation, while NiSi is limited through diffusion. This has significant impact on the final-formed silicide. On the one hand, a nucleation-limited process only has a small number of nucleation sites, and while the line width of the MOSFET was reduced, this resulted in a highly unpredictable phase transformation to C54-$TiSi_2$ and a high roughness, which was one of the prime reasons to abandon C54-$TiSi_2$ below the 25 µm node. On the other hand, a diffusion-controlled mechanism, such as the formation of NiSi, will result in a much smoother interface. However, we shall discuss in the following chapter that the high diffusion rate of Ni is paired with a higher tendency for agglomeration and unwanted Ni migration. More recently, Ni was replaced by the Pt-alloyed variant $Ni_{1-x}Pt_x$ as to enhance the stability of the phase (also further discussed in chapter 3). This results in the formation of $Ni_{1-x}Pt_xSi$, a solid solution of NiSi and PtSi. However, PtSi has almost three times the bulk resistivity of NiSi, thus the incorporation of Pt inside NiSi will increase the resistivity. Moreover, $Ni_{1-x}Pt_xSi$ could even have a higher resistivity due to alloy scattering [28].

With the introduction of fin-FET architecture for MOSFET, and the implementation of trench-contacts instead of SALICIDE contact formation, the use of $Ni_{1-x}Pt_xSi$ as contact material is less straightforward due to effects such as agglomeration and encroachment, as discussed in Chapter 7. This new device architecture altered some of the priorities on the silicides' characteristics, e.g. the silicide-to-silicon contact resistance becomes more important compared to the sheet resistivity for determining the overall parasitic resistance. As a consequence, Ti-based silicides are again observed in MOSFET devices from the 22 nm node.

1.6 OBJECTIVES OF THIS WORK

In this work, we investigated three aspects of the current trends in silicide research.

1. The effect of alloying on nickel silicide formation
2. The effect of thickness reduction on nickel silicide formation
3. The shift to Ti-based silicides.

The thesis is therefore divided into two parts, where the first part focuses on nickel silicides, and the second part focuses on titanium silicides. In the first part, we give an overview of the challenges for nickel silicides and how the addition of ternary elements can influence the phase formation of nickel-silicides and improve their final properties. In addition to the properties of NiSi, we also focus on the formation of epitaxial and morphologically stable $NiSi_2$. From the literature, it was found that the addition of Al significantly promotes the formation of epitaxial $NiSi_2$ with decreased interfacial roughness and low lattice mismatch with the Si substrate. We therefore investigated the changes of nickel silicide phase sequence as a function of Al concentration.

Furthermore, the phase formation sequence of nickel silicides was also investigated as a function of as-deposited Ni thickness. A radically different phase formation can be observed when going to '*ultrathin*' nickel films, e.g. below an as-deposited Ni thickness of 5 nm. This change in solid-phase reaction is the result of a complex balance in formation thermodynamics. Therefore, we explored how the phase formation of ultrathin nickel silicides is influenced through the incorporation of ternary elements.

The last part of this thesis provides an introduction to one of the most recent trends in silicide research. The motivation for an industrial shift from nickel-silicides to titanium-based silicide for state-of-the-art devices is first explained. Most of our current knowledge concerning titanium silicides is based on research dating from the 1990's. Since then, the experimental techniques have evolved considerably and new models on crystalline alignment have been developed as a consequence (e.g. axiotaxy). Therefore, we have re-visited the texture of the C54-$TiSi_2$ phase with modern techniques and report for the first time on the axiotaxial alignment of C54-$TiSi_2$.

Part II

NICKEL SILICIDES

2

NISI FORMATION AND DEGRADATION

The formation of nickel silicides has already been researched for over four decades. The phase sequence was initially established through a cook-and-look approach, where a Ni film was deposited on a Si substrate, subsequently annealed to specific temperatures and where the resulting silicides were investigated *ex situ*, i.e. at room temperature. As we will discuss further in section 2.1, this approach proved vulnerable as to miss phases which only exist within a limited temperature window, or which are unstable upon cooling. Nonetheless, this research resulted in the identification of the following sequential formation of silicides:

$$\mathrm{Ni} \rightarrow \delta - \mathrm{Ni_2Si} \rightarrow \mathrm{NiSi} \rightarrow \mathrm{NiSi_2}$$

The phase sequence indicates a first possible degradation mode of a NiSi-based contact; the NiSi phase is not thermodynamically stable when in contact with an excess of Si, as a transformation to $NiSi_2$ could occur at higher temperatures. However, it appears that this is not the most important degradation path to the thin NiSi film. Instead, Deduytsche *et al.* [1] showed that NiSi is far more sensitive to morphological degradation in the thickness regime of interest for MOSFET applications (i.e. $< 15\,\mathrm{nm}$). This implies that NiSi layers suffer from severe island formation upon annealing, thus destroying the low conductivity of the NiSi film, as explained in section 2.2. The physical origin of agglomeration can be linked with the crystallographic texture of the NiSi films and is further elaborated upon in section 2.3. The formation of NiSi is furthermore challenged through a significant change in the nickel-silicide phase formation sequence, occuring when the as-deposited Ni-film is reduced to thicknesses below 5 nm. This effect, which clearly also limits the applicability of NiSi as a contact material, is explained in section 2.4.

This chapter presents an overview on the known formation process of NiSi and the major challenges for stabilisation. The different degradation mechanisms of the phase are summarised at the end of this chapter. Fortunately, these degradation paths of nickel silicide can be significantly influenced through the introduction of alloying elements which shall be the subject of the following chapters.

2.1 NICKEL SILICIDE FORMATION: RECENT ADVANCES

The introduction of *in situ* measurement techniques allowed a continuous monitoring of the nickel-silicide formation process during heating, which proved the assumed phase sequence, as described above, to be incomplete. This is illustrated in figure 2.2, where an *in situ* X-ray diffraction (XRD) measurement shows the diffraction pattern of the silicide as a function of temperature. The angular position of the individual diffraction peaks is related to the crystalline structure present at that temperature, and can be used to identify the occurring phases (figure 2.1). From the peak positions, one can easily identify the occurrence of δ-Ni_2Si and NiSi (and $NiSi_2$ at higher temperatures). However, the additional diffraction peak observed near $2\theta = 56.5°$ in the small temperature window around 345 °C indicates the presence of an additional phase. Initially, this phase was identified as an orthorhombic Ni_3Si_2 phase [3] but more recent research identified this peak as the hexagonal θ-Ni_2Si phase [4, 5].

By comparing the temperature at which θ-Ni_2Si can be observed during *in situ* XRD and its location on the Ni-Si phase diagram (Fig. 1.2), one can make two remarkable observations. Firstly, the phase diagram shows that θ-Ni_2Si is only stable for temperatures higher than 825 °C, far higher than the temperature where this phase is observed in thin-film research. One has to keep in mind, however, that this phase diagram refers to steady-state equilibrium phases on bulk material, which is not the case during the thin-film *in situ* experiments. Secondly, the phase can exist over a broad compositional range, which can go from 33 % Si concentration up to 40 %.

The presence of θ-Ni_2Si around 300 °C seems exceptional and therefore requires some discussion on the possible mechanisms which allow its formation at low temperatures. This is often addressed as an indication that this phase is capable of enduring significant differences on lattice mismatch or a gradient in Si concentration throughout the film, in contrast to a line-phase such as δ-Ni_2Si or NiSi. Gaudet *et al.* [5] furthermore estimated the free energy diagram for nickel silicide phases near 300 °C, displayed in figure 2.3. As no thermodynamic data were available for θ-Ni_2Si, they estimated its curve's position based upon their experimental observations. They concluded that the phase should only be kinetically favoured at low temperatures under specific conditions. This promotion of θ-Ni_2Si formation is proposed to occur through a texture-inheritance mechanism, which would significantly lower the required atomic mobility to form the phase. The reported values of enthalpy of formation reveal that these values are relatively comparable: δ-Ni_2Si: -46.9, NiSi: -42.4, $NiSi_2$: 29.3 kJ/mol of Atoms [6]. The differences between these values are rather small, espe-

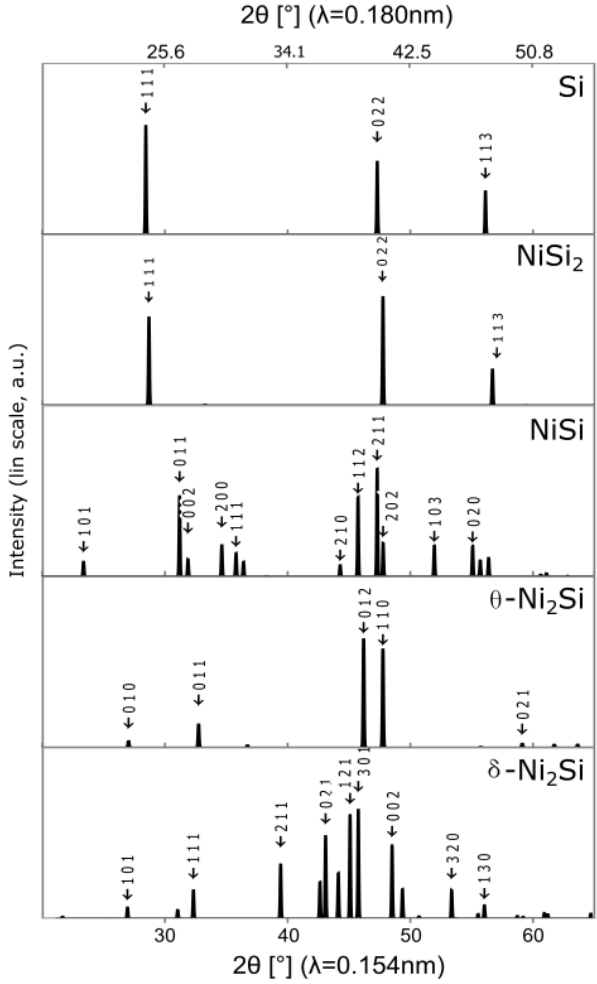

Figure 2.1: Simulated XRD diffraction patterns of the relevant nickel silicide phases in this thesis. The bottom x-axis represents the diffraction angle for x-rays with $\lambda = 0.154\,\text{nm}$, the top x-axis for $\lambda = 0.180\,\text{nm}$ (note that the top x-axis is not linear). Data from JCPDS 00-027-1402, 03-065-2974, 03-065-1475, 01-073-2093 and 00-048-1339

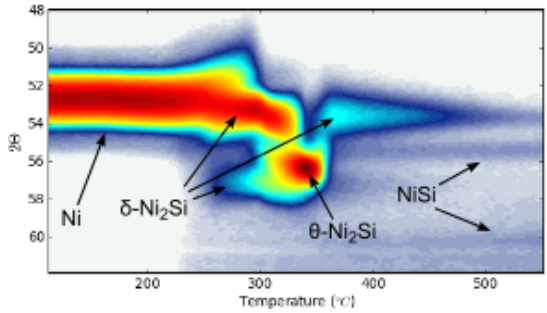

Figure 2.2: *In situ* X-ray diffraction measurement during the annealing of a 10 nm Ni film on a Si(001) substrate ($\lambda = 0.18$ nm). The diffractograms show a complex phase formation sequence between the consumption of the as-deposited Ni film and the formation of NiSi. Adapted from [2].

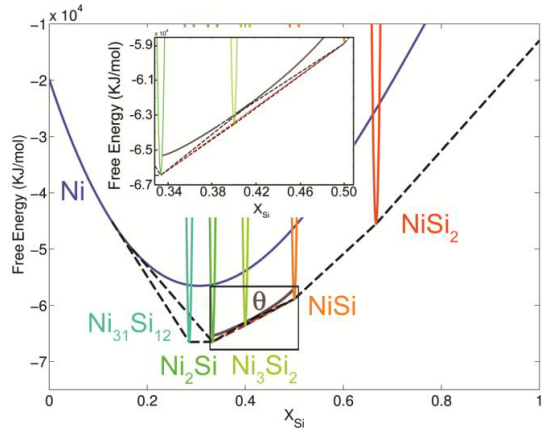

Figure 2.3: The free energy curves of several nickel silicides at 300 °C. The curve for θ-Ni_2Si is estimated from qualitative observations by *in situ* XRD and *ex situ* pole figures. Figure from [5].

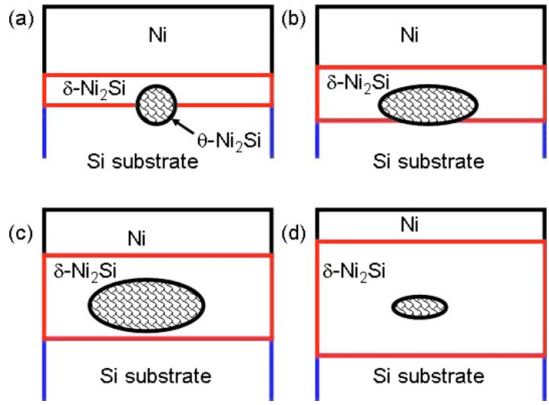

Figure 2.4: Schematic model for the behaviour of δ-Ni_2Si and θ-Ni_2Si. The model was used to simulate *in situ* XRD and differential scanning calorimetry during annealing of a relative-thick (i.e. 60 a*nd*100 nm) as-deposited Ni films on Si(001). Figure from [7].

cially considering that the error on these measurements can be estimated as heigh as 10%. As such, it can be expected that the kinetics of the nickel silicide solid-phase reaction can be influenced through other parameters such as interface energy, annealing conditions and the addition of ternary elements.

The evolution of these metal-rich silicides during annealing was further investigated by Mangelinck *et al.* through complementary *in situ* measurement techniques on relatively thick as-deposited films (e.g. > 60 nm) [7, 8]. A model was proposed by Mangelinck *et al.* concerning the formation and consumption of δ-Ni_2Si and θ-Ni_2Si (Fig. 2.4. (a) First, the δ-Ni_2Si phase grows from the as-deposited Ni film until a critical thickness is reached at which θ-Ni_2Si nucleates and grows laterally. (b) The lateral growth of θ-Ni_2Si partially consumes δ-Ni_2Si, while the δ-Ni_2Si phase is still growing at locations that are not covered by θ-Ni_2Si. (c) The growth of the δ-Ni_2Si phase will separate θ-Ni_2Si from the Si substrate and θ-Ni_2Si-grains will be enclosed by δ-Ni_2Si, (d) where after δ-Ni_2Si consumes the θ-Ni_2Si.

This model, initially developed for 30 nm and thicker Ni films, could significantly differ from the situation of thinner films. Gaudet *et al.* argue that θ-Ni_2Si can only be energetically favoured at low temperatures due to a small shift in formation energy. As the formation energy is a combination of volume-energy Δg_V and surface-energy $\Delta\sigma$ terms, one can expect that the reduction of thickness will alter the net balance, as surface-energy will increase in importance. Therefore, the nucleation and growth of θ-Ni_2Si can be significantly different for thinner films. Furthermore, the

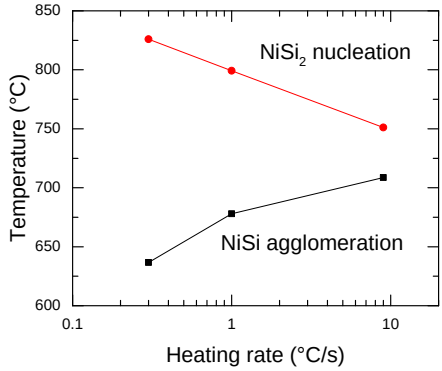

Figure 2.5: NiSi agglomeration temperatures and $NiSi_2$ nucleation temperatures as determined from annealing a 10 nm Ni film on top of poly-crystalline Si substrate at different ramp rates. Adapted from [1].

pole-figure measurements of Gaudet *et al.* [5] also indicated that an additional, epitaxial, phase is also present during the formation of metal-rich silicides. Our own work, presented in chapter 5 further elaborates on the low-temperature formation of the θ-Ni_2Si phase, and how texture inheritance in combination with an epitaxial alignment with the Si substrate contributes to a reduced nucleation barrier.

2.2 NISI PHASE STABILITY AND AGGLOMERATION

The two main mechanisms of NiSi degradation, i.e. NiSi agglomeration or $NiSi_2$ nucleation, were investigated by Deduytsche *et al.* [1]. The stability of NiSi films was investigated through *in situ* X-ray diffraction (for observing $NiSi_2$ nucleation) and *in situ* four-point resistance measurements (for observing agglomeration of NiSi) as a function of annealing rate, substrate orientation and as-deposited Ni thickness. As the formation of $NiSi_2$ is nucleation-controlled, due to a low gain in enthalpy ΔH, one could argue that a slower ramp rate would provide a higher thermal budget, as the sample remains longer at each temperature. Therefore, one would expect the nucleation of $NiSi_2$ to occur at lower temperatures for slower ramp rates, in agreement with the theory of Kissinger for studying the kinetics of solid-phase reactions [9]. Surprisingly, the nucleation temperature of $NiSi_2$ shifted towards *higher* temperatures as a function of decreasing annealing ramp rate (Fig. 2.5).

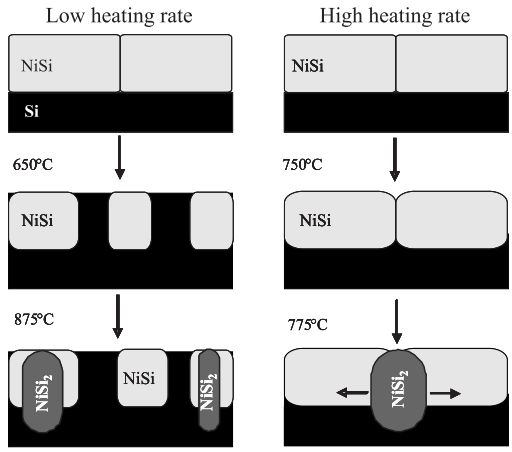

Figure 2.6: Schematic overview on the influence of heating rate on the nucleation of thin NiSi films. Adapted from [1].

This odd observation can be understood when considering changes of the agglomeration behaviour. Similar to the nucleation of $NiSi_2$, one can expect that a slower temperature anneal will also provide a higher thermal budget to induce NiSi agglomeration. Figure 2.5 depicts that NiSi agglomeration occurs at lower temperatures for lower ramp rates. Deduytsche *et al.* then consider that the two degradation mechanisms are in competition with one another, as illustrated in the schematic representation of figure 2.6. For all measured ramp rates, the agglomeration of NiSi occurs prior to the nucleation of $NiSi_2$. The agglomeration process starts at lower temperatures for lower ramp rates, and therefore a slower ramp rate will result in a more degraded morphology at higher temperatures. Therefore, when the $NiSi_2$ nucleates on a severely agglomerated film (e.g. low annealing rate), the growth of a $NiSi_2$ nucleus will only transform a single NiSi-island, whereas if $NiSi_2$ nucleates in a less-agglomerated film (e.g. high annealing rate), the $NiSi_2$ nucleus can grow to span a much broader area, and thus will affect a much higher fraction of the silicide film. Therefore, a severely agglomerated film will be required to initiate nucleation in all of the individual NiSi islands. For smaller islands, this will require a significant higher thermal budget. This was also observed through the slower increase in diffraction intensity of $NiSi_2$ for slower ramp rates.

Due to the continued miniaturisation in micro-electronics industry, the silicide films are trending to thinner films. From equation 1.1 it follows that such a thickness reduction, corresponding to a limit on the critical

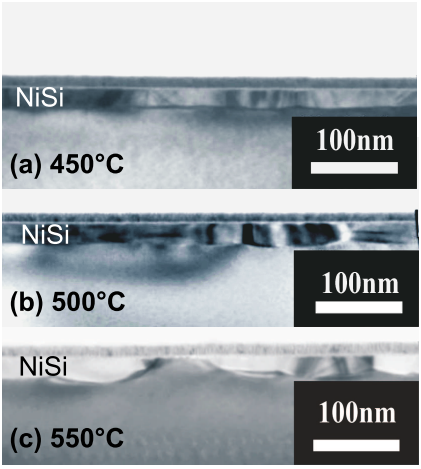

Figure 2.7: TEM cross section for the evolution in grain morphology for a NiSi film on a SOI substrate. A 10 nm Ni layer was heated for 80 s to 450, 500 and 550 °C, respectively. Figure from [1].

dimension r, will increase the relative importance of the interfacial energy. As agglomeration is clearly driven by the reduction of interfacial energy, thinner silicide films are expected to agglomerate more severely. This is indeed confirmed through *in situ* four-point probe measurements by Deduytsche *et al.* for different as-deposited Ni thicknesses [1]. By consequence, the primary mechanism of degradation of thin Ni layers, e.g. grown from a Ni layer with a thickness smaller than 15 nm, is clearly the agglomeration of NiSi, whereas $NiSi_2$ nucleation occurs mainly at higher temperatures, similar to the experiments with different heating rates.

It is worth noting that NiSi agglomeration only results in a roughening at the silicon-silicide interface, while the top surface of NiSi remains remarkably flat (Fig. 2.7). Moreover, NiSi appears to be significantly more sensitive to morphological degradation on mono-crystalline silicon-on-insulator (SOI) substrates in comparison with NiSi formed on poly-crystalline Si. This is illustrated in figure 2.8, where a SEM picture shows a significantly different roughness for NiSi formed on the gate (poly-Si) versus on the source/drain (SOI, mono-crystalline Si) regions of a patterned MOSFET device structure. Both observations suggest that the minimisation of the silicon-silicide interface energy is the main driving force for agglomeration, and not the silicide-silicide or silicide-surface interface, and that some crystalline orientation-dependence is involved.

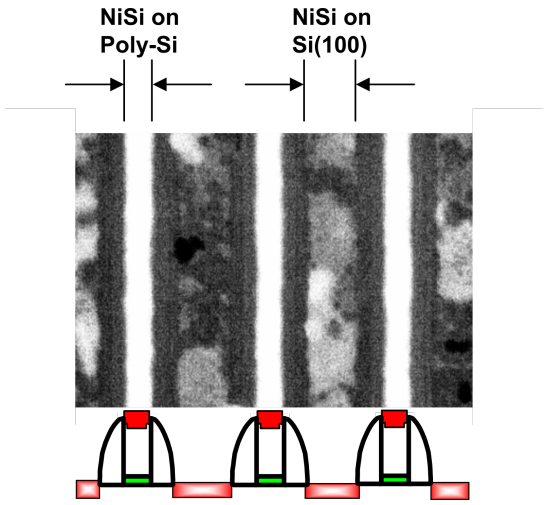

Figure 2.8: Top-view SEM image of NiSi lines formed on poly-crystalline Si (gate region) and single-crystalline SOI (source and drain regions). Although a uniform heat threatment was provided for all NiSi lines, a significantly rougher film is observed for NiSi lines on SOI regions. Figure from [1].

2.3 TEXTURE CONSIDERATIONS ON AGGLOMERATION

The crystalline alignment of NiSi on single-crystal Si substrates facilitates a peculiar texture with the underlying Si substrates. As an illustration of this, figure 2.9 displays the pole figures of the NiSi(112) diffraction plane as a function of quenching temperature. The most intense (red) spots are originating from the Si substrate (i.e. Si(202) diffraction peaks). In addition to these spots, (partial) circular features can be observed, whose center of rotation is around such Si(202) peaks and which are indicative for *axiotaxial* texture.

These circular features become more pronounced as a function of increased quenching temperature, as the background intensity is reduced and the circular features increase in intensity. As an increased quenching temperature coincides with a more agglomerated film, figure 2.9 indicates a possible correlation between axiotaxy and agglomeration. This correlation was first suggested in the first papers on axiotaxy by Detavernier *et al.* [11, 12], and Deduytsche *et al.* proposed that the observed higher sensitivity to agglomeration on single-crystal substrates in comparison with poly-crystalline Si could possibly be explained through axiotaxy [1]. Clear experimental evidence for such correlation was provided by De Keyser *et al.* [2] as shown in figure 2.10, where the diffraction intensity is plotted

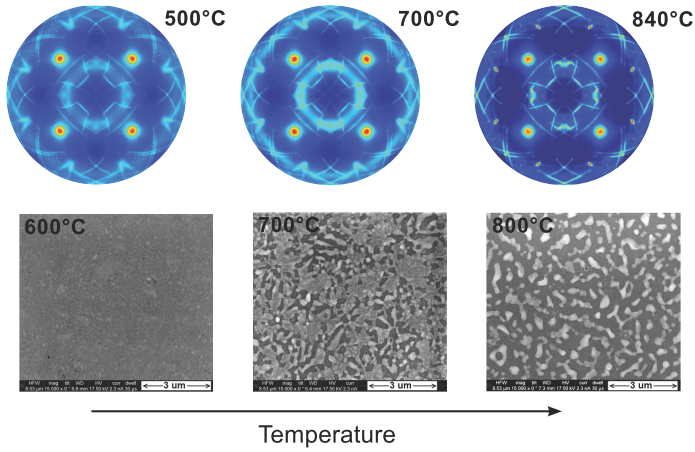

Figure 2.9: (112) pole-figure measurements (top) and SEM (bottom) images of NiSi films after quench-annealing a 20 nm Ni layer on top of Si(001) at a rate of 3 °C s^{-1} to different temperatures. Adapted from [2, 10].

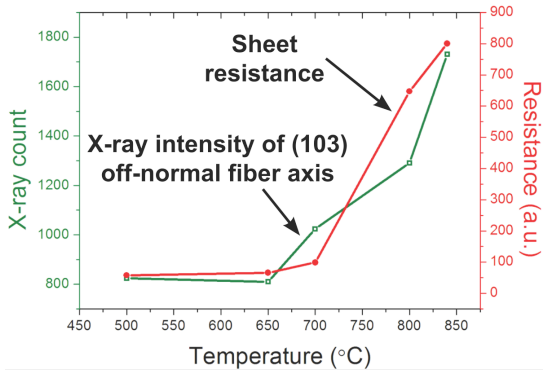

Figure 2.10: The evolution of the measured XRD-intensity of the NiSi(103) diffraction at the χ and ϕ position of the off-normal rotation-axis as obtained from NiSi(103) pole figures taken on quenched samples. The morphological degradation of the samples is characterised by the rise in the sheet resistance values. Adapted from [2].

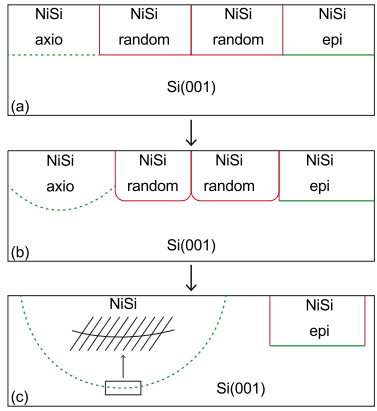

Figure 2.11: Schematic representation of grain boundary grooving between different types of NiSi texture alignments for increasing thermal budget. High, medium or low interface energies are represented by a red, dashed-green or full-green line, respectively. Figure from [2].

of the $(103)_{NiSi}$ axiotaxial alignment together with the measured sheet resistance. From these measurements, one can observe a clear correlation in increase in diffraction intensity and the increase in the sheet resistance of NiSi due to morphological degradation. This correlation can be rationalised through the physical origin of axiotaxial alignment.

As explained in chapter 1.4, axiotaxy originates from the plane-to-plane alignment between the film and substrate. Such a match could easily form, provided a pair of planes exist with similar d-spacings. The axiotaxial alignment of NiSi on Si(001) was linked to the alignment of four different NiSi planes with Si(022) ($d = 1.92\,\text{Å}$): NiSi(202) ($d = 1.92\,\text{Å}$), NiSi(211) ($d = 1.92\,\text{Å}$), NiSi(103) ($d = 1.78\,\text{Å}$) and NiSi(112) ($d = 1.98\,\text{Å}$) ([11]. For those matching planes where Δd is reasonably low, such as for Si(022) with NiSi(211) or NiSi(202), the periodic plane alignment between film and substrate will endure a roughening of the silicon-substrate interface (Fig. 1.7c). Thus, the axiotaxial alignment will persist during the roughening of the interface upon agglomeration. However, for larger values of $\Delta\chi$, there will exist a maximum curvature angle α of the interface at which the one-dimensional periodicity remains preserved, as depicted in figure 1.7c.

As axiotaxy results in a one-dimensional periodicity, it can therefore be considered as a mediocre-ordered texture alignment, which is more ordered than a randomly-aligned texture (no periodicity) but less ordered than an epitaxially-aligned texture (two-dimensional periodicity). By consequence, one can expect that the total interface-surface energy is the high-

est for an ensemble of randomly-aligned grains, lower when the grains are axiotaxialy aligned and the lowest for an epitaxial alignment, provided that the latter two alignments are crystallographically possible. As the NiSi agglomeration process strives for a reduction of the surface energy, one can thus expect that interfaces of randomly-oriented grains will be avoided. By consequence, we expect mass transport from the randomly-oriented grains towards either axiotaxial or epitaxial grains. Through this process, the interface between the epitaxial or axiotaxial grains will curve through the island-formation as mass migrates from randomly textured grains towards the textured grains. However, an epitaxially-aligned interface does not guarantee high flexibility for such changing interfaces, in contrast to axiotaxy, as interface curving would destroy the two dimensional match at the interface. Grain boundary grooving would therefore prefer the growth of axiotaxially-aligned grains instead of epitaxially-aligned grains, as illustrated in figure 2.11. The growth of axiotaxial grains would maintain a low interface energy, while minimising the interface area.

One can subsequently question why agglomeration of NiSi is less of an issue on poly-crystalline Si substrates, as discussed in the previous section. this substrate lacks the uniformly-aligned crystal substrate. Therefore, a NiSi grain which is locally axiotaxially-aligned with a single Si-grain will not be able to grow while keeping a low interface-energy, as the axiotaxial alignment will not be preserved when the growth would exceed to a neighbouring Si grain, which will have a different orientation. The physical plane-to-plane match formed for axiotaxial aligned grains therefore explains the increase of axiotaxial diffraction patterns with quenching temperature, and also the substrate-dependence of agglomeration.

2.4 ALTERED NICKEL SILICIDE FORMATION FOR SUB-10NM FILMS

As described in previous sections, the constant drive for thinner silicide contacts in the micro-electronics industry will render these silicide films more sensitive to agglomeration. The morphological degradation of such nickel silicide films can be monitored through *in situ* sheet resistance measurements, as agglomeration will destroy conductive paths of the silicide, thus resulting in an increase in the measured resistance.

Figure 2.12 displays the evolution of the sheet resistance of a Ni film on top of a SOI substrate as a function of temperature for different as-deposited Ni thicknesses. For temperatures below 200 °C, the sheet resistance displays a rather stable evolution, and no changes in the crystalline phase of the as-deposited film is expected. The resistance then drops to

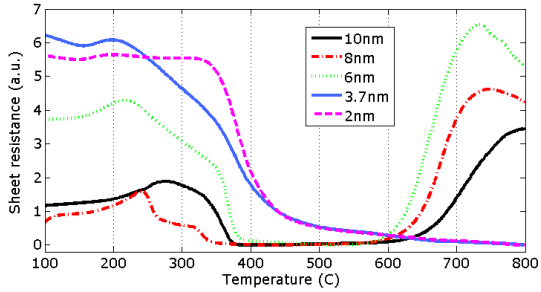

Figure 2.12: *In situ* sheet resistance as a function of temperature and thickness for thin nickel films on SOI. Figure from [13].

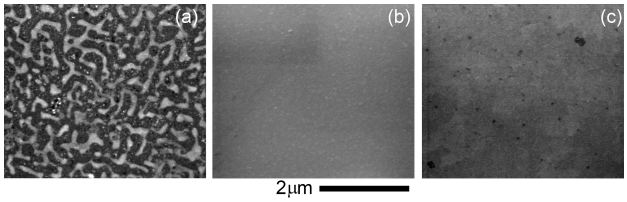

Figure 2.13: Top-view SEM images of quenched-annealed Ni films on top of a Si(001) substrate. **(a)** 6 nm Ni film annealed up to 650 °C, **(b)** 3.7 nm Ni film annealed up to 650 °C and **(c)** 3.7 nm Ni film annealed up to 850 °C. Figure from [13].

lower values between 200 and 450 °C after going through a complex sequence of high-resistive, metal-rich, nickel-silicides, where after a low-resistive nickel silicide is formed. Two different trends of the sheet resistance can then further be distinguished. For thicker films, e.g. 10 , 8 and 6 nm, the low resistance is only stable for a limited temperature range, as an increase in resistance is measured above 600 °C. This behaviour is indicative for the morphological degradation of the formed NiSi film. As described in section 2.2, the agglomeration temperature indeed decreases upon decreasing the silicide film thickness. Surprisingly, this trend only holds true for as-deposited Ni films above 5 nm thickness. For thinner films, e.g. 3.7 and 2 nm Ni films, the resistance does not increase after the formation of the low-resistive silicide. In fact, a slow, continuous, decrease is observed during the full remaining temperature anneal. The morphological stability of these '*ultrathin*' nickel silicides was corroborated with SEM images from a Ni film of 3.7 nm as-deposited thickness, after quenching it at 650 and 850 °C (Fig. 2.13), indeed showing no signs of agglomeration. The lack of agglomeration is in fact originating from the absence of the NiSi phase altogether, and instead low-temperature $NiSi_2$ is reported to form [13–15]. Interestingly, the formed $NiSi_2$ layer is aligned *epitaxially* with the Si substrate. This alternative phase sequence was already reported by Tung *et al.* in the 1980's, as observed from TEM measurements [16, 17]. The establishment of an epitaxial alignment between $NiSi_2$ and Si is no surprise: both structures share a face-centred cubic crystal structure with only a difference of 0.46 % in lattice parameter (5.406 and 5.431 Å for $NiSi_2$ and Si, respectively). Zur *et al.* [18, 19] (see Section 1.4) calculated that $NiSi_2$ can in fact form a single-crystal-like heteroepitaxy with Si, with one of the lowest mismatches in comparison with all the transition-metal silicides that were then known to grow epitaxially to either Si(100), (110) or (111) planes. Therefore, an epitaxial alignment would render very high periodicity along the interface and thus significantly reduce the interface energy.

This epitaxial alignment also allows to interpret this altered phase sequence for thinner as-deposited Ni-films. Through classical nucleation theory, described previously in Section 1.2, we know that the initial nucleation of a silicide phase requires to overcome a specific energy barrier ΔG^*. The driving force, driven by the change in gibbs-free volume energy Δg_V, needs to compete with the energy cost $\Delta\sigma$ through the formation of the interface. We established in equation 1.1 that the energy scales as

$$\Delta G = -ar^3\Delta g_V + br^2\Delta\sigma \tag{2.1}$$

Therefore, a thinner silicide thickness, corresponding with a decrease of the critical dimension r, will in fact reduce the driving force by a factor

raised to the third power, while the energy cost is only reduced by a factor raised to the second power. Therefore, the energy cost $\Delta\sigma$ will become more and more important for thinner films in terms of initial nucleation. The formation energy of the three most-important nickel-silicide phases are of the same order-of-magnitude: $\delta - Ni_2Si$: -46.9, $NiSi$: -42.4, $NiSi_2$: 29.3 kJ/mol of atoms [6]. Therefore, thicker silicide films will only form $NiSi_2$ when higher thermal budgets are applied as it has the lowest formation energy. However, thinner films will favour that phase which has the lowest possible $\Delta\sigma$. As an epitaxial orientation will significantly lower $\Delta\sigma$, an epitaxial-aligned phase will be preferred for thinner films over random or axiotaxially-aligned phases. As no highly-reproducable interface is observed between δ-Ni_2Si or NiSi and the Si substrate, we can understand the promotion of epitaxial $NiSi_2$ for thinner films. [13–17].

The formation of ultra-thin, epitaxial $NiSi_2$ has been recently applied for silicon-based solar cells. The layers showed improved performance through excellent wafer uniformity, high optical transparency and high hole conductivity [20, 21]. This illustrates the technological potential of these ultra-thin epitaxial silicide films.

2.5 FORMATION AND DEGRADATION OF NISI: SUMMARY

This chapter can be summarised through the schematic representation in figure 2.14, where we have indicated the occurrence of stable, low-resistive silicides as a function of temperature and as-deposited Ni thickness. Two regimes are clearly present, namely the regular '*thin*' phase formation regime and the '*ultrathin*' phase formation regime, which are separated through a critical thickness t_c. The former regime, for which agglomeration is the main degradation mechanism, has been studied thoroughly in the literature. A common strategy to delay agglomeration can be found by alloying the as-deposited Ni film with ternary elements, as indicated by the full-line arrows in figure 2.14. As such, the following chapter provides a brief overview on a selection of alloying materials, including the technologically-relevant incorporation of Pt. This work then expands on the influence of ternary elements on the nickel phase formation through a detailed study of the effect of aluminum-alloying in Chapter 4. We report in Chapter 5 on the remarkable difference in phase formation by comparing the phase sequence from the 'ultrathin' and the 'thin' nickel silicide formation. The chapter furthermore explains how Al, Co and Pt-alloying each uniquely change the phase formation above and below the critical thickness and how they influence the preferential alignment of the formed silicides with the Si substrate. Finally, we conclude this part in

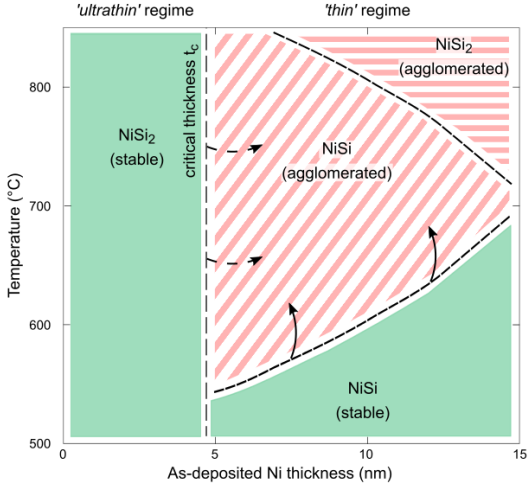

Figure 2.14: Overview of the thermodynamic and morphological stable regimes for nickel silicides as a function of thickness and annealing temperature. To form a stable silicide, one could attempt to either delay the agglomeration temperature (vertical arrows, chapters 3, 4 and 5) or to increase the thickness regime of stable ultrathin $NiSi_2$ formation (horizontal arrows, chapters 5, 6).

Chapter 6 on nickel silicides by researching the specific value of the critical thickness t_c which separates the '*ultrathin*' and '*thin*' nickel-silicide formation regimes from one-another. As we have illustrated in this chapter, the sudden promotion of low-temperature $NiSi_2$ can be interpreted through a complex energy balance. Therefore we investigated how Al, Co and Pt-alloying can alter this delicate energy balance, thus influencing the critical thickness as indicated through the dashed arrows in figure 2.14.

3 ALLOYED NICKEL SILICIDES

The addition of an alloying element to the SALICIDE process can significantly affect the formation and thermodynamic stability of the silicide compound. Unfortunately for the solid-state researcher, the addition of a third element drastically increases the complexity of the silicide reaction, and therefore ternary systems are far less understood than binary systems. The possibility of ternary impurities adds a whole range of parameters (e.g. the choice of ternary element, the quantity or the position relative to the metal: as an alloy, interlayer or capping layer) that can influence the formed silicide and its properties. Ternary silicide systems therefore have a great potential for technological applications. One of the great successes of alloys can be found in the nickel silicide used in MOSFET transistors, where the addition of Pt [1] proved to delay the degradation of NiSi by avoiding both agglomeration and $NiSi_2$ nucleation. The Ni(Pt) alloy therefore replaced pure Ni silicides for smaller MOSFET devices. In the following section, we expand the framework of classical nucleation theory to include ternary elements. Thereafter, we provide an overview on alloyed-nickel silicide formation, with emphasis on those elements which will be subject of interest throughout the course of this work: Al, Co and Pt. This allows us to illustrate the applicability of the classical nucleation theory, but also its limitations as the model does not explain all experimental observations. We therefore also discuss alternative models to explain the effects of ternary elements.

3.1 ALLOYING THROUGH CLASSICAL NUCLEATION THEORY

The effect of alloying on silicides is often discussed within the framework of classical nucleation theory, through the effect of entropy S. Indeed, eq. 1.3 from chapter 1 can also be expressed as [2]:

$$\Delta G^* \propto \frac{\Delta\sigma^3}{(\Delta H_V - T\Delta S)^2} \tag{3.1}$$

where ΔH_V is the change in enthalpy per unit volume.

In most cases, and especially during the initial phase formation, the value of ΔH_V is sufficiently large, and the effect of $T\Delta S$ can be neglected. However, the gain in enthalpy is much smaller for nucleation-controlled

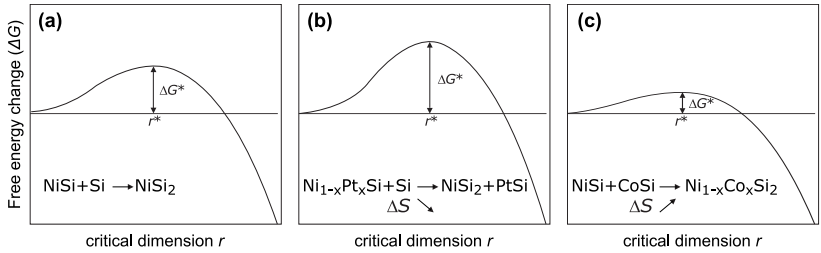

Figure 3.1: Illustration of the effect of alloying on the $NiSi_2$ nucleation barrier, resulting from the change in entropy through the addition of ternary elements. Pt and Co are highly soluble in NiSi and $NiSi_2$, respectively, due to the existence of a isomorph PtSi and $CoSi_2$ phase, thus enabling the creation of a solid solution with NiSi and $NiSi_2$, respectively. Adapted from [2].

phase transitions. For these phase formations, the contribution of *entropy of mixing* can have significant impact on ΔG.

As an example, we consider the nucleation of $NiSi_2$ out of NiSi, as illustrated in figure 3.1. We consider Pt as an alloying element, which is more soluble in NiSi than in $NiSi_2$. Its solubility in NiSi allows the formation of a solid solution, where the position of Pt can randomly replace Ni in the crystal lattice, thus forming $Ni_{1-x}Pt_xSi$. The low solubility in $NiSi_2$ does not allow such a solid solution, and instead the system will secrete Pt atoms and form a two-phase system consisting of separate $NiSi_2$ and PtSi grains. Therefore, the entropy of $Ni_{1-x}PtSi$ will be higher than when a phase transition to $NiSi_2$ would occur. The nucleation of $NiSi_2$ will thus result in a decrease in entropy, and $\Delta H_V - T\Delta S$ will become less negative. The result is that the diffusion barrier ΔG^* for $NiSi_2$ nucleation will be increased due to Pt alloying (eq. 3.1). On the opposite side, Co has a much higher solubility in $NiSi_2$ than in NiSi, and so increases the gain in entropy upon $Ni_{1-x}Co_xSi_2$ nucleation, and by consequence lowers the $Ni_{1-x}Co_xSi_2$ nucleation barrier. The entropy-of-mixing argument has been used in a significant amount of silicide formation systems, as illustrated in the following sections of this chapter.

For the formation of $NiSi_2$ out of NiSi, the entropy-of-mixing argument allows us to distinguish three classes of ternary elements, i.e. those elements which are [3]:

1. soluble in NiSi and less soluble in $NiSi_2$ (e.g. Ge, Pd, Pt)
2. soluble in $NiSi_2$ and less soluble in NiSi (e.g. Al, Co, Fe)

3. not significantly soluble in NiSi or $NiSi_2$ (e.g. Ti, Ta, W)

Entropy will thus be largely affected through alloys that are categorised in the first two classes. The last class of alloys will not really affect the difference in entropy of the solid-phase reaction. Those elements are most likely to be excreted from the nickel silicides upon its formation, and will migrate to grain boundaries or the sample's surface. Although no significant change in entropy is expected for this last class of alloying elements, this does not mean that they won't influence the solid-phase reaction. The accumulation of impurities at grain-boundaries can have drastic influence on e.g. atomic diffusion.

The nucleation barrier also includes the interface energy $\Delta\sigma$. Both soluble and insoluble alloys have the potential to influence this interface energy. For example, a soluble alloy will change the lattice parameters of the silicide (e.g. according to Vegard's law for isomorph phases), thus increasing or decreasing the planar spacing. As we have previously discussed, specific texture alignments are related to crystallographic matching at the interface [4–6]. Therefore, a change in planar spacing will impact the quality of the plane-to-plane matches and thus also affect the interface energy. Insoluble alloys will segregate towards grain boundaries, thus affecting the chemical potential and atomic concentrations of the interface between neighbouring grains, i.e. between two silicide grains or between a silicide grain and the substrate. The accumulation of insoluble alloys at grain boundaries can therefore significantly hinder grain boundary diffusion. As this is the main diffusion mechanism within thin silicide films at lower temperatures, it can drastically alter the growth kinetics.

Finally, we note that the enthalpy of the formed phase may also be influenced. For example, ΔH_V of $Ni_{1-x}Pt_xSi$ will be influenced with the inclusion of Pt, as followed:

$$H_V(Ni_{1-x}Pt_xSi) = H_{V,NiSi} - x\,(H_{V,NiSi} - H_{V,PtSi}) \tag{3.2}$$

3.2 EFFECTS OF ADDITIVE ELEMENTS ON NICKEL SILICIDE FORMATION

A comprehensive study on the addition of impurities to the nickel silicide formation was previously reported by Lavoie *et al.* [3]. The influence of 24 different alloying elements was investigated on the nickel silicide solid-phase reaction for an as-deposited Ni layer of 10 nm. The emphasis of this paper lies on the change in stability of the NiSi layer, which was investigated through *in situ* measurement techniques.

The temperature window at which NiSi could be observed during the anneal of these alloyed Ni layers is displayed in figure 3.2. The measure-

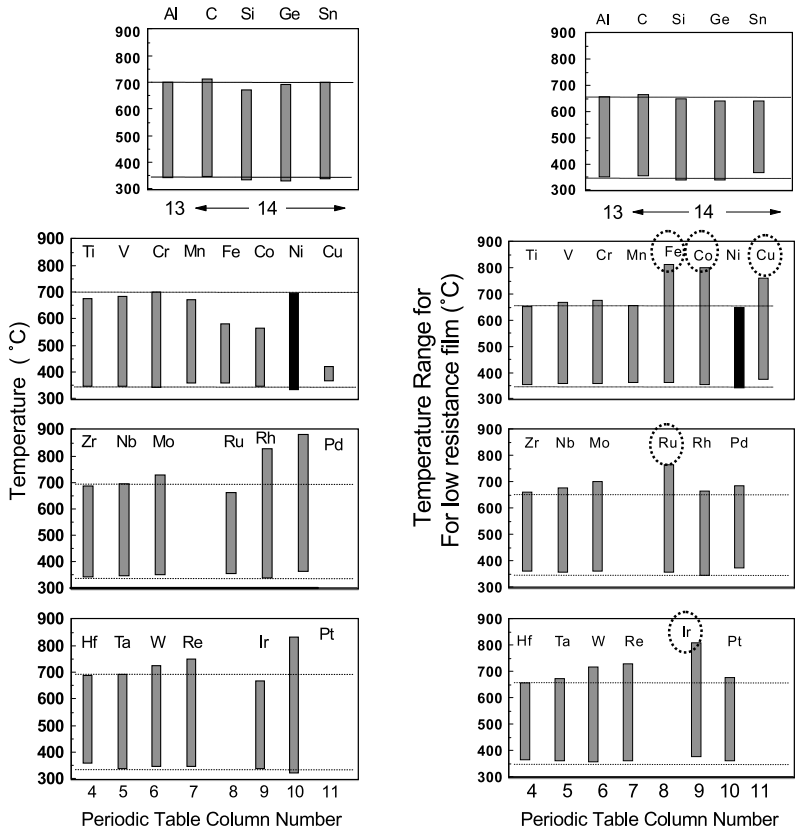

Figure 3.2: Comparison of temperature windows over which **(left)** NiSi is visible trough *in situ* XRD and **(right)** over which a low resistance is measured. Anneals were performed at $3\,^{\circ}\mathrm{C}\,\mathrm{s}^{-1}$ on a poly-Si substrate for nominal concentration of 5 % of the additive element. The graph is organized following the structure of the periodic system. Adapted from [3].

ments clearly indicate that the addition of Fe, Co or Cu significantly reduce the thermal window of NiSi, due to a lower nucleation temperature of $NiSi_2$. On the other hand, Rh, Pd or Pt delay the formation of $NiSi_2$. Other elements appear to have only a limited effect on the temperature window. The results could be interpreted through the classification of the alloying elements in the classes which were discussed in section 3.1: Rh, Pd and Pt are elements which are soluble in NiSi but less soluble in $NiSi_2$ and vice-versa for Co, Fe and Ru. By applying the argument of entropy of mixing, one can therefore understand these observed shifts in temperature windows.

Lavoie *et al.* furthermore discussed the change in morphological stability of the NiSi phase through *in situ* sheet resistance measurements. The evolution of the sheet resistance clearly indicates the formation of NiSi, as it is the first low-resistive phase to form after the high-resistive metal-rich nickel silicides. Figure 3.2 shows that, in agreement with *in situ* XRD, the formation temperatures of NiSi is not significantly changed through alloying. The agglomeration of NiSi is also clearly observable through these measurements, as it coincides with a steep increase in sheet resistance. The agglomeration was delayed by over 100 °C when 5 % Fe, Co, Cu, Ru and Ir was added. The delay in agglomeration can be related to the phase stability of NiSi. The *in situ* XRD measurements indicate that $NiSi_2$ is formed at earlier temperatures for these elements, and as such, these films retain their low resistivity, as $NiSi_2$ is less prone to agglomeration. Alloying with 5 % of Pd, Pt, Nb, Mo and W results in a humble delay in agglomeration, without promoting the earlier formation of $NiSi_2$. These observations are less straightforwardly interpreted. Texture effects should be considered [4], in addition to the effect of a diffusion barrier for both Ni and Si, as agglomeration requires the mobility of both elements.

3.3 INFLUENCE OF PT, CO, AND AL ALLOYING ON THE NICKEL SILICIDE FORMATION

The following subsections discuss the highlights from literature concerning the addition of Pt, Co and Al. We shall discuss the known effects of these alloying materials to NiSi degradation and changes in the phase sequence. These elements were selected, as this set of alloying materials covers elements either soluble in NiSi (Pt), $NiSi_2$ (Al) or both (Co), as discussed in section 3.1. The same set of ternary elements was furthermore used throughout performed research in the scope of this thesis. The available phase diagrams relevant to this research can be found in Appendix C of this thesis.

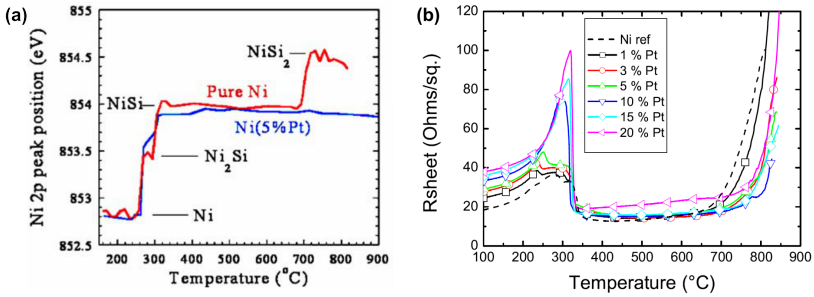

Figure 3.3: **(a)** *In situ* XPS shows the variation of the Ni 2p peak position (binding energy) with the annealing temperature of a pure Ni film (red line) and Ni(Pt) (blue line) films on (100) Si. The delayed nucleation of $NiSi_2$ is observed when Pt is added. **(b)** *In situ* sheet resistance data show the delay in morphological degradation (high temperature increase in sheet resistance) for increasing concentrations of Pt in a Ni layer on SOI substrate. Figures from [7] and [8], respectively.

3.3.1 *Pt - more soluble in NiSi than in $NiSi_2$*

The Ni(Pt)-Si system is one of the most studied ternary silicide systems [1, 3, 4, 7, 9–21]. The pioneering work by Mangelinck *et al.* [1] showed that the nucleation temperature of $NiSi_2$ shifted from 750 °C for pure Ni films to 900 °C for a Ni(5 % Pt) alloy upon annealing, as based on *ex situ* XRD measurements. *In situ* XPS experiments [1, 7] displayed in figure 3.3a monitor the Ni 2p peak position and clearly shows four discrete values, corresponding with the presence of Ni, δ-Ni_2Si, NiSi and $NiSi_2$phases at the sample's surface. This measurement indeed confirms the elongated temperature window of NiSi upon Pt alloying. Further investigation of the Ni(Pt)-Si system also indicated that the morphological degradation of NiSi was significantly delayed, although not completely eliminated (Fig. 3.3b). The addition of Pt in the as-deposited layer therefore delays the two main degradation mechanisms of NiSi contact layers.

Several mechanisms have been proposed to explain the improved stability of $Ni_{1-x}Pt_xSi$ films. First, the entropy-of-mixing argument is in agreement with the observed delay in $NiSi_2$ nucleation, as explained in section 3.1 [1]. Although no ternary phase diagram is available of the Ni-Si-Pt system, we know from previous experiments that the solubility of Pt is high in NiSi, but low for δ-Ni_2Si and $NiSi_2$[11, 18]. Second, the improved morphological stability was linked to a change of the texture of NiSi films. Mangelinck *et al.* observed a shift in the intensity ratio of the NiSi diffraction-peaks, possibly indicating a difference in preferential

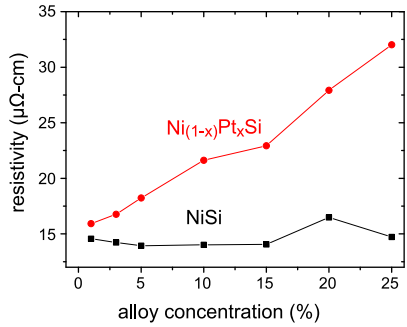

Figure 3.4: Room temperature sheet resistance for NiSi, $Ni_{1-x}Pt_xSi$ as a function of increasing alloying concentration. Adapted from [8].

orientation [1]. Detavernier *et al.* [4] further investigated the NiSi texture through *ex situ* pole-figure measurements, and observed that the two most intense axiotaxial circles of NiSi significantly decrease in intensity when Pt is added in the as-deposited Ni layer. The main texture components of a $Ni_{1-x}Pt_xSi$ film instead can be described through epitaxial alignment. As explained in section 2.3, the agglomeration of a thin film is easier for an axiotaxially-textured film than for an epitaxially-aligned film, as the interface-energy-cost to curve an epitaxial film will be larger than to curve an axiotaxial film. This explanation, however, implies a new question: why does Pt-alloyed NiSi promote epitaxial alignment. This was linked to a lattice expansion upon the incorporation of Pt, as PtSi, isomorph with NiSi, has bigger lattice parameters than NiSi, and through applying Vegard's law [9].

Initially, the Pt concentration was kept relatively low (e.g. 5 at%). However, due to the down-scaling in microelectronics, the silicide thickness decreased and, as discussed in section 2.2, the tendency to agglomerate increases. Higher concentrations of Pt are therefore required to avoid morphological degradation [7]. Unfortunately, PtSi has a three-times higher sheet resistance than NiSi, and thus the increased Pt concentration coincides with an increased resistivity of $Ni_{1-x}Pt_xSi$ (Fig. 3.4 and Tab. 1.1 from chapter 1). The effective resistance can be higher than predicted by a linear extrapolation of these bulk-values, due to alloy scattering [14, 22]. The same holds true for the contact resistance of PtSi, which is significantly higher than that of NiSi (Tab. 1.1 from chapter 1). Therefore, the parasitic resistance through Pt-incorporation will increase in both the bulk-resistivity, as well as through the contact resistivity. This illustrates that

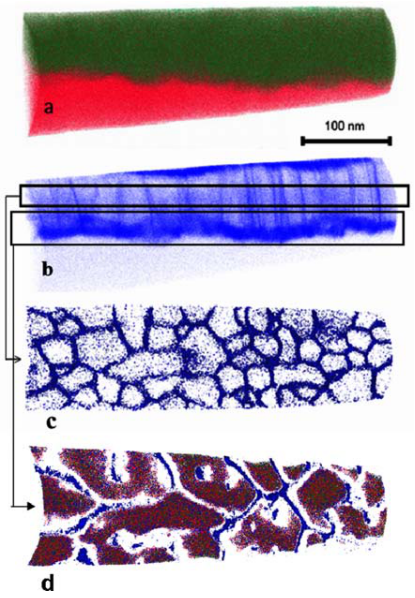

Figure 3.5: APT reconstruction of a large volume of Pt-alloyed Ni silicide structure (5 at% Pt). **(a)** Location of Si (red dots) and Ni atoms (green dots). **(b)** Location of the Pt atoms (blue dots). Pt enrichment is observed at the top of the structure (corresponding to the unreacted Ni layer) and at the interface between silicide and silicon regions. **(c)** A 20 nm slice in depth through the δ-Ni_2Si region: significant grain boundary enrichment of Pt can be seen. **(d)** A 40 nm slice in depth through the silicides/Si interface region illustrate the island structure of the NiSi phase. Figure from [7].

the beneficial influence of Pt alloying on the stability of the NiSi grains comes with a price on the parasitic resistance.

In addition to the effects on phase stability and resistivity, Pt incorporation also influences the growth kinetics of nickel silicide phases. From *in situ* XRD and *in situ* RBS measurements [13, 18], it is shown that small concentrations of Pt (e.g. 5 at%) delay the growth of δ-Ni_2Si, which occurs *simultaneously* with NiSi formation. This is in contrast to pure Ni films, where δ-Ni_2Si is formed first, and is then consumed through NiSi formation [3, 8, 10]. This was related with the very low solubility of Pt in δ-Ni_2Si. As such, Pt first needs to be excreted from the initial Ni(Pt) layer in order to form the δ-Ni_2Si phase, an effect which is known as the *snow-plow effect*. This process is illustrated through atom probe tomography (ATP) by Mangelinck *et al.* and displayed in figure 3.5. An accumulation of Pt can

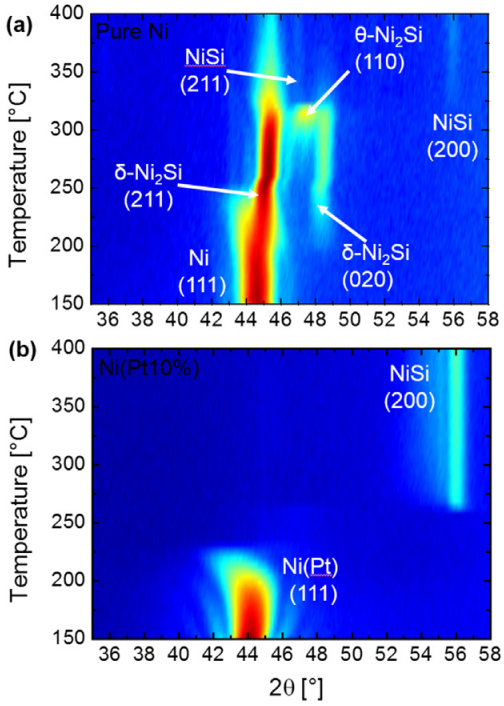

Figure 3.6: *In situ* XRD measurements ($\lambda = 0.154\,\text{nm}$) during annealing of a 11 nm Ni film **(a)** and Ni(10% Pt) **(b)** deposited on a Si(100) substrate. Figure from [20].

be seen at the Ni(Pt)/δ-Ni_2Si interface and between δ-Ni_2Si grain boundaries, which is the result of the snow-plow effect due to the rejection from the δ-Ni_2Si layer [7, 11, 17]. This can significantly hinder the further Ni diffusion required for subsequent δ-Ni_2Si growth. The segregation of Pt is therefore accounted to explain the delayed growth kinetics of δ-Ni_2Si.

A higher concentration of Pt (e.g. 10 at%) even completely eliminates the formation of δ-Ni_2Si. *In situ* XRD measurements show the lack of any diffracting phase (including δ-Ni_2Si) after the consumption of the as-deposited Ni(Pt) layer and prior to NiSi formation in figure 3.6. This does not mean that no crystalline phase is present. Panciera *et al.* showed through TEM-measurements that an epitaxially-aligned θ-Ni_2Si phase is present prior to NiSi in this Pt-alloyed sample [20, 21]. However, the experiments did not verify the presence of epitaxially-aligned θ-Ni_2Si for pure Ni films, which could possibly form in co-existence with δ-Ni_2Si.

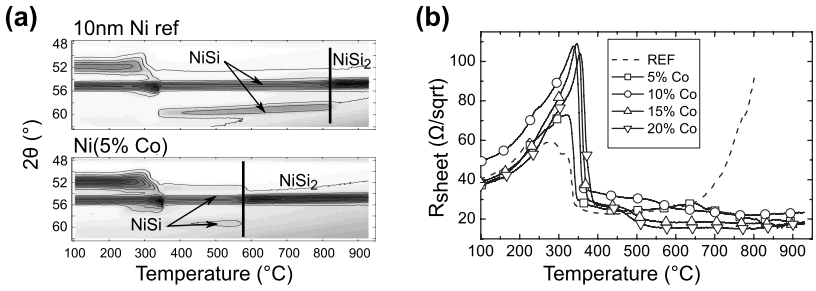

Figure 3.7: **(a)** *In situ* XRD measurements ($\lambda = 0.18\,\text{nm}$) during annealing of a 10 nm Ni film **(top)** and Ni(5% Co) **(bottom)** deposited on a Si(100) substrate. **(b)** *In situ* sheet resistance measurement for different concentrations of Co on a single crystalline SOI substrate. Adapted from [29].

3.3.2 *Co - more soluble in $NiSi_2$ than in NiSi*

The ternary Ni-Co-Si system was already subject of investigation when $CoSi_2$ silicides were explored as contact materials in MOSFET devices, before the implementation of NiSi in state-of-the-art transistors [23–26]. This ternary system is interesting due to the complete miscibility of the $CoSi_2$ and $NiSi_2$ phases. Both disilicides share the same cubic CaF_2 structure, and have nearly identical lattice parameters: 5.364 and 5.406 Å, respectively. Furthermore, the lattice parameters of both phases are only slightly different from the lattice parameter of cubic Si. The cubic Si lattice ($a = 5.431$ Å) is 1.23% bigger than $CoSi_2$ and 0.46% bigger than $NiSi_2$. Therefore, both disilicides have been considered as prototypes for achieving epitaxial silicide films with a low number of defects or dislocations at low temperature [27, 28].

Initially, the influence of Ni-alloying on the cobalt silicide formation was investigated [23–26]. d'Heurle *et al.* reported that the consumption of the CoSi phase occurs much earlier, due to the significant lower formation temperature of the disilicide phase [23]. The Ni- and Co monosilicides do not share their crystal structure and no solid solution between orthorhombic NiSi and cubic CoSi is formed. The solubility of the mono-silicides is limited: up to 12 % solubility of Co in NiSi at 800 °C and up to 20 % vice-versa (the ternary phase diagram is displayed in Appendix C) [30]. Therefore, the lowered dislicide nucleation can be understood through the entropy of mixing. Mangelinck *et al.* investigated the reverse influence, i.e. that of Co-alloying on the nickel silicide solid-phase reaction [31]. Here, the formation temperature of the disilicide was also observed to decrease

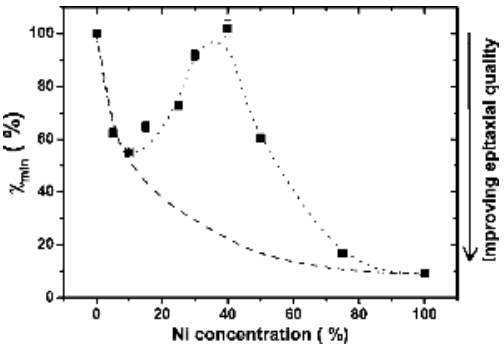

Figure 3.8: The RBS minimum yield for the (Ni-Co) disilicide films on Si(100) as a function of the nominal Ni concentration. The dotted lines are a guide to the eye. The dashed line depicts an example of the expected gradual decrease of the minimum yield (corresponding with an increase in epitaxial quality) with increasing Ni concentration. Figure from [5].

upon the addition of Co (illustrated in Fig. 3.7 a). Moreover, it was also found that the formed nickel silicide with Co-impurities is less prone to agglomeration [29] (Fig. 3.7b). This can of course be related to the lower transition temperature from NiSi to $NiSi_2$, and therefore it is not surprising to observe a delay in agglomeration.

The lower nucleation temperature of the disilicides appears promising in order to form low-temperature epitaxial layers. However, it is observed that $CoSi_2$ forms with an *axiotaxial* texture [32], whereas $NiSi_2$ is reported to align epitaxially on the Si substrate. This can be explained through geometrical arguments as the lattice parameters of $CoSi_2$ deviate significantly more from the Si lattice than $NiSi_2$. Therefore, it requires more strain to form an epitaxial alignment between $CoSi_2$ and Si than between $NiSi_2$ and Si. Vegard's law would imply that a gradual change to the Ni/Co composition would steadily shift the disilicides' lattice parameter. Therefore, one would equally expect on geometrical considerations that texture gradually evolves from axiotaxial $CoSi_2$ to epitaxial $NiSi_2$ with increasing Ni concentration. Smeets *et al.* observed a significantly different trend [5, 33]. Channelling Rutherford Backscattering Spectrometry (RBS-C) indicates that the epitaxial quality is indeed the highest for pure Ni films and that a higher Co concentration results in a decrease of epitaxial quality. However, a surprising improvement on epitaxial alignment is observed with decreasing Ni concentration between 40 % and 15 % (Fig. 3.8). An observation which is furthermore corroborated through XRD measurements. This illustrates that geometrical considerations alone prove insufficient to

completely understand preferential orientation of a silicide. The observed shifts in textures were rationalised through growth kinetics and by considering the location of disilicide nucleation with respect to the interface and separated mono-silicides.

More recently, Co-enriched NiSi is considered to replace Pt-enriched NiSi for fully-depleted p-type SOI MOSFET transistors [34, 35]. Deprat *et al.* showed that Ni(Co) mono-silicide contacts facilitate a slight improvement on I_{on}/I_{off} trade-off by 4 %, an increased thermal stability and 30 % lower sheet resistance with respect to Ni(Pt) mono-silicide [35]. However, the origin of the improved characteristics are not yet fully understood.

In conclusion, Co-alloying lowers the nucleation temperature of $NiSi_2$. However, it is not beneficial to the quality of the epitaxial alignment with the underlying Si substrate.

3.3.3 *Al - more soluble in $NiSi_2$ than in NiSi*

Although the epitaxial alignment of unalloyed $NiSi_2$ films is better than $CoSi_2$ films, they are certainly not perfect. As mentioned in section 1.4, two different alignments can be observed: type-A, which can be considered as a continuation of the Si lattice into the silicide, and type-B, which is a twinned-version of type-A and is formed through rotating the $NiSi_2$ grain around the Si(111) direction by 180° [27, 36]. Furthermore, a very rough $NiSi_2$ / Si interface is most often observed through the formation of pyramidal facets along the Si {111} direction on Si(001) substrates. Through various annealing and deposition experiments, Tung *et al.* showed that the formation of these {111} facets is related to the growth kinetics of $NiSi_2$ and that these are only metastable. Apparently, $\sigma_{\{111\}} \times \sqrt{3} > \sigma_{\{100\}}$ and the facets disappear upon heating towards higher temperature [37].

One can argue that the small lattice mismatch between $NiSi_2$ and Si of 0.4 % is still significant enough in order to induce strain. Richter *et al.* reported that the lattice parameter of bulk $NiSi_2$ can be increased through the incorporation of Al [38]. Al is reported to replace Si in the $NiSi_2$ lattice, which results in a lattice match with the Si substrate at room temperature, as depicted in figure 3.9. Richter *et al.* furthermore reported on the full ternary Ni-Si-Al phase diagram (Appendix C) [39–41]. Al exhibits high solubility in $NiSi_2$, but not in NiSi. Therefore, we expect a lowered phase-formation of $NiSi_2$ comparable with the observations of Co-alloying.

Several papers report on the influence of Al on the formation of nickel silicides [42–46]. The most comprehensive study is given by Mogilatenko *et al.* and reports on *ex situ* examination of quenched samples at discrete temperatures between 500 and 900 °C for several Al concentrations [42].

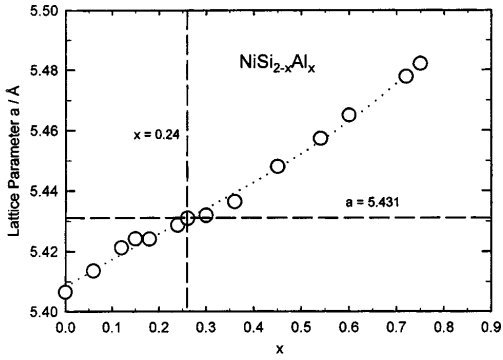

Figure 3.9: The variation of the room-temperature lattice parameter of bulk $NiSi_{2-x}Al_x$. The cubic lattice parameter of Si is indicated by a dashed horizontal line. Figure from [38].

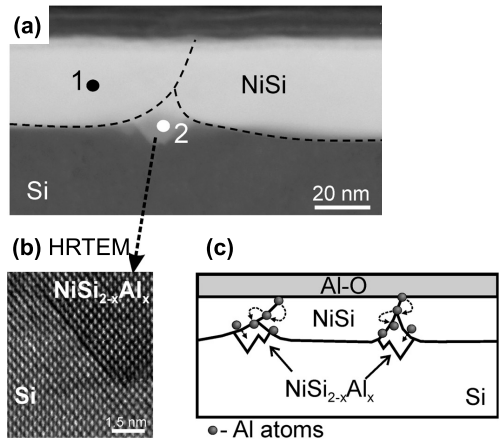

Figure 3.10: **(a)** HAADF STEM image of a sample with Al/Ni ratio of 0.1 at 500 °C. **(b)** HRTEM image shows the type-A oriented disilicide cyrstallite. **(c)** schematic representation of the proposed formation mechanism of ternary $NiSi_{2-x}Al_x$ grains for low Al content during 500 °C annealing. Adapted from [42].

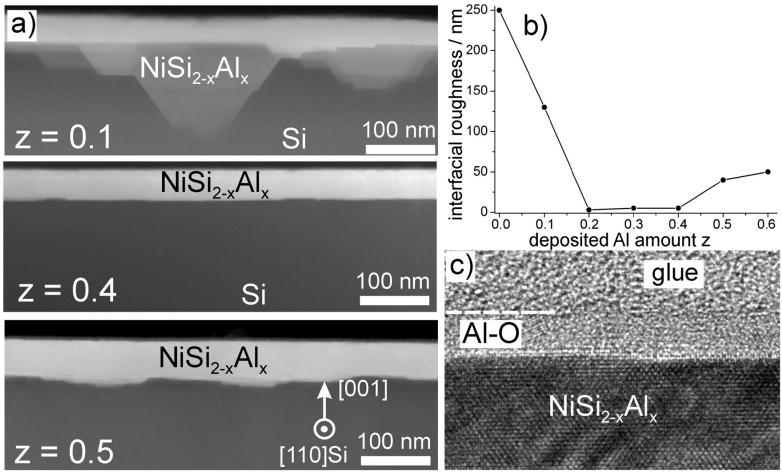

Figure 3.11: **(a)** HAADF STEM images showing cross-sections of $NiSi_{2-x}Al_x$ layers after quenching different as-deposited films (with Al/Ni ratio z) at 900 °C. **(b)** Maximum peak-to-valley values of interfacial roughness of the $NiSi_{2-x}Al_x$ layers as a function of Al/Ni ratio z. **(c)** HRTEM image showing the amorphous Al oxide layer at the $NiSi_{2-x}Al_x$ surface. Figure from [42].

Annealing Ni films with relatively low Al concentrations, i.e. Al/Ni ratio of 0.1, shows the NiSi phase at 500 °C, and Al is here excreted from the NiSi grains, similar to the snow-plow effect of Pt in δ-Ni_2Si. Remarkably, they observed that small grains of $NiSi_{2-x}Al_x$ are formed at triple-points between two NiSi grains and the Si substrate (Fig. 3.10). It is suggested that this low-temperature formation of $NiSi_2$ is promoted through the entropy of mixing, as the Al content at these triple points is relatively high through the snow-plow effect, thus promoting the formation of $NiSi_2$. For higher amounts of Al, i.e. an atomic Al/Ni ratio of 0.2 up to 0.6, no NiSi can be observed at 500 °C. Instead, $NiSi_{2-x}Al_x$ is formed, and appears as a thick continuous film, which facilitates a rough interface with the Si substrate. The high roughness is due to the formation of pyramidal facets, in agreement with the faceting-issue for $NiSi_2$ formed from pure Ni films.

At 900 °C, $NiSi_{2-x}Al_x$ is present for all Al concentrations. Allenstein *et al.* reported that the rough interface due to faceting is significantly reduced for atomic Al/Ni ratios between 0.2 and 0.4 (Fig. 3.11) [43]. An increase in roughness is again observed for higher Al concentrations. One could argue that this is related to the lattice mismatch of the $NiSi_{2-x}Al_x$ film with the Si substrate. However, interfacial-dislocation defects observed through

TEM measurements indicate that the $NiSi_{2-x}Al_x$ lattice parameter is bigger than that of Si for *all* Al concentrations upon formation. This is easily explained by the difference in thermal expansion coefficients for these materials, where $NiSi_2$ expands much faster than Si and therefore the $NiSi_2$ lattice spacing will be bigger than Si at the temperature of $NiSi_2$ formation. The observed increase in roughness for higher Al concentrations is still under debate. In addition, other aspects of the Al-enhanced nickel silicide formation are yet unclear. For example, the incorporation of high amounts could introduce an eutectic liquid, which is already possible for Al-Ni and Al-Si at 639 and 577 °C, respectively. Such a liquid was previously shown to significantly alter the kinetics in Co-Au [47] or Ni-Au [31] layers, due to the low Au-Si eutectic at 370 °C. Therefore, annealing at temperatures above the eutectic point can result in a drastic influence on the atomic mobilities and growth kinetics, which possibly could explain the higher roughness for high Al concentrations. *In situ* experiments are therefore ideal to observe if there is any abrupt change in phases at a specific temperature coinciding with eutectic melting.

3.4 ALLOYING OF NICKEL SILICIDES: SUMMARY

The literature concerning alloyed nickel silicide formation is quite excessive, and this chapter only mentions the highlights which were important for this work. In retrospect of figure Figure 2.14, the available knowledge is mainly focused on the formation regime which forms NiSi. Several publications report on the beneficial effects of these alloys on the thermal stability of the NiSi film, although this is sometimes only a limited improvement. Some of the ternary systems are only recently investigated (e.g. Al), and therefore additional studies can provide additional insights in their effects (Chapter 4). However, the influence of alloying material on the solid-phase reaction for film thicknesses' near the critical thickness t_c is mainly unexplored. Therefore, this will be the focus of investigation for Chapter 5 and Chapter 6.

4 ARTICLE I: THE INFLUENCE OF AL ALLOYING ON NI SILICIDE FORMATION AND TEXTURE

4.1 INTRODUCTION

Epitaxial silicides have been considered interesting for the initial contact in three-dimensional transistor devices and heterostructures [1, 2]. Several silicides have been reported to grow epitaxially with the silicon substrate, such as rare-earth silicides [3], $CoSi_2$ [4] and $NiSi_2$ [5, 6]. The latter two silicides have received considerable attention because they have a similar cubic crystal structure (Fm-3m: CaF_2) and their lattice constants are very close to that of Si. At room temperature, the unit cell of $NiSi_2$ in perticular is only 0.46% smaller than the cubic unit cell of silicon making ideal for studies of epitaxially aligned silicide films. As such, the literature reports numerous studies with the aim of growing $NiSi_2$ layers, which have a long-range mono-epitaxial alignment with a silicon substrate. Overall, three effects can limit the uniformity of epitaxial $NiSi_2$. First, the $NiSi_2$ phase is known to grow in two different epitaxial alignments [6], referenced as the *type A* and *type B* orientation. The former is a continuation of the Si substrate, whereas the latter is a twinned orientation, whereby $NiSi_2$ is rotated by 180° around the Si(111)-axis. In fact, the presence of these two epitaxial variants in a single film leads to in fact a non-single-crystal layer. A second limitation for growing large area epitaxial $NiSi_2$ is that the small lattice mismatch between the silicide and silicon will induce strain and defects at the interface [5]. Thirdly, the $NiSi_2$/Si interface exhibits pyramidal faceting through a beneficial formation of $[111]_{NiSi_2}//[111]_{Si}$ interfaces, resulting in a undesired rough interface on Si(001) [6].

Recent studies show that the epitaxial alignment and interfacial roughness of epitaxial $NiSi_2$ are significantly improved by introducing Al as a ternary element [7–10]. The inclusion of Al in the $NiSi_2$ lattice results in an increase of its unit cell, thus lowering the room-temperature lattice mismatch [11]. The pioneering work of Allenstein *et al.* [7] showed that the addition of Al (e.g. 5 at.%) lowers the temperature at which NiSi transforms into $NiSi_2$, where $NiSi_2$ was already formed at 500 °C, while adding more Al to the initial Ni layer completely hinders the formation of NiSi in favour of $NiSi_2$. The pyramidal faceting of this $NiSi_2$ (or $NiSi_{2-x}Al_x$ to be more specific) layer on Si(001) is reduced in an Al concentration win-

dow between 16 and 28 at.% in a 20 nm Ni layer, which even can result in an atomically smooth interface with the Si substrate [12]. Consequently, Al-alloying of the as-deposited Ni layer has the potential to enhance the formation of long-range epitaxial $NiSi_2$ (or, due to the incorporation of Al, $NiSi_{2-x}Al_x$) films.

The influence of Al on the formed nickel-silicide phase sequence has not yet been studied in great detail. Several aspects may severely influence the solid-phase reaction, either by introducing binary Ni-Al phases (e.g. NiAl) and ternary phases (e.g. $NiAl_{0.5}Si_{0.5}$) or by forming an eutectic liquid, which occurs in the binary Al-Ni and Al-Si systems at 639 and 577 °C, respectively. Therefore, a systematic study on the phase formation sequence of thin Ni(Al) silicides is highly desirable, with a high resolution in both annealing temperature and Al concentration. However, such knowledge is currently limited to the quench-based *ex situ* measurement methodologies. Indeed, Mogilatenko *et al.* [9] indicate the need for *in situ* techniques during annealing to study the phase formation of the ternary Ni-Al-Si system.

This paper reports a study of the phase formation sequence during the solid-state reaction (SSR) of alloyed Ni(Al) films with either monocrystalline Si(001) or poly-crystalline Si substrates through *in situ* measurements during annealing. This *in situ* approach allows one to detect and identify transient phases that occur in a very narrow temperature window during the SSR. As a result, we have constructed a detailed phase formation diagram, representing the occurrence of crystalline phases as a function of Al concentration (0 - 60 at.%) and annealing temperature(25 - 850 °C). Furthermore, we report a drastic change in preferential orientation of the formed $NiSi_2$ grains, and the epitaxial growth of θ-Ni_2Si as a transient phase. These results enable a better understanding of the effect of Al on the phase formation during solid-state reactions in the ternary Ni-Al-Si system in order to obtain a silicide film with a single epitaxial orientation.

4.2 EXPERIMENTAL METHODS

Ni(Al) films were deposited as a concentration gradient by means of combinatorial physical vapour deposition on Si wafers with single-crystalline (001) and poly-crystalline orientations. The poly-crystalline Si wafer consisted of 150 nm poly-crystalline Si film grown by low-pressure chemical vapour deposition on top of a 100 nm thermal SiO_2 layer. The substrate received a rapid thermal anneal to 1000 °C for 20 s in a N_2 ambient prior to the nickel deposition in order to stabilize the poly-Si grain structure. Both

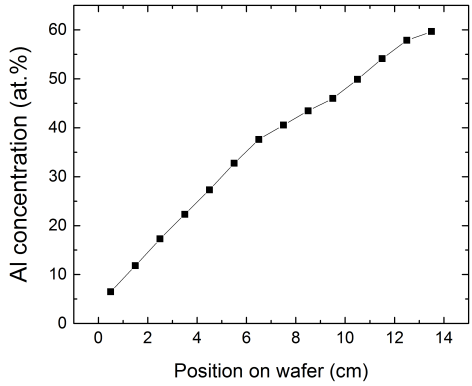

Figure 4.1: The evolution of Al concentration, determined by Rutherford backscattering spectrometry, of the as-deposited Ni(Al) alloy as a function of position on the silicon wafer.

substrates received a standard HF (3 %) dip to remove the native oxide immediately before loading the samples in the physical vapour deposition system.

Al and Ni were co-sputtered in an Ar-ambient of 5×10^{-3} mbar, after the vacuum chamber had reached a background pressure of 6×10^{-7} mbar. The amount of deposited Ni was equivalent to 20 ± 2 nm pure Ni for every position on the 140 mm long substrates. The sputtered flux of Al was modulated through a shadow mask, that was designed to produce a linear increase of the Al concentration across the 140 mm diameter substrates, resulting in Ni(Al) concentration gradients with a varying amount of Al across the wafer [13–15]. Rutherford backscattering spectrometry (RBS) was used to quantify the atomic concentration for every position on the wafer, as displayed in figure 4.1. Since RBS is a mass-sensitive technique, it is not straightforward to distinguish Al from the Si substrate with high precision due to the small mass difference between Al and Si, causing significant overlap between the Al and the Si signal. In order to enhance the accuracy of the determined Al-concentrations, the RBS measurements displayed in figure 4.1 were conducted on Ni(Al) films which were deposited on a carbon substrate, along with the Si(001)-substrate samples.

The resulting concentration gradients on the Si substrates were then cut in small pieces, 10 mm long, resulting in 14 samples with an average step in Al concentration of 4 at.%. A pure Ni sample was also deposited as a reference sample with the same equivalent Ni thickness of 20 nm. *In situ*

X-ray diffraction (XRD)[1] was used to monitor the SSR for these 14 samples as a function of temperature up to 850 °C at a constant rate of 1 °C s^{-1} in a He(5 %H_2) ambient. A CuKα ($\lambda = 0.154$ nm) X-ray source illuminated the sample while the Bragg diffraction was monitored using a linear detector. Both source and detector remained in a fixed position, with the central detector pixel in Bragg-Brentano geometry. Due to the limited acquisition window of 20° in 2θ diffraction angle, we performed measurements in different 2θ windows (15 to 35°; 30 to 50° and 45 to 65°). Because of the fixed set-up geometry during the *in situ* XRD measurements, this technique can only detect lattice planes which are oriented (nearly) parallel to the sample surface, thus potentially missing planes which are non-parallel to the surface, e.g. for specific epitaxial orientations with respect to the mono-crystalline Si(001) substrate. Measurements of samples deposited on the poly-crystalline substrate will not have this limitation, as no mono-crystalline template is present to form such fixed alignment. The *in situ* XRD measurements are displayed as a function of temperature and 2θ, using a grayscale map for the recorded intensities (with black corresponding to the highest intensity).

The analysis of epitaxial phases on Si(001) is enabled through *ex situ* X-ray pole figures, measured for samples quenched at relevant temperatures. A pole figure acquires the diffraction of a given $\{hkl\}$ plane while tilting and rotating the sample out-of-plane (defined as the χ angle) and in-plane (ϕ angle). A polar plot of the diffraction intensity then represents the statistical distribution of the selected crystalline plane's preferred orientations, also denoted as the *texture* of the crystal grains. The pole figures reported in this work were acquired using a four-circle diffractometer at the X20A beamline of the National Synchrotron Light Source (NSLS), using X-rays with a wavelength of $\lambda = 0.154$ nm, a custom linear detector covering 20 to 60° in 2θ and by scanning the sample in χ and ϕ in steps of 1°. The pole figures are displayed using a grayscale map for the recorded intensities (with black corresponding to the highest intensity). The $\chi = 90°$ is represented by the black circular border at the edge of the pole figures. Further details concerning these pole-figure measurements, the experimental configuration and the analysis of the data can be found in our earlier work [16, 17].

The epitaxial alignment was also investigated by Rutherford backscattering spectrometry/channeling (RBS-C) experiments, using mono-energetic He^+ particles of 1.57 MeV. The detectors were positioned at scattering angles of 105° and 168°. The energy of backscattered He^+ particles, which

1 Appendix B provides a more detailed description on the different X-ray diffraction measurements that were conducted in this thesis

is recorded by the detectors, then depends on the mass of the scattering atom, as well as on the energy lost due to the distance travelled by the ion in the sample. The number of backscattering collisions between the incident ions and the atoms in the sample can be drastically lowered by orienting the ion beam along a crystal axis of the substrate, steering the ions into axial channels and decreasing the cross section for large-angle scattering [18]. In this geometry, the measured yield will be significantly lower, and the ratio of the measured intensity from an aligned spectrum to a random-oriented spectrum depends on the volume fraction of epitaxial silicide grains.

X-ray photoelectron spectroscopy (XPS) was performed to investigate the composition of the layered structures of the samples. The composition was estimated through analysis of the area of the Al 2s, C 1s, Ni 2p, Si 2p and O 1s peaks. Measurements were performed on a Thermo Scientific Theta Probe system, operating at a base pressure of $\approx 10^{-10}$ mbar. Several sputter steps were performed EX05 Ar ion gun in order to obtain data throughout the samples' depth profile. Due to changes to the experimental apparatus, the sputter yield can not be compared between different samples. However, the sputter yield was not changed while measuring an individual sample and can be considered constant throughout the depth profiling.

4.3 RESULTS

We provide an overview of the observed phase formation sequences on both poly-crystalline Si and Si(001). We are able to distinguish four different phase formation sequences that are dependent upon the Al concentration, but independent of the investigated substrate orientations. The complementary experimental techniques allows us to evaluate the possible mechanism responsible for the observed change in solid-state reaction as a function of Al concentration.

Solid-state reaction on poly-Si

The *in situ* XRD data can be analysed by using the observed diffraction peaks for identifying the different crystalline phases that occur as a function of temperature during the SSR. This type of analysis applied to the reaction of a pure Ni film with a poly-crystalline Si substrate (Fig. 4.2a) results in the known phase formation sequence of $Ni \rightarrow \delta - Ni_2Si \rightarrow NiSi \rightarrow NiSi_2$, which is in agreement with previously reported studies [19–21]. Also observed is the formation of the recently-reported transient

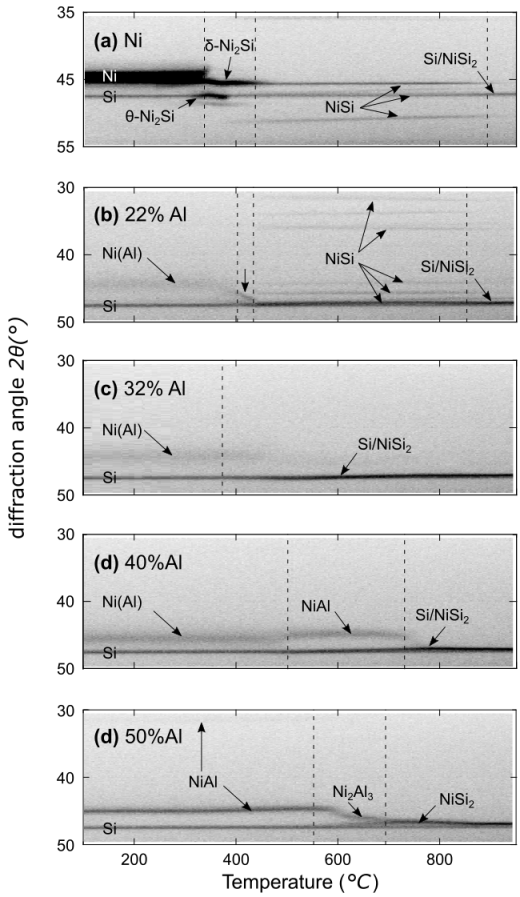

Figure 4.2: *In situ* XRD measurements for 20 nm Ni films, deposited on polycrystalline Si and alloyed with *(a)* 0, *(b)* 22, *(c)* 32, *(d)* 40 and *(e)* 50 at.% Al, illustrating the phase formation sequence for the four observed Ni(Al) concentration regions.

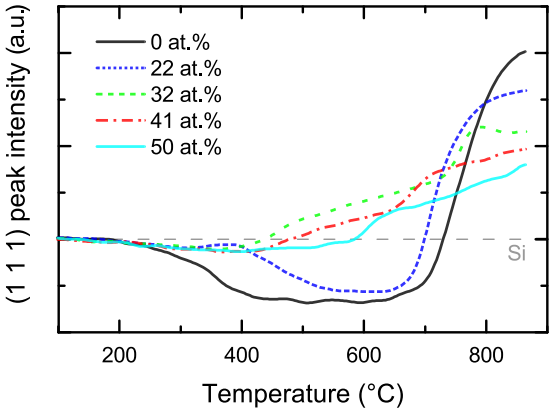

Figure 4.3: The total intensity of the coinciding $NiSi_2$ and Si (111) peaks, as a function of temperature, during the reaction between pure and Al-alloyed Ni films on poly-crystalline Si. The plotted intensities are normalised to the (111) peak intensity of an uncoated poly-crystalline Si reference measurement.

θ-Ni_2Si in the intermediate temperature regime prior to the formation of NiSi, simultaneous with δ-Ni_2Si [21]. Figures 4.2b - e show similar data measured for samples that were alloyed with a specific amount of Al. Vertical dashed lines indicate the temperature window of the observed phases, as determined through the maximum (or minimum) in the first derivative of the relevant diffraction peaks' intensities. By looking at the raw data, it is clear that the addition of Al has a significant impact on the phase formation sequence during the SSR. The data in figure 4.2 are representative of different types of reaction behaviour that were observed for different ranges of Al concentration. This enables us to identify four different reaction sequences, or Al-concentration *regions*, which will be further discussed below.

Each observed phase was identified through the 2θ value of its diffraction peaks. However, the peak position of $NiSi_2$ coincides with the diffraction originating from the Si substrate, due to the similar crystal structure and small lattice mismatch. As a result, the peak position alone is not sufficient to differentiate the diffraction from the substrate or the $NiSi_2$ film. By integrating the intensities of the (111) peak of both Si and $NiSi_2$ (i.e. the peak near $2\theta = 28.3°$) for these poly-crystalline substrates, a more quantitative analysis can be made, representing the rate of Si consumption during

the initial stage of the SSR, as well as the growth of $NiSi_2$. The extracted peak intensity is plotted for a selected number of samples in figure 4.3 and each curve will be discussed with the corresponding concentration-based reaction region. The $NiSi_2$/Si(111) peak was chosen since it is isolated from the diffraction peaks of almost all other observed binary Ni-Al, Ni-Si and ternary Ni-Al-Si phases. For the pure Ni reference (black line), a decrease in intensity of the (111) peak is first observed (Fig. 4.3), followed by an increase in intensity at higher temperatures. The initial decrease can be explained by the consumption of the Si substrate caused by the formation of the intermediate Ni_2Si silicides and NiSi up to 400 °C. The subsequent increase, slightly above 700 °C, indicate the formation of either $NiSi_2$ or Si.

Region 1 - The incorporation of a limited amount of Al (e.g. 6 to 28 at.%) does not drastically change the phase formation sequence, as illustrated by comparing figures 4.2a and b. Most notable differences are a decrease in diffraction intensity of the as-deposited layer, which is due to the amorphization of the metallic Ni through Al alloying, and a delayed initial consumption of Si which coincides with the formation of θ-Ni_2Si diffraction. δ-Ni_2Si was not observed during the solid-phase formation. More remarkably, the diffraction peak of the transient θ-Ni_2Si phase shifts by 0.8° in 2θ between 350 and 390 °C, as indicated by the white arrow and discussed in more detail below. The evolution of the (111) peak intensity (Fig. 4.3, blue, short-dashed curve) does not show remarkable differences, except for the aforementioned delay in Si consumption and a slightly earlier formation of $NiSi_{2-x}Al_x$.

Region 2 - Adding 32 at.% Al, figure 4.2c, severely alters the phase formation sequence. At this Al concentration, no other phase is observed by *in situ* XRD other than the low-diffracting Ni(Al) layer. The transition between the previous concentration region and this one is complete and occurs fully over this 4 % step in concentration: NiSi, which has a high diffraction intensity in the sample with 28 at.% , is completely unobserved in this concentration region. This concentration region only detects Si/$NiSi_{2-x}Al_x$ diffraction after the consumption of the initial Ni(Al) layer, a transition which occurs around 380 °C, significantly lower than the formation of $NiSi_2$ from a pure Ni film.

Region 3 - Between 37 and 43 at.%, the SSR first results in the formation of NiAl, which forms from the as-deposited layer above 440 °C. The identification of NiAl was confirmed through additional *ex situ* XRD measurements, where both (100) and (110) NiAl peaks (respectively $2\theta = 31.0$ and 44.4° were visible. NiAl has a relatively low diffraction intensity for 37 at.%, which intensifies as the Al concentration is increased to 40 and

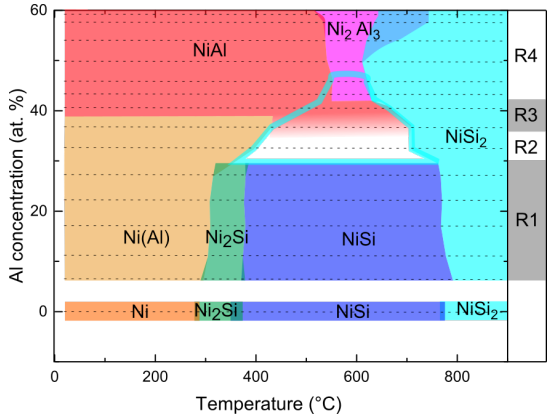

Figure 4.4: Phase formation diagram for the solid-state reaction of Ni_xAl_{1-x} layers on poly-crystalline Si substrates, determined by *in situ* XRD measurements. The horizontal dashed lines indicate the average Al concentration of the 15 samples for which *in situ* XRD data was measured and analyzed, whereas the right-hand side of the graph indicates the span of the observed phase formation sequence regions.

43 at.% . Interestingly, the (111) peak of $NiSi_{2-x}Al_x$ starts to gain in intensity from 440 °C, indicating a low-temperature growth of $NiSi_{2-x}Al_x$ as in region 2, but now in co-existence with binary NiAl and slightly delayed. Figure 4.3 shows a significantly higher increase in intensity rate around 660 °C, which is the temperature where all NiAl is consumed (Fig. 4.2d).

Region 4 - Between 45 to 59 at.% Al, the NiAl phase is already observed at room temperature, indicated by two diffraction peaks at 31 and 44.3°. This layer first transforms into binary Ni_2Al_3 between 540 °C to 580 °C, which is present up to temperatures above 750 °C (Fig. 4.2e) and shows additional diffraction at 18° in 2θ. The growth of $NiSi_{2-x}Al_x$ is delayed by nearly 150 °C, and now occurs simultaneously with the formation of the binary Ni_2Al_3 phase slightly above 600 °C .

The above described phase formation sequences are summarised in figure 4.4. We have determined the formation and consumption from each observed phase as the temperature at which the increase in diffraction intensity is the highest (i.e. the maximum of the first derivative of the total intensity of the relevant XRD peaks). However, figure 4.3 shows for region 2 and 3 that $NiSi_{2-x}Al_x$ already starts to form slightly above 400 °C, although its maximum increase in intensity only occurs above 600 °C. The

low-temperature formation of $NiSi_{2-x}Al_x$ is therefore indicated with a cyan contour for regions 2 and 3.

Phase formation on Si(001)

The *in situ* XRD measurements on monocrystalline Si(001) substrates (Fig. 4.5) show phase concentration regions similar to those observed on poly-crystalline Si. An overview of the observed phases is given in figure 4.6, which has comparable phase formation sequences as on poly-crystalline Si. However, we note the lack of diffraction, and hence the lack of information concerning the occuring phases, in several temperature regions: (1) between 300-400 °C in region 1, when transient Ni-rich phases should be formed; (2) above 800 °C for all concentration regions and (3) above 350 °C after the consumption of Ni(Al) in region 2. As we will show below, this lack of diffraction peaks can be related to the mono-crystalline Si template, causing the formed grains to align preferentially with the substrate. Such a preferential alignment hinders the observation during the *in situ* XRD measurements. This limitation is overcome by *ex situ* pole figure measurements, which we have performed on quenched samples and which are discussed in the following paragraphs.

Intermediate Ni-rich phases Figure 4.5b indicates the complete absence of diffraction peaks after the consumption of the as-deposited Ni(Al) layer and prior to the formation of NiSi (i.e. between 360 and 405 °C) for 22 at.% Al. This was not the case for an unalloyed Ni reference (figure 4.5a), which clearly shows diffraction from θ-Ni_2Si and δ-Ni_2Si. Similar temperature and Al concentration conditions on poly-crystalline Si gave rise to the formation of θ-Ni_2Si, which exhibited a significant change in diffraction angle in a limited temperature window (figure 4.2b). This intermediate phase was investigated through *ex situ* pole-figure measurements for samples with 22 at.% Al, quenched at 370 and 405 °C on a Si(001) substrate. The resulting pole-figure data allow us to calculate the average diffraction pattern as a function of ϕ and χ, as displayed in Figure 4.7, which was used for identification of the occurring phases. The quench at 370 °C indicates the formation of θ-Ni_2Si, as corroborated by the diffraction peaks at $2\theta = 27.0$, 32.8, 36.7 and 47.8° (respectively the $(10\bar{1}0)$, $(10\bar{1}1)$, (0002) and $(10\bar{1}2/(11\bar{2}0))$ planes). The θ phase was also observed for the quench at 405 °C, but in addition to several other diffraction peaks. We found a reasonable match with $Ni_{13\pm x}Si_{9-y}Al_y$ [22], a hexagonal phase which is related to θ-Ni_2Si through the formation of a vacancy-rich superstructure of the θ phase. Richter *et al.*, who investigated the bulk ternary Ni-Al-Si

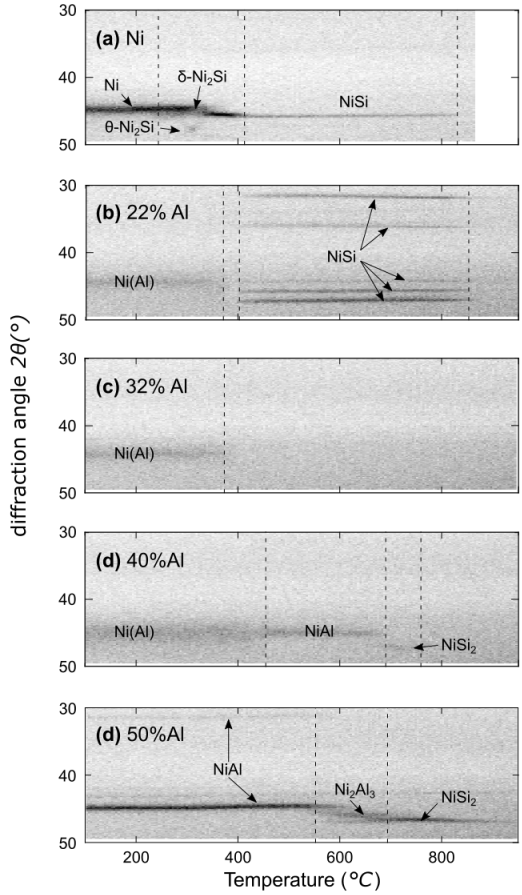

Figure 4.5: *In situ* XRD measurements for a 20 nm Ni film on Si(001) alloyed with *(a)* 0, *(b)* 22, *(c)* 32, *(d)* 40 and *(e)* 50 at.% Al, illustrating the phase formation sequence for the four observed Ni(Al) concentration regions.

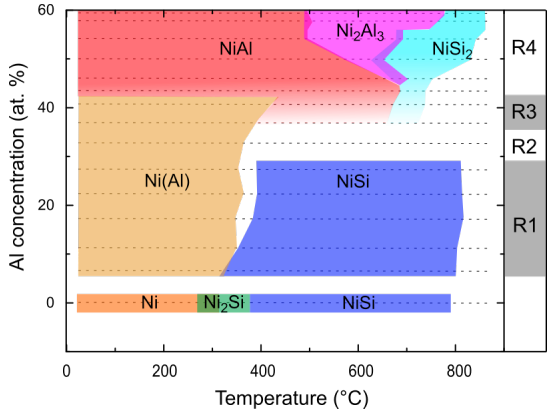

Figure 4.6: A phase formation diagram for the solid-state reaction of Ni_xAl_{1-x} layers on Si(001) substrates, as determined from the *in situ* XRD measurements. The horizontal dashed lines indicate the average Al concentration of the 15 samples for which *in situ* XRD data was measured and analysed.

phase diagram, observed no evidence for two separate phase fields for $Ni_{13\pm x}Si_{9-y}Al_y$ and θ-Ni_2Si and both phases were in fact treated as a single phase field [23].

The individual pole figures, which are measured at specific values of 2θ, represent the preferred orientation of a specific diffraction plane's normal, and as a consequence allow us to determine the epitaxial relationship between the formed phase and the substrate. Figure 4.8 displays the recorded pole figures for the quenched θ-Ni_2Si at 370 °C for the $(10\bar{1}0)$, $(10\bar{1}1)$ and $(10\bar{1}2)$ planes (resp. 27.0, 32.7 and 46.2°). Two epitaxial orientations are also displayed, which were determined to be (a) $(02\bar{2}1)_\theta \sim //(\bar{2}22)_{Si}$ & $(\bar{2}110)_\theta \sim //(220)_{Si}$ and (b) $(02\bar{2}1)_\theta \sim //(222)_{Si}$ & $(\bar{2}110)_\theta \sim //(\bar{2}20)_{Si}$ [24]. The quench made at 405 °C also contains these θ-Ni_2Si epitaxial features, now accompanied by additional epitaxial spots. No clear epitaxial relationship could be found for these features, and as a consequence the identification of this phase as $Ni_{13\pm x}Si_{9-y}Al_y$ is uncertain.

The $NiSi_2$ phase at low temperature The formation of NiSi in the SSR of Al-alloyed Ni films with the mono-crystalline Si(001) is limited for AL concentrations between 0 and 28 at.% (Fig. 4.6). A slightly higher amount of Al, i.e. 32 at.% , results in a complete absence of diffraction peaks after the consumption of the initial Ni(Al) film. Our measurements

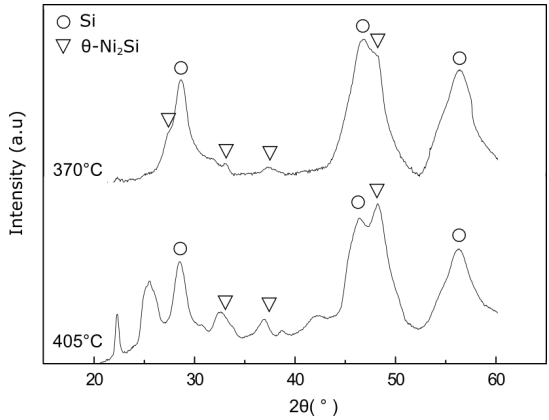

Figure 4.7: The average diffraction intensities for each value of 2θ are calculated from pole-figure measurements on samples quenched at 370 (top) and 405 °C (bottom). The former phase can be identified as θ-Ni_2Si, whereas the latter pattern could not be identified.

on poly-crystalline Si suggested that $NiSi_{2-x}Al_x$ can be formed at low temperatures after the consumption of the initial Ni(Al) layer, either as a single phase (region 2) or simultaneous with the formation of binary Ni-Al phases (regions 3 and 4). However, no such low-temperature occurence of $NiSi_{2-x}Al_x$ is observed by the *in situ* XRD measurements on Si(001). Therefore, samples from all four concentration regions were quenched at 650 °C and investigated through XPS for depth-sensitive stoichiometry information and pole-figure measurements for texture evaluation.

X-ray photo-electron spectroscopy (XPS) measurements (Fig. 4.9) reveal the layered structure of all samples. For all samples, a relatively thick Al_2O_3 top layer is present, indicating that a large fraction of the Al atoms were not able to react with the Ni or Si in the film. The $NiSi_{2-x}Al_x$ stoichiometry is present for samples with initial Al-concentrations from regions 2 and 3 (e.g. 37 and 43 at. %). As we do not expect the formation of an amorphous layer, a crystalline nickel-disilicide should be formed in the samples, in corroboration to the measurements on poly-Si substrates. The absence of diffraction during the *in situ* XRD measurements on single-crystalline Si(001) can be explained by a potential epitaxial alignment of the $NiSi_{2-x}Al_x$ grains with the Si substrate.

The *ex situ* pole-figures (not shown) contain diffraction features from the Si substrate (all samples), NiSi (region 1 samples), NiAl (region 3 samples) or Ni_2Al_3 (region 4 samples), but no clear signal indicating $NiSi_{2-x}Al_x$. However, the performed XPS measurements indicate that such a layer is

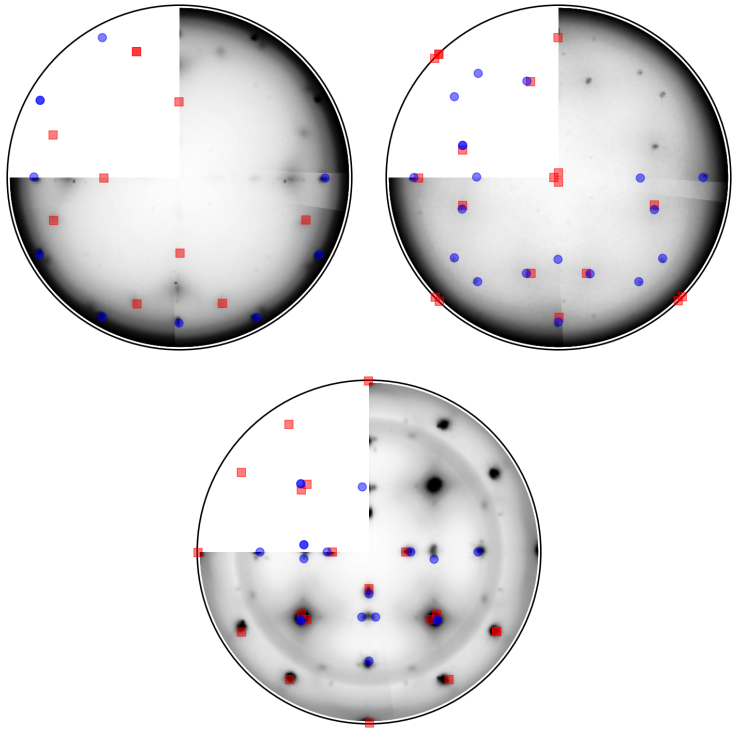

Figure 4.8: Pole figures for the θ-Ni_2Si $(10\bar{1}0)$, $(10\bar{1}1)$ and $(10\bar{1}2)$ planes, respectively. The epitaxial features were simulated and found to correspond to $(02\bar{2}1)_\theta \sim //(\bar{2}22)_{Si}$ & $(\bar{2}110)_\theta \sim //(220)_{Si}$ (red squares) and $(02\bar{2}1)_\theta \sim //(222)_{Si}$ & $(\bar{2}110)_\theta \sim //(\bar{2}20)_{Si}$ (blue circles).

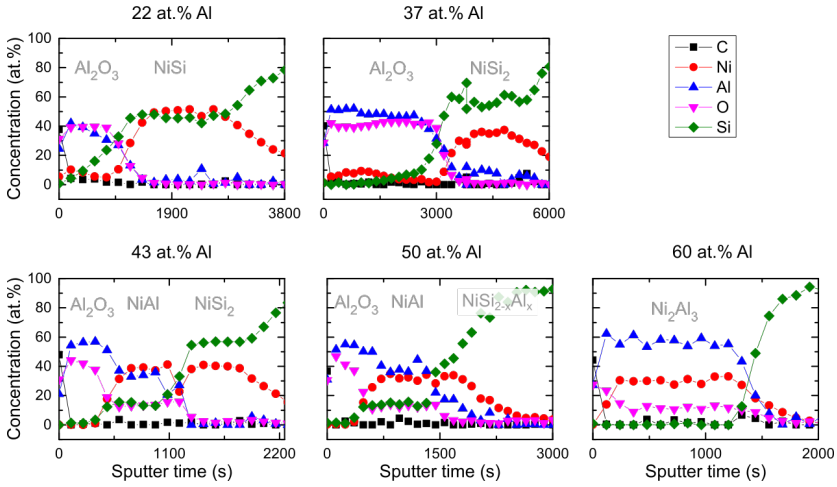

Figure 4.9: XPS measurements of Ni(Al) films deposited on Si(001) and quenched at 650 °C, revealing the layered structures of these samples.

present in concentration regions 2 and 3 (e.g. 37 and 43 at. %). This can be explained by supposing a specific orientation of $NiSi_{2-x}Al_x$, where its diffraction patterns overlap with diffraction from the Si substrate. Indeed, diffraction from $NiSi_{2-x}Al_x$ would occur at very similar angles 2θ to the substrate, and a type-A oriented $NiSi_{2-x}Al_x$ film would also coincide in in-plane and out-of-plane angles χ and ϕ. Thus the strong diffraction intensity from the substrate would saturate the detector, which results in an undistinguishable signal between type-A $NiSi_{2-x}Al_x$ and the substrate on the acquired pole figures of the $NiSi_2$ (202), (111) and (113) planes.

This suggests that the initial formation of $NiSi_{2-x}Al_x$ occurs with a type-A epitaxial texture and at much lower temperatures than when annealing a pure Ni film. For the highest Al concentrations (region 4), no clear $NiSi_{2-x}Al_x$ layer can be observed at this low temperature. We thus conclude that for regions 2 and 3, the Ni(Al) film must partially be transformed into type A $NiSi_{2-x}Al_x$, in agreement with the TEM-based studies on the SSR of thin Ni(Al) films on Si [7, 9]. Since pole-figure measurements are a non-local technique, in contrast to TEM measurements, this observation indicates the long-range coverage of the type A crystalline orientation.

The $NiSi_2$ phase at high temperature A selection of samples quenched at 900 °C was used to study the texture evolution of $NiSi_{2-x}Al_x$ as a function of Al concentration at high temperature. All samples at this temper-

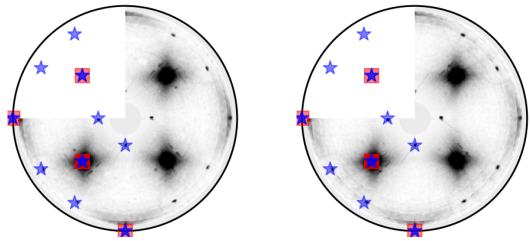

(a) Ni ref - 0 at.%

(b) 17 at.%

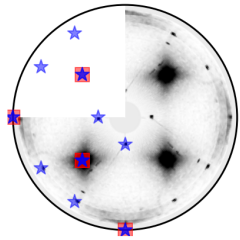

(c) 27 at.%

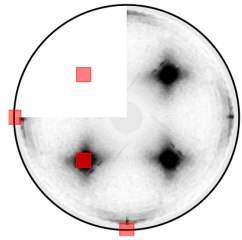

(d) 32 at.%

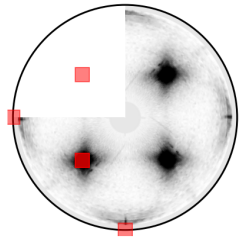

(e) 37 at.%

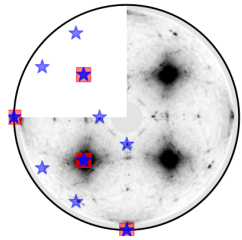

(f) 43 at.%

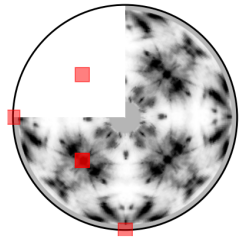

(g) 55 at.%

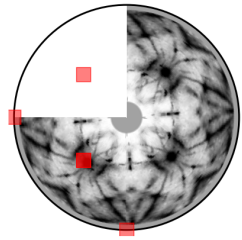

(h) 60 at.%

Figure 4.10: Evolution of pole figures as a function of Al concentration for the (220) $NiSi_{2-x}Al_x$ diffraction peak for samples quenched at 900 °C. The red □ and blue ⋆ icons indicate the position of epitaxial type A and type B-oriented $NiSi_2$, respectively.

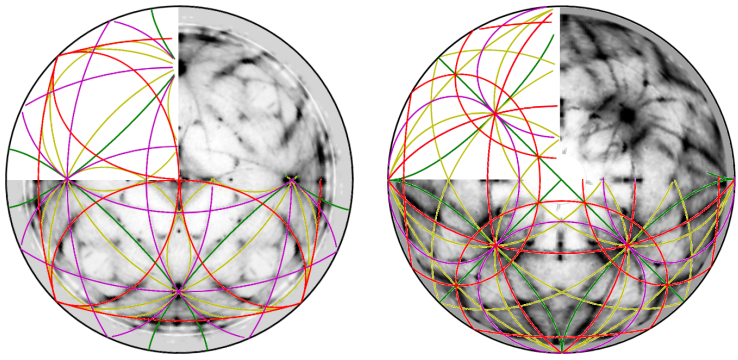

(a) (111) peak (b) (220) peak

Figure 4.11: Detailed fitting of the axiotaxial components of $NiSi_{2-x}Al_x$, for a sample annealed to 900 °C with an as-deposited Al concentration of 60 at.%

ature have formed $NiSi_{2-x}Al_x$, as indicated by both the *in situ* XRD measurements and XPS measurements (not shown). *Ex situ* pole figure measurements are displayed in figure 4.10. Two known epitaxial orientations can be expected, *type A* and *type B*. However, as described previously, we are not able to differentiate diffraction from the type A oriented grains and the Si substrate, since both diffract at the same alignment angles χ and ϕ and diffraction angles 2θ. By consequence, pole figures are limited to detecting only non-type-A textures (e.g. random, type-B epitaxy, axiotaxy) of $NiSi_2$. A noticeable change in texture can be observed through the pole figures as a function of Al concentration. The Ni reference, as well as all samples in the first concentration region up to 28 at.% clearly display type B epitaxy. Measurements on region 2 samples (i.e. 32 at.% Al), however, revealed no other texture except diffraction that can originate from type-A $NiSi_{2-x}Al_x$or the Si substrate, an identical observation as made at the low-temperature quench at 650 °C.

Samples from regions 3 (Fig. 4.11f) and 4 (Fig. 4.11g, h) display intriguingly more complex patterns with increasing intensity as more Al was incorporated. These are indicative of an axiotaxial texture [16, 25], and although this particular texture has been observed for several silicide-silicon systems [17, 26], it is the first time that such a texture is observed for the $NiSi_2$ phase. The axiotaxial texture lowers the interface energy between a thin film and a substrate through an alignment at the interface. One specific set of crystalline planes from the film is geometrically matched at the interface with a crystalline plane from the substrate, which can occur on

Table 4.1: Observed axiotaxies of the $NiSi_{2-x}Al_x$ phase, for samples quenched at 900 °C with an as-deposited Al content of 55 and 60 at.%

SYMB.	$NiSi_{2-x}Al_x$ ROTATION AXIS	χ (°)	ϕ (°)	ALIGNED WITH SI AXIS	COLOR
α	(100)	90	45	(100)	green
β	(110)	45	45	(110)	yellow
γ	(111)	55	90	(111)	pink
η	(100)	55	90	(111)	red

the condition that the planar distances of those planes are similar. No secondary orientation is fixed, contrary to epitaxy, and therefore the aligned $NiSi_{2-x}Al_x$ planes' normal then acts as a rotation axis, resulting in circular diffraction features visible on the pole figures. The circular radius is indicative to determine the axis of rotation of the $NiSi_{2-x}Al_x$ phase. These features could be reproduced by our home-developed GUSTAV software package [27], as shown in figure 4.11. The individual axiotaxial components are listed in Table 4.1. Three out of four axiotaxial rotation axes (α, β and γ) are in fact closely related to the type A epitaxial orientation. However, the observation of the axiotaxy texture instead of epitaxy indicates a difficulty for $NiSi_{2-x}Al_x$ grains to align in more than one direction with the substrate. Indeed, an epitaxial orientation requires two or more crystalline directions to align with planes of the substrate, whereas axiotaxy requires only one plane alignment. Hence, axiotaxy is formed more easily when the crystal structure between film and substrate do not perfectly match at the substrate-silicide interface.

The observation of axiotaxial alignment of $NiSi_{2-x}Al_x$ indicates that the Al concentration not only influences the phase reaction sequence, but also the epitaxial quality of the finally formed $NiSi_{2-x}Al_x$. Hence, it is interesting to determine the Al-concentration window for which the $NiSi_{2-x}Al_x$ film has the best epitaxial quality. RBS-C measurements allow such a qualitative assessment of the epitaxial quality, and were conducted on samples from all four concentration regions (i.e. 27, 33, 43 and 58 at.% Al) (Fig. 4.12). Two spectra were measured for each sample: one with the incident ion beam aligned with the $< 001 >$ direction of the Si substrate, and another one randomly aligned to the substrate. The quality of the epitaxial orientation of the silicide is represented by the minimal yield Y_{min} of the Ni-signal, i.e. the fraction of counts measured with an aligned sample over the counts measured with a randomly-chosen orientation. This yield

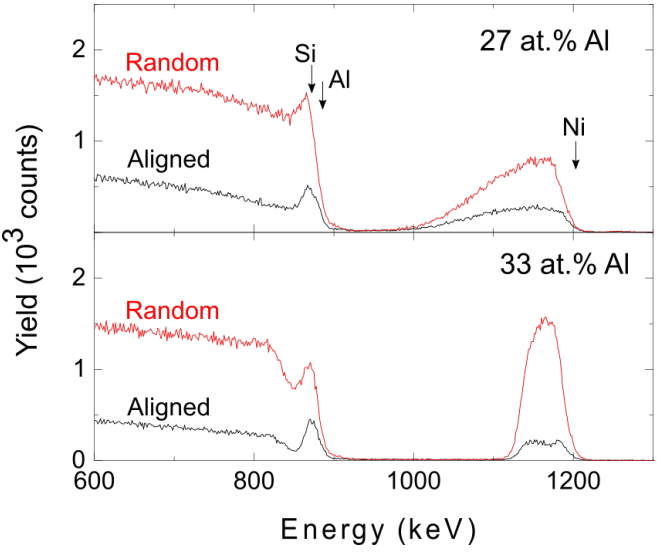

(a)

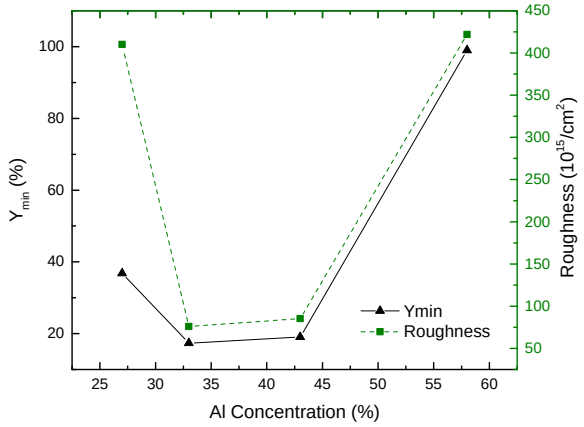

(b)

Figure 4.12: RBS-C allow to quantify the epitaxial alignment of the Ni atoms within the samples of samples quenched at 900 °C. **(a)** The intensity drop of the Ni signal when aligning the sample along a low-index Si plane is correlated to the epitaxial alignment of the Ni-containing layers with the substrate. The arrows indicate the energies if a particle would collide with an Al, Si or Ni atom at the samples' surface. **(b)** The minimum yield and calculated roughness for these measured samples indicate the best epitaxial layers for concentration regions 2 (33 at.%) and 3 (43 at.%).

is significantly low for samples originating from regions 2 (e.g. 33 at.%) and 3 (e.g. 43 at.% Al), corroborating that these samples are indeed epitaxially oriented, and with high epitaxial quality. The broadness of the RBS peaks can also be used to estimate the interface roughness of the silicide, as expressed through a standard deviation of the interface. The obtained values for samples with 27 and58 at.% Al show high roughness, whereas samples with 33 and43 at.% Al are very low, where the obtained value for the roughness are close to, or even below, the detector resolution. These observations, together with the conducted pole-figure measurements indicate no other orientation except type A epitaxy. As the XPS measurements revealed that these samples contain an Al_2O_3 top layer, the Y_{min} of the actual $NiSi_2$ film will be even lower. Moreover, our measurements show that $NiSi_2$ roughness is a lot higher for 27 and 58 at.% Al than in comparison with 33 or 43 at.% Al. This is in confirmation with the TEM-measurements conducted by Allenstein *et al.* [7], which showed a similar trend as a function of Al concentration.

4.4 DISCUSSION

In general, we observe that an increasing amount of Al promotes the formation of binary Ni-Al phases, as well as $NiSi_{2-x}Al_x$ for mid-range Al concentrations on both substrates. The promotion of $NiSi_{2-x}Al_x$ over NiSi through Al alloying was studied previously by Mogilatenko *et al.* [9] and was related to the insolubility of Al within a NiSi grain. Al needs to be expelled from the existing Ni-Al-Si mix when forming a NiSi grain, causing an accumulation of Al at NiSi grain boundaries, as such acting as a barrier for Ni grain-boundary diffusion and hindering further NiSi growth. They also reported on the low-temperature formation of $NiSi_{2-x}Al_x$, either in co-existence with NiSi grains or as a stand-alone phase for higher Al concentrations. The promoted formation of $NiSi_{2-x}Al_x$ was related to a lowered energy barrier for $NiSi_{2-x}Al_x$ formation, since the inclusion of Al within the $NiSi_2$ crystal structure results in a higher entropy, hence promoting its formation. However, when comparing these studies, we observe a difference in Al-concentration for which only $NiSi_{2-x}Al_x$ formation is observed instead of NiSi (an as-deposited concentration of 33 at.% Al for our measurements, compared to 16 at.% Al in reference [9]). This difference can possibly be related by the large amount of Al that is lost to the solid phase formation by the formation of an Al_2O_3 layer. Our sample with an as-deposited concentration of 33 at.% Al roughly contains 10 at.% Al in the top of the $NiSi_2$ layer through XPS (Fig. 4.9). As a consequence,

the effective Al concentration related to the observed changes in phase sequence can be much lower than the reported as-deposited concentrations.

The formation of binary Ni-Al phases (i.e. NiAl and Ni_2Al_3) from the as-deposited layer is observed in both the third and fourth concentration region. Our XPS-measurements (Fig. 4.9) reveal a layered structure, with a nickel-based silicide layer at the interface with the substrate, which is covered by a binary Ni-Al layer which has a higher Al concentration than the initial as-deposited layer. Moreover, *in situ* measurements reveal that the formation of the binary phase richer in Al occurs simultaneous with the initial formation of $NiSi_{2-x}Al_x$, as seen in figure 4.2d-e and figure 4.4. Forming $NiSi_{2-x}Al_x$ should require a larger amount of Ni than Al, since the maximum solubility of Al in $NiSi_{2-x}Al_x$ is limited to $x < 0.8$ [9, 11] and the actual Al concentration within a $NiSi_{2-x}Al_x$ grain is possibly even lower. By consequence, the initial Ni(Al)-layer becomes richer in Al concentration as Ni diffuses into the substrate to form $NiSi_{2-x}Al_x$, which explains the observed formation of binary NiAl and Ni_2Al_3. A schematic of this phase formation sequences is shown in figure 4.13, where the observed phase formation sequence for different Ni-Al starting conditions has been schematically indicated with arrows which are overlaid on the Ni-Al-Si ternary phase diagram with all thermodynamically stable phases [11, 23, 28].

The pole-figure measurements also allow us to determine the diffraction angles of the (111) and (220) $NiSi_{2-x}Al_x$ planes for those samples where non-type-A texture is present. Differentiation between diffraction from Si and $NiSi_{2-x}Al_x$ can be made through the selection of a specific region of the reciprocal space, based on the out-of-plane χ angle, and is displayed in Figure 4.14. Remarkably, the diffraction angle, hence the lattice parameter, does not significantly change within the first concentration region. As the incorporation of Al should induce an increase in lattice parameter, this shows that only a small fraction of the Al is incorporated within the CaF_2-type lattice, as corroborated by the XPS measurements. Only those samples with 55 or 60 at.% show a significantly lower diffraction angle of the (111) and (220) peaks. These measurements suggest that the lattice parameter of $NiSi_{2-x}Al_x$ has expanded to a value *larger* than Si. Moreover, this difference will be much larger during the annealing procedure, due to the higher thermal expansion coefficient of $NiSi_2$ than Si. We speculate that this difference in lattice parameter is then too large to form a large-area type-A epitaxial thin film on the Si substrate. Contrary to epitaxy, the axiotaxial texture can still be formed, even when there is a relative large difference in lattice parameter.

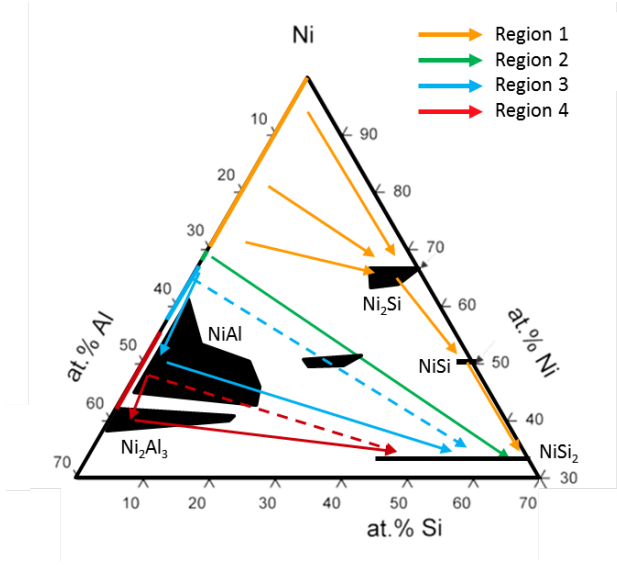

Figure 4.13: Schematic of the phase formation sequence on the ternary Ni-Al-Si diagram. The solid-state reaction in region 3 and 4 is characterised with a two-fold forked formation path, where the initial phase formation of $NiSi_{2-x}Al_x$ (dashed lines) coincides with the occurrence of binary Ni-Al phases.

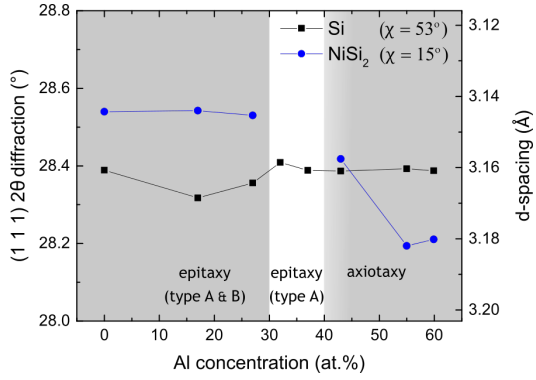

(a) (111) peak

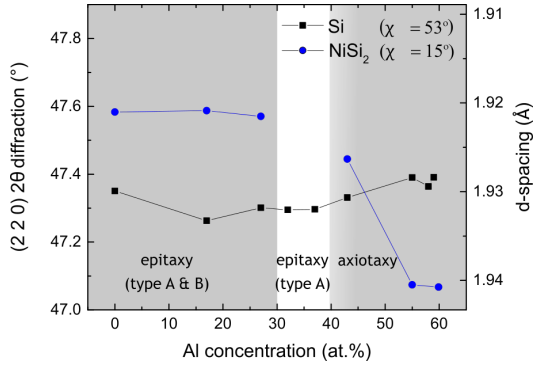

(b) (220) peak

Figure 4.14: The (111) and (220) peak position of $NiSi_{2-x}Al_x$ diffraction at a selected part of reciprocal space, corresponding to diffraction originating from the Si substrate ($\chi = 53°$) or the $NiSi_{2-x}Al_x$ film ($\chi = 15°$).

These observations, together with published texture studies of $CoSi_2$ (also sharing the CaF_2-type lattice of $NiSi_2$ and Si) indicate the importance of a good lattice match for epitaxial growth. Indeed, the films with the smallest lattice parameter, i.e. $CoSi_2$, form mostly with type B-epitaxy, together with minor type A epitaxy and axiotaxial texture [6, 29]. The axiotaxial features decrease in intensity when adding Ni to the $CoSi_2$ films, correlated with an increase in the lattice parameter towards the value of unalloyed $NiSi_2$ [30], which is closer to the lattice parameter of Si (5.364 Å for $CoSi_2$, 5.406 Å for $NiSi_2$, and 5.431 Å for Si). Pure $NiSi_2$ films grow only with type A and B epitaxies, with type A as the dominant orientation [6]. Further increase in lattice parameter was obtained here through Al alloying, and correlates with the elimination of type B epitaxy. However, adding too much Al causes the lattice parameter to increase beyond the value for the Si substrate, where we again observe axiotaxial texture. Hence, our observations suggest that the texture of $NiSi_2/NiSi_{2-x}Al_x$ evolves as a function of expanding d-spacing as $type\ A\&B \rightarrow type\ A \rightarrow axiotaxial$, where a lower alignment symmetry is observed when deviating from the Si lattice parameter. RBS-C measurements confirm that the best epitaxial films are found for samples from concentration region 2. By consequence, the temperature window for which the Al alloying results in a single epitaxial orientation, is limited to 32-42 at.% .

4.5 CONCLUSIONS

The phase formation sequence of the solid-state reaction between Al alloyed Ni films on Si(001) and poly-crystalline Si was monitored for an Al concentration up to 60 at.%. Both substrates result in similar phase formation sequences as a function of Al concentration. We observed that $NiSi_{2-x}Al_x$ is promoted through Al alloying, and that an excess of Al promotes the crystallisation of binary NiAl or Ni_2Al_3 through out-diffusion of Ni. On a mono-crystalline Si(001) substrate, the intermediate formation of θ-Ni_2Si was observed and its preferential orientation with respect to the Si substrate was determined. Furthermore, the preferential orientation of $NiSi_{2-x}Al_x$ shows a remarkable dependence as a function of Al concentration, where axiotaxial $NiSi_2$ is observed for the first time. As a consequence, it is shown that the epitaxial alignment of $NiSi_2$ can be significantly improved through Al incorporation, although the Al concentration window is limited. This work also shows how minor differences in lattice parameters influence the formed texture, improving our under-

standing of the nickel-based silicidation process in order to potentially achieve high-quality epitaxial silicides.

5

ARTICLE II: ON THE INFLUENCE OF ALLOYING ON THE NI SILICIDE SOLID STATE REACTION AND TEXTURE, ABOVE AND BELOW THE CRITICAL THICKNESS

5.1 INTRODUCTION

The nickel silicides have been studied thoroughly in the past due to the beneficial properties of NiSi (e.g. low sheet resistance, low Schottky Barrier Height, low formation temperature) for usage as contact material in Si-based transistor devices [1–3]. The phase formation process typically involves the annealing of an as-deposited Ni film on top of a Si substrate, resulting in the sequential formation of δ-Ni_2Si, θ-Ni_2Si, NiSi and $NiSi_2$ [4–7]. Recent investigation of this *'regular'* phase sequence for relatively thick Ni films (i.e. for an as-deposited Ni thickness of e.g. 6 - 30 nm) showed that the solid-phase reaction (SPR) includes a complex balance in thermodynamic parameters, indicated through the formation of a transient metastable θ-Ni_2Si phase [5–7] . In addition to the observation of θ-Ni_2Si, an unidentified epitaxial phase was also observed in the SPR at the lowest investigated temperature, i.e. 290 °C.

Due to the constant urge for miniaturisation in micro-electronic applications, the silicide contacts are trending to ever-thinner films. Surprisingly, for as-deposited and pure Ni films of only a few nanometres thickness, no NiSi is formed [8–10]. It was already observed by Tung *et al.* in the early 80's that the phase sequence is significantly different when the as-deposited Ni layer is thinner than ca. 5 nm [11, 12]. In this '*ultrathin*' SPR, the δ-Ni_2Si and NiSi phases are not formed and instead, $NiSi_2$ is already present at temperatures as low as 400 °C, at least 300 °C earlier than in the '*regular*' SPR. Intriguingly, an epitaxial, intermediate phase - with similar diffraction signature as observed in the 'regular' phase formation by Gaudet *et al.* [6] - was observed during this ultrathin SPR, prior to the formation of low-temperature $NiSi_2$. The observation that both silicide formation regimes first form the same epitaxial phase, indicates that the origin of the shift from the regular regime to the ultra-thin regime lies in the formation of subsequent phases.

An intriguing question is how the phase formation in both the regular, as well as in the ultrathin film regimes, can be affected through the addi-

tion of ternary elements. Indeed, silicides are often tailored through the addition of alloying elements to the as-deposited metal film, in order to alter the final properties of the formed phases [4, 13–15]. As one of the more contemporary examples, Pt-incorporation in NiSi films is known to improve the films' morphological stability, as well as to alter the preferential orientation to the Si substrate [15, 16]. Moreover, it is also reported that Pt can influence the thermodynamic stability of the intermediate silicide such as δ-Ni_2Si [17, 18]. However, the influence of ternary elements on the solid-phase formation during the sequential growth of silicides in this sub-10 nm thickness region has not been studied in a systematic way.

Films with these low thicknesses will receive a high energetic drive to optimise the interface alignment with the substrate. This paper investigates the phase formation in both the 'thin' (i.e. with an as-deposited Ni thickness = 9 nm) and in the 'ultrathin' (i.e. Ni thickness = 3 nm) SPR regime and how this is influenced by alloying with Pt, Co and Al. These alloying elements were selected because of their different solubility in the various nickel silicide phases. Through complementary X-ray diffraction measurements, we obtain a comprehensive understanding of the silicide formation, and preferential orientation of the resulting phases to the Si(001) substrate, as a function of film thickness and alloying elements.

5.2 EXPERIMENTAL METHODS

Thin Ni films of both 3 and 9 nm thick were deposited through physical vapour deposition (PVD) on top of single crystalline Si substrates with (001) orientation. Samples for *in situ* sheet resistance measurements were sputtered on silicon-on-insulator (SOI) substrates with identical orientation and a top Si thickness of 100 nm. Prior to the deposition, these wafers received a standard chemical cleaning, following the guidelines of the Radio Corporation of America (RCA), ending with a 20 s dip in 3 % HF solution.

After reaching a base pressure of 6×10^{-7} mbar, the deposition chamber was filled with Ar up to 5×10^{-3} mbar. The deposition of Ni was performed at a relatively low sputter rate of 1.3 nm/ min, as determined through *ex situ* X-ray reflectivity (XRR) measurements. The samples were optionally alloyed with an estimated concentration of 10 at.% of Al, Co or Pt through simultaneous co-sputtering with separate sputter targets, after careful calibration of the Al, Co and Pt sputter rates on the basis of XRR. We note that the alloying species were added in *addition* to the initial Ni content. As Co and Pt are known to replace Ni atoms during silicide

formation, the addition of these alloying elements render an effective increase in the metal supply to form $Ni_xM_ySi_z$ (M = Co, Pt) compounds. Other papers therefore prefer to keep the metal supply constant by reducing the Ni content when adding a ternary alloy, but such an approach is not easily translated to Al alloying, which is known to replace the Si atoms during silicide formation. For conciseness, these samples will be referred to as Ni(Al), Ni(Co) and Ni(Pt).

The samples were then annealed in a dedicated *in situ* X-ray diffraction (XRD) set-up at the X20C-beamline of the NSLS synchrotron (Brookhaven, USA). The synchrotron provides adequate X-ray brightness to investigate these ultra-thin samples. The solid-phase reaction between the film and the substrate was monitored during an anneal at a rate of 1 °C/ sec in a He(5 %H_2) ambient, as these samples are otherwise prone to oxidation during the annealing process. The X-rays, with a wavelength of $\lambda = 0.180\,\text{nm}$ (i.e. an energy of 6.88 keV) diffract on the sample in a fixed incidense geometry, therefore only monitoring diffraction signal originating from planes nearly-parallel to the sample's surface. The diffracted intensities were monitored using a custom-build linear detector with a total angular acceptance of 14° in 2θ. These diffractograms are plotted as a function of temperature and diffraction angle using a grayscale map for the recorded intensity values, where black indicates the highest intensity. A similar annealing set-up was used for *in situ* sheet resistance measurements during temperature treatment through a four-point probe approach with identical annealing conditions. The set-up does not guarantee an identical probe geometry between separate measurements, and as such the measured resistances will be plotted on a relative scale, instead of an absolute scale, as a function of temperature.

As-deposited samples were alternatively quenched from specific temperatures for *ex situ* pole-figure measurements for crystal phase identification and characterisation of the preferential orientation, also known as crystalline texture. A total of 100 samples were measured in order to obtain a quasi-continuous dataset as a function of quench temperature. These *ex situ* measurements were performed at the DiffAbs beamline of the SOLEIL synchrotron (Gif-sur-Yvette, France) [19]. The incidence X-ray beam is monochromatized using a double-crystal monochromator to a wavelength of $\lambda = 1.55\,\text{nm}$ (i.e. an energy of 8 keV). A 6-circles diffractometer in kappa geometry was used together with a hybrid pixel area detector (XPAD detector of 240×560 pixels, with a pixel size of 130 by 130 µm)[1]) [20–23]. The long side of the detector was mounted in the 2θ direction, resulting in an angular acceptance determined to be 32°, and

1 More details on the XPAD detector can be found in [20–23] and Appendix B

Table 5.1: Overview of the binary nickel-based phases observed in this paper.

PHASE	LATTICE	a (Å)	b (Å)	c (Å)	JCPDS NO.
Ni	FCC	3.524	-	-	00-004-0850
δ-Ni_2Si	Orth.	7.066	5.008	3.732	00-048-1339
θ-Ni_2Si	Hex.	3.805	-	4.890	01-073-2093
NiSi	Orth.	5.233	3.258	5.659	00-038-0844
$NiSi_2$	FCC	5.406	-	-	03-065-2974

around 13° in the perpendicular direction. The area detector acquired a snapshot every 100 ms during a continuous in-plane rotation of the samples' azimuth (denoted as the ϕ angle), rotating at a speed of $8\,^{\circ}\,s^{-1}$ and covering 110° in ϕ. The sample was then rotated in the elevation angle χ in steps of 5° from 0 to 85°, rendering significant overlap between two sequential χ steps. This set-up enables the measurement of a set of pole figures within 4.5 min. Every sample was measured at least three times without re-aligning the sample, in order to obtain adequate diffraction statistics for these sub-10 nm thin films.

The raw data were re-calculated to angular (χ, ϕ and 2θ) space and the resulting datasets are presented in this paper in polar coordinates with an equal-area projection and a logarithmic-intensity gray-scale with black indicating the highest intensities. The acquired data were symmetrized to a full 360° ϕ coverage, exploiting the four-fold symmetry of the Si(001) substrate. These pole figures were analysed using a home-developed software package, GUSTAV [24], in order to determine the preferential orientations of the silicides.

5.3 RESULTS

We report on the SPR between the (un)alloyed Ni films with the Si substrate for two different Ni thicknesses: 3 and 9 nm. As mentioned in the previous paragraph, *in situ* XRD measurements allow continuous phase identification as a function of temperature, on the condition that the diffracting planes are oriented (nearly) parallel to the sample's surface. Epitaxial phases, which do not necessarily fulfill this condition, are alternatively observed through the *ex situ* pole figures. The latter measurements will also be used to assess the preferential orientation of the silicide grains with respect to the Si(001) substrate. Table 5.1 gives an overview of the occurring silicide phases and their lattice parameters.

9 nm *Ni films*

The *in situ* XRD measurement of an unalloyed, 9 nm Ni film is displayed in figure 5.1a. The SPR shows the transformation of the initial Ni diffraction peak at room temperature, into the δ-Ni_2Si around 230 °C. The peak at $2\theta = 56.4°$, observed in a small temperature window of ca. 20 °C around 300 °C was discussed in the recent study by Gaudet *et al.* [6], and is related to a fiber-textured θ-Ni_2Si. This θ-Ni_2Si phase is then consumed, after which δ-Ni_2Si and NiSi are present. Around 450 °C, δ-Ni_2Si is also consumed leaving NiSi as the only observed phase during the rest of the *in situ* annealing experiment.

Similar measurements on Ni samples which are alloyed with 10 at.% Al, Co and Pt (Fig. 5.1 b,c and d) show clear differences with the above observations. (i) The as-deposited Ni(Al) layer diffracts with much lower intensity, which can be explained by a lower crystalline-order of the as-deposited layer due to the incorporation of Al in the Ni lattice through the co-sputtering of both materials. However, the Ni-diffraction peak at $2\theta = 53.0°$ is still observable and is consumed around 300 °C. No clear silicide phase can be identified immediately thereafter. Instead, a broad background is observed, which diminishes for a small temperature window of 20 °C just prior to the formation of NiSi. The latter phase is then the only phase remaining throughout the annealing experiment. Comparing the relative diffracted intensities of the NiSi (112) peak ($2\theta = 54.0°$) to the (202/211) peak ($2\theta = 55.8°$) already hints that the texture of this phase is different from the NiSi texture formed from the pure Ni film. No intermediate phases such as δ-Ni_2Si or θ-Ni_2Si are observed via *in situ* XRD during the annealing process. (ii) The annealing of a Ni(Co) layer is comparable to the pure Ni reference measurement up to 500 °C, with the similar observation of δ-Ni_2Si and θ-Ni_2Si. At higher temperatures, the formation of $NiSi_2$ is observed as seen through the occurrence of its diffraction peak at $2\theta = 56.0°$ and 33.5° (the latter visible through measurements at a different 2θ diffraction window), far earlier than for unalloyed Ni, where it would only form above 850 °C. (iii) Finally, the *in situ* XRD of Ni(Pt) does not contain clear diffraction of intermediate Ni_2Si phases. Furthermore, similar to the Ni(Al) sample, there is a significant difference in observed intensity of the NiSi peaks, where now the most intense peak is originating from the (202)/(211) planes, again indicating a significant change in preferential orientation.

The *in situ* XRD measurements indicate that most of the formed phases are observed between 200 and 400 °C. Therefore, *ex situ* pole figures are measured for samples quenched every 25 °C in this temperature window,

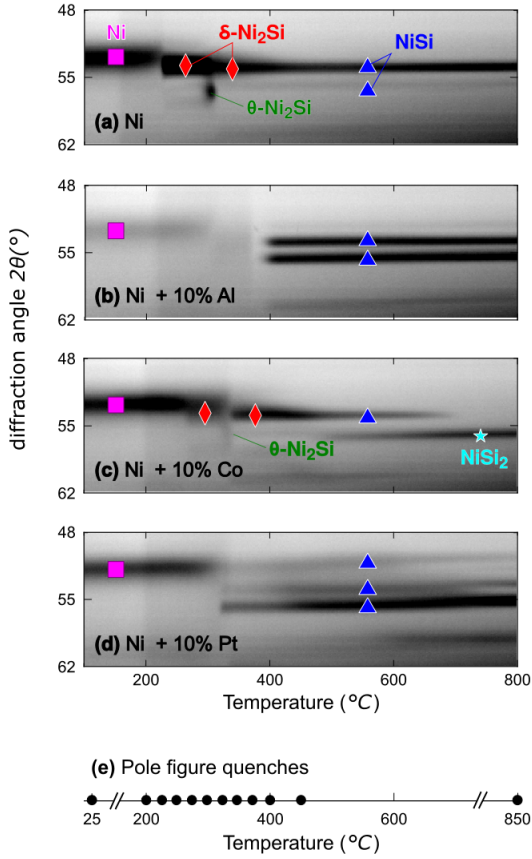

Figure 5.1: *In situ* XRD measurements of 9 nm thick Ni films: unalloyed **(a)**, and alloyed with 10 at.% Al **(b)**, Co **(c)** and Pt **(d)**. These measurements allow to determine the important temperature regions where quenches were made for further *ex situ* investigation **(e)**, in addition to a measurement at room temperature.

in addition to an as-deposited sample, and quenched samples at 450 and 850 °C (Fig. 5.1e). For each of these 48 samples, sets of *ex situ* pole figures were acquired using an area detector, resulting in one pole figure for every value of 2θ in between 30 and 62° in a quasi-continuous fashion, due to the 540 pixels along the 2θ direction. A selection of the measured pole-figure data is shown in figure 5.2, which contains the integrated diffracted intensities around $2\theta = 45.5° \pm 0.4°$ (d = 1.98-2.01 Å, corresponding to $2\theta = 53.6° \pm 0.5°$ for the X-ray wavelength used during the *in situ* XRD measurements). This broad 2θ window includes diffraction intensities from the Ni(111), δ-Ni_2Si(301/121), θ-Ni_2Si(102/110) and NiSi(112) planes and serves as an overall illustration of all observed phases. Si(220) diffraction is also measured, and the position of these epitaxial spots are indicated on the pole figures. Other pole figures from the complete set of pole figures (of which a selection will be discussed further) were used to corroborate the phase identification and their texture during the analysis.

In the following overview of our results concerning the 9 nm Ni films, we first discuss the texture of every occurring phase, as observed for the four differently-alloyed samples. Thereafter, the change in diffracted intensities of those phases is addressed as a function of temperature, which allows to interpret the rate of formation and consumption of these phases and compare these with *in situ* XRD measurements.

OVERVIEW OF OBSERVED TEXTURES The pole figures of unannealed samples (not shown) indicate that the crystalline grains of Ni, Ni(Al) and Ni(Pt) do not have a strong preferential orientation, and as such, the pole figures do not show significant changes in intensity as a function of χ or ϕ. Ni(Co), on the other hand, exhibits higher diffraction signal at the center of the pole figure (comparable to Fig. 5.2c-i) and a diffraction ring near $\chi = 70°$. The concentric diffraction ring is typically observed for a fiber texture, for which a specific crystalline direction acts as a rotation axis perpendicular to the sample's surface. The higher diffraction at the center of the pole figure indicates that the Ni(Co)(111) plane is oriented perpendicular to this center of rotation, which coincides with a diffraction ring at $\chi = 70.5°$ due to the cubic symmetry of the Ni unit cell, and also explains the diffraction ring of the Ni(200) plane (not shown) at $\chi = 54°$.

Annealing these samples up to 200 °C provides a slight increase of small diffraction spots (figure 5.2 a-i), indicating the presence of an epitaxial phase. The same diffraction pattern is observed for all samples annealed at 300 °C, and is identical to the epitaxial phase observed for 3 nm films at 350 °C [8, 25] which was identified as an epitaxial θ-Ni_2Si. The observed diffraction spots of θ-Ni_2Si can be explained by two different epitaxial

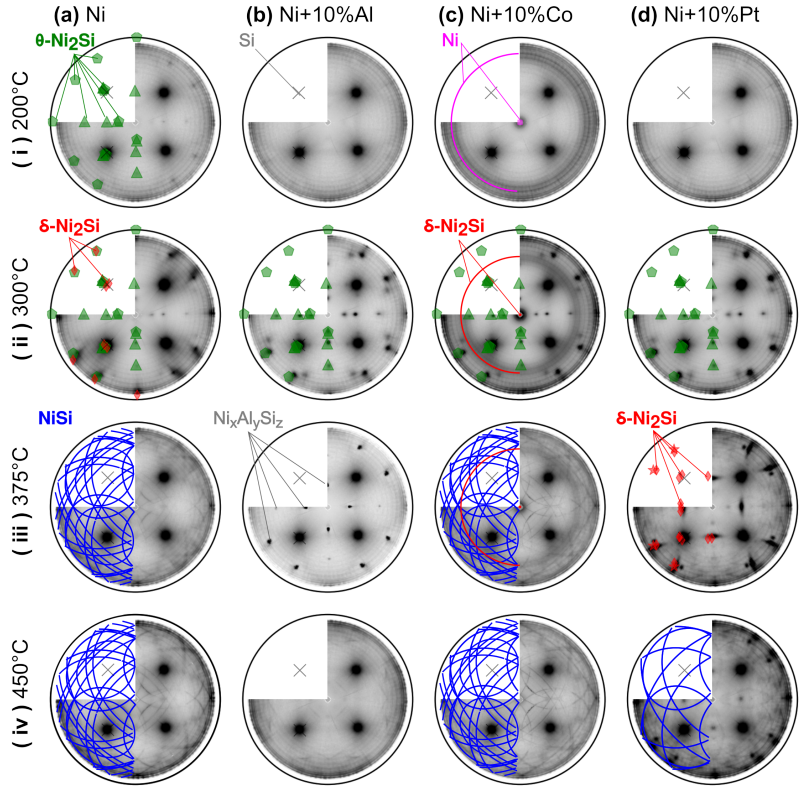

Figure 5.2: A selection of the aquired pole-figure dataset for alloyed and unalloyed 9 nm Ni films, displaying the integrated diffraction intensities around $2\theta = 45.5° \pm 0.4°$. These images examplify the observed phases and their textures. The identified silicide textures are overlapped on the left half of the dataset (using the symbols defined in tables 5.2, 5.3 and 5.4). The Si(220) diffraction peak is always visable and indicated with a gray cross.

Table 5.2: Overview of observed epitaxial orientations of the θ-Ni_2Si phase for all 3 and 9 nm films (symbols used in figures 5.2 and 5.7). The angular mismatch between the film and substrate, as calculated from the proposed alignments, are given in terms of $\Delta\chi$ and $\Delta\phi$.

SYMBOL	PLANE ALIGNMENTS	$\Delta\chi$ (°)	$\Delta\phi$ (°)
A_θ (⬟)	$(02\bar{2}1)_\theta \sim //(\bar{2}22)_{Si}$	0.2	0.0
	$(\bar{2}110)_\theta \sim //(220)_{Si}$	0.1	0.1
	$(000\bar{1})_\theta \sim //(1\bar{1}1)_{Si}$	0.6	0.8
B_θ (▲)	$(02\bar{2}1)_\theta \sim //(222)_{Si}$	0.2	0
	$(\bar{2}110)_\theta \sim //(\bar{2}20)_{Si}$	0.1	0.1
	$(0001)_\theta \sim //(\bar{1}\bar{1}5)_{Si}$	0.16	0.85

Table 5.3: Overview of observed epitaxial (A_δ, B_δ) and fiber (C_δ) orientation of the δ-Ni_2Si phase as observed for 9 nm Ni, Ni(Co) and Ni(Pt) films (symbols used in figures 5.2 and 5.3). The angular mismatch between the film and substrate, as calculated from the proposed alignments, are given in terms of $\Delta\chi$ and $\Delta\phi$.

SYMBOL	PLANE ALIGNMENTS	$\Delta\chi$ (°)	$\Delta\phi$ (°)	OCCURRENCE
A_δ (⧫)	$(001)_\delta \sim //(110)_{Si}$	0	0	Ni, Ni(Pt)
	$(301)_\delta \sim //(20\bar{2})_{Si}$	1.9	0.8	
	$(0\bar{1}0)_\delta \sim //(1\bar{1}1)_{Si}$	0	0.4	
B_δ (★)	$(001)_\delta \sim //(110)_{Si}$	0	0	Ni(Pt)
	$(121)_\delta \sim //(20\bar{2})_{Si}$	2.7	1.4	
	$(010)_\delta \sim //(\bar{1}\bar{1}5)_{Si}$	0.2	0.4	
C_δ (–)	$(301)_\delta \sim //(00\bar{2})_{Si}$	0.0	0.0	Ni(Co)

alignments with the Si substrate (Table 5.2, where A_θ has the highest observed diffracted intensity) [25, 26], whose positions are overlaid by green circles in figures 5.2ii. The approximate alignment for the $\{0001\}$ planes are also given to initiate further discussion.

The δ-Ni_2Si phase can be observed for Ni, Ni(Co) and Ni(Pt) in figures 5.2a-ii, c-ii and d-iii films but did not occur for any quenched Ni(Al) sample. Remarkably, the texture of the δ-Ni_2Si is significantly affected by alloying the Ni film. Additional pole figures of the δ-Ni_2Si(002) and (021) planes are shown in figure 5.3. Two different texture types are observed: epitaxial alignment for unalloyed Ni and Ni(Pt), and fiber-aligned δ-Ni_2Si for Ni(Co). For unalloyed Ni, the preferential orientation can be mostly described as randomly distributed without any relation with the

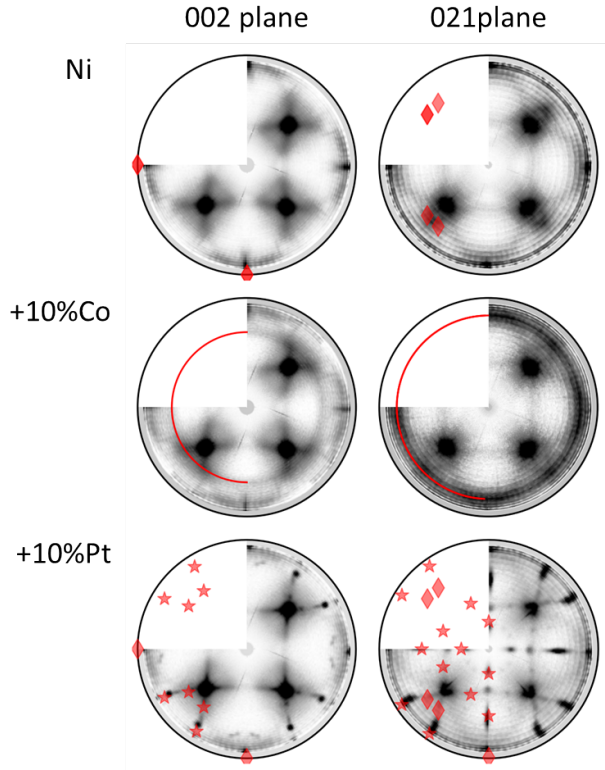

Figure 5.3: The pole figures which contain diffraction of δ-Ni_2Si show that both epitaxial and fiber-aligned silicide are present, depending on the composition of the initial 9 nm Ni film.

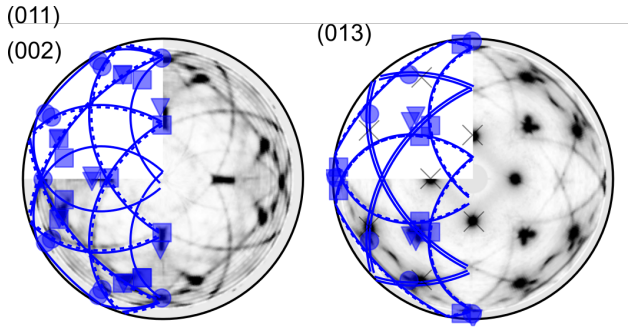

Figure 5.4: The 9 nm Ni(Pt) pole figures which display diffraction of NiSi contain both axiotaxial (circular lines) as well as epitaxial (local spots of higher intensity) features. The overlayed epitaxies are listed in table 5.4.

underlying substrate, in addition to the low-intense epitaxial alignment. The identification of the epitaxial alignments observed within the Ni and Ni(Pt) samples are given in table 5.3. The fiber-texture observed in the Ni(Co) sample was determined to be originating from a $(301)_{\delta}//(002)_{Si}$ alignment.

For Ni(Al), an epitaxial phase is observed at 375 °C (labeled as $Ni_xAl_ySi_z$ in Fig. 5.2b-iii), in agreement with the phase observed in a recent study on the Ni(Al) silicide formation process for thicker Ni films [27]. Its occurrence is indicated by additional diffraction peaks at $2\theta = 22.4$, 24.9, 32.1, 36.7 and 38.6°, but no match could be found with reference diffraction patterns in the JCPDS database, preventing a clear phase identification. The ternary Ni-Al-Si phase diagram [28–30] does include several ternary phases, and not all of the crystal structures are available in the literature.

At higher temperatures, the NiSi phase is present within all of the samples. Pole figures for this NiSi phase exhibit a complex pattern of circular features, which is indicative for the axiotaxial texture previously discussed by Detavernier *et al.* [31]. The axiotaxy originates from the preferential alignment of lattice planes with a similar d-spacing across the interface. Two axiotaxial axes are observed here: $(202)_{NiSi}//(202)_{Si}$ and $(211)_{NiSi}//(202)_{Si}$, in agreement with our earlier work [31, 32]. The patterns for the unalloyed Ni sample are almost identical to the patterns observed from a Ni(Co) sample (Fig. 5.2a,b-iii,iv). The intensity of these circular features is, however, significantly reduced for the Ni(Al) sample, where the NiSi phase diffracts more uniformly for every χ and ϕ value, indicating a more random distribution of the grains' orientations (Fig. 5.2b-iv). NiSi formed from the Ni(Pt) sample also contains local diffraction spots of higher intensity along the circular features, indicating that the

Table 5.4: Overview of observed epitaxial orientation of the NiSi phase (symbols used in Fig. 5.4). The angular mismatch between the film and substrate, as calculated from the proposed alignments, are given in terms of $\Delta\chi$ and $\Delta\phi$.

SYMBOL	PLANE ALIGNMENTS	$\Delta\chi$ (°)	$\Delta\phi$ (°)	OCCURRENCE
A_{NiSi} (■)	$(\bar{1}0\bar{1})_{NiSi} \sim //(101)_{Si}$	0	0	Ni(Pt), 9 & 3 nm
	$(300)_{NiSi} \sim //(2\bar{2}\bar{2})_{Si}$	3.7	2.9	
	$(010)_{NiSi} \sim //(10\bar{1})_{Si}$	0	0	
B_{NiSi} (▼)	$(21\bar{1})_{NiSi} \sim //(\bar{2}20)_{Si}$	0	0.96	Ni(Pt) 9 nm
	$(013)_{NiSi} \sim //(1\bar{1}0)_{Si}$	0	0	
	$(100)_{NiSi} \sim //(111)_{Si}$	4.78	0	
C_{NiSi} (●)	$(211)_{NiSi} \sim //(02\bar{2})_{Si}$	1.36	3.93	Ni(Pt), 9 nm
	$(013)_{NiSi} \sim //(\bar{1}10)_{Si}$	3.13	0.1	
	$(100)_{NiSi} \sim //(\bar{1}\bar{1}\bar{5})_{Si}$	0.0	4.1	

rotational freedom allowed by the axiotaxial alignment, is reduced with a second alignment orientation, thus pinning these grains in an epitaxial alignment (Fig. 5.2d-iv). The fitted epitaxial components are displayed in figure 5.4 and listed in Table 5.4.

EVOLUTION OF TEXTURED DIFFRACTION AS A FUNCTION OF TEMPERATURE From every observed phase in the *ex situ* pole-figure measurements, a specific region within χ, ϕ and 2θ was selected that was isolated from the diffraction of other phases, and the diffraction intensity was subsequently fitted with a local background. The evolution of the fitted intensities as a function of temperature is displayed in figure 5.5. In order to compare the evolution of the different phases as a function of temperature, we have plotted the relative intensity, i.e. normalized to the maximum observed intensity of that particular phase for each of the as-deposited compositions. This provides an overview similar to the *in situ* XRD technique, but the pole figures allowed to include textured phases such as epitaxial θ-Ni_2Si. In the *in situ* XRD measurements, a small temperature window exists for the Ni and Ni(Co) sample where diffraction was observed at $2\theta = 56.4°$, related to a fiber-textured θ-Ni_2Si [6], which is not observed within the pole-figure measurements. We relate this inconsistency to either an instability of this phase during quenching, or that this particular phase's temperature window is slightly smaller than the temperature difference between two *ex situ* pole-figure quenches.

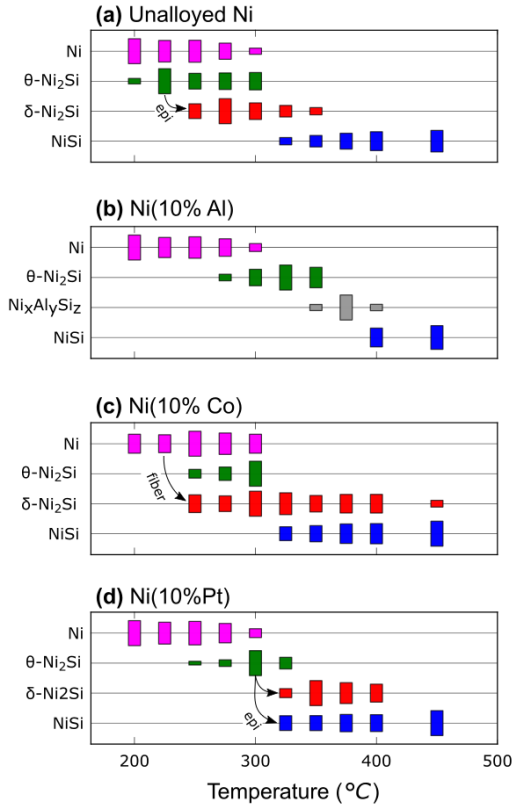

Figure 5.5: Overview of the observed silicides' diffraction intensity as a function of temperature for pure and alloyed 9 nm Ni films. The observed intensities are proportional to the height and normalised to the maximum occuring intensity per sample. Arrows indicate examples of texture inheritance across multiple phases, as explained in the discussion.

3nm Ni films

For Ni films of 3 nm as-deposited thickness, a slightly different approach was needed, as the *in situ* XRD diffraction of the Ni, Ni(Al) and Ni(Co) samples did not contain any distinguishable change in diffraction signal, and thus doesn't provide any information on the SPR. Alternatively, *in situ* sheet resistance measurements can be used to monitor transitions of the formed silicides during the annealing. Indeed, as shown in figure 5.6a, the sheet resistance of an unalloyed Ni film shows relatively high resistance between 150 and 300 °C, followed by a decrease between 300 and 400 °C. Thereafter, the resistance decreases at slower pace further up to 850 °C. Similar behaviour is observed for Ni(Al) and Ni(Co). The sheet resistance in Ni(Pt) also contains a decrease in sheet resistance around 340 °C, within a narrower temperature window. However, the low-resistive state is only stable up to 600 °C, after which the resistance dramatically increases, which is typically observed when NiSi is agglomerating [4, 8, 33].

The *in situ* sheet resistance measurements allow to determine that a significant change in the sample structure is occurring between 300 and 400 °C. Therefore, quenches were made for *ex situ* pole-figure investigation every 12.5 °C between 325 and 400 °C, in addition to an as-deposited film and samples quenched at 150, 200, 300, 450 and 850 °C (Fig. 5.6e). A selection of the acquired pole-figure datasets is displayed in figure 5.7.

The absence of diffraction from an as-deposited layer can be understood, as it is known that the sputter deposition process of the first Ni monolayers form an amorphous, intermixed, Ni(Si) layer [8, 34]. It is suggested that this amorphous layer contains an inherent concentration gradient, which could promote the formation of θ-Ni_2Si as this phase can locally adapt its Ni-Si ratio within a range of 33 up to 42 % [35, 36]. For these ultrathin films, the formation of NiSi is only observed for the Ni(Pt) sample, coinciding with the consumption of θ-Ni_2Si around 325 °C. Similar to the 9 nm Ni(Pt) film, NiSi forms with clear epitaxial features along epitaxial rings (Table 5.4). For the 3 nm Ni, Ni(Al) and Ni(Co) as-deposited samples, epitaxial θ-Ni_2Si is also present, but no silicide phase appears while θ-Ni_2Si is consumed. No other phases, such as as-deposited Ni, δ-Ni_2Si or $NiSi_2$, could be observed in any of the quenched 3 nm samples.

We can assume that the slow consumption of θ-Ni_2Si for Ni, Ni(Al) and Ni(Co) is associated with the formation of epitaxial $NiSi_2$, based on the literature [8–12, 25, 37]. This is corroborated by the slow decrease of the *in situ* sheet resistance measurements: as $NiSi_2$ exhibits a lower resistance due to an increase in layer thickness and an assumed lower bulk-resistivity than θ-Ni_2Si. Due to the very similar crystal structure of $NiSi_2$ and the Si

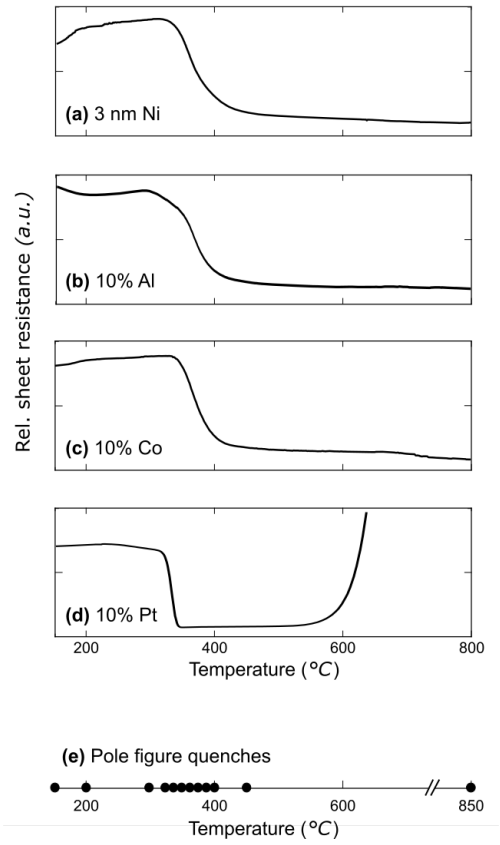

Figure 5.6: Relative evolution of the sheet resistance of 3 nm Ni films with variable as-deposited composition, as measured through *in situ* sheet resistance measurements on SOI substrates. The bottom panel **(e)** shows the quenching temperatures of the samples prepared for *ex situ* pole-figure measurements, in addition to a room-temperature sample.

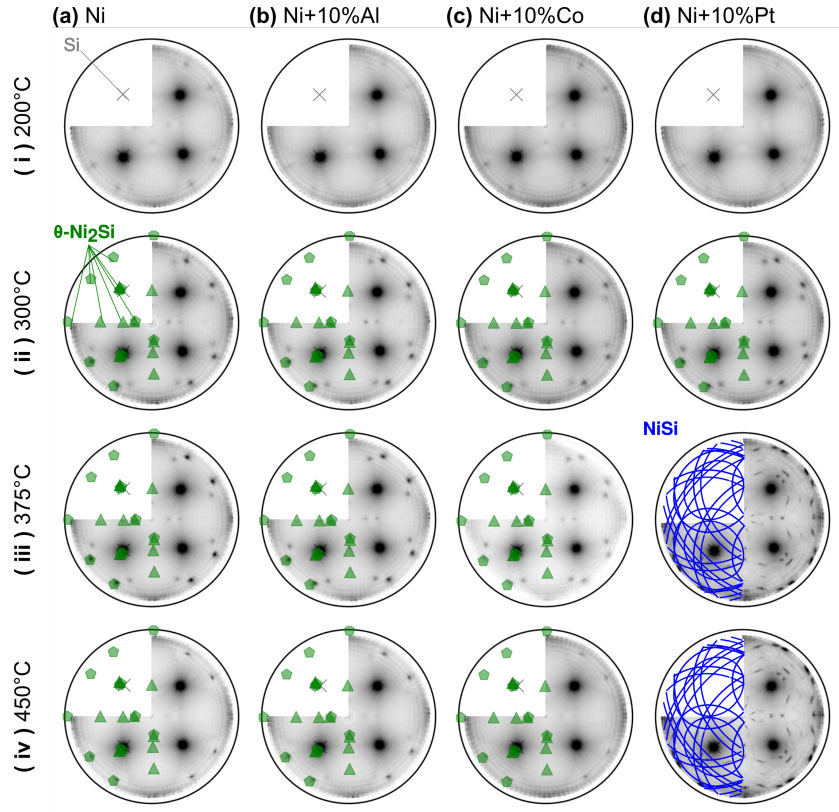

Figure 5.7: A selection of the aquired pole-figure dataset for alloyed and unalloyed 3 nm Ni films, displaying the integrated diffraction intensities $2\theta = 45.5° \pm 0.4°$. These images examplify the observed phases and their textures. The identified silicide textures are overlapped on the left half of the dataset (using the symbols defined in tables 5.2 and 5.4). The Si(220) diffraction peak is always visable and indicated with a gray cross.

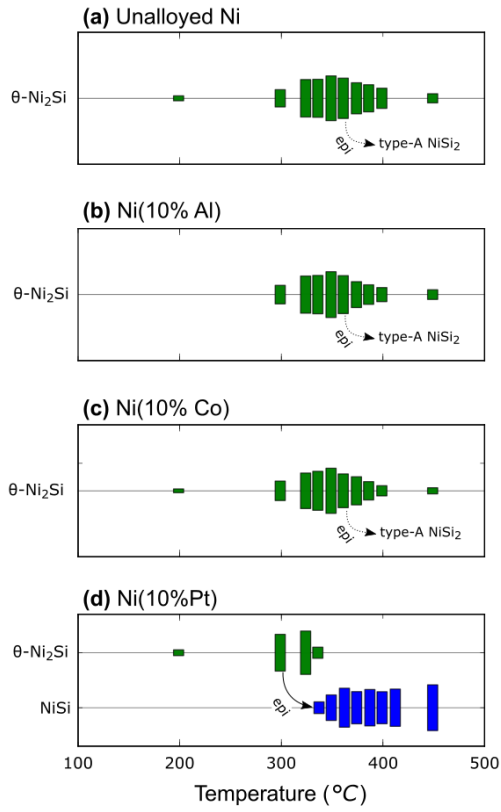

Figure 5.8: Overview of the observed silicides' diffraction intensity as a function of temperature for pure and alloyed 3 nm Ni films. The observed intensities are proportional to the height and normalised to the maximum occuring intensity per sample. Arrows indicate examples of texture inheritance across multiple phases, as explained in the discussion.

Table 5.5: The maximum atomic concentrations of Al, Co and Pt ternary elements in nickel silicides. * indicates that a full replacement of Ni is possible. Arrows indicate an observed increased or decreased width of the temperature window of the phase presence, according to *ex situ* pole-figure and *in situ* XRD measurements (Fig. 5.5, 5.1)

ALLOY:	Al (%)		Co (%)		Pt (%)	
δ-Ni_2Si	20	–	66*	↗	< 5	↘
θ-Ni_2Si	20	↗	unknown	↘	soluble	–
NiSi	1.5	↘	10	↘	50*	↗
$NiSi_2$	29	–	33*	↗	< 5	–
Ref.	[28–30]		[38]		[17, 35, 39, 40]	

substrate (with only 0.46% difference in lattice parameter), the diffraction angles 2θ are almost identical. Moreover, it is known that the $NiSi_2$ phase can grow in an identical alignment with the Si substrate for these initial Ni thicknessess, i.e. $(100)_{NiSi2}//(100)_{Si}$ and $(001)_{NiSi2}//(001)_{Si}$ (also known as the type-A epitaxial alignment of $NiSi_2$). This particular orientation is not observable from our *ex situ* pole-figure measurements, as the recorded scattered intensity is highly dominated by the vicinity of the Si substrate Bragg peaks.

The formation and consumption of the observed phases is illustrated in figure 5.8. It is clear that the epitaxial θ-Ni_2Si slowly forms (or is consumed), at the same temperatures at which the signal within *in situ* sheet resistance measurements increases (or decreases).

5.4 DISCUSSION

Our *in situ* XRD and *ex situ* pole-figure measurements clearly indicate that alloying not only influences the temperature windows in which specific silicide phases occur, but also can change the phase sequence (e.g. through the formation of NiSi in the ultrathin thickness regime with Pt alloying) as well as the preferential orientation of the occurring phases. We first discuss the observed change in phase sequence and temperature window in the context of alloy solubility. Thereafter, we discuss and rationalise the observed preferential orientations.

Influence of alloying on phase formation

The temperature windows of the presence of δ-Ni_2Si, θ-Ni_2Si, and NiSi are significantly influenced through alloying for 9 nm Ni films, as depicted in figures 5.1 and 5.5. For example, we observe that the formation of δ-Ni_2Si is delayed when Pt is present as alloying element, whereas Co, on the other hand, seems to stabilise the δ-Ni_2Si phase up to higher temperatures. We correlate these changes in the observed temperature windows with the solubility of the alloying element in the silicide phase (values are tabulated in Table 5.5) together with the observed changes of the phases' existence temperature windows. The enthalpy of formation of these nickel silicides are comparable: $\delta - Ni_2Si$: -46.9, $NiSi$: -42.4, $NiSi_2$: 29.3 kJ/mol of atoms [41]. However, the nucleation barrier of these phases will be influenced through alloying. An alloy with low solubility in a particular silicide phase will indeed hinder the formation of this new phase, as the alloying element should first be expelled before the new crystal structure can nucleate. This effect has in fact been observed by Mangelinck *et al*. through atom probe tomography, as Pt is segregated to the grain boundaries of δ-Ni_2Si, also known as the snowplough effect [17, 18]. On the other hand, a soluble alloy will enable an increase in entropy within a silicide grain, and as such, potentially lower the nucleation energy barrier to form this new phase. Through this argument, we can understand several aspects of the observed phase sequence for the 9 nm films, including the larger temperature window of δ-Ni_2Si with Co-alloying, how the same alloy promotes the low-temperature $NiSi_2$ formation, and the delay in NiSi formation through Al alloying. The solubility argument is, of course, not the only condition for changes in the temperature window (e.g. the absence of δ-Ni_2Si when Al alloying is used). Other thermodynamic parameters, such as interfacial energy through substrate alignment and change in diffusion rates at grain boundaries will also contribute to the observed shifts in temperature windows.

For 3 nm Ni layers, it is remarkable that the formation of the epitaxial θ-Ni_2Si does not seem to be influenced by Al or Co alloys. Indeed, θ-Ni_2Si has similar growth profiles and diffraction intensities for Ni, Ni(Al) and Ni(Co) samples at this thickness, and its formation does not seem to be hindered by the alloying element. One may argue that the lattice of θ-Ni_2Si, which can cover from 33 to 42 %Si according to the binary Ni-Si phase diagram [35], can easily adapt to the incorporation of the alloys. This would imply a significant strain in the lattice, and by consequence a shift in the diffraction angle of θ-Ni_2Si. To verify this, we fitted the 2θ peak positions of the θ-Ni_2Si epitaxial peak at $\chi = 18°$, which has a

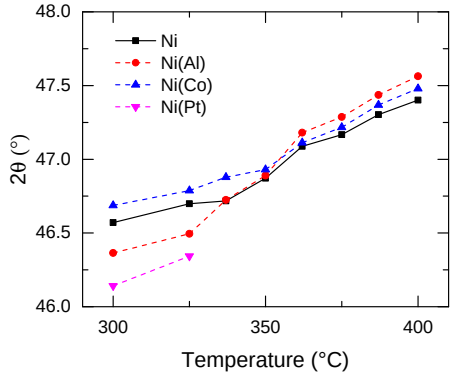

Figure 5.9: Evolution of the 2θ position of an epitaxial peak of the θ-Ni_2Si (near $\chi = 18°$ and $\phi = 0°$) as observed in 3 nm Ni films.

high diffraction intensity and its low elevation angle χ ensures a decent resolution in 2θ (Fig. 5.9). Two significant changes can be observed. (i) As function of temperature, the diffraction angle increases linearly, corresponding to a decrease in lattice parameters from 1.95 to 1.92 Å over a 100 °C temperature range. This decrease can be related to a change in film strain, composition or due to a negative coefficient of thermal expansion of at least one lattice parameter. The reduction of the crystalline lattice is significantly higher when compared to other silicides with a negative coefficient of thermal expansion [42]. Unfortunately, too little diffraction planes with sufficient intensity were observed in these measurements to further investigate this effect. (ii) As function of alloying species, one can observe that the diffraction peak is systematically higher in 2θ when Co alloying is used in comparison with an unalloyed sample, which is similar to the effect of Co-alloying on the NiSi or $NiSi_2$ phase [43]. Al and Pt seem to increase the initial θ-Ni_2Si lattice spacing (corresponding to a lower 2θ angle), and the subsequent evolution of the Ni(Al) sample indicates a complex change in the films' composition or strain. This illustrates the flexibility of the θ-Ni_2Si to accomodate alloying elements and compositional gradients, which possibly explains why no significant change can be observed in the growth profile within the ultrathin film region. This is again corroborated through the texture of θ-Ni_2Si: although the texture of other silicides changes remarkably with the addition of a ternary element, the same epitaxy is always observed for θ-Ni_2Si, independent of as-deposited composition or thickness.

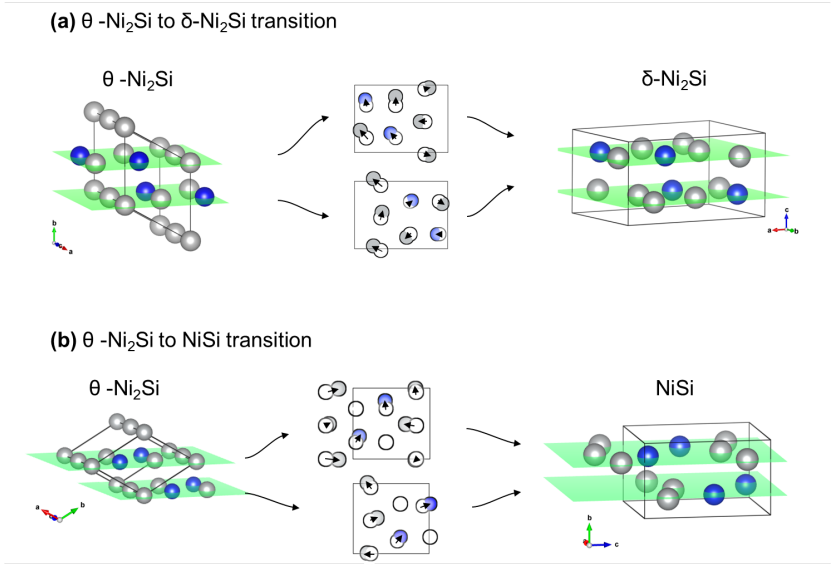

Figure 5.10: The transition from **(a)** θ-Ni_2Si to δ-Ni_2Si or from **(b)** θ-Ni_2Si to NiSi involves only minimal atomic movement, thus possibly introducing texture inheritence.

Influence of alloying on preferential orientation - examples of texture inheritance

Not only the temperature windows of the observed phases is influenced through alloying, but also the silicides' preferential orientation with respect to the Si substrate. The most remarkable changes can be found in the texture of δ-Ni_2Si, where an epitaxial orientation is observed for Ni and Ni(Pt) and a fiber texture for Ni(Co) (Fig. 5.3 and Table 5.3)). Moreover, the overview of pole-figure measurements (Fig. 5.2) illustrates that the fiber texture is only observed in the as-deposited Ni(Co) layer. This could indicate that the texture of a specific silicide is influenced by the orientation of the preceding phase. Indeed, Gaudet *et al.* [6] reported, for the unalloyed nickel silicide solid-phase reaction, that a transformation from one phase to another phase could result in an inheritance of fiber-textures, provided that the crystal structures are similar. A similar reasoning applied here for the fiber-inheritance between the as-deposited Ni(Co)(111) fiber-axis and δ-Ni_2Si (301), where the respective crystalline planes evolve from a d-spacing of 2.03 to 1.99 Å.

In addition to this fiber-inheritance, our measurements clearly indicate that texture inheritance is also applicable to some of the observed epitaxial

orientations. We explain this phenomenon on the basis of the epitaxially textured δ-Ni_2Si when Pt is added as a ternary element. The epitaxial alignment, which is higher and more distinguished than when δ-Ni_2Si is formed from an unalloyed Ni film, would be hard to explain on solubility arguments alone, as Pt is insoluble in δ-Ni_2Si. However, this phase is formed at expense of the preceding, epitaxially-aligned, θ-Ni_2Si (Fig. 5.5), and thus texture inheritance is possible provided that the crystal structures are related. Indeed, a minimal atomic movement is required to transform the θ-Ni_2Si into δ-Ni_2Si, as illustrated in figure 5.10a. The corresponding transforming planes are then: $\{001\}_\delta // \{11\bar{2}0\}_\theta$ or $\{301\}_\delta // \{11\bar{2}0\}_\theta$, depending on a rotation of 60° due to the hexagonal symmetry of θ-Ni_2Si, and $\{010\}_\delta // \{0001\}_\theta$ for the basal plane. These transformation rules well explain the change of A_θ and B_θ epitaxy into A_δ and B_δ, respectively. This is easily seen by transforming the epitaxies from Table 5.3 into those listed in Table 5.2, taking into account the symmetry of θ-Ni_2Si and the Si(001) substrate, and that an epitaxial orientation is defined by fixating the orientation of two sets of non-parallel planes. This texture inheritance not only minimises the required atomic mobility for the Si atoms, but also reduces the interface energy between the nucleated δ-Ni_2Si grain and the existing θ-Ni_2Si grain.

The epitaxial alignment of NiSi, which is also observed when Pt is added to the as-deposited Ni layer, can also be understood through similar epitaxial-texture inheritance arguments. Figure 5.10b shows that a minimal atomic movement is required to transform θ-Ni_2Si to NiSi. This deformation, however, requires the out-diffusion of some nickel atoms. Ellner *et al.* [36] reported that θ-Ni_2Si can in fact be highly vacancy-rich, so this transformation is not as abrupt as displayed in figure 5.10b. The corresponding planes are: $\{013\}_{NiSi} // \{11\bar{2}0\}_\theta$ or $\{010\}_{NiSi} // \{11\bar{2}0\}_\theta$, and $\{100\}_{NiSi} // \{0001\}_\theta$ for the basal plane. In addition to atomic movement, this transformation requires significant deformation of the unit cells, e.g. the lattice spacing of the θ-Ni_2Si basal plane needs to expand from 4.89 to 5.18 Å. These plane transformations explain the observed transitions of A_θ to both A_{NiSi} and B_{NiSi} and B_θ into C_{NiSi}. The fact that the A_θ θ-Ni_2Si orientation results into two slightly different epitaxial phases can be related to the fact that the texture inheritance requires some relaxation of the unit cell. It appears that the NiSi (101) and (211) planes along Si{101} orientation match with good alignment. The second orientation cannot match perfectly, due to the relaxation of the unit cell, and as such, the texture inheritance will allow small deviations around the original orientation of θ-Ni_2Si along the axiotaxial alignment.

Finally, the formation of $NiSi_2$ out of θ-Ni_2Si for the ultra-thin, 3 nm Ni films potentially also correlates with texture inheritance. The transformation rules for the formation of type-A epitaxial $NiSi_2$ out of the epitaxial A_θ θ-Ni_2Si can indeed be associated with minimal atomic movement. This is, however, less evident for the transition between B_θ and A_{NiSi_2}. It was previously suggested [9] that the low-temperature $NiSi_2$ formation in the ultra-thin regime, instead of NiSi, is the result of a much lower interface energy. Our observations corroborate this, as one epitaxial phase transforms into another, and by consequence the interface energy remains low throughout the transition.

The identified pathways for texture inheritance are depicted in figures 5.5 and 5.8 through arrows from the original phase to the succeeding phase. The absence of texture inheritance, for example when forming NiSi for the Ni(Al) sample, can be understood as the θ-Ni_2Si- NiSi phase sequence is interrupted by the formation of the $Ni_xAl_ySi_z$ phase. Similarly, the *in situ* XRD of Ni and Ni(Co) samples show the occurrence of non-epitaxial θ-Ni_2Si in a short temperature window just prior to the formation of NiSi. As *in situ* XRD, in the geometry used in this paper, only detects planes nearly-parallel to the surface, this observation means that the θ-Ni_2Si has lost (partially) its epitaxial alignment with the Si substrate, thus loosing the epitaxial template for epitaxial texture inheritance.

5.5 CONCLUSIONS

The phase formation between thin Ni films of 3 and 9 nm thickness deposited on Si(001) was investigated by means of *in situ* XRD, *in situ* sheet resistance and *ex situ* pole-figure measurements. The same measurements were also performed on samples alloyed with 10 at.% Al, Co and Pt. The measurements allowed to investigate the effect of film thickness and the presence of a ternary element on the phase formation and texture of the thin nickel-silicide layers. Changes in the phase formation sequence could be interpreted on the basis of nucleation theory and the effect of entropy of mixing. Differences in the preferential orientation of the formed silicides indicate the significant effect of texture inheritance during the phase sequence. The latter effect succeeds in explaining the occurrence or absence of specific epitaxial, axiotaxial and fiber textures in the context of the full phase sequence during the solid-phase reaction.

6 ARTICLE III: CHANGING THE CRITICAL THICKNESS FOR EPITAXIAL AND STABLE NICKEL SILICIDE FORMATION

6.1 INTRODUCTION

Metal silicides are used in micro-electronics to establish low-resistance contacts to the source and drain regions of Si-based transistors. The currently preferred material, NiSi, exhibits limited morphological stability and suffers from significant agglomeration upon annealing (e.g. $> 500\,^{\circ}C$) [1–4]. Moreover, NiSi transforms into $NiSi_2$ at higher temperature (e.g. $> 700\,^{\circ}C$), inducing significant change in silicon consumption and resistive properties. The addition of small amounts of Pt (e.g. 10 at.%) is currently being used to delay both the agglomeration process and high-temperature $NiSi_2$ transformation [5]. Because agglomeration is driven by surface and interface energy, it is significantly more difficult to avoid for thinner silicide films. [6, 7]. This can partly be compensated by incorporating a higher Pt concentration, but this results in a higher parasitic resistivity and only delays agglomeration instead of completely stabilising the morphology. Therefore, there is an ongoing interest in alternative contact materials with improved morphological stability, for such thin (e.g. $<$ 10 nm) layers.

Pioneering work by Tung *et al.* [8] demonstrated that the deposition of sub-10 nm thin Ni films onto Si substrates can result in a completely different silicide phase sequence, which forms epitaxial $NiSi_2$ instead of NiSi at low temperature. Recently, the effect of this ultrathin phase formation has regained interest [9–11], as the industry is evolving towards sub-10 nm silicide thicknesses. These studies indicate that there exists a well-defined boundary between the '*regular*' regime - where reaction of e.g. 10 nm Ni at 450 °C is known to result in a polycrystalline NiSi film with axiotaxial texture - and the '*ultrathin*' regime - where reaction of e.g. 3 nm Ni at similar temperatures results in the formation of an epitaxial $NiSi_2$ layer. De Keyser *et al*. [9] showed that the ultrathin phase regime (i.e. below the critical thickness) exhibits very high morphological stability. Knoll *et al*. [12, 13] furthermore reported on the beneficial effect of the lower Schottky barrier height of these epitaxial $NiSi_2$ films.

As the silicide contacts in the state-of-the-art micro-electronics industry are trending to sub-10 nm thickness values, it is important to determine and control the exact value of the *critical thickness* which differentiates these two phase-formation regimes. Gao *et al*. [14] recently reported on a biased-sputter-deposition strategy with pure Ni films, which increases the as-deposited mixed Ni/Si interface region and increases the maximum thickness of the formed epitaxial $NiSi_2$ films, thus increasing the critical thickness.

This paper discusses a different strategy based on the incorporation of ternary elements in the as-deposited film, very similar to the current approach of using Pt-alloying to enhance the performance of NiSi films. The effective value of the critical thickness t_c is determined through a methodology based on the deposition of thickness gradients on Si(001) wafers, which can be used as combinatorial thickness libraries to assess t_c with high accuracy.

6.2 EXPERIMENTAL METHODS

Ni films were deposited on 150 mm diameter Si(001) and silicon-on-insulator (SOI) substrates through physical vapour deposition with a combinatorial approach. The thickness gradient was achieved by modulating the amount of deposited Ni with a triangular-shaped shadow mask, which resulted in a high deposition rate at one side of the substrate while almost eliminating the deposition rate at the other side of the wafer. The final deposited Ni gradient can be described as a thickness library, where the deposited Ni thickness varies quasi-linearly in the direction of the gradient as a function of the position on the substrate. The Ni content of the gradient was determined to vary from 0.5 to 15 nm equivalent thickness as determined through Rutherford backscattering spectrometry (RBS) measurements, and thus covers the thickness region of interest to study the critical thickness in the Ni-Si phase formation. This combinatorial approach is not only resource and time efficient, but also ensures that identical experimental conditions were applied for all Ni thickness values of interest.

The substrates received standard (Radio Corporation of America, RCA) chemical cleaning, ending with a 20 s dip in a 3 % HF solution prior to loading into the vacuum chamber. Sputter deposition was performed in an Ar ambient of 5×10^{-3} mbar, after first reaching a background pressure of 6×10^{-7} mbar. The Ni thickness gradient was optionally alloyed with 10 ± 2 at.% Al, Co or Pt by co-sputtering. This was obtained through a second shadow mask for the alloy which resulted in a constant ratio

between the Ni and alloy signals as verified through X-Ray Fluorescence (Co, Pt) and RBS (Al) along the thickness gradient. Ni films with 10 at.% of Pd and Ge were also deposited with discrete equivalent Ni thicknesses (i.e. without thickness gradient) of 2, 3, 6 and 9 nm and are discussed supplementary to the gradient datasets.

These unalloyed and alloyed thickness gradients are compared as function of their Ni content. The alloying species are added in *addition* to the original Ni thickness gradient, and therefore the total thickness of the as-deposited layer is higher for the alloyed films. As Co and Pt (and Pd) are known to replace Ni atoms during silicide formation, the addition of these alloying elements render an effective increase in the metal supply to form $Ni_xM_ySi_z$ (M = Co, Pt, Pd) compounds. Other papers therefore prefer to keep the as-deposited total metal supply constant by reducing the Ni content when adding an alloying species. Such approach is not easily translated to Al (or Ge) alloying, which is known to replace the Si atoms during silicide formation. For conciseness, the amount of nickel present at every position on each gradient will be referred to by using the *equivalent* Ni thickness of the gradient, i.e. the as-deposited Ni thickness which would be measured when no alloy would be added to the layer.

The thickness library was then used in two complementary experimental approaches. In a first approach, a 150 mm long strip from the thickness library was annealed up to a specific temperature and its properties were characterised after quenching as a function of position within the library (i.e. as a function of as-deposited Ni thickness). *Ex situ* techniques were used, such as scanning electron microscopy (SEM) to evaluate layer morphology, pole-figure measurements to investigate crystalline phase, and texture and transmission electron microscopy (TEM) to assess roughness and local composition. In a second approach, a 150 mm long thickness gradient strip was cut into 15 smaller pieces of $\sim$ 10 mm, resulting in a set of discrete samples with an average thickness difference of 1 nm. Subsequently, these individual samples were studied with *in situ* techniques, which consisted of a continuous acquisition of the sheet resistance (SR) and X-ray diffraction (XRD) during annealing. To enable a straightforward comparison in the measurements acquired by both the *in situ* and *ex situ* temperature treatments, we used the same annealing settings (i.e. heating at a constant rate of $1\,^{\circ}C\,s^{-1}$ in a He(5 %H_2) ambient).

In situ XRD was used to monitor the solid-state reaction as a function of temperature and was performed at the X20C beamline of the National Synchrotron Light Source (NSLS). The wavelength of the incidence X-rays was selected at 0.180 nm with an energy resolution of 1.5 % by a multilayer monochromator. The diffraction pattern was monitored through a linear

detector having an angular range of 14° in 2θ. These diffractograms are plotted as a function of temperature and diffraction angle using a linear gray-scale map for the recorded intensities, where darker represents a higher intensity.

Further identification of the formed phases is enabled through *ex situ* X-ray pole figures, measured for samples quenched at 700 °C. For recording such pole figures, the sample is tilted around both the in-plane and out-of-plane axes (denoted as the χ and ϕ angle, respectively), to obtain information on the preferential orientation of the probed crystalline planes. A polar plot of the diffraction intensity then represents the distribution of the crystalline plane's preferred orientation, also denoted as the *texture* of the crystal grains. The pole figures reported in this work were acquired using a four-circle diffractometer at the X20A beamline of the NSLS, using X-rays with a wavelength of $\lambda = 0.154\,\text{nm}$, and a custom linear detector covering 20 to 60° in 2θ, and by scanning the sample in χ and ϕ in steps of 1°. The pole figures of the thinnest samples, i.e. an as-deposited Ni thickness of 3 nm, were acquired with a double acquisition time, to ensure that adequate intensities could be collected. The pole figures are displayed using a grayscale map for the recorded intensities (with black corresponding to the highest intensity). They are aligned so the Si substrates are oriented in the same direction, as depicted in figure 6.11 of the supplementary material. A ring of higher intensity was observed at $\chi \sim 60°$ and is present in most of the acquired pole figures, including a measurement of a Si reference sample, indicating that this is related to background. Further details concerning the set-up used for these pole-figure measurements can be found in our earlier work [15, 16]. The extensive literature available on silicide and germanide textures was recently reviewed by De Schutter *et al*. [17].

Bright field transmission electron microscopy (BF-TEM) overview images were acquired by using a FEI-Tecnai electron microscope operated at 200kV. Scanning transmission electron microscopy energy dispersive X-ray spectroscopy (STEM-EDS) measurements were made using a FEI-Osiris electron microscope operated at 200kV, equipped with a ChemiSTEM system [18]. For the acquisition and quantification of the maps, the ESPRIT software was used.

6.3 RESULTS

The unalloyed Ni thickness library was first investigated *ex situ* after applying an anneal to 700 °C. After the temperature treatment, visual inspection of the gradient indicates an abrupt boundary between two regions in

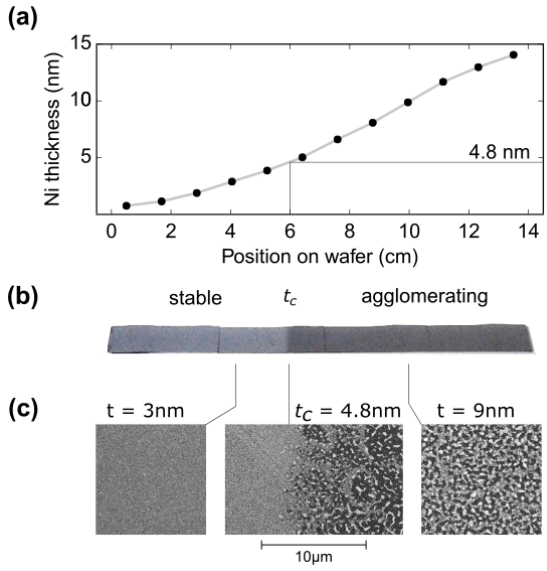

Figure 6.1: Thickness gradients were used to study the solid-state reaction between Ni and Si(001). **(a)** The equivalent Ni thickness was determined from RBS measurements, showing a quasi-linear dependence of de thickness with the position on the wafer. **(b)** Photographic picture of a 150 mm long strip from the thickness gradient after annealing to 700 °C, exhibiting a clear color change at a Ni thickness of t_c= 4.8 nm. **(c)** SEM micrographs conducted at several positions on the annealed gradient show a significant difference in morphology at t_c.

the thickness library with a clear difference in color. This boundary is situated at a thickness of t_c= 4.8 nm (Fig. 6.1b) and SEM images in figure 6.1c show that the color change is due to a different morphology of the sample. Films thicker than t_c showed agglomerated grains and those thinner than t_c were almost feature-less (Fig. 6.1).

In situ XRD confirms that the observed critical boundary t_c is the demarcation line between the two thickness regimes that are described in the literature [9–11]. Indeed, samples above the critical thickness (e.g. 6, 9 and 13 nm, Fig. 6.2a, b and c) show the well-known phase sequence which forms NiSi above 400 °C, after first forming intermediate δ-Ni_2Si and transient θ-Ni_2Si [19]. However, *in situ* XRD from samples below the critical thickness (e.g. 3 nm, Fig. 6.2d) do not show any clear diffraction signal from silicide phases formed during the anneal. We equate the absence of diffraction to the formation of epitaxial silicides. Due to the fixed geometry of the *in situ* XRD set-up, diffracting planes will only be observed if they are oriented (nearly) parallel to the substrate's surface. Consequently, an epitaxial phase does not necessarily diffract in the probed reciprocal space.

The sudden change in phase formation at the critical thickness is further corroborated by *ex situ* pole-figure measurements. Powder-like diffraction patterns, calculated by integrating the measured diffracted intensity at a given 2θ for all χ and ϕ values acquired during the pole-figure measurement, allow unambiguous identification of the phases present, as these measurements include diffraction from planes non-parallel to the samples' surface (Fig. 6.3). Samples above the critical thickness clearly include diffraction from both the Si-substrate and the NiSi silicide, whereas samples below the critical thickness only contain higher intensity near $2\theta \sim 28.5°$, 47.5° and 56.4°, corresponding to diffraction of either the Si substrate or $NiSi_2$, whose diffraction angles coincide due to a similar crystal lattice.

Inspecting the individual pole figures at the interesting diffraction angles, such as those displayed in figures 6.3b-e, further corroborates the above observations. The presence of NiSi for thicker films is evidenced by the circular features on the pole figures, indicating a poly crystalline NiSi layer with axiotaxial texture. Below the critical thickness, no silicide diffraction can be observed. However, from the literature, we expect that epitaxial $NiSi_2$ is formed below the critical thickness. Due to the very similar face-centered cubic lattices of $NiSi_2$ and the Si substrate, with only 0.46 % difference in lattice parameter, the $NiSi_2$ grains can epitaxially align with the substrate, resulting in an overlap in pole-figure diffraction at the same χ, ϕ and 2θ angles as the Si substrate. This specific alignment, which

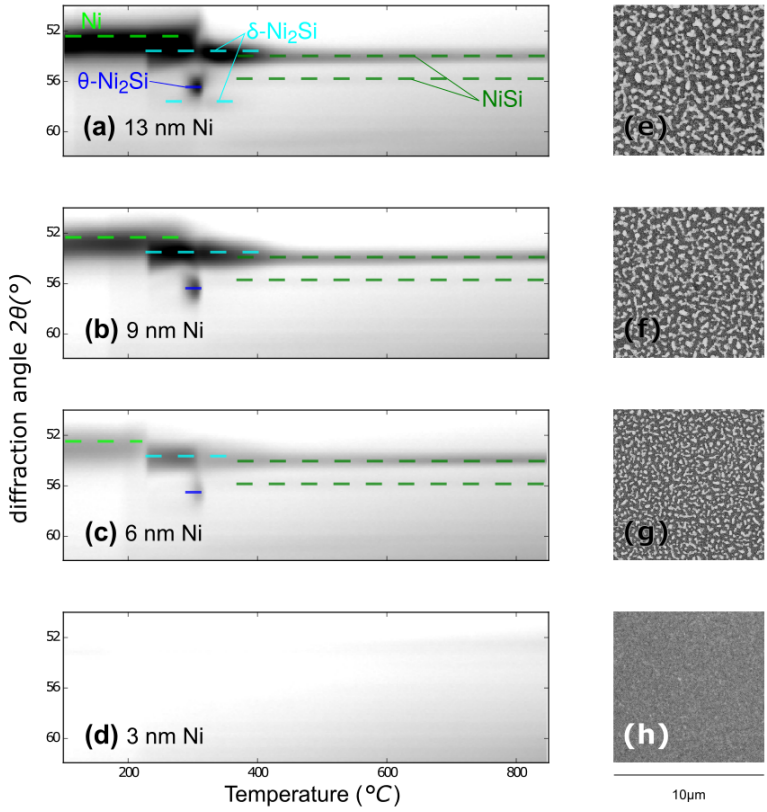

Figure 6.2: *In situ* XRD measurements during annealing indicate a significant difference in phase formation above and below the critical thickness t_c= 4.8 nm. The sequence of several silicides is observed for films thicker than t_c, whereas thinner films do not show any diffraction, indicating the possible formation of epitaxial silicides.

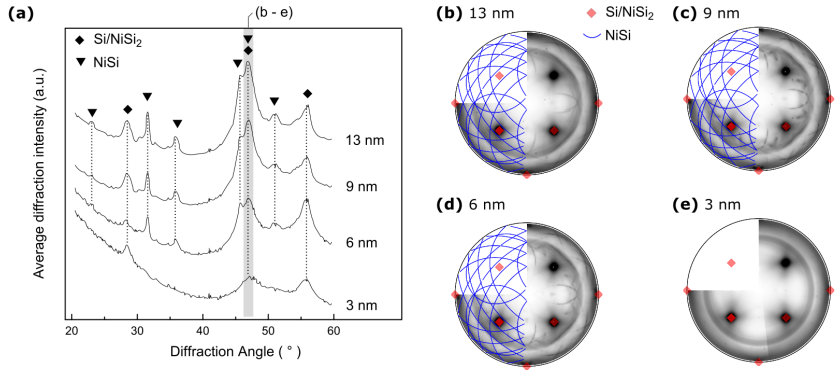

Figure 6.3: **(a)** Pole figures acquired from Ni samples quenched at 700 °C integrated in χ and ϕ result in a powder-like diffraction pattern, allowing unambiguous phase identification. Further investigation of the individual pole figure at $2\theta \simeq 47.5°$ (covering diffraction of NiSi(211)/(202) and $NiSi_2$(202) planes) shows the axiotaxial texture of the NiSi phase for 13 **(b)**, 9 **(c)** and 6 nm **(d)** Ni. 3 nm **(e)** Ni instead only contains features originating from either the Si substrate and/or type-A epitaxial $NiSi_2$.

is called *type-A* epitaxy, has been observed previously in the literature for these thin films [8, 9]. Pole figures are not able to distinguish the diffraction between the Si substrate and the $NiSi_2$ film, as the former saturates the detector due to high diffraction intensities. These pole-figure measurement exclude the presence of any other silicide except type-A oriented $NiSi_2$ below the critical thickness at this temperature. The occurrence of type-A epitaxial $NiSi_2$ at these as-deposited Ni thicknesses is in confirmation with the literature [8–11]

The observation of such a clear thickness-dependent effect through the use of combinatorial libraries illustrates the unique capability of these thickness gradients to investigate the critical thickness in the Ni-Si solid-state reaction as a function of position.

6.3.1 *Effect of alloying on the critical thickness*

Thickness gradients were subsequently used to investigate the critical change in phase formation when ternary elements are included in the as-deposited layer. Thickness gradients, alloyed with 10 at.% Al, Co or Pt, were again quenched at 700 °C. Samples with Al or Pt show a similar critical change in morphology at positions equivalent to a Ni thickness

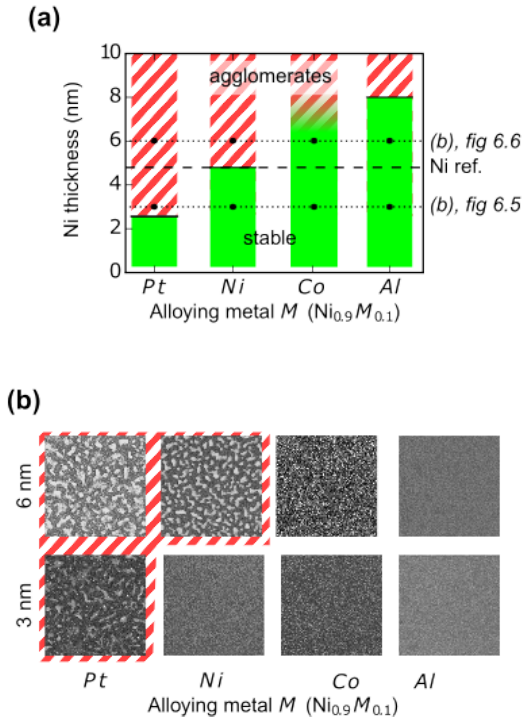

Figure 6.4: Unalloyed and alloyed (10 at.% Al, Co and Pt) thickness gradients were quenched at 700 °C in order to determine the critical thickness differences in morphological stability. Co-alloying shows a continuous increase in roughness as a function of Ni thickness.

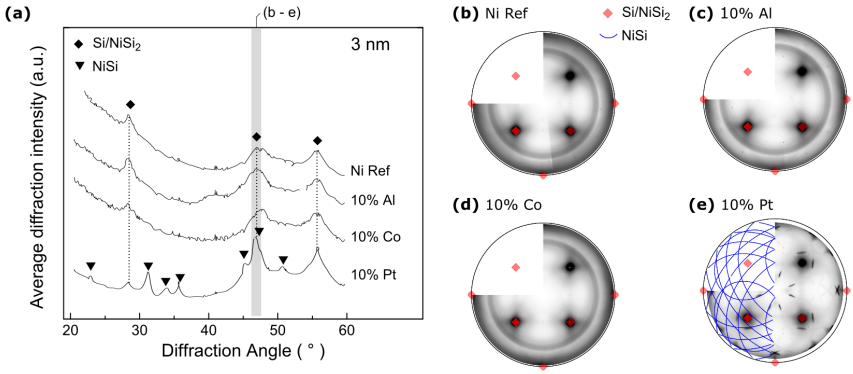

Figure 6.5: **(a)** The constructed powder-like diffraction patterns are used to identify the formed silicde after annealing 3 nm thick Ni films, which are alloyed with 10 at.% Al, Co or Pt, to 700 °C. The individual pole figures at $2\theta \simeq 47.5°$ exclude the occurence of any other silicide phase except type-A epitaxial $NiSi_2$ being formed for an unalloyed Ni film **(b)**, or when alloyed with Al **(c)** or Co **(d)**. NiSi is clearly present when alloyed with Pt **(e)**.

of $t_c = 8.0$ and 2.6 nm, respectively (Fig. 6.4). The changes in equivalent thickness is not the consequence of a merely increased metal supply, e.g. the combination of 2.6 nm Ni in addition to 10 at.% Pt) is far less than the critical thickness $t_c = 4.8$ nm for unalloyed Ni films. When the gradient strip was alloyed with Co, no visual abrupt difference in morphology was observed as a function of thickness. SEM images (not shown) instead show an increased roughness for Ni thicknesses between 5 and 11 nm, but do not show the severe agglomeration as observed for an unalloyed film.

Further investigation of these alloyed thickness gradients through *ex situ* pole figures confirms that the value of t_c can indeed be varied through alloying. A selection of these measurements is displayed for 3 and 6 nm as-deposited Ni thickness in figures 6.5 and 6.6, respectively. When 3 nm films are alloyed with Al or Co, no significant differences are observed by comparing these measurements with those of an unalloyed Ni film. However, Pt alloyed samples now clearly contain NiSi diffraction.

Films with a slightly higher equivalent Ni thickness, e.g. 6 nm, are also significantly influenced through alloying. Although NiSi was observed for an unalloyed film to form at this thickness, no such diffraction patterns are observed when Ni was alloyed with either Co or Al. No other silicide diffraction can be observed except $NiSi_2$, a clear indication that Co and Al alloying favours the low-temperature phase formation of $NiSi_2$.

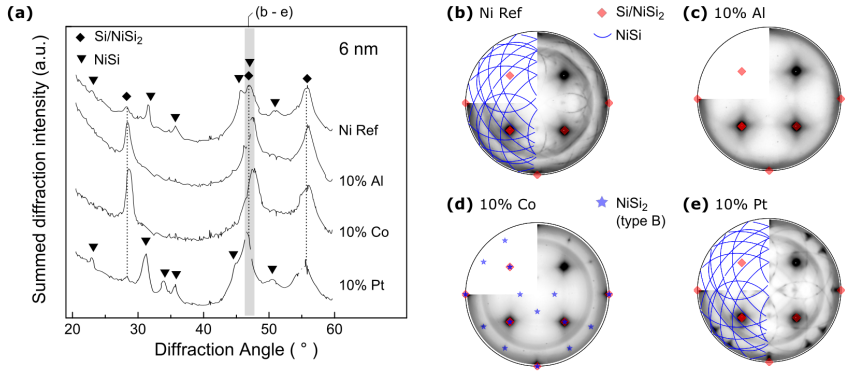

Figure 6.6: **(a)** The constructed powder-like diffraction patterns are used to identify the formed silicde after annealing 6 nm thick Ni films, which are alloyed with 10 at.% Al, Co or Pt, to 700 °C. NiSi is clearly present for the unalloyed film **(b)**, or when Pt is used as ternary element **(e)**. The individual pole figures at $2\theta \simeq 47.5°$ confirm the absence of any silicide other than $NiSi_2$ when 10 at.% Al or Co are added.

Closer inspection of the pole figures reveals an intriguing difference in $NiSi_2$ texture. Indeed, the sample containing 10 at.% Co now clearly contains diffraction of epitaxial $NiSi_2$ identified as the *type-B* orientation. This epitaxial orientation is characterised by diffraction spots on the displayed pole figures, and can be related to type-A $NiSi_2$ epitaxy through a rotation of 180° around the {111} direction. Furthermore, randomly-oriented $NiSi_2$ grains are evident from an overall increase in diffraction intensity for all χ and ϕ angles at the specific 2θ values for $NiSi_2$ after evaluating the complete pole-figure dataset. Al-alloying does not include these features and the pole figures exclude type-B or randomly oriented $NiSi_2$, suggesting that only type-A $NiSi_2$ is present, similar to the case of an unalloyed Ni film thinner than t_c.

Although Al and Co clearly favour the low-temperature formation of $NiSi_2$, these observations at 700 °C do not guarantee that the silicide phase formation is identical to the ultrathin phase sequence, as low-temperature NiSi can still be formed prior to the formation of $NiSi_2$. This question is answered through the *in situ* XRD measurements for 6 nm thick samples, as displayed in figure 6.7. From these measurements, we observe that the silicide phase sequence still includes NiSi at low temperatures when Co is used as alloy, while no NiSi is observed for the Al-alloyed sample. We thus conclude that the critical thickness is not shifted to higher values by Co-alloying, as the phase sequence is not drastically altered and instead

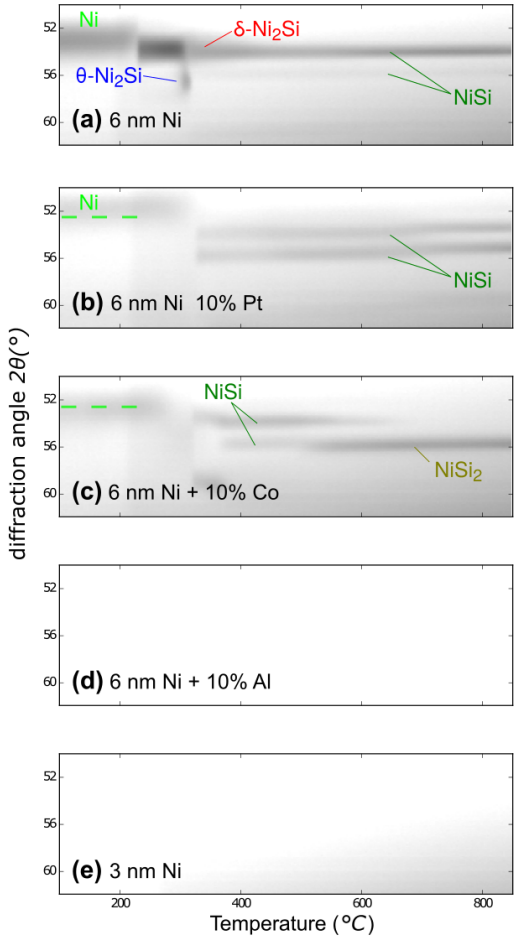

Figure 6.7: *In situ* XRD measurements of 6 nm thick Ni films during annealing indicate a significant difference in phase formation when comparing an unalloyed film **(a)** with a Pt **(b)**, Co **(c)** or Al-alloyed **(d)** film. The latter sample shows remarkable resemblance with an unalloyed 3 nm Ni film **(e)**, where no diffraction patterns can be recognised.

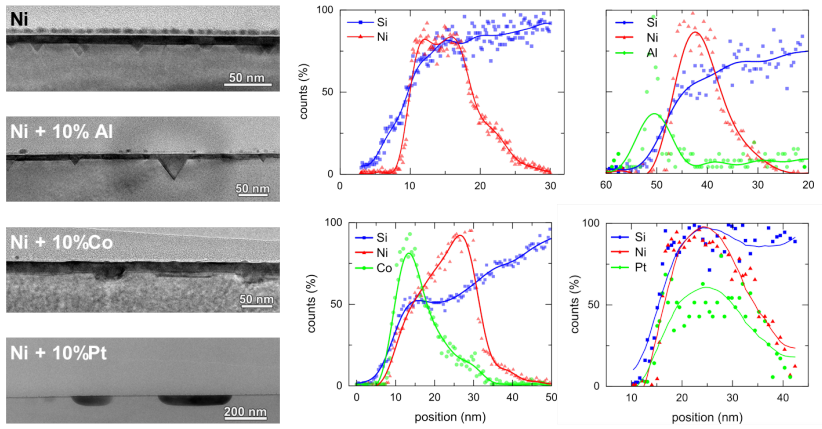

Figure 6.8: **(left)** BF-TEM images show the interface roughness of 3 nm Ni films with or without alloying. The EDS line scans **(right)** show the distribution of the alloying atoms throughout the layer thickness.

the transformation temperature of NiSi to $NiSi_2$ is significantly reduced. On the other hand, Al alloying lacks all diffraction peaks through the full temperature anneal, similar to the solid-state reaction as observed for unalloyed Ni films below t_c and indicating a promotion of the ultrathin phase sequence to thicker films. We thus conclude that the critical thickness t_c can indeed be changed by alloying, both to higher values (Al), as well as to lower values (Pt). Although Co-alloying does promote low-temperature formation of $NiSi_2$, it does not change the phase sequence above the original value of t_c.

In order to evaluate the final distribution of the ternary elements, samples of 3 nm Ni, unalloyed and alloyed, were studied through TEM-imaging after quenching (Fig. 6.8). The BF-TEM images clearly show a difference in interfacial roughness. The unalloyed sample shows atomically-sharp interfaces along both the Si{100} and Si{111} directions. The latter creates triangular facets, which submerge deep into the Si substrate. Al alloying does not change this image, although Allenstein *et al.* report that the typical {111} faceting disappears when alloying 20 nm Ni films with higher Al concentrations (i.e. > 20 at.%) [20]. On the other hand, $NiSi_2$ formed with the addition of Co exhibits less faceting but manifests a rough interface. NiSi, which was formed through the addition of Pt, is clearly agglomerated. More interesting, however, is the positioning of the alloying species throughout the silicide as determined through EDS-mapping. Co and Pt are observed within the silicide layers, although the majority of Co and almost all Al remain largely on the surface.

6.4 DISCUSSION

The critical change in phase formation in these ultra-thin films is indicative of the competitive behaviour in the low-temperature formation of either NiSi and $NiSi_2$ [21]. The energetic threshold for atoms to nucleate into either of these phases can be described to be proportional to $\Delta\sigma^3/(\Delta H - T\Delta S)^2$, with $\Delta\sigma$, ΔH and ΔS representing the differences in interface energy, enthalpy and entropy due to the nucleation, respectively. The enthalpy of formation of the nickel silicides are comparable with one-another [19] $\delta - Ni_2Si$: -46.9, $NiSi$: -42.4, $NiSi_2$: 29.3 kJ/mol of atoms [22]. As such, effects that change the interface energy and entropy have the potential to significantly alter the phase stability and solid-phase reaction. One can use the above equation as a framework to interpret and rationalize the effect of ternary elements on the phase formation.

An alloy which is soluble in the forming phase will increase that phases' entropy, whereas an insoluble alloy will instead require that it should be excreted before the silicide can be formed. By consequence, soluble alloys will decrease the energy threshold for silicide nucleation whereas insoluble alloys will increase the threshold due to the required atomic transport. This argument has been used in the past to understand observed changes in ternary silicide formation for thicker films [23–29]. We can thus categorise the three used alloys in three different classes, according to their solubility in NiSi or $NiSi_2$. According to high-temperature ($> 800\,^{\circ}C$) equilibrium ternary phase diagrams, $NiSi_2$ allows relatively high incorporation of Al and Co atoms (20 at.% for Al [30], and complete miscibility of Co instead of Ni [31]), but not of Pt. Pt is highly soluble in NiSi, whereas the solubility of Al and Co is limited to respectively 1.5 [30] and 10 % [31]. On the basis of the above, one then expects Pt to promote the formation of NiSi but to delay the formation of $NiSi_2$, and vice versa for Al. Co, however, is reasonably soluble in both phases, although to different extents. We therefore speculate that Co will not hinder the initial nucleation of NiSi grains, and so does not shift the critical thickness. However, it will significantly lower the nucleation temperature of $NiSi_2$, similar to the discussion of Lavoie *et al.* [25] and Smeets *et al.* [32], so $NiSi_2$ is formed before NiSi can severely agglomerate, resulting in a non-agglomerated film after annealing to 700 °C, as observed from the morphology evaluation of the gradient shown in figure 6.4. Experiments with 10 at.% Ge and Pd alloying at discrete Ni thicknesses (i.e. 2, 3, 6 and 9 nm, Fig. 6.13, 6.12) indicate that the value of the critical thickness has decreased to below $t_c = 3$ nm. These data are attached to this paper as supplementary information but are not further discussed in the body of this paper. As Ge and Pd have similar

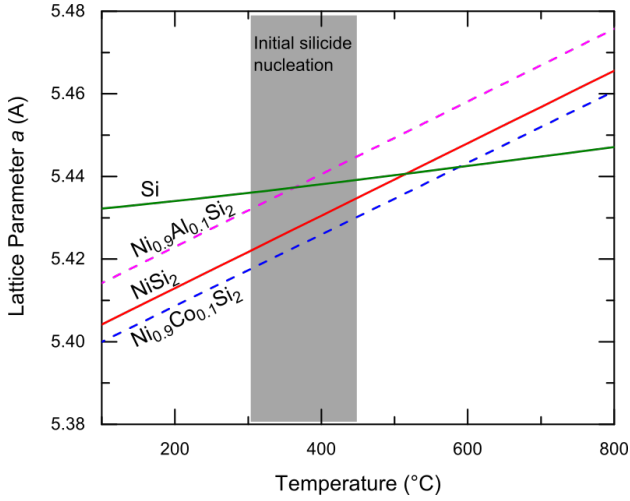

Figure 6.9: Evolution of the lattice parameters of Si and $NiSi_2$. The influence of the alloyed elements was estimated based upon their room-temperature lattice parameter and by assuming a similar coefficient of thermal expansion.

solubility properties as Pt, these experiments corroborate the solubility argument for explaining the effect of alloying on the phase formation.

Luo *et al*. argued that the drastically altered silicide phase sequence as a function of thickness is related to the silicide-silicon interface. The energy required to facilitate this interface will become increasingly important in the total energy balance when going to thinner films. Therefore, epitaxial $NiSi_2$ is expected to be favoured on a non-epitaxial phase such as NiSi. One can argue that the interfacial energy of the silicide-silicon interface will also be influenced through alloying. Indeed, this is indicated through the significant change in interfacial roughness as seen in the TEM-image of Co-alloyed film. In the ultra-thin phase formation regime below the critical thickness, the formation of epitaxial type-A $NiSi_2$ requires an almost perfect lattice match across the interface during initial nucleation and subsequent growth. Such a crystal match is indeed possible due to the same crystal lattice and similar lattice parameter between $NiSi_2$ and the Si substrate. The lattice constant of $NiSi_2$ differs only 0.46% at room temperature, and due to the different thermal expansion coefficients ($\alpha = 16.25 \times 10^{-6}\,K^{-1}$ for $NiSi_2$ [33] and $\alpha = 2.55 \times 10^{-6}\,K^{-1}$ for Si [34]), an exact lattice match is expected during the heating process around 520 °C (Fig. 6.9). However, due to the smaller lattice parameter of $CoSi_2$, a delay in lattice-match is expected during the heating process when using Co as

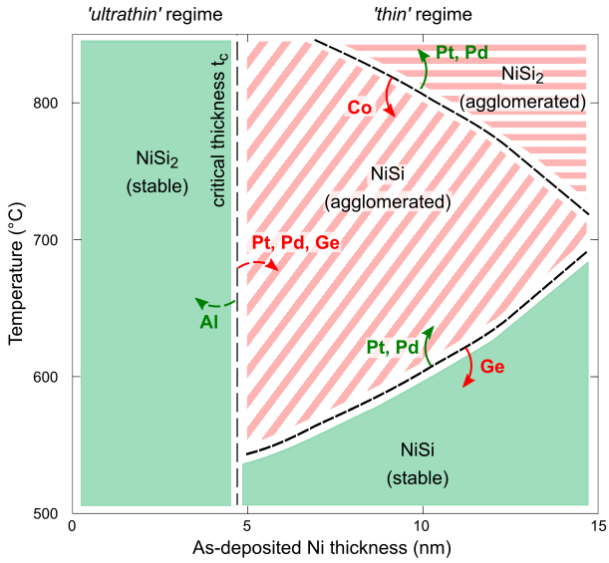

Figure 6.10: Overview of the thermodynamic and morphological stable regimes for nickel silicides as a function of thickness and annealing temperature. Alloying the initial Ni film with low (< 10%) concentration of Al, Co, Ge, Pd, Pt are known to influence these degradation temperatures.

an alloying element. On the other hand, Al is reported to increase the lattice parameter of $NiSi_2$, and as such, lowers the temperature at which we expect an exact lattice match. From *in situ* sheet resistance data [9], we expect the initial nucleation of $NiSi_2$ grains in the ultrathin phase formation regime between 300-400 °C. By consequence, we propose that Al-alloying will require less strain or interfacial defects at nucleation to compensate the difference in the lattice parameter than Co-alloying. In other words, on the basis of lattice matching arguments one would also conclude that alloying with Al is expected to lower the energy threshold to form epitaxial $NiSi_2$ at low temperatures.

Our results can be put into the broader context of stable nickel silicide contacts. The degradation of nickel silicides is discussed ever since NiSi was first considered as a contact material for the transistors' source and drain regions. The stability of a NiSi film is challenged through (1) agglomeration and (2) nucleation into $NiSi_2$. For 'ultrathin' (< 5 nm) Ni films, the agglomerating NiSi phase is not formed and instead $NiSi_2$ was found to be stable (both morphologically as well as thermodynamically) up to 900 °C. Figure 6.10 shows a diagram to indicate the temperature and

thickness regions at which a stable nickel silicide is present. Three borders limit the formation of a stable silicide compound: the critical thickness t_c, the agglomeration temperature of NiSi and the nucleation temperature of NiSi into $NiSi_2$. The agglomeration temperature decreases with decreasing film thickness, which can be explained as a thinner film has a higher surface-to-volume ratio [9]. The nucleation temperature of NiSi to $NiSi_2$ was studied by Deduytsche *et al.* [3] and is observed to increase for decreasing Ni thickness. Therefore, agglomeration is the most important degeneration mechanism for these thin-film silicides. Alloying proves a valuable strategy to alter positions of these three borders as a function of thickness and temperature, and numerous publications have previously elaborated on the beneficial effect of alloys on NiSi stability. Figure 6.10 displays the shifts through alloying for those alloying species which are relevant to this article: Al, Co [25, 32, 35], Ge [36, 37], Pd [25] and Pt [5]. Our study represents a first systematic investigation of several alloying elements on the critical thickness t_c.

6.5 CONCLUSIONS

The Ni-Si solid-state reaction was studied in the sub-15 nm Ni thickness regime. The morphological stability of the formed silicides indicates a critical thickness t_c= 4.8 nm that separates the '*regular*' phase sequence, which forms agglomerating NiSi, from the more stable '*ultrathin*' phase sequence, which forms epitaxial $NiSi_2$ at low temperatures. Thickness gradient libraries were fabricated to investigate the effect of ternary elements (10 at.% Al, Co and Pt) on the value of t_c as a function of thickness in a semi-continuous fashion. We found that t_c can be increased or decreased at will, by the addition of Al (t_c= 8.0 nm) and Pt (t_c= 2.6 nm) as alloy. Co did not change the phase sequence, did not display an abrupt critical thickness. It did, however, alter the transformation temperature of NiSi into $NiSi_2$ which resulted in a rough but non-agglomerating silicide film. Several energetic parameters are discussed to understand the observed shift in relation to mixing entropy and interface energy. This study shows that the solid-phase reaction of silicides exhibits drastic non-linear behaviour upon thickness scaling, and which can be influenced and controlled by altering the as-deposited composition.

SUPPLEMENTARY MATERIALS

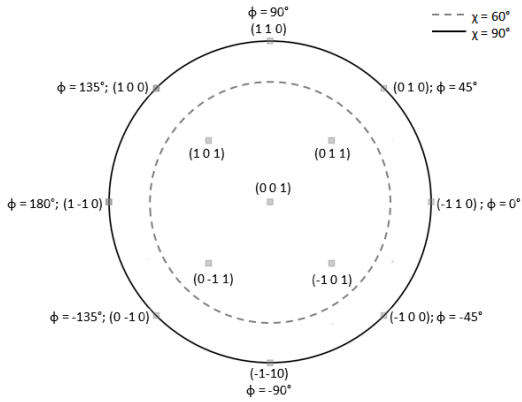

Figure 6.11: Position of the substrate diffraction poles on the displayed pole figures. A background ring is also apparent on most of the measured pole figures at $\chi \sim 60°$

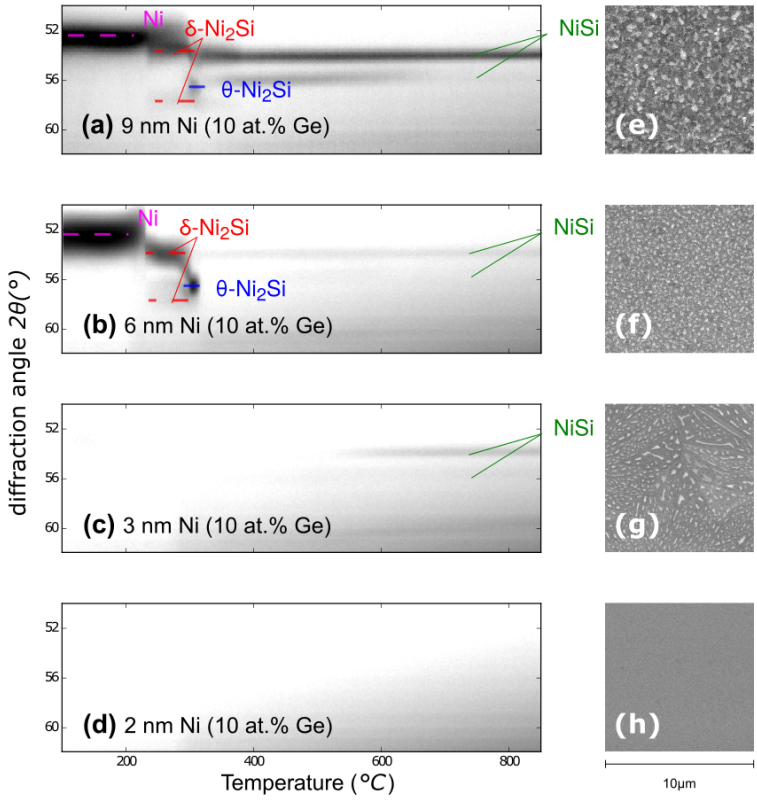

Figure 6.12: Overview of *in situ* XRD measurements of 10 nm Ni, alloyed with 10 at.% Ge **(a, b, c, d)** . NiSi can be observed for Ni thicknesses exceeding 3 nm. SEM micrographs furthermore indicate an agglomerated surface for these samples after quenching at 700 °C **(e, f, g, h)**. When only 2 nm Ni is present, no NiSi could be observed and the surface morphology indicates no agglomeration.

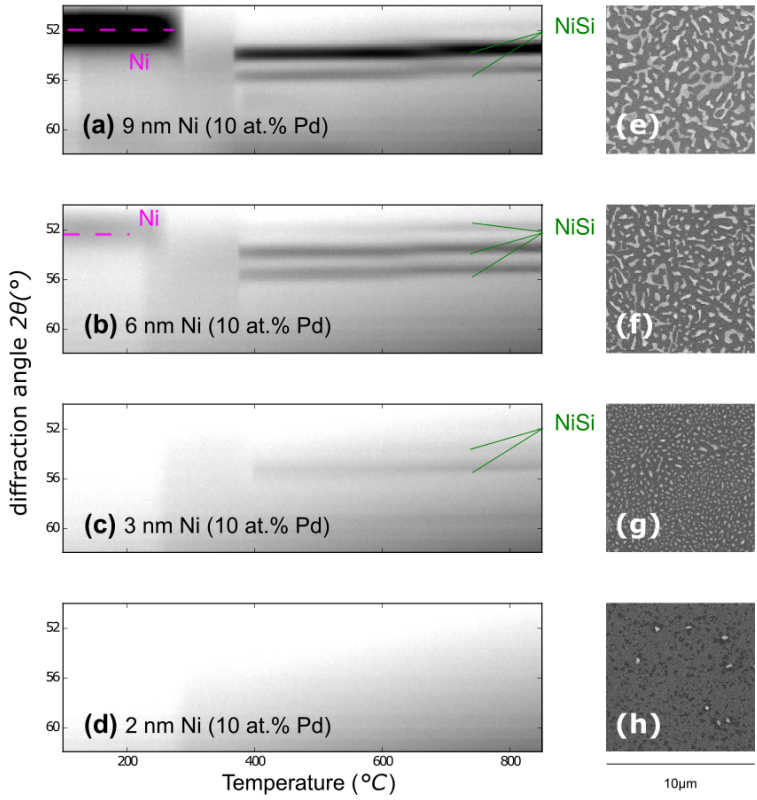

Figure 6.13: Overview of *in situ* XRD measurements of 10 nm Ni, alloyed with 10 at.% Pd **(a, b, c, d)** . NiSi can be observed for Ni thicknesses exceeding 3 nm. SEM micrographs furthermore indicate an agglomerated surface for these samples after quenching at 700 °C **(e, f, g, h)**. When only 2 nm Ni is present, no NiSi could be observed and the surface morphology indicates no agglomeration.

Part III

TITANIUM SILICIDES

7 TI-BASED SILICIDES

The $C54\text{-}TiSi_2$ was the first SALICIDE-compatible silicide used as contact material in MOSFET devices, and was introduced in the 0.35 µm node during the early '90s [1–3]. The application of $C54\text{-}TiSi_2$ in state-of-the-art transistors was, however, short-lived as $C54\text{-}TiSi_2$ required a too high annealing temperature to form a low-resistive contact for smaller technology nodes. The Ti-based silicide was already replaced by $CoSi_2$ contacts in the 0.18 µm node. It is therefore rather remarkable that Ti-based contacts are again present in the 22 nm node. As explained in section 7.1, the industry is replacing Ni by Ti because of the uncontrolled formation of Ni silicides. This recent evolution advocates to provide an overview on the solid-phase formation of Ti-silicides, which is given in section 7.2. The revived interest in the Ti-based silicides inspired us to re-investigate the texture of these silicides with modern pole-figure measurements, which are now performed with a much higher resolution as in the 90's. The results of such a study are reported in Chapter 8.

7.1 THE SCALABILITY OF NI SILICIDES FOR NOVEL MOSFET STRUCTURES

The constant drive to scale-down MOSFET devices has led to some big and small changes in the design and the preferred materials of the transistor, as explained in section 1.5. Up to 2012, all the integrated devices shared a similar two-dimensional *planar* structure. The scaling of this planar structure proved challenging from the 22 nm node on as to attain the desired switching speed, transistor size and power consumption. One of the reasons is that part of the channel area is too far away from the gate contact, resulting in a higher leakage current [3, 4].

A first approach is to use fully-depleted silicon-on-insulator substrates (FD-SOI) in order to create a MOSFET structure on top of an extremely-thin (e.g. 5 to 20 nm) Si layer [5, 6]. The thin Si layer therefore reduces the maximum distance between the channel and the gate contact, thus lowering the leakage current. Although this methodology has several advantages, not in the least a continuation of the planar architecture, it requires a far more expensive substrate as starting material. The FD-SOI technology requires an astonishing control on the Si thickness with very low variation

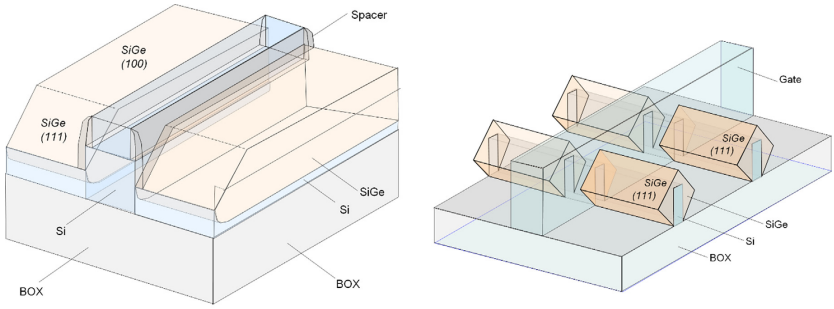

Figure 7.1: **(a)** Schematic view of a gate-first planar device on a SOI substrate. A Si(111) facet typically appears during the epitaxial overgrowth of an embedded source or drain area **(b)** Schematic view of a 3D finFET device on a SOI substrate. Because of different epitaxial growth kinetics on Si(111) facets, the epitaxial process results in the formation of diamond-shaped source and drain regions. Figure from [8].

throughout the wafers' area. A second approach is to change the architecture from planar to 3D. The first generation of such 3D devices was commercially available with Intel's 22 nm node MOSFET. This 3D architecture, which is now known as a finFET design, was also introduced by other manufacturers in more recent nodes, such as the 14 nm node of Samsung or the 16 nm node device of TSMC [7]. Although the substrate cost for such finFET-devices is not as expensive as for FD-SOI-based devices, it introduces a significant increase in overall complexity of the device and the fabrication process.

A complete comparison of these two architectures goes beyond the scope of this work. However, it is important to note that both architectures have some *non-planar* regions, as depicted in figure 7.1 [8]. Although the planar structures' epitaxial regions are oriented along the (001) plane, they exhibit (111) facets near the shallow trench isolations (Fig. 7.1a). The 3D structure of the finFET architecture facilitates epitaxially-grown contact regions at the source and drain regions. The epitaxial region has a diamond shape, of which the sides are oriented along the (111) orientation. Breil *et al.* [8] showed that these non-planar regions are attractive locations for undesired silicide formation when nickel silicides are being used as contact material.

In order to explain the uncontrolled growth of Ni-silicides, we start by comparing the silicide phases which have been used in the SALICIDE formation process. Figure 7.2 displays the silicides since the introduction of

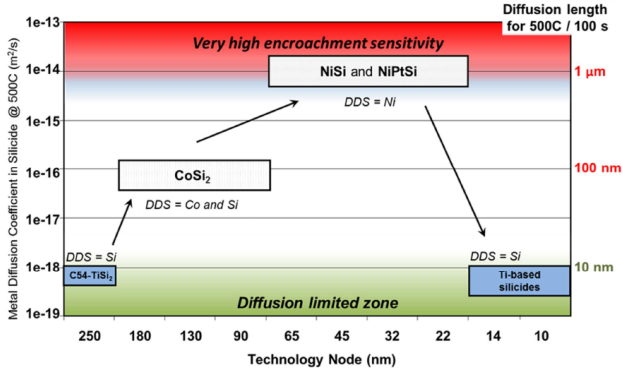

Figure 7.2: Evolution of the silicidation materials used for the various CMOS technology nodes at IBM and in the industry. The silicide growth constant is shown on the left axis, from which the effective diffusion length is calculated of the dominant diffusing species (DDS) in the silicide at 500 °C during 1 s. Figure from [9].

$C54\text{-}TiSi_2$. One can easily see that NiSi (or $Ni_{1-x}Pt_xSi$) could endure the scaling-down process longer than $TiSi_2$ or $CoSi_2$. However, the application of Ni has significantly limited the thermal window of further process steps in the back-end-of-line (BEOL) in order to avoid agglomeration or $NiSi_2$ nucleation, as previously explained in Chapter 2. For smaller technology nodes, an additional *encroachment*-defect will furthermore limit the application of Ni-based silicides. The left y-axis of figure 7.2 represents the growth rates of the displayed silicides at 500 °C. This temperature is representative for further processing in BEOL. As shown, the growth rate of NiSi silicide is almost five orders of magnitudes higher than Co- or Ti-based silicides. One can calculate that this corresponds with a far larger diffusion length of the dominant diffusing species (DDS, Ni in the case of NiSi) in the formed silicide, as displayed in the right y-axis of figure 7.2. Therefore, any amount of unreacted Ni that is present during those BEOL anneals can diffuse over great lengths along the transistor device. We can then expect that it will migrate to where it can easily form a silicide, thus creating an undesired conductive path in the MOSFET device.

Examples of such *encroachment* defects are shown in figure 7.3 for both planar and 3D structures. However, an abundance of Ni is not expected through the salicide formation process. Therefore, it is important to identify the Ni source which is responsible for the presence of mobile Ni during these BEOL anneals. Breil *et al.* [8] have found that the chemical etching, which removes unreacted Ni from the device as part of the SALICIDE

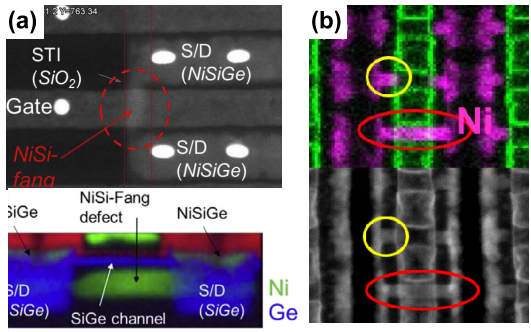

Figure 7.3: Examples of Ni encroachment defects (also called Ni-fangs) in **(a)** a planar and **(b)** a finFET geometry. Ni is the dominant diffusing species and moves fast towards defects in the substrate material, even at low temperatures. Figure from [10].

formation process, also partially transforms some of the formed nickel monosilicide into a Ni-rich silicide. These Ni-rich silicides (e.g. δ-Ni_2Si) are observed after the reactive ion etching process, and one can argue that it acts as a metal source for the formation of encroachment-defects. This process is even more pronounced when SiGe semiconductor regions are present, as the Ge-content significantly delays the mono-silicide reformation process, and thus the Ni atoms can migrate over an even larger distance. Breil *et al.* suggest that this mechanism has been a potential source for increased leakage current as early as the 45 nm node [8].

7.2 THE SOLID-PHASE FORMATION OF TI-BASED SILICIDES

The Ni-silicide system was abandoned for contact formation for 3D finFET architecture [7, 10, 12]. This is due to the encroachment-effect of Ni-silicides described earlier, together with an alternative silicide contact procedure, i.e. trench-contact formation (Fig. 7.5) instead of planar SALICIDE contacts [11]. Instead, Ti-silicide systems are again observed in these devices, as illustrated in figure 7.4. The exact crystalline phase of the used $TiSi_x$ contact is yet unreported in the publicly available literature. The following discussion therefore focuses on the phase formation sequence as established for the salicide-formation process.

The solid-phase reaction between a thin (e.g. $10-100$ nm) Ti film and a Si substrate results in the sequential formation of two disilicide phases: the C49-$TiSi_2$ phase and the C54-$TiSi_2$ phase [1]. The resistivity of the C49 structure is roughly four times higher than the C54-$TiSi_2$ phase, as

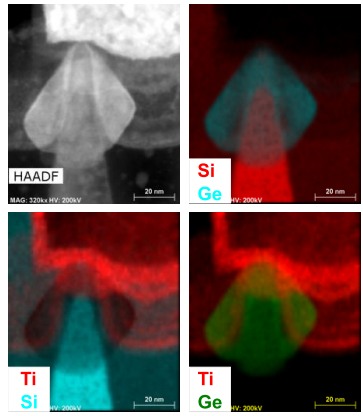

Figure 7.4: EDS-map of the drain region from a finFET geometry (Intel, 22 nm Xeon PMOS device). A Ti-based silicide is clearly present instead of a Ni-based silicide contact. Figure from [7].

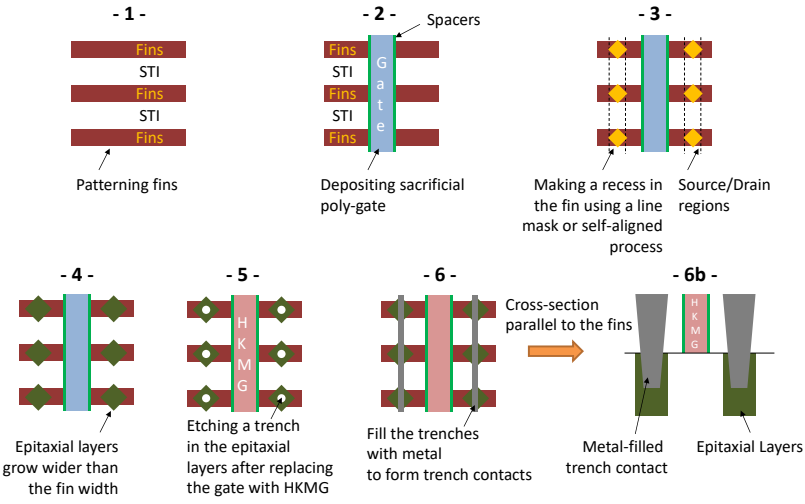

Figure 7.5: Schematics of forming the trench contacts in finFET devices. (1) Fin definition and creation of shallow trench isolation (STI) regions. (2) Dummy-gate patterning and spacer definition. (3-4) Formation of source and drain regions. (5) Dummy gate removal, and replacement with high-k metal gate (HKMG). Contact trench opening, implantation and annealing. (6) Metal deposition for contact formation and annealing. Figure from [11].

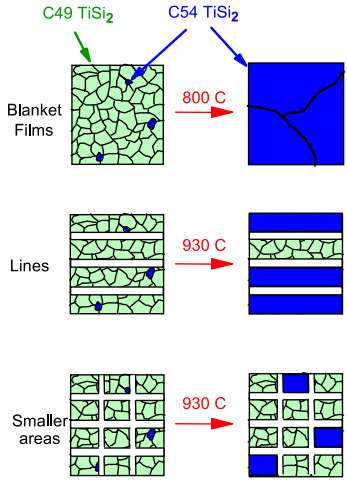

Figure 7.6: The nucleation of C54-$TiSi_2$ out of C49-$TiSi_2$ results in uncontrolled phase transformation for narrow lines due to the limited number of nucleation centers . Figure from [2].

previously mentioned in Table 1.1 of chapter 1 [13]. From an electrical contact perspective, the C54-phase is therefore preferred. However, the formation of Ti-disilicides is initiated with the high-resistive C49-phase around $500-600\,^{\circ}C$, whereas the transformation towards C54-$TiSi_2$ only occurs thereafter, typically above $700\,^{\circ}C$.

The SALICIDE formation process of C54-$TiSi_2$ includes a two-step anneal in order to obtain a low-resistive contact. A first anneal brings the film to the high-resistive C49-$TiSi_2$ phase, where after unreacted Ti is removed through etching. A second anneal to higher temperatures is required to transform the C49 silicide to the C54-$TiSi_2$ grains. This phase formation of C54-$TiSi_2$ is nucleation controlled, as only a small gain in free energy of 0.45kJ/g-atom is obtained through the transformation [2, 14]. As a consequence, the number of initial nuclei is limited.

This can directly be related to nucleation issues of C54-$TiSi_2$ when the line width of the transistor was further limited, as illustrated in figure 7.6. For the displayed area, it is shown that three initial nuclei are sufficient to transform the whole surface into three large C54-$TiSi_2$ grains. By subdividing the area into four lines, the growth of these individual nuclei is significantly hampered. A full transformation of the substrate therefore requires a higher number of nucleation sites. As such, an increase in thermal budget is needed in order to obtain a full C54-$TiSi_2$ line. This effect, also known as the *fine-line* effect, increases the difficultly to create C54-

grains for smaller lines. From the observed grain sizes, one can estimate that the nucleation density is around $0.1-0.3\,\mu m^{-2}$ [2], although a significant spread was found on the grain sizes. This was also one of the biggest challenges with C54-$TiSi_2$-based contacts, which eventually led to the replacement with $CoSi_2$ silicides for planar CMOS devices.

In addition to the issues related with reduced line widths in order to transform a C49-film to C54-$TiSi_2$, the effect of thickness reduction was also important during the scale-down process of transistors. This was initially investigated through *in situ* resistivity measurements by Allen *et al.* [15] between 25 and 100 nm as-deposited Ti. It was found that the nucleation temperature of C54-$TiSi_2$ increases with decreasing film thickness. We illustrate this by our own *in situ* XRD measurements, as displayed in figure 7.7. It is clearly observed that the formation of the C49-$TiSi_2$ phase occurs within the same temperature window of 30 °C. However, the transition to the C54-phase is clearly delayed as the initial Ti layer is thinned. The explanation for this behaviour was found by Ma *et al.* [16] in terms of energetic considerations. They found an unusual transition between nucleation sites for C54-nucleation as a function of initial Ti thickness. Thicker films, e.g. 100 nm Ti films, are preferentially formed at grain boundaries between two-grain junctions of C49-grains. Thinner films, e.g. 25 nm Ti films, are predominantly formed at triple grain junctions [16, 17]. These results can be understood by taking into account the decrease in available nucleation sites at two-grain junctions as a function of thickness. In addition, kinetic analysis revealed an increase in energy barrier for C54-formation as a function of decreasing Ti thickness. For these thinner films with largely increased surface-to-volume ratio, the surface contribution $\Delta\sigma$ in classical nucleation theory becomes more important with respect to the volume term. This also explains the observed increase in nucleation temperature of the C54-phase for thinner films.

One can argue that the alignment with the substrate will become increasingly important for thinner films. The preferential orientation of the $TiSi_2$ films were mainly investigated prior to the abandonment of C54-$TiSi_2$ contacts in the 90's [16–21]. Therefore, these investigations occurred prior to the discovery of axiotaxial texture [22]. As this particular alignment was observed in several silicide and germanide systems [23], it is not unlikely that it would also occur for these C54-$TiSi_2$ films. A reinvestigation of the C54-texture, given in the following chapter, is therefore interesting to investigate the texture evolution as a function of thickness, as well as to identify the possible axiotaxial orientation of this phase and the relationship with the previously-reported epitaxies.

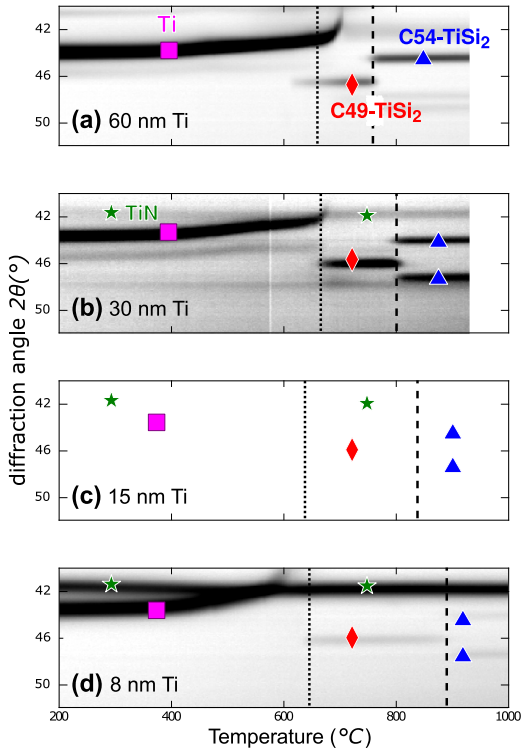

Figure 7.7: *In situ* X-ray diffraction measurement during the annealing of a Ti film on a Si(001) substrate ($\lambda = 0.18\,\text{nm}$) for several thicknesses. The formation temperatures of C49 and C54-$TiSi_2$ are indicated by dotted and dashed lines, respectively. A 8 nm TiN capping layer was present on the 30 , 15 and 8 nm films to prevent oxidation.

8

ARTICLE IV: AXIOTAXY AND EPITAXIAL TEXTURES IN C54-$TISI_2$ FILMS ON SI(001) AND SI(111) SUBSTRATES

8.1 INTRODUCTION

Metal silicides are extensively used in micro-electronics for contacting the source and drain regions of Si-based transistors [1]. C54-$TiSi_2$ was introduced in Complementary Metal Oxide Semiconductor (CMOS) devices for ultra-large scale integration during the early 90's and has since then been replaced by sequentially $CoSi_2$ and NiSi for high-performance applications [2]. C54-$TiSi_2$ is still being used in traditional planar CMOS technology for applications with high reliability demands, e.g. the automotive industry or high temperature applications. In recent years, Ti-based contacts have regained considerable attention for implementation in FinFET-technology through the formation of a thin Ti-Si compound, where Ti-based contacts offer a significant advantage over Ni because of the lower mobility of Ti in Si [3, 4].

Silicide films for CMOS applications are usually formed through a solid-state reaction, where a thin metallic film is deposited on a Si substrate and subsequently heated to form a silicide compound [2]. The solid-phase reaction often induces a preferential crystallographic orientation between the formed silicide film and the single-crystal Si substrate. Crystalline texture is known to affect functional properties such as the morphological stability [5, 6] and interface contact resistance [7] of the silicide film. The texture of several metal silicides has therefore been studied in detail over the past decades [8].

Most texture studies on titanium silicides date from the 90's and focused on the epitaxial orientation of the $TiSi_2$ film with the substrate [9–13]. Several epitaxial orientations were reported (Table 8.1) and their origin was discussed within the frameworks of geometric-based models such as the o-lattice [10] and edge-to-edge matching models [14] or by simply overlaying the atomic structure of both film and substrate [12]. Since then the improvement of the used experimental techniques have led to the discovery of other types of texture, such as axiotaxy [15] and also a particular plane rotation across crystalline grains of Ni-Si compounds termed trans-rotational domains [16], rendering novel insights on how the texture of the

Table 8.1: Overview of epitaxial orientations reported in the literature for orthorhombic C54-$TiSi_2$ films on Si(001) and Si(111) substrates.

SUBSTRATE	1ST ALIGNM.	2ND ALIGNM.	REF.
Si(111)	(100)//(111)	[004]//[02$\bar{2}$]	[9][10][11]
	(001)//(111)	[400]//[0$\bar{2}$2]	[9][10][11]
	(101)//(111)	[31$\bar{3}$]//[2$\bar{2}$0]	[10][11]
	(010)//(111)	[001]//[1$\bar{1}$0]	[10]
	($\bar{2}\bar{1}$1)//(111)	[1$\bar{1}$1]//[1$\bar{1}$0]	[10]
Si(100)	(10$\bar{1}$)//($\bar{1}$11)	($\bar{3}\bar{1}\bar{3}$)//(01$\bar{1}$)	[12]
	($\bar{1}\bar{3}$0)//($\bar{1}\bar{1}$1)	(004)//(1$\bar{1}$0)	[12]
	(10$\bar{1}$)//($\bar{1}$11)	(121)//(110)	[12]

silicide film affects its stability. A recent review by Deschutter *et al.* [8] provides an overview on the complex textures possible in such thin-film systems. Currently, no publications are available that investigates these novel texture-types for $TiSi_2$-thin films in great detail, since $TiSi_2$ was mostly researched prior to their discovery.

This paper reports on the axiotaxial nature of C54-$TiSi_2$ films on both Si(001) and Si(111) substrates. Synchrotron X-Ray-Diffraction (XRD) pole-figure measurements reveal the presence of multiple axiotaxial features and their importance in interpreting the different previously-reported epitaxial orientations.

8.2 EXPERIMENTAL METHODS

Ti films with a thickness of 8 and 30 nm were deposited using Physical Vapor Deposition (PVD) on Si substrates. Two orientations of Si substrate were used: Si(001) and Si(111). Both substrates received a short HF dip prior to loading in the deposition chamber. Ti was sputtered in an Ar atmosphere with a pressure of 1.33×10^{-3}Torr, after a base pressure of 1×10^{-7}Torr had been reached in a Materials Research Corporation PVD system. A 8 nm TiN capping layer was subsequently deposited on the Ti film without breaking the vacuum, in order to protect the film from oxidation after the deposition process.

Samples were subsequently heated in a purified He atmosphere at a constant rate of 3 °C s^{-1} at the *in situ* heating set-up of the X20C beamline

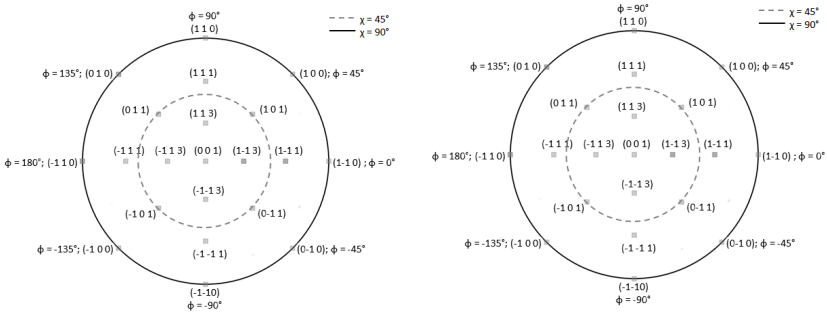

(a) Si(001) (b) Si(111)

Figure 8.1: Orientation of the pole-figure maps are fixed with respect to the substrate orientation, as shown in this figure.

at the National Synchrotron Light Source (NSLS, Brookhaven National Laboratory). The C54 crystalline structure was confirmed through *ex situ* X-Ray Diffraction (XRD) measurements (JCPDS No. 00-035-0785).

XRD pole-figure measurements were performed to determine the silicide's texture. Pole figures are obtained by measuring the diffraction intensity from a set of crystallographic planes at a fixed diffraction angle 2θ, while tilting and rotating the sample both in-plane and out-of plane, respectively parametrised by the angles ϕ and χ [17]. The diffraction angle 2θ is related to a specific $\{hkl\}$ lattice plane of a certain crystalline phase through Bragg's law of diffraction. The measured diffraction intensity I for a specific $\{hkl\}$ plane is dependent on the angles ϕ and χ, as I scales with the total volume of grains for which the $\{hkl\}$ plane is oriented normal to the direction determined by ϕ and χ. Thus a polar plot of $I(\phi, \chi)$ correlates with a statistical distribution of the preferred orientation of the corresponding $\{hkl\}$ plane, covering all grains illuminated by the incident X-rays (i.e. a surface area of minimum 2.3 mm^2 in this study). Pole figures therefore offer a significant statistical advantage in comparison with TEM-based texture research, where the number of grains measured and investigated are significantly limited.

In this work, pole figures were measured at the X20A synchrotron beamline of the NSLS, using an x-ray wavelength of $\lambda = 0.154$ nm, as selected using a Ge(111) monochromator. The diffracted x-rays were detected using a custom linear detector (8 cm Si strip detector, 640 pixels) which allows the simultaneous acquisition of pole figures covering 20 to 60° in 2θ, which includes diffraction of the (311), (313), (202), (004) and (022) planes of orthorhombic C54-$TiSi_2$ (JCPDS No. 00-035-0785). The pole figures were

acquired in steps of 1.0° in ϕ and χ ($0 \leq \chi \leq 85°$ and $-10 \leq \phi \leq 100°$ for Si(100) or $-10 \leq \phi \leq 130°$ for Si(111)). Complete pole figures were obtained by extending the measured data to the full range $0 \leq \phi \leq 360°$, taking into account the symmetry of the substrate. The samples were oriented so that the Si poles are located at the ϕ and χ coordinates as displayed in Fig.8.1. The diffracted intensity is represented by a stereographical projection for χ and ϕ, and by using a logarithmic gray-scale map, where white and black represent respectively a low or high intensity. A more detailed description of pole-figure measurements and their analysis can be found in earlier works describing the formation and texture of NiSi [15, 17, 18]. The pole figures were analysed using the GUSTAV [19] software package.

8.3 RESULTS AND DISCUSSION

In the following paragraphs, we categorise the observed features on the measured pole figures into texture components. The observed features are discussed for the (311) and (313) planes of the orthorhombic C54-phase (a=8.26 Å, b=4.79 Å and c=8.55 Å), which allows a clear interpretation because they occur in a window where there is no diffraction from other planes having a similar inter-planar distance. Texture components are proposed which explain the observed features, and the analysis was corroborated by pole figures for the C54-$TiSi_2$ (202), (004) and (022) planes (not shown here).

8.3.1 *Texture on Si(001)*

The recorded pole figures for C54-$TiSi_2$ films on Si(001) clearly contain several non-random patterns (Fig. 8.2), indicating preferential alignment with the substrate. Circular features can be associated with *axiotaxy* and dotted features with *epitaxy*. The fact that these epitaxial features are overlapping with some of the axiotaxial circles suggests that the two types of texture components are inter-related and will be discussed further. Figure 8.3 shows the diffraction intensities for regions in ϕ and χ, selected specifically to represent the different textures as oriented for the C54-$TiSi_2$ 311) plane. It is clear that the randomly-oriented grains represent a lower fraction of the film when going from 30 to 8 nm as-deposited Ti thickness, and that a relative larger fraction of the C54-film is oriented along the epitaxial texture. .

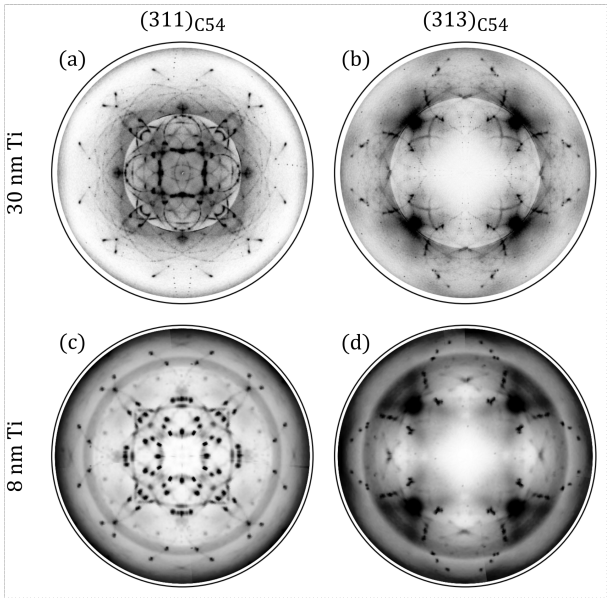

Figure 8.2: Pole-figure data for $C54$-$TiSi_2$ (311) and (313) diffraction planes for samples with an as-deposited Ti thickness of 30 nm (**a, b**) and 8 nm (**c, d**) on Si(100).

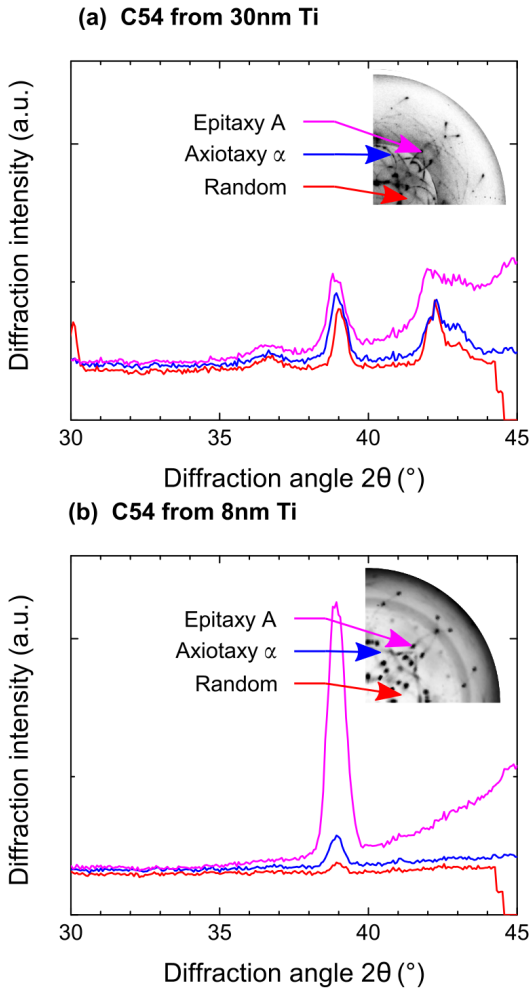

Figure 8.3: The diffraction intensity plotted for selecting specific regions in both ϕ and χ, associated with axiotaxy, epitaxy and random distribution of the grains' orientations. The regions in ϕ and χ are selected for the diffraction at $2\theta = 39.1°$ (i.e. C54-$TiSi_2$ 311).

Axiotaxial alignment

In general, circular patterns on a pole figure are generated by either an axiotaxial or a fiber alignment between the film and the substrate. Both textures require one of the film's planes to have a fixed orientation with respect to the substrate. The direction perpendicular to these planes then acts as an axis of rotation, and every individual grain is oriented into a random rotation angle around this axis of symmetry. By consequence, diffracting planes which are inclined to this axis of rotation will result in circular features on the associated pole figure.

Two different kinds of circular features are reported in literature: *fiber* and *axiotaxial*. The axis of rotation for a fiber alignment is always perpendicular to the substrate surface, and by consequence the diffraction rings are always concentric on the pole figures. An axiotaxial alignment does not have this restriction, and by consequence the non-concentric circular features in figure 8.2 [1] indicate axiotaxial texture.

The axiotaxial texture can occur when planes from the film and the substrate have a similar inter-planar distance and orientation. This allows a plane-to-plane match across the interface, and the axiotaxial features are uniquely defined by identifying these matching planes. A total of four different axiotaxial relationships allow us to reconstruct the complex pattern of observed circular features in figure 8.2: $(404)_{C54} \sim // (222)_{Si}$ (Fig. 8.4a, b), $(404)_{C54} \sim // (113)_{Si}$ (Fig. 8.4c,d), $(511)_{C54} \sim // (113)_{Si}$(Fig. 8.4e,f) and $(115)_{C54} \sim // (113)_{Si}$ (Fig. 8.4g,h) .

Axiotaxy originates from a plane-to-plane match across the interface between film and substrate. The quality of this match is often discussed in the literature with respect to the small difference in the planar distance between these to two matching planes, typically less than 5 %[6, 8, 15, 20]. It is then remarkable that the (404) plane of $TiSi_2$ would not only match with $(222)_{Si}$ ($\Delta d = 4.2\,\%$) but also with $(113)_{Si}$ ($\Delta d = 8.2\,\%$). Nevertheless, Detavernier *et al.* [15] argue that a mismatch in d-spacing can be compensated by a small tilt in χ of the orientation of the film's axis of rotation, resulting in a matching *projected* planar distance d_p on the interface (Fig. 8.5a), which is in fact observed for all axiotaxies reported in this paper ($\Delta(\chi)_{exp}$ in Tab. 8.2). However, they also point out that although a high tilt $\Delta\chi$ can in principle force matching across a perfectly planar interface, the matching quickly vanishes along a realistic interface which includes non-planarity and interfacial roughness (Fig. 8.5b). This can be expected

1 The pole-figure measurement was paused for some time in order to increase the synchrotron X-rays intensity, resulting in a discontinuity in diffraction background, with a lower (whiter) background around the center of the pole figure and a higher (darker) background at the edge of the pole figure.

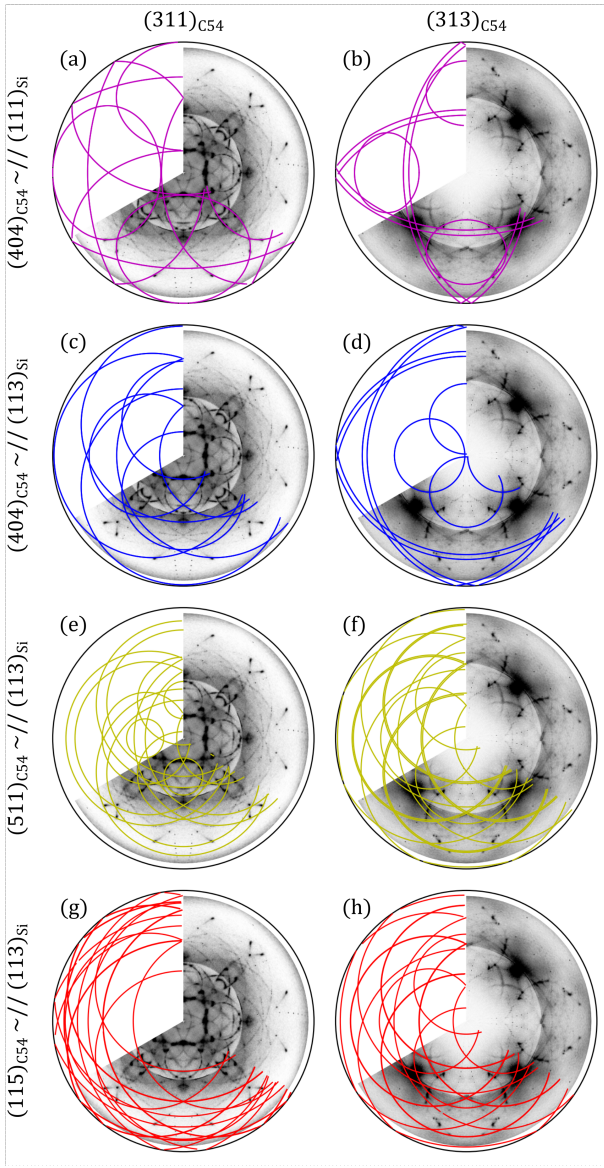

Figure 8.4: $(311)_{C54}$ and $(313)_{C54}$ pole figures of a C_{54} $TiSi_2$ layer with an as-deposited Ti thickness of 30 nm, overlayed with axiotaxial features related to matching of specific $TiSi_2$ planes with the (111) (**a**, **b**) and (113) (**c,d,e,f,g,h**) planes of Si across the interface.

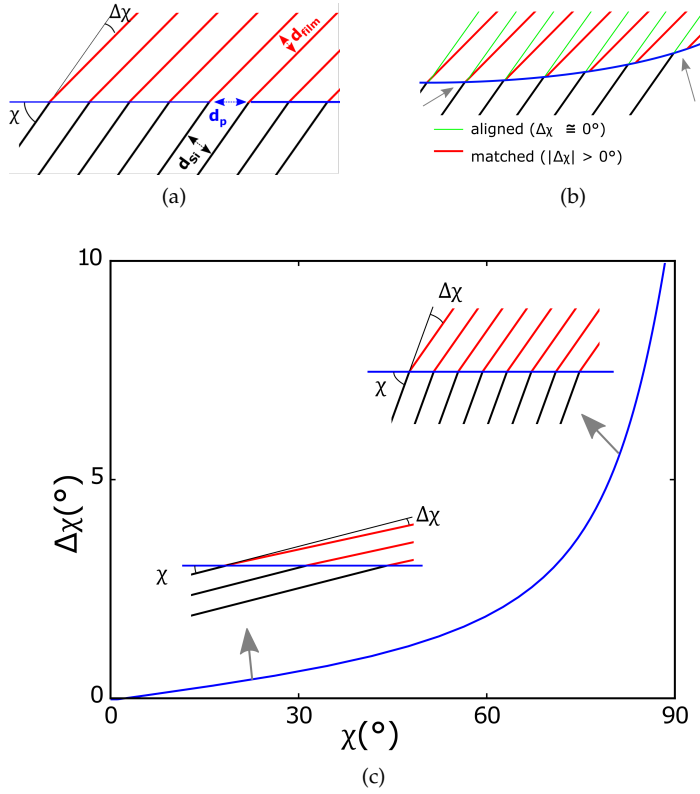

Figure 8.5: To achieve axiotaxial match between at a flat interface (**a**), the difference in planar distance between d_{Si} and d_{film} can be compensated by a slight tilt $\Delta(\chi)$, resulting in an identical projected spacing d_p at the interface to achieve plane-to-plane match. At a rougher interface (**b**), small values of $\Delta(\chi)$ are more stable to roughening of the interface [15]. In addition, the angle required to compensate a given difference in d-spacing (e.g. $d_{Si} = 1.02 \cdot d_{film}$) is also dependant on the inclination angle χ of the substrate plane with the interface, (**c**).

Table 8.2: Fitted axiotaxial texture components between C54-TiSi$_2$ and Si(001) substrate. A difference in d-spacing between the film and substrate planes will result in a mismatch at the interface. The small difference in d-spacing (D) between the axiotaxial component and the substrate can be compensated at the interface through a small tilt in χ.

	MATCHING PLANES	χ_{exp} (°)	$\Delta(\chi)_{exp}$ (°)	D (Å)	Δ d (%)	χ_{th} (°)	$\Delta(\chi)_{th}$ (°)
	Si(222)	-	54.7	1.57	-	54.7	-
$\alpha_{Si(100)}$	C54(404)	51.5	3.2	1.51	4.2	51.5	3.2
	Si(113)	25.2	-	1.64	-	25.2	-
$\alpha'_{Si(100)}$	C54(404)	23.4	1.8	1.51	8.2	23.0	2.2
$\beta_{Si(100)}$	C54(511)	24.0	1.2	1.56	5.2	23.8	1.4
$\gamma_{Si(100)}$	C54(115)	24.5	0.7	1.60	2.5	24.6	0.6

to be particularly important during the nucleation of a new phase during a solid-state reaction, which is exactly when the grain orientation will be selected. We here add to this discussion that $\Delta\chi$ not only is dependant on the difference Δd, but is also dependant on the inclination angle χ of the rotation axis with respect to the interface (Fig. 8.5c) through

$$\chi = \frac{\arctan(\sin\Delta\chi)}{\cos(\Delta\chi) - d_p} \tag{8.1}$$

Indeed, on Si(001), a $(404)_{C54}$ plane only needs a tilt of 2.2° to align with $(113)_{Si}$, whereas a tilt of 3.2° is required to compensate the difference in Δd with $(222)_{Si}$, despite the relatively smaller Δd of the latter alignment. Therefore, the evaluation of an axiotaxial alignment should not only focus on the difference in d-spacing, but also include the dependence of $\Delta\chi$ on the inclination angle χ to obtain a lattice match at the interface.

Epitaxial alignment

The high intensity spots on the pole figures indicate *epitaxial* alignment of the thin film. An epitaxial alignment completely fixes the relative orientation of a crystalline grain with respect to the single crystal substrate, thus eliminating the rotational symmetry. Therefore, a diffracting $\{hkl\}$ plane within each epitaxial-oriented grain will also have a specific orientation, which translates into local spots of high diffracted intensity on the pole

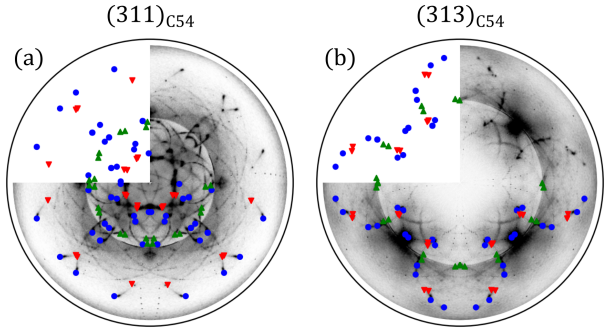

Figure 8.6: Pole figures overlayed with identified epitaxial features for data from a $C54$-$TiSi_2$ sample with an as-deposited Ti thickness of 30 nm.

Table 8.3: Overview of observed epitaxial components of $C54$-$TiSi_2$/Si(001).

EPITAXY (SYMB.)	1ST ALIGNM.	2ND ALIGNM.
$A_{Si(001)}$ (●)	$(101)_{C54} \sim // (111)_{Si}$	$(\bar{3}\bar{1}3)_{C54} \sim // (\bar{1}01)_{Si}$
$B_{Si(001)}$ (▼)	$(101)_{C54} \sim // (111)_{Si}$	$(1\bar{1}\bar{1})_{C54} \sim // (\bar{1}10)_{Si}$
$C_{Si(001)}$ (▲)	$(5\bar{1}1)_{C54} \sim // (11\bar{3})_{Si}$	$(400)_{C54} \sim // (001)_{Si}$

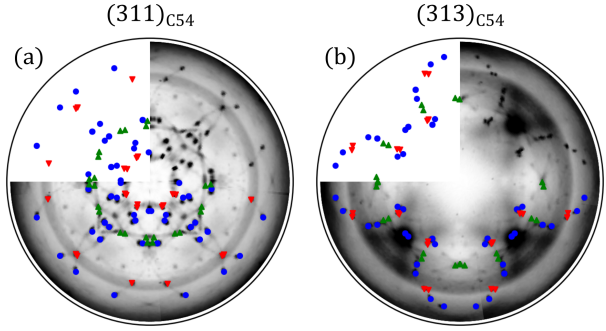

Figure 8.7: Pole figures overlayed with identified epitaxial features for data from a $C54$-$TiSi_2$ sample with an as-deposited Ti thickness of 8 nm.

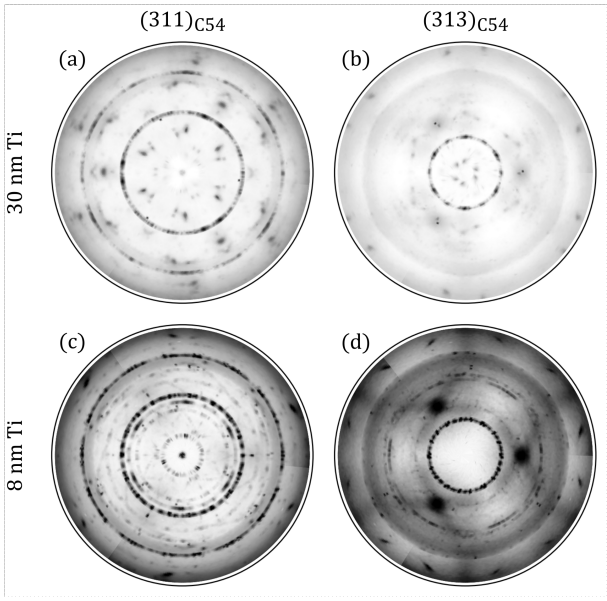

Figure 8.8: Pole-figure data of two C54-TiSi$_2$ diffraction planes as measured from a sample with an as-deposited Ti thickness of 30 nm (**a,b**) and 8 nm (**c,d**) on Si(111).

figure. A total of three epitaxial orientations were identified (Fig. 8.6) and the relative orientation of each with respect to the Si substrate was determined (Tab. 8.3). Intriguingly, all observed spots of high intensity are in fact located along axiotaxial features, a relationship which shall be discussed further on. For C54 films formed from a thinner 8 nm Ti layer, the axiotaxial features are barely visible, while the epitaxial features are very intense (Fig. 8.7). These epitaxies are identical to the epitaxies determined for films originating from the 30 nm Ti film (Tab. 8.3).

8.3.2 *Texture on Si(111)*

The preferential alignment between the C54-film and the Si(111) substrate is characterized by circular and epitaxial features (Fig. 8.8). Some of these circles, those associated with planar alignment of the planar alignment of $(404)_{C54}$ $\sim//(222)_{Si}$, are observed for both thickness. However, other preferential orientations are significantly different and therefore shall be discussed separately for each thickness.

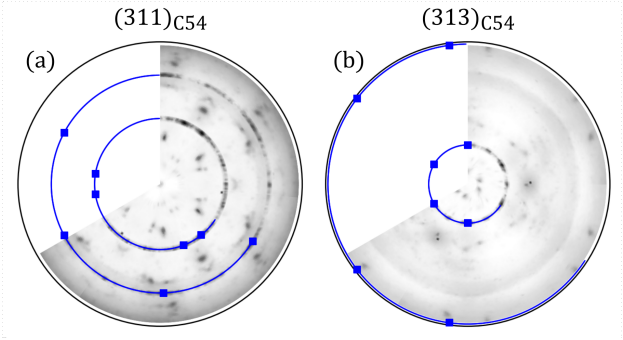

Figure 8.9: Pole figures from a $C54$-$TiSi_2$ sample with an as-deposited Ti thickness of 30 nm on Si (111). The measurement is overlayed with a $(404)_{C54}//(222)_{Si}$ fiber-like texture, together with an epitaxy partly coinciding with this axiotaxy.

Texture for 30 nm *Ti*

The concentric circles for the thickest films can be explained by supposing a $(404)_{C54} \sim//(222)_{Si}$ axis of rotation (Fig. 8.9). Remarkably, the diffraction intensity varies as a function of ϕ along the ring, which is unusual for fiber-textures. Moreover, the width of the concentric rings is very small (i.e. $< 2°$FWHM). The driving force for a traditional fiber texture is usually a realization of surface energy. Here, it seems more plausible to interpret the apparent fiber texture based on axiotaxy-type plane matching *across* the interface, as the $(404)_{C54}$ and $(222)_{Si}$ planes only differ by 0.06 Å. Evidently, such plane-to-plane matching would not be possible on a perfectly flat interface, as the planes would be parallel to the flat interface, and therefore never meet edge-to-edge. However, it was previously reported that $C54$-$TiSi_2$ can heavily agglomerate on Si(111) [10], resulting in a very rough interface.

A total of four epitaxial orientations are identified for this film (Fig. 8.10), and their orientation with respect to the Si substrate was determined (Tab. 8.4).

Texture for 8 nm *Ti*

Different axiotaxial and epitaxial textures are observed after annealing a thinner Ti layer on Si(111). In addition to the $(404)_{C54} \sim//(222)_{Si}$ fiber-like features (Fig 8.11, blue curve), we can also observe fiber-like rings originating from $(500)_{C54} \sim//(222)_{Si}$ (Fig 8.11, cyan curve) and $(511)_{C54} \sim//(222)_{Si}$ (Fig. 8.11, yellow curve), although the intensity of the latter

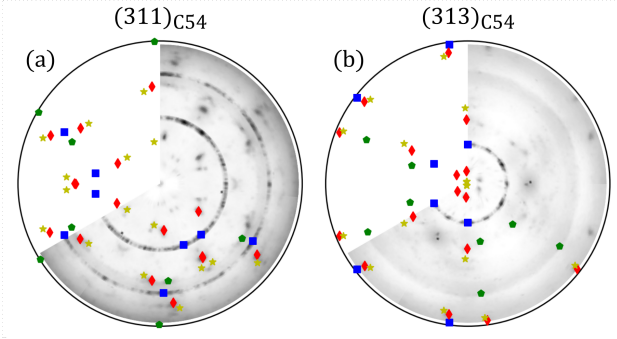

Figure 8.10: Additional epitaxial features are present for C54-$TiSi_2$ sample with an as-deposited Ti thickness of 30 nm on Si(111).

Table 8.4: Overview of observed epitaxial components of C54-$TiSi_2$/Si(111) for C54-films grown from 30 nm (A-D) and 8 nm (A, E) Ti.

EPITAXY (SYMB.)	1ST ALIGNM.	2ND ALIGNM.	FIG.
$A_{Si(111)}$ (■)	$(404)_{C54} \sim //(222)_{Si}$	$(050)_{C54} \sim //(220)_{Si}$	8.10
$B_{Si(111)}$ (●)	$(300)_{C54} \sim //(\bar{1}11)_{Si}$	$(\bar{2}0\bar{2})_{C54} \sim //(0\bar{1}\bar{1})_{Si}$	8.10
$C_{Si(111)}$ (♦)	$(01\bar{2})_{C54} \sim //(1\bar{1}\bar{1})_{Si}$	$(110)_{C54} \sim //(100)_{Si}$	8.10
$D_{Si(111)}$ (★)	$(\bar{2}10)_{C54} \sim //(1\bar{1}\bar{1})_{Si}$	$(110)_{C54} \sim //(00\bar{1})_{Si}$	8.10
$E_{Si(111)}$ (×)	$(500)_{C54} \sim //(222)_{Si}$	$(001)_{C54} \sim //(10\bar{1})_{Si}$	8.11

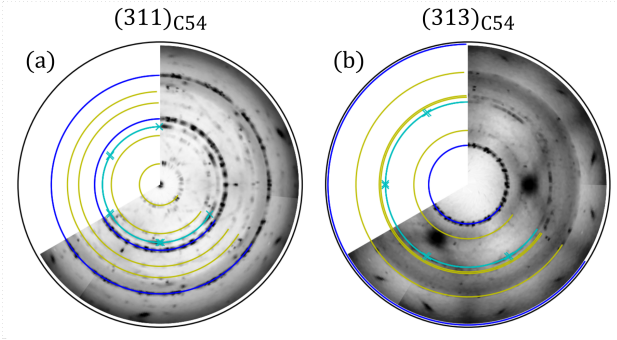

Figure 8.11: Additional epitaxial features are present between a C54-$TiSi_2$ film originating from a 8 nm Ti film on Si(111).

Table 8.5: Fitted axiotaxial texture components between C54-$TiSi_2$ and Si(111) substrate.

	SYMMETRY Axis	χ_{obs} (°)	D-SPACING (Å)	Δ d (%)	FIGURE (color)
	Si(222)	0	1.57	-	-
$\alpha_{Si(111)}$	C54(404)	0	1.51	4.2	8.9, 8.11 (blue)
$\beta_{Si(111)}$	C54(511)	0	1.56	0.0	8.11 (yellow)
$\eta_{Si(111)}$	C54(500)	0	1.65	5.1	8.11 (cyan)

alignment is significantly lower than the other fiber-like features. Again, the width of these concentric circles, as well as the variable intensity along ϕ suggests that these textures are in fact axiotaxial alignments with the substrate, where Table 8.5 gives an overview of the coinciding lattice planes.

All three fiber-like orientations are defined by a parallelism with similar planar spacings in film and substrate. The fiber-like circles also exhibit significant variation in diffraction intensity along ϕ, again indicating a preferential alignment closer towards an epitaxial orientation. Bright spots on the circles related to $(500)_{C54} \sim //(222)_{Si}$ can be explained by introducing $(004) \sim //(02\bar{2})$ as a secondary orientation condition. This epitaxial orientation was previously reported (Tab. 8.1), and now the arc-shape revealed by the higher-resolution synchrotron pole figures indicates a dependence on the axiotaxial orientation. The bright spots along the $(404)_{C54} \sim //(222)_{Si}$ fiber-axis cannot be explained by a single additional constraint, but also correspond to the many epitaxial orientations observed by Catana *et al.* [10], listed also in Table 8.1.

It is interesting to note that the $(511)_{C54}$ plane now aligns with $(222)_{Si}$, instead of $(113)_{Si}$ as reported earlier for the Si(001) substrate. We can again understand this when considering the alignment of the substrate planes with respect to the interface (Fig. 8.5c), where χ of $(222)_{Si}$ is lower on Si(111) than on Si(001)-oriented substrates (0 and 54.7°, respectively), and thus the alignment requires a smaller tilt $\Delta\chi$ on Si(111) to compensate for the small lattice mismatch.

A question remains: which bonding is favoured as to explain the observed preferential orientations, i.e. which atoms are potentially bonding across the interface. It is especially intreguing that some of the aligning planes have unsueally high indices, such as $(115)_{C54} \sim //(113)_{Si}$. The

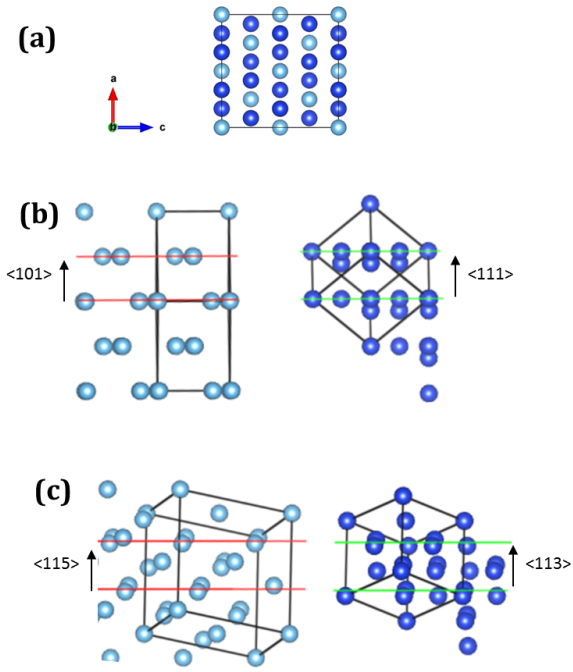

Figure 8.12: **(a)** The C54-$TiSi_2$ unit cell can aproximatly be described as a pseudo-tetragonal unit cell since $a \approx c$ (neglecting the positioning of the Si atoms). Hence explaining the observed symmetry between the a and c axis for several observed preferential orientations. **(b)** The interface determined by $(404)_{C54}//(222)_{Si}$ enables matching between nearly-closed packed Ti-atoms from the C54 silicide and the Si atoms of the substrate. **(c)** Other axiotaxial alignments, such as $(115)_{C54}//(222)_{Si}$, can also be described as a function of nearly-closed-packed Ti planes within the silicide.

most reoccurring texture, $(404)_{C54} \sim //(222)_{Si}$, has been discussed previously by Catana *et al.*, where the orientation was interpreted as favourable due to the presence of Ti-planes from C54-$TiSi_2$ along $\{101\}_{C54}$ with similar d-spacing and densities as the {111} planes of Si [10]. By focusing on the Ti atoms, we can also explain the observed symmetry with respect to the a and c axis of the C54-unit cell (e.g. axiotaxies $\alpha_{Si(100)}$, $\alpha'_{Si(100)}$, $\beta_{Si(100)}$ & $\gamma_{Si(100)}$, $\alpha_{Si(111)}$ or epitaxies $A_{Si(001)}$, $A_{Si(001)}$, $A_{Si(111)}$, $C_{Si(001)}$ & $D_{Si(001)}$). Indeed, the C54-unit cell can be described as symmetrical in a and c, or even pseudo-tetragonal, when only assessing the positions of the Ti-atoms, since $a = 8.26\,\text{Å} \approx c = 8.55\,\text{Å}$ (Fig. 8.12a). The reduction to mainly look at the Ti-atoms of the silicide phase to assess the bonding across the interface, allows to understand that the observed alignments indeed allow a continuation of nearly-closed-packed Ti-planes from the silicide to nearly-closed packed Si-planes from the substrate, as illustrated in Fig. 8.12b and c for orientations containing both low-index and high-index silicide directions.

8.4 CONCLUSIONS

The preferential orientation between C54-$TiSi_2$ films and Si(001) and Si(111) substrates was investigated through high-angular-resolution synchrotron XRD pole figures. This enabled us to identify the axiotaxial texture in the C54-$TiSi_2$/Si system, in addition to known epitaxial alignments. The majority of the observed epitaxies are in fact special cases of the same $(404)_{C54} \sim //(222)_{Si}$ axiotaxial alignment, indicating the importance of this plane-to-plane matching along the interface. From the diffraction intensities, one can derive that a lower Ti thickness corresponds with a higher fraction of the C54 grains with an epitaxial orientation.

Part IV

CONCLUSIONS

9 SUMMARY AND CONCLUSIONS

Silicides are formed as a crystalline structure of metal and silicon atoms. They are conventionally formed by a solid-state reaction between a metal film (e.g. Co, Ni, Ti) deposited on a silicon substrate which is subsequently heated. These silicides are an important part in modern micro-electronic devices, as they allow a low-resistive and stable electrical contact at the Si-based terminals of a transistor. The used silicides in modern MOSFET devices are drastically challenged due to the constant engineering of smaller transistors. A silicide that is reliable in one technology node is not necessarily useful as a contact material in a future, smaller node. The point-of-interest in this thesis is to investigate the consequence of thickness reduction on the silicide phase formation sequence and stability.

The first major part of this work is focused on nickel-based silicides. The currently-used contact materials in planar MOSFET devices rely on nickel monosilicide (NiSi). Regrettably, NiSi has a high tendency to agglomerate, and thinner NiSi films are more sensitive to agglomeration than thicker films due to an increased surface-to-volume ratio. This morphological degradation process results in a dramatic increase in resistivity of the contact layer. This utterly destroys the conductive properties of the silicide to use as a contact material. A common strategy to delay the agglomeration process is by adding alloying elements in order to shape up the silicide contact. Pt-alloying is currently used to delay agglomeration. However, this solution does not completely eliminate the degradation mechanism, and alternative solutions are vital to be investigated.

The solid-phase reaction between Ni and Si can also form $NiSi_2$, a cubic phase which is highly similar to the Si substrate. The close resemblance with Si allows $NiSi_2$ to grow epitaxially on the substrate. Epitaxial silicides are interesting candidates to form a contact layer, as they are reported with a lower contact resistance and with a higher stability. However, the controlled growth of long-range epitaxial films is still a challenge. For example, it is known that $NiSi_2$ grows on top of the Si substrate in two epitaxial variations, which is found to be correlated with an increased contact resistance. Moreover, $NiSi_2$ formation through a solid-phase reaction between a Ni film and a silicon substrate only occurs at relatively high temperatures above 800 °C.

It was recently shown that the incorporation of Al in the initial Ni film strongly promotes the formation of epitaxial $NiSi_2$ at lower temperatures.

In chapter 4, we have systematically investigated the phase formation within the ternary Ni-Al-Si system by annealing Ni-Al concentration gradients deposited on Si substrates. This resulted in a detailed overview of the solid-phase reaction as a function of Al concentration. It is shown that the Al concentration in the initial Ni film significantly influences the phase formation, resulting in four different concentration-dependent phase-sequence regimes:

- $5 - 28$ at % Al: Ni(Al) $\rightarrow$ θ-Ni_2Si (epi) $\rightarrow$ NiSi $\rightarrow$ $NiSi_2$ (epi)
- 32 at % Al: Ni(Al) $\rightarrow$? $\rightarrow$ $NiSi_2$ (epi)
- $37 - 43$ at % Al: Ni(Al) $\rightarrow$ NiAl $\rightarrow$ $NiSi_2$ (epi)
- $45 - 59$ at % Al: NiAl $\rightarrow$ Ni_2Al_3 $\rightarrow$ $NiSi_2$ (rand)

The formation of $NiSi_2$ at low temperatures is strongly promoted for Al concentrations at 32 at.% and above. We also report on the preferential alignment of the formed $NiSi_2$ grains with the Si(001) substrate as a function of increasing Al concentration. The epitaxial quality is the highest in the concentration window between 30 and 50 at % Al. Lower Al concentrations result in the simultaneous occurrence of two different epitaxial orientations, and higher Al concentrations result in the formation of an axiotaxial alignment between $NiSi_{2-x}Al_x$ and the Si substrate. The obtained results on the Ni(Al) alloys can be used as guidance in order to determine the desired Al concentration as well as the necessary annealing temperature in order to form a mono-epitaxial $NiSi_2$ film. As such, our results on the Ni-Al-Si system clearly show how small changes in lattice spacing is correlated with a significant change in texture of the formed films. Moreover, the fact that the lowest interfacial roughness is observed when no other texture than type-A alignment is occurring, is indicative for the increasing importance of texture-based studies.

Intriguingly, a second strategy can also be employed to establish epitaxial $NiSi_2$ films at relative low annealing temperatures. The solid-phase reaction of nickel silicides exhibits a drastic alternation when the as-deposited Ni film is reduced below a *critical thickness* t_c of 5 nm. Ni films thicker than this value follow the conventional phase sequence where a polycrystalline NiSi film is formed upon annealing above 450 °C, which subsequently transforms into $NiSi_2$ above 800 °C. Thinner Ni films instead form epitaxial $NiSi_2$ films already when annealing to 450 °C and completely lack the formation of nickel monosilicide. These films exhibit a remarkable resistance towards agglomeration. The thickness regime at which this critical change in phase sequence occurs is of particular interest for the modern MOSFET technology, as the silicide contacts in state-of-the-art devices are

trending towards sub-10 nm thicknesses. Therefore, a good understanding is required of this striking change in nickel silicide phase sequence near the thickness values of t_c.

In chapter 5, we investigate the phase sequence of nickel silicides which are formed from 'thin' (i.e. 9 nm) as well as 'ultra-thin' (i.e. 3 nm) Ni films deposited on top of Si(001) substrates. In addition, we also study the effect of Al, Co and Pt alloying of the as-deposited Ni layer on the phase sequence, phase stability and silicides' crystalline alignment with the substrate. A first observation is that the addition of these alloying elements can alter the temperature windows at which a specific silicide is observed. This can be comprehended through classical nucleation theory and by considering the effect of entropy of mixing. We observe that elements which are soluble within a certain nickel silicide (e.g. Co in δ-Ni_2Si) appear to extend the temperature window at which the phase is present during the solid-phase reaction. Alloys which are not able to dissolve in specific silicide phases (e.g. Pt in δ-Ni_2Si) delay the formation of these phases. These insoluble elements need to be excreted from the original mixture in order to be able to form the silicide phase, thus hindering its nucleation. A second observation is that the crystalline alignment of the silicides with respect to the Si substrate is significantly modified through alloying. Our measurements indicate a *texture inheritance* effect, where a forming phase inherits its texture from the preceding phase. This inheritance is interpreted through close resemblance between the crystal lattices of sequential phases: θ-Ni_2Si & δ-Ni_2Si, θ-Ni_2Si & NiSi and θ-Ni_2Si & $NiSi_2$. The atomic positions in their lattices allow a phase transition through minimal atomic migration. As a consequence, a crystalline alignment with the underlying substrate can be maintained upon formation of the new phase, as identified by the transformation from epitaxial θ-Ni_2Si into subsequent epitaxial phases. By comparing the crystal lattices, we are able to determine transformation rules to translate the epitaxial alignment of the consumed θ-Ni_2Si phase into the epitaxial alignment of the forming phase. We suggest that the mechanism of texture inheritance can avoid a drastic increase of the surface energy during the phase formation, which aids in lowering the overall energy barrier that needs to be overcome during the silicide nucleation.

As alloying can significantly alter the phase sequence of nickel silicides, one can argue that also the critical thickness t_c can potentially be adapted through alloying. For industrial applications, it is of utmost importance to assess the critical thickness with high certainty so the desired silicide is certainly formed at the contact pads of the transistor. In addition, depending on the aimed contact material the value of t_c should be increased

or decreased, and methodologies to do so should be explored. In chapter 6, we investigate the solid-phase reaction of Ni films between 0 and 15 nm with the underlying Si substrate. This is performed through the use of nickel thickness gradients, which provide semi-continuous information on silicide formation and stability as a function of as-deposited Ni thickness. The alloying of these Ni layers with 10 % Al, Co, Ge, Pd or Pt render a significant change in the critical thickness. Depending on the alloying element, a different phase sequence is observed through X-ray diffraction measurements, which coincides with a different phase morphology as observed through scanning electron microscopy. The results are again discussed within the framework of classical nucleation theory and entropy of mixing. We have found that Pt, Pd and Ge significantly reduce the critical thickness, i.e. promote the formation of polycrystalline NiSi at lower Ni thicknesses, whereas Al increases the critical thickness, i.e. promotes the formation of epitaxial $NiSi_2$ at higher Ni thicknesses. Co, which has a mediocre solubility in NiSi and a high solubility in $NiSi_2$ does not delay NiSi formation, but significantly promotes the transformation of NiSi into $NiSi_2$ at lower temperatures. As such we conclude the first part of this thesis on nickel silicides by providing a summary on the different degeneration mechanisms of nickel silicides as a function of thickness and temperature and how the application of an alloying strategy can tailor the morphological and thermodynamic stability of the formed phases.

In the second part of this thesis, we elaborate on a recent development for silicide contact materials. The introduction of 3D-structured finFETs have re-established titanium-based silicides as a contact material for state-of-the-art devices. The C54-$TiSi_2$ phase was previously used in early 90's for microelectronic applications of the 250 nm technology node. Although the phase is very difficult to form for the current dimensions of state-of-the-art transistors, C54 is still present as contact material for several applications which require a high reliability such as the automotive industry. The renewed interest in titanium-based silicides inspired us to re-investigate the texture of the C54 phase on Si(100) and Si(111) in chapter 8. Pole-figures measurements revealed axiotaxial alignment of C54-$TiSi_2$ films, which is reported upon for the first time, in addition to the previously-observed epitaxial alignments. The physical origin of the axiotaxy is interpreted through plane-to-plane matching across the interface. Furthermore, we could relate axiotaxial texture to the epitaxial alignment. Reducing the Ti film thickness from 30 to 8 nm drastically favours the epitaxial alignment above the axiotaxial alignments. Thinner films have an increased surface-to-volume ratio and this means that the silicide grain is more influenced by its interface with neighbouring crystalline grains. The

tendency to form a low-energetic interface will thus be higher for thinner films. Once again, we have observed a trend as a function of thickness that can be understood through the increasing importance of a well-aligned interface and low interface energy for thinner films.

Summarizing, this work revealed the increasing importance of texture alignment for thinner silicides, both in the nickel- and titanium-based silicides. As the dimensions in micro-electronics is trending to ever-smaller values, similar effects as texture inheritance are expected to occur for other silicides, for solid-phase reactions on other substrates (e.g. SiGe, SiC) or even for other nano-scale heterophase systems in general. At this moment, it is clear that the interaction between the thickness of the as-deposited metal and its composition plays a crucial role in phase selection, phase kinetics and film characteristics such as texture.

SUGGESTIONS FOR FUTURE RESEARCH

The high mobility of Ni in MOSFET devices leads to a shift to use other silicides than (Pt-alloyed) NiSi as contact material. Future research will therefore be focusing on these alternative materials. As long as Si-based transistors are considered, there will always be a contact material in the form of a silicide compound. The build-up of knowledge and expertise on the Ni-Si system will prove useful for these future contact materials, as it is likely that effects such as texture inheritance will also be important during the solid-phase reaction of other compounds. Without a doubt, the trend for thinner contact materials will promote the formation of epitaxially-aligned phases. For example, a recent study by Hsin *et al.* shows that an epitaxially-aligned C40-$TiSi_2$ phase is part of the Ti-Si solid-phase reaction when reducing the as-deposited thickness to ultra-thin values [1]. The promotion of this phase during the solid-phase reaction for ultra-thin Ti films should be further explored due to the promising properties of this silicide.

Throughout the first part if this thesis, we have focused on the changes in phase-formation sequence of the nickel silicide system. Nickel monosilicide was, without any doubt, the most important contacting material since the 64 nm node. The introduction of 3D-structured transistors have drastically changed some of the requirements on the initial contact, and therefore the use of NiSi for future devices is challenged. Our work shows that a shift towards epitaxial $NiSi_2$ effectively avoids agglomeration of the silicide contact and improves the overall stability of the contact. However, interfacial roughness due to pyramidal faceting of the $NiSi_2$/Si(001) interface is still observed in the investigated layers. These facets can drastically

reduce the uniformity of the silicide contact and should be avoided. As the literature indicates that these facets disappear upon annealing, the thermodynamic driving force is towards the formation of a flat, facet-free interface and the pyramidal facets can be considered as meta-stable. Therefore, it is not unlikely that the facets can be eliminated, as suggested by our work on Al-alloying in thick films in chapter 4. A systematic investigation on these facets therefore is the next point-of-interest in order to form defect-poor, uniform and epitaxial $NiSi_2$ layers. Further investigation of these results from a diffusion perspective, for example through tracer experiments, would potentially elucidate the role of interface alignment on the phase kinetics and vice versa.

In chapters 5 and 6, we have illustrated that the effect of thickness reduction clearly amplifies the importance of a low-energetic silicide-silicon interface. As a similar effect can be expected for other thin-film solid-phase reactions, the prediction of texture and the evaluation of thermodynamic quantities such as the interface energy $\Delta\sigma$ is highly desired, not only for binary but also for ternary (i.e. alloyed) or even quaternary (e.g. alloyed contacts on SiC) systems. The lack of high-quality thermodynamic data renders it impractical to quantitatively analyse (or even predict) effects such as texture, texture inheritance and the occurrence of a critical thickness. This deficit in the literature can be filled in through established techniques such as XRD and TEM, which allow to determine some of the unknown parameters. In appendix A of this work, we report on the coefficients of thermal expansion for several silicide and germanide phases. Furthermore, Kousseifi *et al.* recently published on the phase formation enthalpies and interfacial energy [2] of the nickel silicide system. New cutting-edge technologies allow novel approaches to determine some of these parameters. For example, during the course of this thesis, we have acquired an *in situ* pole figure data-set which covers the phase (and texture) sequence of the Co, Ni, Pd, Pt and Ti silicide and germanide systems. Unfortunately, a detailed analysis of these data could not be completed within the time frame of this work due to the large quantity of data. This dataset should definitely be picked up and analysed in the near future, as it would be highly interesting to evaluate possible texture inheritance. Further development of the *in situ* pole-figure technique could be considered in the future, for example to determine the texture-dependent growth-parameters of the forming phases.

Silicide research is now exploring the next contact material for future devices. The use of silicides for future CMOS devices will strongly depend on the device architecture and characteristic dimensions. The finFET design was only a first step into 3D-structures. Nanowire-based devices (e.g.

tunnel-FET, gate-all-around FET) furthermore optimize the architecture of a transistor device. As the confinement of the contact material in one or more dimensions is clearly altering the phase sequence, it is yet an open question how the solid-phase reaction of silicides will alter in these 1D-confined environments. Besides the use of silicides at the source and drain terminals of the transistor, the compound can potentially also prove valuable further back-end-of-line. Cu via's, which are currently being used for the interconnect lines in transistor devices, have a mean free path of electrons of the order of $\approx 40\,\mathrm{nm}$. A reduction of the interconnects' width will eventually scale to this order-of-magnitude. When this happens, the surface and interface scattering will dominate the overall parasitic resistivity of the Cu interconnect. It is recently proposed [3, 4] that silicide interconnects with low sheet resistance and lower mean-free-path for the electrons (e.g. NiSi) are a potential candidate to replace Cu as the conductive material for the narrowest interconnect lines. The investigation of solid-state contact materials therefore provides ample of open questions and opportunities to be revealed by the material researcher.

Part V

APPENDICES

A

ARTICLE V: ANISOTROPIC THERMAL EXPANSION OF NI, PD AND PT GERMANIDES AND SILICIDES

Silicon or germanium-based transistors are nowadays used in direct contact with silicide or germanide crystalline alloys for semiconductor device applications. Since these compounds are formed at elevated temperatures, accurate knowledge of the thermal expansion of both substrate and the contact is important to address temperature depending effects such as thermal stress. Here we report the linear coefficients of thermal expansion of Ni, Pd and Pt-based mono-germanides, mono-silicides and di-metal-silicides as determined by powder-based X-ray diffraction between 300 and 1225 K. The investigated mono-metallic compounds, all sharing the MnP crystal structure, as well as Pd_2Si and Pt_2Si exhibit anisotropic expansion. By consequence, this anisotropic behaviour should be taken into account for evaluating the crystal unit's cell at elevated temperatures.

A.1 INTRODUCTION

In current field-effect transistors, the source and drain regions are contacted by forming a silicide or germanide thin film for respectively silicon or germanium-based devices. These silicide and germanide films are conventionally formed by first depositing a metal film on top of the semiconductor substrate. During subsequent annealing, the metal film transforms into the desired crystalline phase at a certain temperature, typically between 600−1100 K, after which the film is cooled to room temperature. This process will introduce a thermal stress if there is a mismatch at the interface between the substrate and the thin film due to a difference in thermal expansion between these two materials. This stress can severely influence the performance of the transistor [1]. Therefore, accurate knowledge of the Coefficient of Thermal Expansion (CTE) is necessary to evaluate or simulate this thermal stress during the growth process or in the final device.

The CTE has been investigated previously for those silicides which were technologically relevant in the past, such as $TaSi_2$, $TiSi_2$, $CoSi_2$, $NiSi_2$ and NiSi [2–7]. Some of these studies show that these silicides sometimes exhibit anisotropic expansion, where a significant difference in thermal expansion is observed between different lattice parameters of the same unit

Table A.1: List of the investigated powder samples.

POWDER NAME	LATTICE	S.G.	JCPDS PATTERN
NiSi	Orthorhombic	Pnma	03-065-1475
PdSi	Orthorhombic	Pnma	03-065-1481
PtSi	Orthorhombic	Pnma	01-071-0523
δ-Ni_2Si	Orthorhombic	Pbnm	00-048-1339
Pd_2Si	Hexagonal	P-62m	00-006-0559
Pt_2Si	BC-tetragonal	I4/mmm	00-017-0683
NiGe	Orthorhombic	Pnma	03-065-1478
PdGe	Orthorhombic	Pnma	01-089-7085
PtGe	Orthorhombic	Pnma	03-065-1485

cell. An example of such a silicide is orthorhombic NiSi, where the smallest unit cell axis is known to contract whereas the two other axes expand upon heating [4–6]. By consequence, a systematic study of the thermal expansion should distinguish between the different plane directions of the investigated crystal.

Furthermore, the literature shows that some of the cited studies investigated the crystal as a thin film while others used a powder-based methodology. Although these silicides and germanides are used and formed in transistor-based technology as a thin film, using such an approach for the investigation of the thermal expansion of the crystal should not be preferred. This is due to the strain which is introduced at the interface between film and substrate, which can locally alter the observed lattice parameters of the studied crystal. A direct measure of the silicides' or germanides' intrinsic CTE therefore requires a powder-based approach instead of a thin-film approach.

This study presents a systematic powder-based evaluation of the CTE for several technologically relevant silicide and germanides phases by *in-situ* X-Ray Diffraction at elevated temperatures. A selection was made for the Nickel-group (Ni, Pd, Pt) mono- and bi- metallic silicides and mono-metallic germanides (Table A.1). This set includes the currently preferred materials for local contacting on both Si and Ge substrates [8, 9]. Additionally, the mono-metallic phases all share the orthorhombic MnP-type structure, so the observed anisotropy can be evaluated within this crystal structure in a systematic way. The di-metallic silicides were included as they are formed just prior to the formation of mono-metallic silicides

during the heating process, and are then important to evaluate the strain during the formation of these mono-silicides.

A.2 EXPERIMENTAL METHOD

To determine the CTE of the crystal phases under investigation, three steps were performed and are described in the following paragraphs. Powder samples were first manufactured in the desired crystalline phase. These powders were subsequently loaded in an annealing chamber equipped for *in situ* X-Ray Diffraction (XRD) measurements at elevated temperatures. The measured diffraction pattern, recorded for every 50 K, were finally analysed to determine the lattice parameters of the crystalline phase.

Fabrication of powder samples

As described in the introduction, powder samples were used so that the compounds could expand freely without being hindered by geometric constrains due to the presence of a substrate. To manufacture such powders, bulk metal was heated with the semiconductor material in the appropriate mass ratio ($\pm\ 1 \cdot 10^{-3}\ g$) in an arc furnace. After evacuating the furnace to $3.5 \cdot 10^{-5}$ mbar, the chamber was flushed five times after which it was filled with Argon, resulting in a chamber pressure slightly higher than one atmosphere. The remaining oxygen in the chamber was then absorbed by first melting Zr, prior to the meting of the silicide/germanide compounds. This procedure was repeated after rotating the sample, five times in total. To remove any inhomogeneity in the samples, the samples where subsequently annealed for three days at high ($\geq$ 800 K) temperatures to obtain a homogeneous compound.

These samples were then crushed to a powder in an agate mortar until the grain sizes were smaller than 200 µm, as verified with secondary electron microscopy. The purity of the resulting powder was checked by Energy-dispersive X-ray spectroscopy and the crystalline composition by XRD powder diffraction. Although several secondary phases are detected (Table A.2), the diffraction intensity of these phases is less then one fifth of the desired phase. Oxygen was the only foreign element to be detected in two compounds: PdGe and PtGe. The other secondary phases indicate that the used metal/semiconductor mass ratio resulted in the co-formation of neighbouring phases in the metal-semiconductor phase diagram. The formation of neighbouring phases is the highest for the PdSi and the NiGe samples. The difficulty of forming such a pure compound can be explained by their binary phase diagrams [10]. During the forma-

Table A.2: List of detected compounds from XRD patterns and the XRD peak intensity of the contaminant, relative to the targeted phase.

COMPOUND	SECONDARY PHASE	REL. XRD INTENSITY (%)
NiSi	Ni_3Si_2	9
PdSi	Pd_2Si	17
PtSi	not detected	–
δ-Ni_2Si	not detected	–
Pd_2Si	Pd_3Si	8
Pt_2Si	$Pt_{12}Si_5$	6
NiGe	Ge	19
	$Ni_{2.75}Ge_2$	3
PdGe	Pd_2Ge	9
	GeO_2	17
PtGe	GeO_2	6

tion of PdSi, the sample is cooled below the eutectoid point, meaning that it is metastable when cooled from 1097 K to room temperature [11]. The second compound with a relatively high diffraction contribution of secondary phases, NiGe, does not have a congruent formation point but has a peritectoid point. As a consequence, the NiGe line phase is not directly formed from a liquid state but needs to be formed from a two-phase equilibrium, which also increases the probability for remaining neighbouring phases.

In-situ study of heated compounds

The powders were annealed in a helium atmosphere from room temperature to high temperatures (between 925-1225 K, depending on the crystal phase's eutectic point). The anneal was performed stepwise every 50 K and at each step an XRD measurement was performed. One single XRD-scan covered diffraction angles between $2\theta = 20 - 80°$ using a CuK_α source in steps of 0.08° (Bruker D8 diffractometer). During the heating, the height of the sample changes due to thermal expansion of the sample holder. This effect was taken into account by first calibrating the height at each temperature by heating a silicon reference powder. The difference between the measured Si peak position and the theoretical value at the same temperature [12] allowed us to calculate the change in sample alignment

Table A.3: List of XRD peaks used to fit the lattice parameters of all systems

POWDER	PLANES			
NiSi	(0 1 1)	(2 0 0)	(2 1 0)	(1 0 3)
PdSi	(2 0 2)	(2 1 1)	(0 1 3)	(0 2 0)
PtSi	(2 1 1)	(1 1 2)	(2 0 2)	(0 1 3)
δ-Ni_2Si	(0 1 1)	(1 1 2)	(2 1 0)	(2 0 3)
Pd_2Si	(1 1 0)	(3 0 0)	(0 0 2)	(2 1 2)
Pt_2Si	(0 0 2)	(1 1 2)	(2 2 0)	(1 1 4)
NiGe	(2 0 1)	(2 1 0)	(1 1 2)	(1 0 3)
PdGe	(1 1 2)	(2 0 2)	(2 1 1)	(0 2 0)
PtGe	(1 0 2)	(1 1 1)	(1 1 2)	(2 0 2)

and thus correct for changes of the sample height at all measurements temperatures.

From these diffraction measurements, four diffraction peaks were carefully selected for each investigated phase in order to evaluate the crystalline lattice. The selected peaks needed to have a high diffraction intensity and should be isolated from other peaks for all measured temperatures, including peaks originating from the low-intensity secondary phases. Each plane's diffraction angle was determined with a Gaussian fit, after which the lattice parameters were determined with a least-square fitting for the four selected diffraction peaks. This methodology is explained more in detail in the following section for the NiGe powder.

A.3 RESULTS AND DISCUSSION

We first present a detailed investigation of the NiGe phase as an example of the followed procedure. NiGe was chosen for this purpose since it allows us to compare our results with those of Perrin *et al* [6]. This comparison will confirm that the methodology is reliable and that the secondary phases present in our samples do not severely influence the obtained results. This case study is then followed by the obtained results for all selected phases.

A.3.1 *Case study: NiGe*

The powder diffraction of NiGe at room temperature (Fig. A.1) shows several high-intensity XRD peaks. However, not all of these peaks are usable

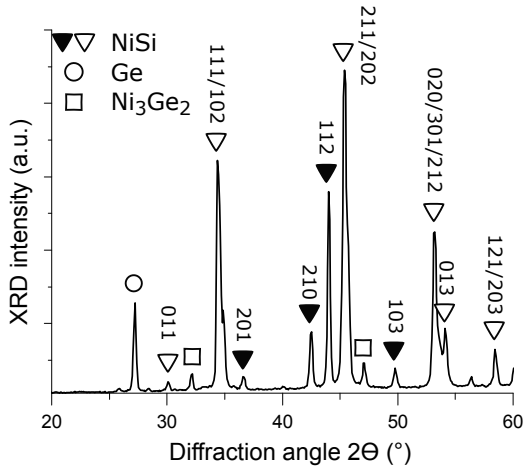

Figure A.1: All observed diffraction peaks for the fabricated NiGe powder are identified, including some diffraction from secondary phases (Ge and Ni_3Ge_2). NiGe (2 0 1), (2 1 0), (1 1 2) and (1 0 3) have a sufficient diffraction intensity and were selected for the calculation of the CTE.

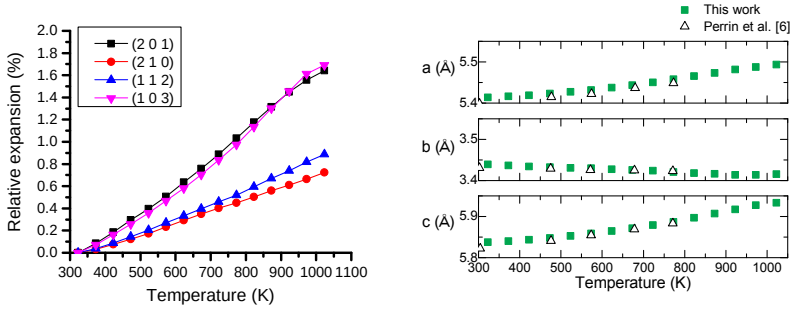

Figure A.2: **(left)** The relative change in interplanar distance ($d_{hkl}(T)/d_{hkl}(T_0)$) as a function of temperature of four different NiGe planes. These distances allowed to evaluate the lattice parameters by applying a least-square fit **(right)**.

for the evaluation of the lattice parameters, since some of them overlap (partly) with other peaks. In fact, the criteria that the peaks should be isolated results in the following usable diffracting planes: (0 1 1), (2 0 1), (2 1 0), (1 1 2), (1 0 3). The four peaks with the highest value in 2θ were selected for further evaluation, since a higher diffraction angle corresponds with a better resolution of the interplanar distance.

The spacing of the selected crystalline plane are then determined for every 50K up to 1023K, as illustrated in Fig. A.1a. We observe that the (2 1 0) & (1 1 2) planes have a significantly slower expansion than (2 0 1) & (1 0 3), which we can understand since the *b*-axis of the NiGe structure is known to contract instead of expand, thus limiting the expansion of (2 1 0) & (1 1 2). Based on these four interplanar distances, a least-square fitting procedure allowed us to evaluate the three underlying lattice parameters of NiGe. This fitting procedure results in the values of 5.41, 3.44 and 5.83 Å at room temperature for resp. the *a*, *b* and *c* parameter, which is within 0.02 Å precision when compared with the reported value (JCPDS 03-065-1478). Fig. A.1b displays the obtained values for the complete measured temperature window, which is also within 0.02 Å in confirmation with the work of Perrin *et al* [6]. The error on these lattice parameters was calculated to be maximum 0.015 Å, which is smaller than the used markers. This value was obtained by including the 2θ step-size and a variety in sample height due to sample displacement. The latter effect was assessed to the size of a powder grain (i.e. 200 µm).

In the following paragraph, we report the *a*, *b* and *c* values for all studied phases. From these values, we then determine the CTE of all studied samples.

A.3.2 *Determination of the coefficients of thermal expansion*

Figures A.3, A.4 and A.5 display the calculated values of the lattice parameters of resp. the studied monosilicides, monogermanides and dimetalsilicides for all measured temperatures. Similar to what we noticed for NiGe, the values at room temperature are comparable with the reported values in the literature, with a maximum deviation of only 0.02 Å. The error on the obtained values is smaller than the used markers. For those phases where literature provides powder-based data for elevated temperatures, the data at elevated temperatures was also in agreement with our measurements (NiSi, PtSi, NiGe and PtGe [6, 7]).

A linear coefficient of thermal expansion γ_a was fitted with the obtained lattice parameters through

$$a(T) = a_0\,(1 + \gamma_a(T - T_0))$$

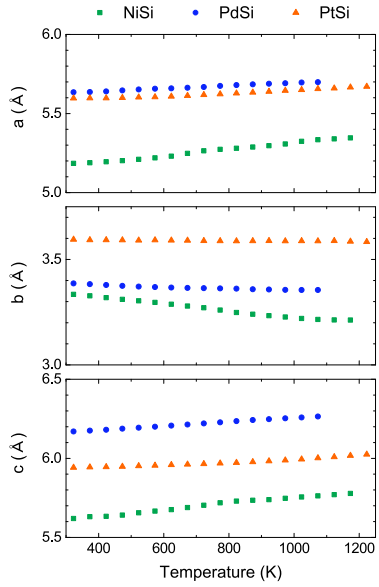

Figure A.3: Evolution of the lattice parameters of NiSi, PdSi and PtSi

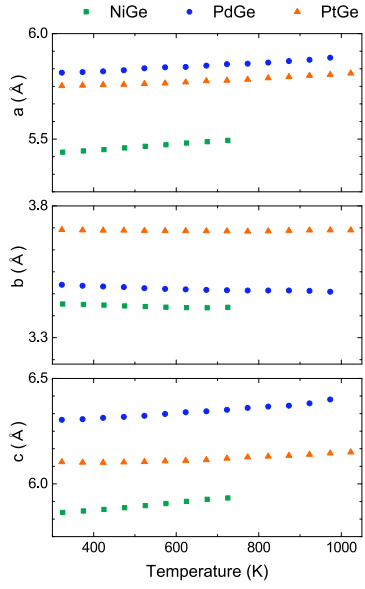

Figure A.4: Evolution of the lattice parameters of NiGe, PdGe and PtGe

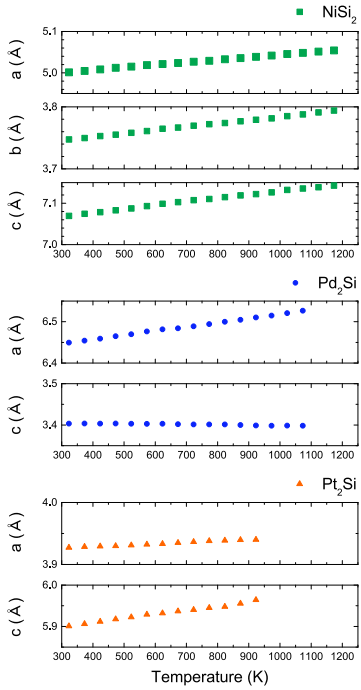

Figure A.5: Evolution of the lattice parameters of Ni_2Si, Pd_2Si and Pt_2Si

Table A.4: Linear coefficient of thermal expansion γ for each lattice parameter and of the unit cell's total volume. All values are in units $ppm\ K^{-1}$.

	γ_a	γ_b	γ_c	γ_V	
NiSi	40	-47	35	29	This work
	45	-47	40		[6]
PdSi	16	-12	21	25	This work
PtSi	16	-2	15	29	This work
	13	-1	16		[7]
Ni_2Si	12	14	12	39	This work
Pd_2Si	16	–	-2	29	This work
Pt_2Si	6	–	17	28	This work
Si	4	–	–	12	[12, 13]
NiGe	22	-11	25	36	This work
	20	-5	23		[6]
PdGe	18	-11	22	30	This work
PtGe	14	0	12	27	This work
	6	1	7		[7]
Ge	7	–	–	21	[13]

where a_0 is the lattice spacing at $T_0 = 298K$. The obtained values are reported in Tab A.4. The fitted curves for $a(T)$ had a maximum deviation with the experimentally calculated lattice parameters of 0.01 Å, so a linear temperature dependence is sufficient to explain the observed behaviour and no second-order approximation for the CTE is required. For those phases where a comparison is possible with reported values of γ, the obtained values are in reasonable agreement with the literature. A larger deviation for the value of γ is found for PtGe compared with the values from ref. [7]. However, the difference in lattice parameters is limited to 0.02 Å. It is interesting to note that the anisotropic expansion of PdGe and Pd_2Si is in confirmation with the qualitative observations of previous studies [8, 14].

The obtained CTE indicate that anisotropic expansion is present in all measured MnP-type lattices and also for Pd_2Si and Pt_2Si, whereas no anisotropy is observed for Ni_2Si. Although some of the CTE are negative, the thermal expansion of the unit cell's *volume* γ_V, defined as $V(T) = V_0\,(1 + \gamma_V(T - T_0))$, is always positive.

In order to explain the anisotropic expansion of the MnP-lattices, it is suggested in some studies that this would result from a tendency of the MnP to evolve towards a NiAs-type structure [7]. The MnP lattice is only slightly different from hexagonal NiAs, with the following conversion of lattice parameters: $a_{MnP} = c_{NiAs}$, $b_{MnP} = a_{NiAs}$ and $c_{MnP} = \sqrt{3}a_{NiAs}$, although local atomic displacements are also necessary. Several MnP-NiAs phase transformations are reported for a large group of materials [15–18], and a study by Graeber et al. [7] suggests that the same transition is occurring for PdSi, PdGe, PtSi and PdGe. This thesis would imply that $\sqrt{3}b_{MnP}/c_{MnP}$ would converge towards unity as the structure is gradually evolving towards a NiAs-type structure during heating. As seen in Fig. A.6, the only compounds where $\sqrt{3}b_{MnP}/c_{MnP} \approx 1$ are NiSi and NiGe, where NiSi temporarily obtains this value and does not show any relaxation, in confirmation of the results of Perrin et al.[6]. This indicates that a transformation towards a NiAs-type structure does not occur and does not explain the observed anisotropy. Evaluating a_{MnP}/c_{MnP} as a function of temperature indicates that this ratio remains constant through the full temperature window, implying that these two axis expand isotropically, which is also indicated by the similar values for γ_a and γ_c.

Although we can not provide an explanation for the observed anisotropy or negative expansion coefficient for some of the compounds, a few trends are revealed by these measurements for the compounds sharing the MnP-structure. First, the linear thermal expansion coefficient is negative, or close to zero, for the small axis parameter for all measured MnP-com-

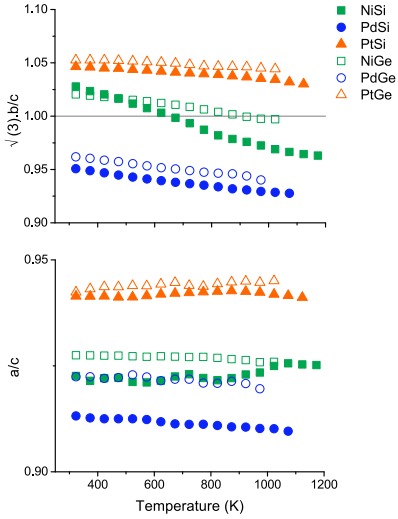

Figure A.6: If the studied MnP-structured phases would exhibit a tendency to evolve towards a hexagonal NiAs-structured phase during heating, then the ratio $\sqrt{3} \cdot b/c$ **(top)** would converge to unity and the ratio a/c **(bottom)** would remain constant. Although the latter is valid, the first condition is only true for NiGe.

Table A.5: The anisotropy of the thermal expansion, represented by the ratio $\gamma_b/\bar{\gamma}$ for all studied MnP-type structures.

	Ni	Pd	Pt
Si	-4.9	-1.4	-0.2
Ge	-0.9	-1.1	0.0

pounds resulting in an anisotropic lattice expansion. Substituting Si with Ge results in a significantly lower CTE for Ni whereas Pt and Pd-containing alloys have comparable CTE for silicides and germanides. Substituting the metallic component, Ni, Pd or Pt, gives the highest absolute value for CTE for Ni and the smallest for Pt. The anisotropy of the expansion, studied by the ratio $\gamma_b/\bar{\gamma}$ (Table A.5), follows the same trend. As such, this suggests that the thermal expansion is mostly dominated by the metal. The same trends concerning Si/Ge or Ni/Pd/Pt were previously observed in the calculated Young modulus of the studied MnP-structured phases [19]. It is interesting to note that it is rare to observe both a high CTE and a high elasticity modulus, as one is usually inversely proportional to the other.

Comparing the CTE of the film with those reported values of bulk Si or Ge enables to estimate the changing displacement mismatch, proportional to $\Delta\gamma\Delta T$, at a heterogeneous interface between a silicide (or germanide) film on top of a Si (or Ge) substrate. This difference is higher for silicides than for germanides. In order to estimate the stress development on this interface, one should also take into account elastic moduli of the material. Ab-initio calculations by Connétable *et al.*[19] show that germanides have a smaller Young modulus. Both the Young modulus and CTE thus indicate that the extrinsic thermal stress would be lower for germanides than for silicides, and the highest for Ni-containing compounds. However, a preferred orientation of the germanide or silicide film could still severely alter the extrinsic thermal stress due to the anisotropy in both the CTE and the Young modulus. An experimental study on the effect of crystalline texture on the resulting thermal stress for MnP-germanides and silicides would therefore be interesting.

A.4 CONCLUSIONS

The linear coefficient of thermal expansion are determined for Ni, Pd and Pt-based mono-germanides, mono-silicides and di-silicides for each of the lattice parameters. Anisotropic expansion is observed for all studied phases with the exception of Ni_2Si. As the mono-germanides and mono-silicides all share the same MnP-structure, the observed trends within the same crystal structure are discussed and are highly similar to reported values of the elastic modulus of the compound. The observed results enable to evaluate thermal stress between film and substrate. The anisotropic thermal expansion indicates that the thermal stress would depend on the preferred crystalline orientation of the film.

B

X-RAY DIFFRACTION AND POLE FIGURE MEASUREMENTS

X-ray diffraction (XRD) is without a doubt one of the most important techniques for solid-state material research. The majority of the discussed experimental data in this thesis was obtained through diffraction measurements. In this appendix, we provide a brief overview on the conducted XRD-based experiments. In paragraph B.1 we elaborate on the fundamental concepts of X-ray diffraction, and why a standard XRD measurement will not always include all the diffraction peaks that are expected for silicide films. A more complete image can be acquired through full-reciprocal XRD *pole-figures* measurements.

In order to increase the time efficiency of such experiments, we have acquired XRD data with several types of detectors and set-ups. The practical implications on selecting either a point detector, a linear detector or an area detector are explained in paragraph B.2. The fastest measurements were performed by using an area detector in combination with the *fly-by* acquisition methodology employed at the DiffAbs beamline of the SOLEIL synchrotron. This resulted in an large number of pole-figure datasets. The total number of datasets in this thesis alone exceeds over one hundred, and their analysis is a time-consuming task. In paragraph B.3, we elaborate on possible plotting strategies for a fast and efficient assessment of the data. To this end, we have employed a so-called *diffracted intensity contour map* plots for the initial analysis of the pole figure datasets. These diffraction maps were previously introduced by Gaudet *et al.* [1] with the aim for a fast initial evaluation of the huge amount of diffraction data for a single sample. We have further expanded this plotting technique so it allows a better assessment of the different textures.

B.1 INTRODUCTION TO POLE-FIGURE XRD

The first experimental observation of X-ray diffraction occurred in 1912 by von Laue *et al.* [2], 16 years after the introduction of X-rays in laboratory set-ups by Röntgen. The discovery by von Laue allowed to measure on the nano-meter length scale and to determine the distances between atoms within a crystal. Von Laue received the Nobel prize in physics only two years after this publication. However, calculating the crystal lattice

spacings through von Laue's formulae was an exceedingly complicated task for it included numerous unknown quantities. In 1913, W.H. and W.L. Bragg reported on a rather simple mathematical expression which relates the observed diffraction angle θ (i.e. half of the angle between the incidence x-ray beam and the diffracted beam) and the inter-planar spacing d of crystal lattice through what now is known as *Bragg's law*:

$$2d \sin\theta = n\lambda, \tag{B.1}$$

where λ represents the wavelength of the incidence x-rays and n is a positive integer. The discovery by father and son Bragg allowed to quantify the crystalline structure at the sub-nanometer scale. Their research was honoured by a Nobel prize nomination in 1915. The simple formulation has led to a revolution in the analysis of crystal structures by means of X-rays.

The most commonly-used experimental methodology is the so-called $\theta/2\theta$-measurement in which a monochromatic X-ray beam hits the sample at an angle θ, while the detector is positioned at an angle 2θ with respect to the incidence beam (Fig. B.1a). The recorded intensities as a function of angle θ (or 2θ) then represents a single diffractogram. Peaks of higher intensity at specific angles 2θ indicate that the specimen contains atomic planes which are separated by a distance d, as calculated through Bragg's law. The position of these diffraction peaks is unique for every crystal structure, and allows to identify the lattice similar to a fingerprint on a crime scene investigation (CSI). For example, figure B.1b displays the diffractogram of a NiSi powder. Deviations from the room-temperature lattice spacings are often observed, and are related to a contraction or expansion of the crystalline lattice. In their original publication, W.H. and W.L. Bragg showed the influence of heat on the lattice spacings. Other effects may also cause deviations of the lattice spacings, e.g. a strained crystal or a compositional variation.

The acquired diffraction intensities from a $\theta/2\theta$ scan originate only from crystal planes which are oriented parallel to the samples' surface, i.e. perpendicular to the plane determined by the incident X-rays and the observed diffracted beam. For crystalline powders, which consist of a collection of randomly-oriented grains, this characterization method is sufficient, since every lattice plane will satisfy this condition in some of the crystal grains. However, for a textured film the crystalline grains have a strong preferential orientation with respect to the epitaxial substrate. Depending on the specific alignment, not every lattice plane will be oriented parallel to the samples' substrate, and as such certain diffraction peaks will be absent.

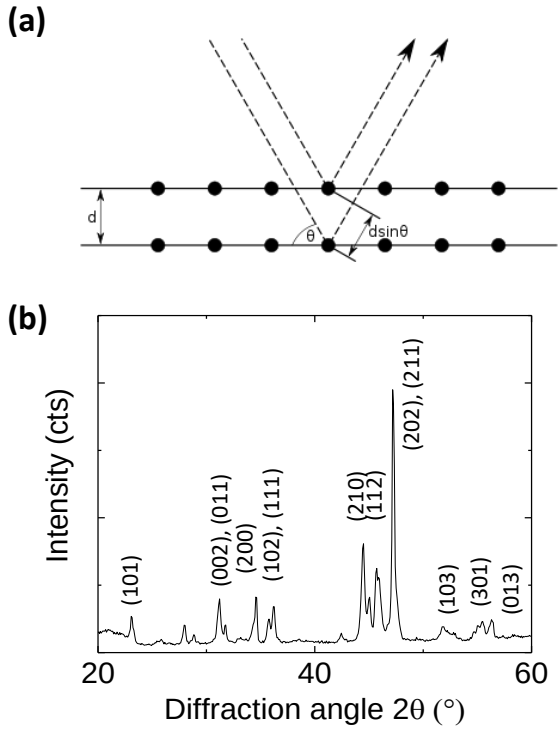

Figure B.1: **(a)** Illustration of the application of Bragg's law, with d the interplanar spacing and θ the diffraction angle. **(b)** XRD pattern of a NiSi powder ($\lambda = 0.154\,\text{nm}$).

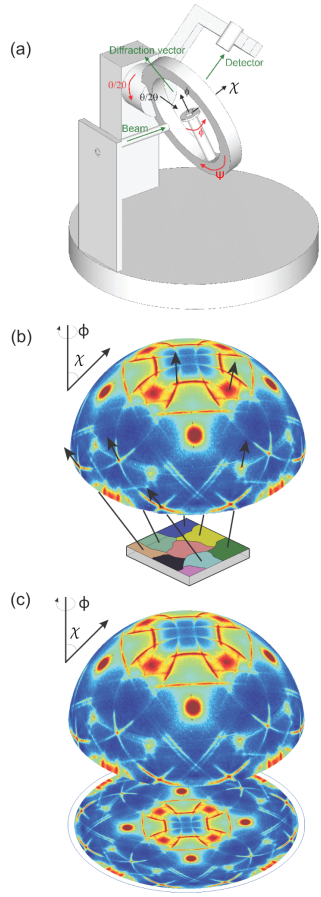

Figure B.2: **(a)** Illustration of a four-circle diffractometer used in the Schulz method. The different relevant angles χ, ϕ and θ are depicted along with the corresponding rotation directions. **(b)** The distribution of the recorded intensities (with red corresponding to the highest intensity) as a function of the sample's orientation χ, ϕ can be represented on a imaginary hemisphere by marking the intersection of the normals of the diffracting planes that fulfil the Bragg condition at that orientation. **(c)** These intensity distributions are projected on a 2D surface. This *pole figure* then represents the statistical distribution of the orientation of a specific family of $\{hkl\}$ planes. Figure from [3].

XRD pole figures are measured in order to overcome this limitation. Pole figures allow to gain statistical information about the orientation of a collection of crystal grains. A commonly-used geometry is based on the Schulz method [4] and was introduced in 1949 (Fig. B.2). The sample is placed on a four-circle diffractometer which allows to tilt the sample along the inclination angle χ[1] and rotate along the azimuthal angle ϕ. The angle 2θ between the incidence X-ray beam and the position of the detector determines which crystalline plane is being measured and remains fixed for a single pole figure. This pole figure then displays the diffraction intensity of this particular plane for every orientation of the sample in terms of χ and ϕ. The recorded intensity increases when a larger volume of the crystal is diffracting, and therefore the intensity distribution displayed in a pole figure correlates with the statistical distribution of the plane's orientations. The combination of several pole figures, each containing information of one specific crystalline plane, allows to identify the governing preferential alignments of the crystalline grains. In silicide films, this alignment is then described with respect to the orientation of the underlying silicon substrate.

B.2 POINT DETECTORS, LINEAR DETECTORS, AREA DETECTORS

The measurement of a single pole figure is not sufficient to identify the preferential orientation of the ensemble of crystalline grains. Multiple pole figures are a necessity, where each pole figure corresponds to the orientation distribution of a different crystalline plane $\{hkl\}$. By using the Schultz method with a point detector, such acquisition is very time consuming. For example, experiments conducted at the X20A beamline of the NSLS with a point detector could easily take up to 6 hours per pole figure[2]. One can obtain a significant gain in time-efficiency by using a linear or an area detector instead. The different set-ups are displayed in figure B.3 and are explained in the following subsections.

Linear detectors

A linear detector can be positioned so that different pixels of the detector correspond to different diffraction angles 2θ with respect to the incident

1 Some publications denote this angle as Ψ instead

2 These high-resolution pole figures take discrete steps of 0.5 or 1.0° in both χ and ϕ, with a 1 s acquisition per step. The inclination angle χ ranges of 0 up to 90°, as an angle higher than 90° would require to measure X-rays in transmission of the specimen. The azimuthal angle ϕ depends on the symmetry of the silicon substrate (e.g. 90° for four-fold Si(001)-oriented substrate or 120° for three-fold Si(111)-oriented substrate).

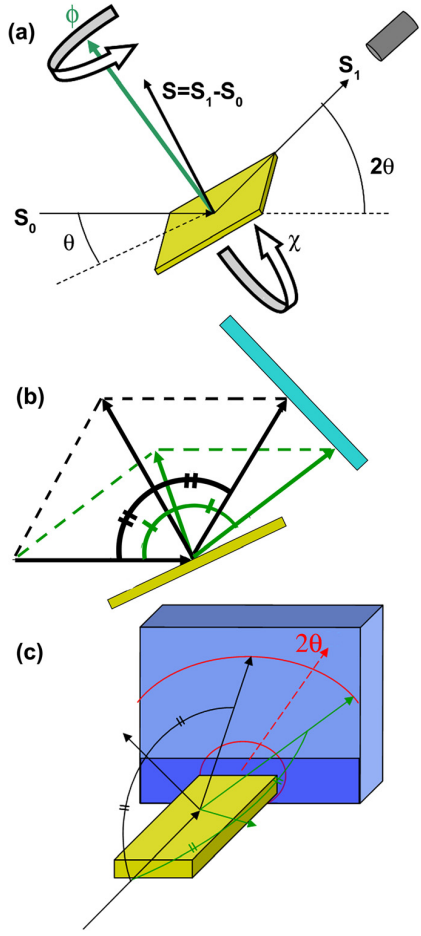

Figure B.3: Schematic representation of the incidence X-ray beam and the detected diffraction intensities for **(a)** a point detector, **(b)** a linear detector and **(c)** an area detector. Figure from [5].

X-ray beam (Fig. B.3b). Therefore, a linear detector allows to acquire the diffraction data over a semi-continuous range in d-spacings. A single experiment obtains the pole figures of several $\{hkl\}$ planes of the specimen *in parallel*. This set-up has the additional advantage that one does not need to know the exact phases present in the specimen. When working with a point detector, one needs to determine the specific 2θ angles at which a pole figure measurement will be interesting, which requires an assumption on the present crystal phases. As a linear detector covers a broad range of 2θ angles, such pre-requisite knowledge is not needed. Unfortunately, the different pixels will acquire diffraction from the sample at slightly altered angles χ and ϕ, despite the same position of the specimen. This is illustrated in figure B.3b, where the middle pixel of the detector (black) corresponds to a scatter vector which is perpendicular to the samples' normal (i.e. represent the diffraction of planes parallel to the samples surface). A higher or lower pixel (Fig. B.3b, green arrows) will deviate from this orientation and corresponds to the diffraction of planes that are slightly tilted with respect to the samples' surface. On a pole figure, the pixel indicated by the black arrow in figure B.3b would correspond to intensity at the center, whereas the green arrow would correspond to a point which is positioned somewhere at a concentric circle with a small radius near the center of the pole figure.

In situ XRD with a linear detector

The above allows to understand an important limitation of our conducted *in situ* XRD measurements. During *in situ* XRD, a linear detector simultaneously acquires the detection of several 2θ diffraction angles. This has the advantage that the formation and consumption of several crystalline phases, which each have diffraction peaks at different 2θ angles, can be monitored without altering the diffraction geometry. The linear detector records the diffraction intensities between e.g. $2\theta = 38°$ and $52°$ within half of a second. This fast acquisition allows to perform XRD measurements during an annealing experiment, and as such monitor the phase-formation sequence as a function of temperature. The diffraction detected by the linear detector is however limited to crystal planes which are oriented parallel with the sample's surface (or slightly tilted from this orientation). Therefore, textured phases are not always observed in these experiments. This limitation is illustrated in figure B.4, where an epitaxial ϵ-Ni_5Ge_3 phase is present during the *in situ* XRD measurement between 200 and 400 °C. In figure B.4a, the pixel at $2\theta = 42°$ corresponds to diffraction with $\chi = 0°$, i.e. diffraction from ϵ-Ni_5Ge_3 planes parallel to the samples' surface. The epitaxial phase is clearly present during the annealing. A tilt of

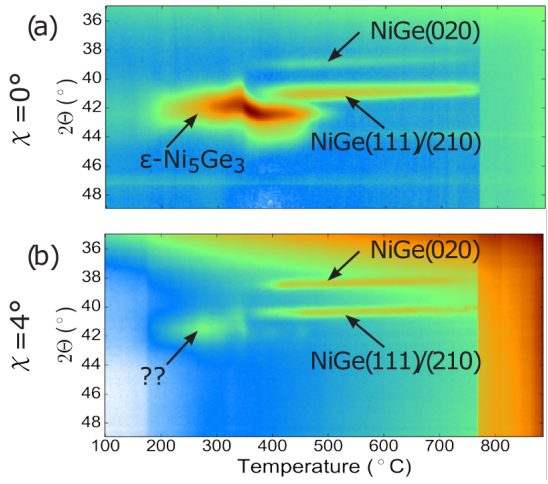

Figure B.4: *In situ* XRD data ($\lambda = 0.18\,\text{nm}$) recorded during annealing of a 30 nm Ni film on Ge(111) substrate. **(a)** Corresponds to data where the central pixel of the detector (i.e. 42°) corresponds to diffraction from planes parallel to the samples' surface. **(b)** The same sample was also measured while the substrate was slightly tilted, which clearly reduces the diffraction intensity of the intermediate ϵ-Ni_5Ge_3 phase. Figure from [6].

the samples' inclination angle χ by 4° with respect to the incidence X-ray beam is sufficient to avoid detection during these *in situ* XRD measurements (Fig. B.4b). The pixel at $2\theta = 42°$ now corresponds with diffraction originating from planes which are tilted by 4° with respect to the samples' surface. Due to the epitaxial nature of the ϵ-Ni_5Ge_3 phase, almost no crystalline planes have such inclined orientation, and the diffraction intensity is drastically diminished. *In situ* XRD data should therefore be interpreted carefully, as it clearly does not always reveal diffraction from all phases present within the specimen.

Area detectors

When using an area detector, the acquired data now contains several pixels which correspond to the same diffraction angle 2θ. These pixels follow an arc-shape on the detector, as illustrated in figure Fig. B.3c. Although these pixels share the same diffraction angle, they each correspond to a different angle in χ and ϕ. One must calculate the diffraction vector for each individual pixel and determine its corresponding orientation in the sample reference frame. The mathematical expressions for these calculations can be found in the literature [5, 7, 8].

A diffraction experiment drastically gains in time efficiency by replacing a point detector with a linear or an area detector. The use of a linear detector leads to the simultaneous acquisition of several pole figures of different 2θ values. As explained above, this reduces the total measuring time to acquire the pole figures of different crystalline planes. The use of an area detector also leads to a similar parallel acquisition in 2θ, and every 2θ value is monitored over a range of angles in χ and ϕ. The use of an area detector furthermore reduces the measuring time as less steps in χ and ϕ are required to obtain complete pole figures. The details of this transition are well-explained by Mocuta *et al.* [8]. In their paper, they combine the use of an area detector with a so-called *fly-scan* acquisition mode. Here, the sample stage moves continuously in ϕ during the experiment instead of moving sequentially in steps of 0.5°. The continuous movement avoids unnecessary motor acceleration and deceleration, and drastically reduces the dead time during the experiment. Depending on the angular acceptance of the detector (which is determined by its dimensions and distance to the sample), and the required range in χ and ϕ, one can now measure within a few minutes instead of a few hours.

In this work, we used an XPAD area detector [9–12] with a total size of approximately $75 \times 31\,\text{mm}$. The detector exist of two modules, each subdivided into 7 Si chips with a total of 560×240 pixels. The pixel size is

$130 \times 130\,\mu m$, except those pixels at the boundary between different chips or modules, which are $2.5\times$ larger in the direction perpendicular to the boundary. The detector allows to quantify X-ray intensities over a dynamic range of approximately 6 decades for exposures of 1 s. Although this range in sensitivity is impressive, the detector should still be protected from direct exposure of substrate diffraction peaks (e.g. the Si(220) peak) which can potentially destroy the detector due to the high synchrotron intensity. In this work, this was achieved by rotating the sample in ϕ at maximum rotation speed of the motor (approximately $4.4\,°/\,\mathrm{sec}$), thus limiting the photons per second per pixel while measuring near a substrate Bragg peak.

A *python*-based software package has been programmed as part of this thesis in order to transform the raw images of the area detector to usable XRD-pole figures in the following steps.

1. The integer x and y coordinates of each pixel is translated to the geometrical position on the detector, expressed in mm. This step also takes into account possible deviations in pixel sizes, which is the case for e.g. the XPAD detector where pixels at the edge of a detector module are doubled in size.

2. These geometrical positions on the detector are translated to the angular position of the pixel with respect to the laboratory reference frame, by taking into account the angular position of the detector with respect to the incidence X-ray beam.

3. The correct angles 2θ, χ and ϕ are calculated in the samples' reference frame, by taking into account the motor position of the sample with respect to the incidence X-ray beam.

These calculations are achieved for each pixel on every frame acquired by the area detector. In total, there are about 1530 images to analyse, which add up to a total of 1 GB raw data per measurement cycle. The total dataset is then merged, resulting in an array of average diffraction intensity as a function of 2θ, χ and ϕ. The code was drastically optimised and can do these calculation slightly faster than the acquisition time of 4.5 min on a modern desktop computer. The software therefore allows to monitor the acquired data in *real time* during the experiment and is available for the user community of the DiffAbs beamline.

In situ pole-figure measurements with a linear detector

The combination of synchrotron-intensity X-ray luminescence and an area detector ensures high-quality pole figures, even for very short acquisition

Figure B.5: The Anton-Paar DHS 800 heating chamber allows to anneal a sample up to approximately 800 °C while conducting X-ray experiments. The heater is covered by a polymer polyether ether ketone (PEEK) dome, which allows annealing in vacuum or in a gas ambient of chose.

times as described above. This enables *in situ* pole-figures measurements during annealing at a relatively slow ramp rate (e.g. 2 °C min^{-1}, thus obtaining one pole figure every 5 °C). Through these measurements, one can identify all formed crystalline phases, and their preferred alignment, during the solid-phase reaction, even if these phases are strongly textured (e.g. epitaxial).

The DiffAbs beamline of synchrotron SOLEIL uses an Anton-Paar DHS 800 heating chamber (Figure B.5). The polymer dome is semi-transparent for X-rays, although it lowers the signal-to-noise ratio of the measured X-ray intensities. The set-up described above has been tested with the aim to obtain pole-figure data during the silicide phase formation reported in Chapter 5. Due to the low thickness of our initial Ni films (3 or 9 nm), we first examined the quality of the pole figures in the annealing set-up with and without a PEEK dome. To this end, we measured an *ex situ* pole figure from a 3 nm Ni(10 % Pt) film on top of Si(001) which was quenched at 850 °C. This particular sample contained both epitaxial and axiotaxial features, as displayed in figure 5.2*d-iv*. The resulting pole figures, displayed in figure B.6, were averaged over three subsequent *ex situ* measurements. Even though this ensured a better signal-to-noise ratio, the axiotaxial lines were not clear when we measured with the PEEK dome. Note that, despite the small thickness, the epitaxial peaks were clearly visible. To improve the statistics, we could have averaged over more measurements[3], and hence increase the measurement time, which would lower the temperature resolution during the *in situ* measurements to less than one pole figure every

3 A decrease of the rotation speed would also improve the measurement quality, but this would potentially destroy the detector due to the diffraction peaks of the Si substrate.

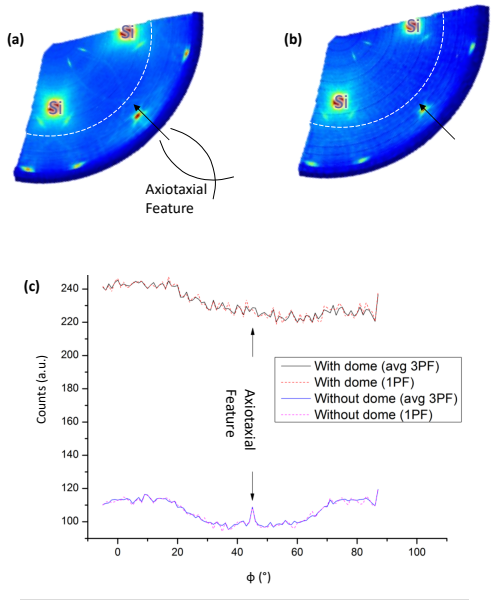

Figure B.6: The average of three pole-figure measurements of a 3 nm Ni(10 % Pt) film on top of Si(001) which was quenched at 850 °C **(a)** without PEEK dome and **(b)** with PEEK dome. **(c)** displays the intencity along the concentric circle indicated by the dashed white line in (a) and (b). The arrow indicates the position of an axiotaxial diffraction feature.

25 °C. Instead, we measured on quenched samples *ex situ*, resulting in a full set of pole figures every 25 °C in the temperature region of interest. The analysis of the pole figures reveals that this approach was not perfect: the *in situ* XRD measurement of figure 5.1a clearly shows a change in diffraction at 320 °C, as indicated by the θ-Ni_2Si peak around $2\theta = 56°$. No similar drastic trend in diffraction can be identified in our *ex situ* pole figure measurements near this temperature. We relate this deficiency to the low resolution in quenching temperature, thus potentially missing phases and textures that occur in a short temperature range. This latter example illustrates the potential of *in situ* measurements, where the continuous acquisition during annealing would ensure the observation of such fast phase transformations.

B.3 PLOTTING OF POLE FIGURES

The novel developments in synchrotron-based pole figure acquisition have resulted in a significant reduction of the measuring time. One of the consequences is that the subsequent analysis of an individual pole figure has to go faster in order to reduce the cycle-of-learning of an experiment. For example, in chapter 5 we have measured pole figure datasets for over 100 samples. As every dataset covers a semi-continuous range in 2θ, the total number of pole figures to analyse is quite substantial. Different approaches are possible in order to reduce the workload to analyse the dataset.

Powder diffractogram: $I(2\theta)$

In a first approach, one can average every pole figure over χ and ϕ (Fig. B.7a). A pole figure is then converted to a single number which represents the average diffraction intensity at the specific value 2θ of the pole figure. As the dataset contains a pole figure for every value of 2θ within the range of the detector, the result is a simulation of a powder-like diffractogram. The diffractogram now lacks any information regarding texture, but can be used for easy phase identification based upon the position of diffraction peaks. These intensity curves now also include diffraction of epitaxial phases, which would not be the case for a standard $\theta/2\theta$ measurement of a textured sample. This means that the diffraction of the epitaxial Si substrate is also part of this diffractogram, for which the high intensity sometimes hinders the observation of diffraction peaks occurring from phases with lower intensities. The results of plotting a powder-like diffrac-

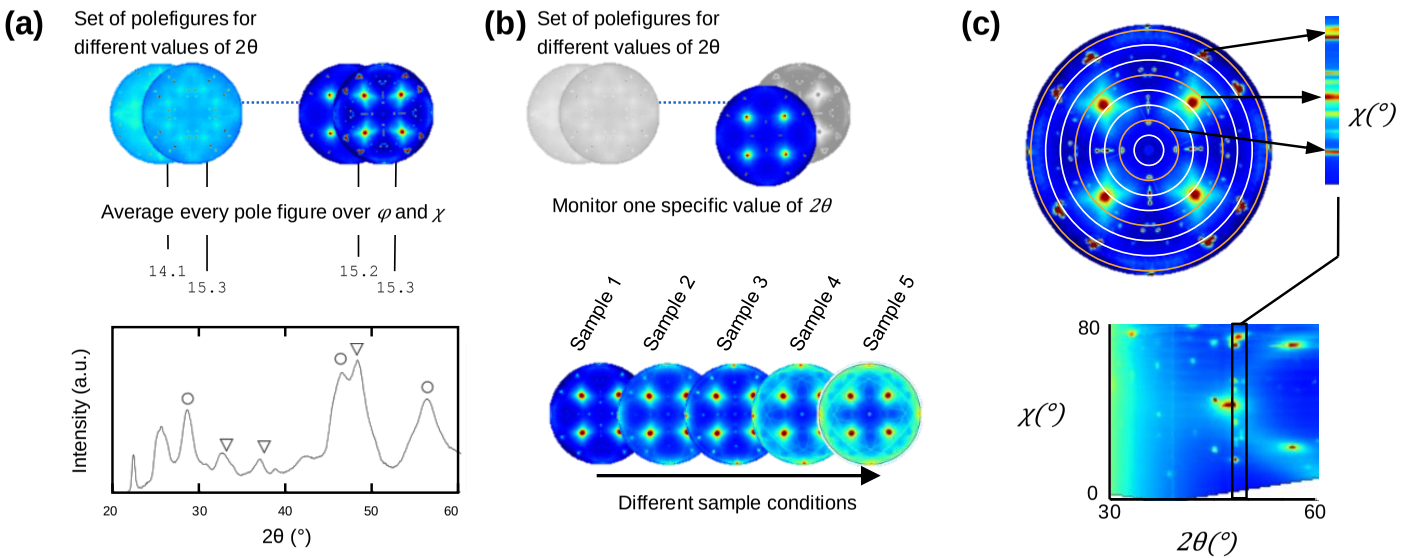

Figure B.7: A single pole-figure dataset contains one pole figure for every 2θ value within a specific range in 2θ. Several approaches are possible to enable an efficient initial analysis of the measured sample. **(a)** By averaging over χ and ϕ for every 2θ value, one obtains a single diffractogram of the sample which allows easy phase identification. **(b)** In some experiments, it is sufficient to only investigate those pole figures at a specific angle of 2θ, in which case the dataset is also drastically reduced. **(c)** By averaging the acquired diffraction intensity over ϕ for every angle χ and χ, one can construct diffraction intensity contour maps.

tion pattern can be seen throughout this thesis, e.g. in figures 4.7, 6.3 and 6.5.

Select a single pole figure: $I(\phi, \chi)$

For specific experiments, it can be sufficient to select one or several values of 2θ and only analyse those particular pole figures (Fig. B.7b). For example, if the goal is to compare the texture of a specific phase for different sample conditions (e.g. alloying concentration, annealing temperature, substrate orientaton), or if several phases diffract at roughly the same 2θ angle e.g. as is the case for figures 5.2 and 5.7. Pole figures of other 2θ values are then initially ignored. This approach is also useful when several phases diffract around the same value of 2θ.

Diffraction intensity contour map: $I(2\theta, \chi)$

A third approach is to average the recorded intensities of a single pole-figure over the angle ϕ. As such, one obtains an average intensity value for every concentric circle on the pole figure (Fig. B.7c, top). By calculating these average values for every value of χ and 2θ, one obtains a two-dimensional graph such as displayed in the bottom part of figure B.7c. In this graphical representation, one still can perform phase identification through determining the positions of higher diffraction intensity as a function of 2θ. In addition, these diffraction maps also contain some information concerning the texture of the phase.

A *random* aligned sample would diffract at specific values of 2θ (corresponding to the $\{hkl\}$ planes of that phase) and for every value of χ. The diffraction contour map would therefore display vertical lines at these 2θ positions (Fig. B.8a). A highly-textured, *epitaxial* film would only diffract at specific regions in 2θ, χ and ϕ. The corresponding diffraction maps therefore contains only local spots of higher intensity as a function of 2θ and χ (Fig. B.8d). The four displayed examples in figure B.8 all contain three high-intense diffraction spots, which originate from the Si(001) substrate. A *fiber* texture, which diffracts in concentric circles on a pole-figure representation, will also correspond to local spots at specific 2θ and χ angles (Fig. B.8b). A fiber texture can sometimes be distinguished from an epitaxial texture due to a more elongated spot as a function of χ, corresponding to the width of the concentric diffraction rings of the fiber texture. However, this is not always the case. An axiotaxially-textured film, such as displayed in figure B.8c, will have some diffraction for almost every value of χ, resulting in vertical lines on the diffraction contour map. In contrast to

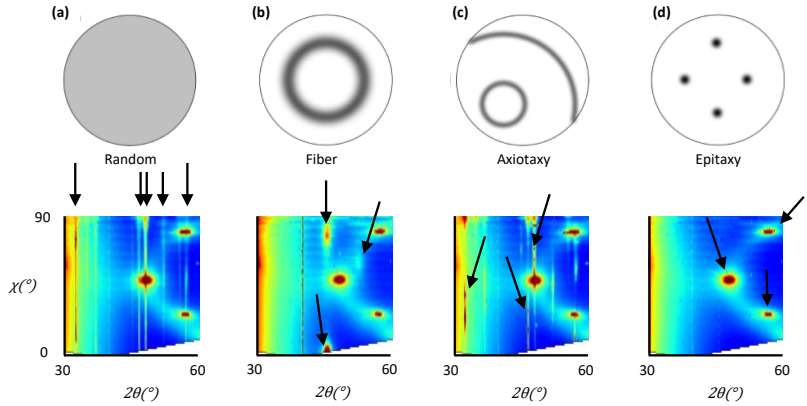

Figure B.8: Some illustrations how specific types of texture are displayed in pole figures (top) and in their corresponding diffraction contour maps (bottom) **(a)** random alignment **(b)** fiber alignment **(c)** axiotaxial alignment **(d)** epitaxial alignment.

random diffraction, the axiotaxial circles are not evenly distributed along χ, and these vertical lines can be distinguished from randomly-textured phases through a variation in intensity as a function of χ.

The diffraction contour maps therefore provides a tool for quick assessment of the phases present in the film, as well as of the textures of these phases. However, the preferential orientation is not always clear, for example if multiple phases are present in the film, or if the silicides' texture is a combination of multiple different alignments. The aforementioned similarities between the displayed patterns of a fiber and an epitaxy, or between an axiotaxy and a randomly textured film can result in ambiguous identification when relying on these diffraction contour maps.

We have further enhanced the display methodology so it can (partly) compensate these differences. Figure B.9a depicts the diffraction contour map of a sample after averaging the intensity over ϕ as a function of 2θ and χ. An alternative contour map is displayed in figure B.9b. Instead of averaging over ϕ for every concentric circle on a pole figure (Top image in Fig. B.7c), we have hereby taken the *median* value over ϕ. The median value is almost insensitive for diffraction which is only locally present along ϕ. Therefore, axiotaxy or epitaxy are not included in this intensity contour map. Indeed, the Si(001) substrate peaks, which are clearly visible in figure B.9a, are absent in figure B.9b. Comparing these two plots thus allows to distinguish between a random texture and an axiotaxy or between a fiber

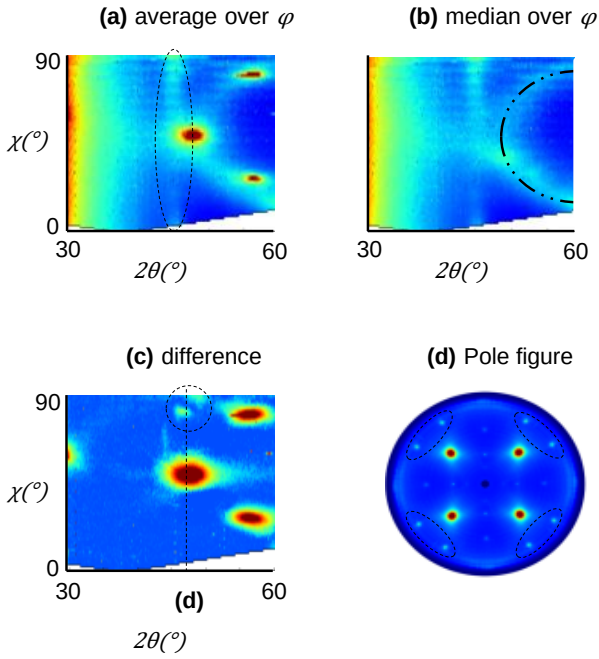

Figure B.9: The diffraction contour maps can be calculated in different ways: **(a)** by averaging over every value of χ and 2θ, **(b)** by taking the median value over χ for every value of 2θ, or **(c)** by taking the difference between (a) and (b). The latter representation is highly sensitive for low-intense epitaxies or axiotaxies, as displayed in **(d)**

and an epitaxy. One can also calculate, for every value of 2θ and χ, the difference between the intensity's average over ϕ and the intensity's median over ϕ (Fig. B.9c). This latter has the particular advantage that any random diffraction is eliminated, not only from randomly-textured silicides, but also any background radiation due to the experimental set-up. The result is that this plot is highly sensitive for low-intensity epitaxial phases. Figure B.9c indeed contains a low-intensity diffraction spot for high χ values, indicated by the dashed line, which was not visible in figures B.9a or b. When examining the specific pole figure at that particular value of 2θ (Fig. B.9d), one indeed observes a low-intensity epitaxial diffraction spot at high χ angle.

One is not only interested in the identification of the different textures in the film, but also in knowing which texture is more dominantly present. Indeed, whether or not an epitaxial alignment occurs in 80% of the film volume or in only 1% makes in a huge difference for the final characteristics of the film. In an ideal case, a complete representation of the texture statistics is given by an orientation distribution function (ODF). Polefigures, however, do not allow direct measurement of the ODF. A standard procedure would be by selecting a specific region in both χ and ϕ which is representative for a specific texture component, and compare its intensity as a function of 2θ with the diffraction from a random χ and ϕ value, as shown in Figure 8.3. This ratio is then a figure-of-merit on the volume fraction of the texture under investigation. The plotting mechanism described in de previous paragraph was altered with the aim of obtaining such a figure-of-merit with a single plot for all values of χ and 2θ. The average intensity values along χ and 2θ are again a first step to identify on the textures in the film (Fig. B.10a). In a following step (Fig. B.10b), the background scattering was estimated by taking the lowest diffraction intensities (e.g. the 5th percentile of the ϕ direction) over a broad range in χ and 2θ (e.g. within a box of $\Delta\chi = 5°$ and $\Delta 2\theta = 5°$). This is then used to calibrate the diffraction intensities that are very local in ϕ, such as is the case for epitaxy or axiotaxy (e.g. the 95th percentile along ϕ divided by the background estimation, fig. B.10c) or to calibrate the diffraction intensities representing randomly-distributed or fiber-aligned grains (e.g. the 20th percentile along ϕ divided by the background estimation, fig. B.10d).

In the example displayed in figure B.10a, one can see that the diffraction intensities of TiN and the C54-$TiSi_2$ phase are local in the χ direction, thus indicating fiber or epitaxial-textured features. From figures B.10c and d, one can see that the 95th percentile diffraction intensity of a TiN peak (approximatly 30% higher than the background) is almost the same as the 20th percentile (also approximatly 30% higher than the background). As

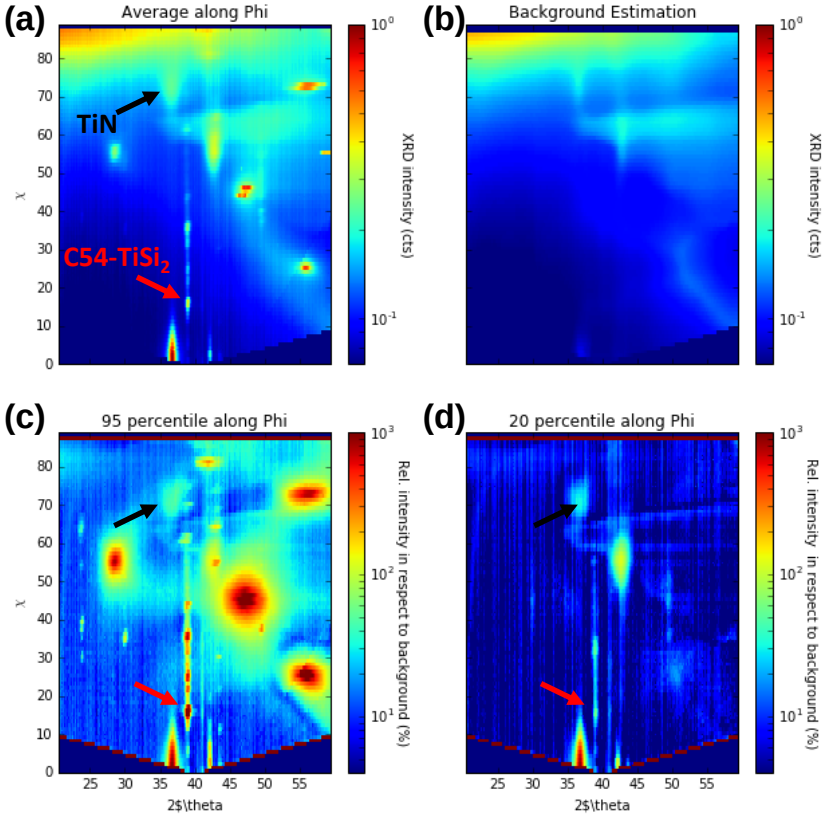

Figure B.10: The diffraction contour maps can be used in the following way, to obtain scaled intensities for the different textures: **(a)** by averaging over every value of χ and 2θ, **(b)** by estimating a diffraction background value over χ for every value of 2θ. This background can then be used to scale both the **(c)** 95th intensity percentile or the 20th intensity percentile over χ for every value of 2θ.

Table B.1: Overview of the different ways of plotting complete data-sets of pole figures in order to perform phase and texture identification

Plotting method	$I(x)$	Identification of:	
		phases	textures
Powder-like diffraction pattern	$I(2\theta)$	+	-
Select single 2θ pole-figure	$I(\phi,\chi)$	-	++
Diffraction map	$I(2\theta,\chi)$	+	$\pm$
Enhanced diffraction maps	$I(2\theta,\chi)$	+	+

such, there are no big diffraction variations along ϕ, indicating that this is a rather pure fiber texture. More interesting is the C54-$TiSI_2$ phase, where the diffraction peak localized at the red arrow is 1000% (i.e. 10×) higher than the diffraction background, whereas the 20th percentile is only 30% higher than the diffraction background. As such, one can estimate that the volume fraction represented by this epitaxial alignment has a relatively large volume fraction in the film. This way of plotting thus offers a quick way to evaluate the occurrence of most textures present in the same pole-figure dataset.

Summary

An overview of the discussed plotting strategies for high-throughput pole figure data is displayed in Table B.1. Throughout this thesis, all four methods have been applied, where each method has its advantages. The diffraction intensity maps proved highly valuable in the initial analysis of the pole figures in chapter 5. As this plotting method is not a standard way of displaying the acquired diffraction data, we have not displayed these plots in the published papers.

As the measuring time of a set of pole figures is reduced to only a few minutes, one can now perform *in situ* XRD-pole figure measurements. The total dataset of such a measurement can then easily contain a few hundred pole-figure sets. These plotting techniques are therefore a crucial step to avoid a bottleneck in the analysing process. However, they only aid in selecting the interesting sample conditions (e.g. quenching temperature, as deposited concentration) and 2θ angles which should be investigated in more detail. The precise assessment of the texture (i.e. determining which planes are running parallel with each-other in film and substrate) still requires to investigate the individual pole figures at these interesting

2θ angles, for example with the GUSTAV software package [13]. Advances on these fitting procedures are therefore a next step in high-throughput XRD pole figure measurements.

C

BINARY AND TERNARY PHASE DIAGRAMS

C.1 NICKEL

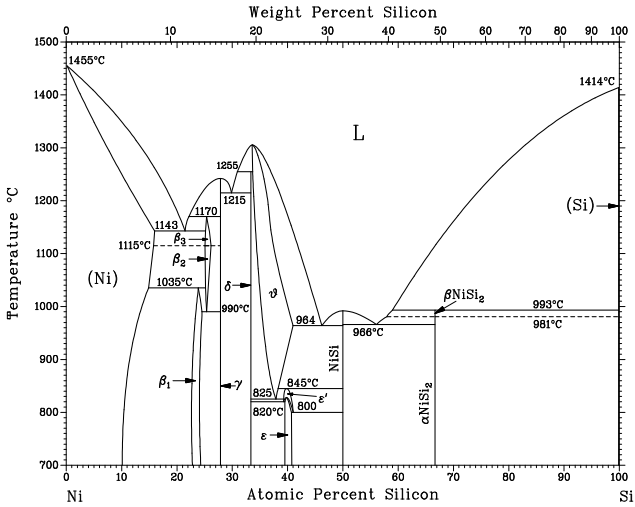

Figure C.1: Phase diagram for the Ni-Si system. Figure from [1].

C.2 ALUMINUM

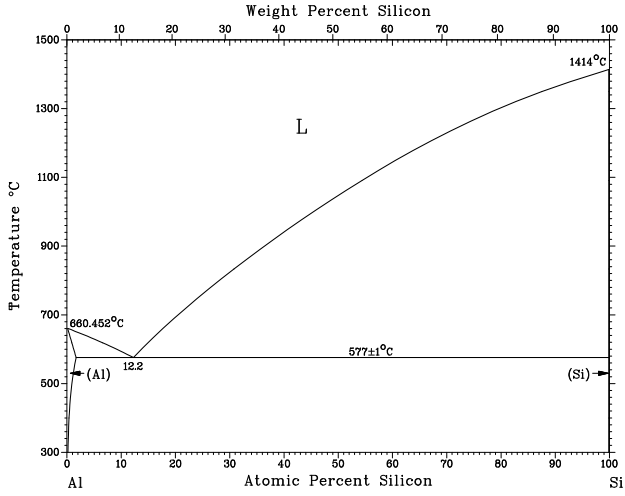

Figure C.2: Phase diagram for the Al-Si system. Figure from [1].

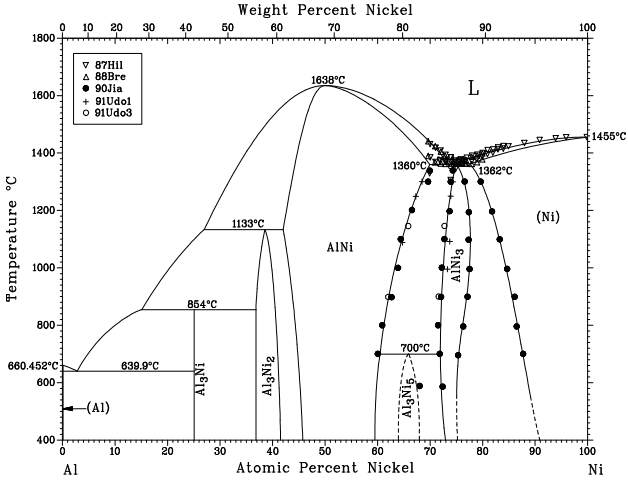

Figure C.3: Phase diagram for the binary Al-Ni system. Figure from [1].

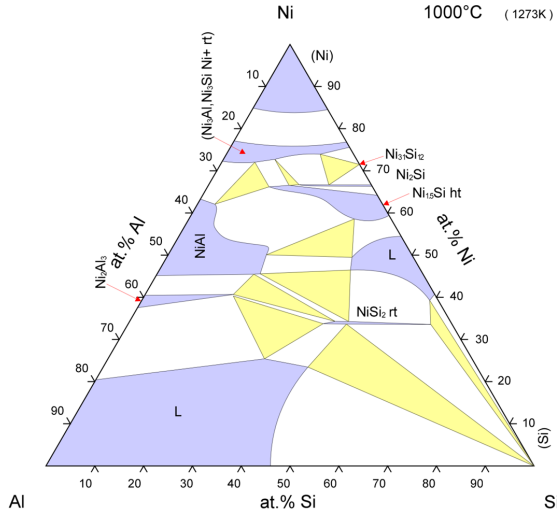

Figure C.4: Phase diagram for the ternary Al-Ni-Si system. Figure from [2].

C.3 COBALT

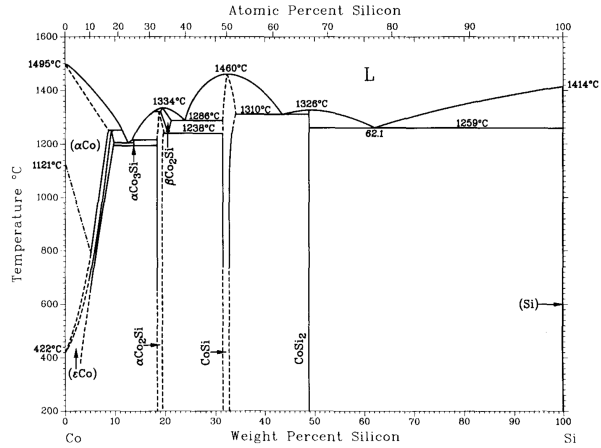

Figure C.5: Phase diagram for the Co-Si system. Figure from [1].

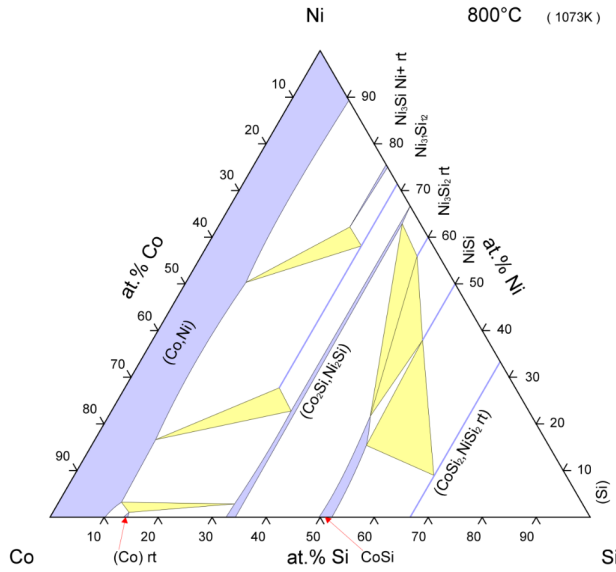

Figure C.6: Phase diagram for the Co-Ni-Si system. Figure from [3].

C.4 PLATINUM

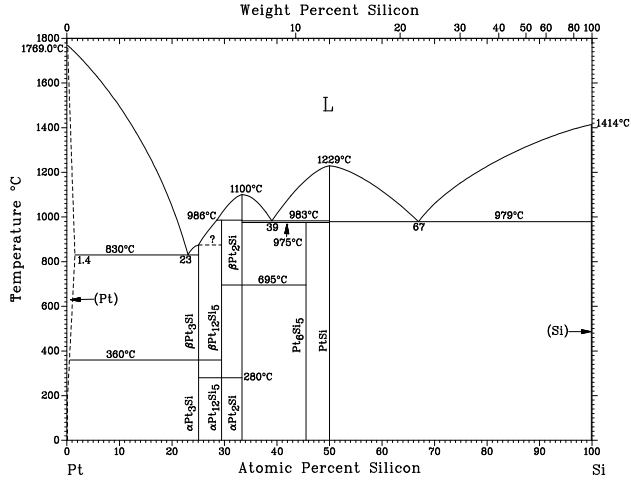

Figure C.7: Phase diagram for the Pt-Si system. Figure from [1].

C.5 TITANIUM

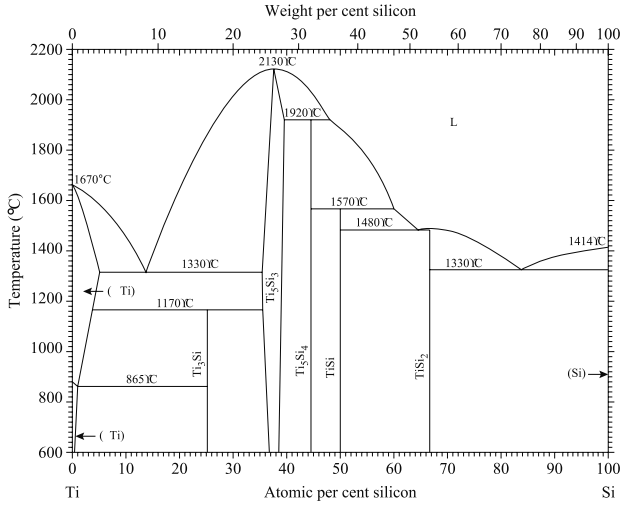

Figure C.8: Phase diagram for the Ti-Si system. Figure from [1].

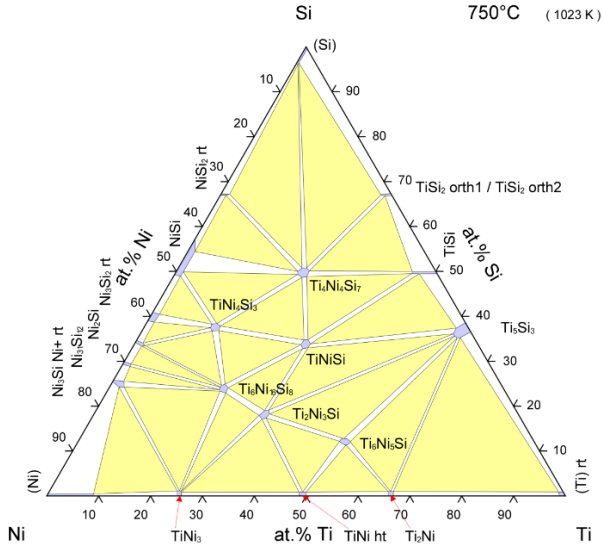

Figure C.9: Phase diagram for the Ni-Si-Ti system. Figure from [4].

PUBLICATIONS

PUBLICATIONS IN INTERNATIONAL PAPERS

- *Formation and texture of palladium germanides studied by in situ X-ray diffraction and pole figure measurements*

  F. Geenen, W. Knaepen, K. De Keyser, K. Opsomer, R. Vanmeirhaeghe, J. Jordan-Sweet, C. Lavoie and C. Detavernier

  Thin Solid Films, **551** (2014), 86

- *On the formation and structural properties of hexagonal rare earth (Y, Gd, Dy, Er and Yb) disilicide thin films*

  F. Geenen, W. Knaepen, J. Demeulemeester, K. De Keyser, J. Jordan-Sweet, C. Lavoie, A. Vantomme and C. Detavernier

  Journal of Alloys and Compounds, **611** (2014), 149

- *Anisotropic thermal expansion of Ni, Pd and Pt germanides and silicides*

  F. Geenen, W. Knaepen, F. Moens, L. Brondeel, A. Leenaers, S. Van den Berge and C. Detavernier

  Journal of Physics D - Applied Physics, **49** (2016), 0022

- *Monte Carlo simulations of atomic layer deposition on 3D large surface area structures: required precursor exposure for pillar- versus hole-type structures*

  V. Cremers, **F. Geenen**, C. Detavernier and J. Dendooven

  Journal of Vacuum Science & Technology A, **35** (2017), 0734

- *Axiotaxy in oxide heterostructures: preferential orientation of $BaCeO_3$ nanoparticles embedded in $YBa_2Cu_3O_{7-\delta}$*

  E. Solano Menuesa, **F. Geenen**, P. Teresa, X. Obradors, C. Mocuta and C. Detavernier

  Submitted to Thin Solid Films

- *The influence of Al alloying on nickel silicide formation and texture*

  F. Geenen, K. van Stiphout, M. Minjauw, J. Jordan-Sweet, A. Vantomme, C. Lavoie and C. Detavernier

  Manuscript in preparation (Chapter 4)

- *The influence of alloying on the phase formation sequence and texture of ultra-thin nickel silicide films*

  F. Geenen, E. Solano Menuesa, J. Jordan-Sweet, C. Lavoie, C. Mocuta, C. Detavernier

  Manuscript in preparation (Chapter 5)

- *Controlling the formation and stability of ultra-thin nickel silicides - an alloying strategy for preventing agglomeration*

  F. Geenen, K. van Stiphout, A. Nanakoudis, S. Bals, A. Vantomme, J. Jordan-Sweet, C. Lavoie, C. Mocuta, C. Detavernier

  Manuscript in preparation (Chapter 6)

- *Axiotaxy and epitaxial textures in C54-$TiSi_2$ films on Si(001) and Si(111) substrates*

  F. Geenen, J. Jordan-Sweet, C. Lavoie, C. Detavernier

  Manuscript in preparation (Chapter 8)

- *Formation of ultrathin Ni germanides: solid-phase reaction, morphology and texture*

  K. van Stiphout, **F. Geenen**, N.M. Santos, S.M.C. Miranda, V. Joly, B. De Schutter, C. Detavernier, L.M.C. Pereira, K. Temst, A. Vantomme

  Manuscript in preparation

CONTRIBUTIONS AT INTERNATIONAL CONFERENCES

* Presenting author
** Invited speaker

- *Thermal expansion coefficients of Ni, Pt and Pd germanides and silicides*

  F. Geenen*, W. Knaepen, F. Moens, L. Brondeel, A. Leenaers, S. Van den Berghe and C. Detavernier

  Materials for Advanced Metallization, Chemnitz (Germany), March 2-5 2014

- *The influence of Al alloying on silicide formation, morphology and texture between a thin (<20 nm) Ni film and Si(001)*

  F. Geenen*, K. van Stiphout, J. Jordan-Sweet, A. Vantomme, C. Lavoie and C. Detavernier

  European Materials Research Society, spring meeting, Lille (France), May 11-15 2015

- *Study of Ni-germanide phase formation in Ge(001) with Pd or Pt interlayer*

  S. Miranda*, **F. Geenen**, C. Detavernier, K. Temst and A. Vantomme

  International Interconnect Technology Conference and Materials for Advanced Metallization Conference, Grenoble (France), May 18-21 2015

- *Influence of alloying elements on the phase formation of ultrathin Ni (<10nm) on Si(001) substrates*

  F. Geenen*, K. van Stiphout, J. Jordan-Sweet, A. Vantomme, C. Lavoie and C. Detavernier

  International Interconnect Technology Conference and Materials for Advanced Metallization Conference, Grenoble (France), May 18-21 2015

- *Formation of nickel silicides in the ultra-thin film regime (<10nm)*

  F. Geenen*, E. Solano Menuesa, C. Mocuta and C. Detavernier

  Materials for Advanced Metallization Conference, Brussels (Belgium), March 20-23 2016

- *Formation of ultrathin, stable and epitaxial silicides for semiconductor contacts*

  F. Geenen, C. Mocuta and C. Detavernier**

  International Conference on Solid-State and Integrated Circuit Technology, Hangzhou (China), October 25-28 2016

- *On the inheritance of crystallographic texture during the nickel silicide solid-phase reaction*

  F. Geenen*, E. Solano, C. Mocuta, J. Jordan-Sweet, C. Lavoie and C. Detavernier

  Materials for Advanced Metallization Conference, Dresden (Germany), March 26-29 2017

- *Texture evolution during solid-state reactions - silicides and germanides*

  F. Geenen**, K. De Keyser, D. Deduytssche B. de Schutter and C. Detavernier

  International Conference on Diffusion in Materials, Haifa (Israel), May 7-12 2017

- *Ultrathin Epitaxial Silicides for Semiconductor Contacts*

  F. Geenen, C. Mocuta and C. Detavernier**

  The Electrochemical Sociaty meeting, National Harbor, MD (USA), October 1-6 2017

BIBLIOGRAPHY

REFERENCES FOR CHAPTER 1

[1] G Moore. "Cramming more components onto integrated circuits." In: *Proceedings of the IEEE* 86 (1998).

[2] LJ Chen. *Silicide technology for integrated circuits*. Vol. 5. The Institution of Electrical Engineers, 2004.

[3] C Lavoie, FM d'Heurle, C Detavernier, and C Cabral. "Towards implementation of a nickel silicide process for CMOS technologies." In: *Microelectronic Engineering* 70.2 (2003), pp. 144–157.

[4] "Handbook of semiconductor manufacturing technology." In: CRC Press, 2007. Chap. Silicides.

[5] A Lauwers, M De Potter, O Chamirian, R Lindsay, C Demeurisse, C Vrancken, and K Maex. "Silicides for the 100-nm node and beyond: Co-silicide, Co (Ni)-silicide and Ni-silicide." In: *Microelectronic Engineering* 64.1 (2002), pp. 131–142.

[6] SL Zhang and Ml Östling. "Metal silicides in CMOS technology: past, present, and future trends." In: *Critical Reviews in Solid State and Materials Sciences* 28.1 (2003), pp. 1–129.

[7] K Barmak and K Coffey. "Metallic films for electronic, optical and magnetic applications: Structure, processing and properties." In: Woodhead Publishing, 2014. Chap. Metal silicides in advanced complementary metal-oxide-semiconductor (CMOS) technology.

[8] *Binary Alloy Phase Diagrams*. ASM international, 1996.

[9] S Gaudet, C Coia, P Desjardins, and C Lavoie. "Metastable phase formation during the reaction of Ni films with Si (001): The role of texture inheritance." In: *Journal of Applied Physics* 107.9 (2010), p. 093515.

[10] FM d'Heurle. "Nucleation of a new phase from the interaction of two adjacent phases: Some silicides." In: *Journal of Materials Research* 3.01 (1988), pp. 167–195.

[11] FM d'Heurle and P Gas. "Kinetics of formation of silicides: A review." In: *Journal of Materials Research* 1.01 (1986), pp. 205–221.

[12] T Barge, P Gas, and FM d'Heurle. "Analysis of the diffusion controlled growth of cobalt silicides in bulk and thin film couples." In: *Journal of Materials Research* 10.05 (1995), pp. 1134–1145.

[13] R Pretorius. "Prediction of silicide formation and stability using heats of formation." In: *Thin Solid Films* 290 (1996), pp. 477–484.

[14] R Pretorius. "Prediction of silicide first phase and phase sequence from heats of formation." In: *MRS Proceedings*. Vol. 25. Cambridge Univ Press. 1983, p. 15.

[15] RM Walser and RW Bene. "First phase nucleation in silicon–transition-metal planar interfaces." In: *Applied Physics Letters* 28.10 (1976), pp. 624–625.

[16] AM Brown and MF Ashby. "Correlations for diffusion constants." In: *Acta Metallurgica* 28.8 (1980), pp. 1085–1101.

[17] K De Keyser, RL Van Meirhaeghe, C Detavernier, J Jordan-Sweet, and C Lavoie. "Texture of cobalt germanides on Ge (100) and Ge (111) and its influence on the formation temperature." In: *Journal of The Electrochemical Society* 157.4 (2010), H395–H404.

[18] B De Schutter, K De Keyser, C Lavoie, and C Detavernier. "Texture in thin film silicides and germanides: A review." In: *Applied Physics Reviews* 3.3 (2016), p. 031302.

[19] C Detavernier, AS Ozcan, J Jordan-Sweet, EA Stach, J Tersoff, FM Ross, and C Lavoie. "An off-normal fibre-like texture in thin films on single-crystal substrates." In: *Nature* 426.6967 (2003), pp. 641–645.

[20] A Zur, TC McGill, and M-A Nicolet. "Transition-metal silicides lattice-matched to silicon." In: *Journal of Applied Physics* 57.2 (1985), pp. 600–603.

[21] A Zur and TC McGill. "Lattice match: An application to heteroepitaxy." In: *Journal of Applied Physics* 55.2 (1984), pp. 378–386.

[22] LJ Chen and KN Tu. "Epitaxial growth of transition-metal silicides on silicon." In: *Materials Science Reports* 6.2 (1991), pp. 53–140.

[23] RT Tung, JM Poate, JC Bean, JM Gibson, and DC Jacobson. "Epitaxial silicides." In: *Thin Solid Films* 93.1 (1982), pp. 77–90.

[24] RT Tung, JM Gibson, and JM Poate. "Formation of Ultrathin Single-Crystal Silicide Films on Si: Surface and Interfacial Stabilization of Si-$NiSi_2$ Epitaxial Structures." In: *Physical Review Letters* 50.6 (1983), p. 429.

[25] RT Tung. "The physics and chemistry of the Schottky barrier height." In: *Applied Physics Reviews* 1.1 (2014), p. 011304.

[26] K Dawon. *Electric Field Controlled Semiconductor Device*. US Patent 3,102,230. 1963.

[27] K Maex and M Van Rossum. *Properties of metal silicides*. 14. IET, 1995.

[28] Z Zhang, SL Zhang, B Yang, Y Zhu, S M Rossnagel, S Gaudet, A J Kellock, J Jordan-Sweet, and C Lavoie. "Morphological stability and specific resistivity of sub-10 nm silicide films of Ni Pt_x on Si substrate." In: *Applied Physics Letters* 96 (2010), p. 071915.

REFERENCES FOR CHAPTER 2

[1] D Deduytsche, C Detavernier, RL Van Meirhaeghe, and C Lavoie. "High-temperature degradation of NiSi films: Agglomeration versus $NiSi_2$ nucleation." In: *Journal of Applied Physics* 98.3 (2005), p. 033526.

[2] B De Schutter, K De Keyser, C Lavoie, and C Detavernier. "Texture in thin film silicides and germanides: A review." In: *Applied Physics Reviews* 3.3 (2016), p. 031302.

[3] C Lavoie, C Coia, C Detavernier, C Cabral, P Desjardins, AJ Kellock, et al. "Reactive diffusion in the Ni-Si system: phase sequence and formation of metal-rich phases." In: *Defect and Diffusion Forum*. Vol. 237. Trans Tech Publ. 2005, pp. 825–836.

[4] K Hoummada, I Blum, D Mangelinck, and A Portavoce. "Composition measurement of the Ni-silicide transient phase by atom probe tomography." In: *Applied Physics Letters* 96.26 (2010), p. 261904.

[5] S Gaudet, C Coia, P Desjardins, and C Lavoie. "Metastable phase formation during the reaction of Ni films with Si (001): The role of texture inheritance." In: *Journal of Applied Physics* 107.9 (2010), p. 093515.

[6] M E Schlesinger. "Thermodynamics of solid transition-metal silicides." In: *Chemical Reviews* 90.4 (1990), pp. 607–628.

[7] D Mangelinck, K Hoummada, and I Blum. "Kinetics of a transient silicide during the reaction of Ni thin film with (100) Si." In: *Applied Physics Letters* 95.18 (2009), p. 1902.

[8] D Mangelinck, K Hoummada, F Panciera, M El Kousseifi, I Blum, M Descoins, M Bertoglio, A Portavoce, C Perrin, and M Putero. "Progress in the understanding of Ni silicide formation for advanced MOS structures." In: *Physica Status Solidi (a)* 211.1 (2014), pp. 152–165.

[9] HE Kissinger. "Reaction kinetics in differential thermal analysis." In: *Analytical Chemistry* 29.11 (1957), pp. 1702–1706.

[10] K De Keyser, C Detavernier, and L Van Meirhaeghe. "The texture of thin NiSi films and its effect on agglomeration." In: *Applications of Texture Analysis: Ceramic Transactions* 201 (2008), p. 3.

[11] C Detavernier, AS Ozcan, J Jordan-Sweet, EA Stach, J Tersoff, FM Ross, and C Lavoie. "An off-normal fibre-like texture in thin films on single-crystal substrates." In: *Nature* 426.6967 (2003), pp. 641–645.

[12] C Detavernier, J Jordan-Sweet, and C Lavoie. "Texture of NiSi films on Si (001),(111), and (110) substrates." In: *Journal of Applied Physics* 103.11 (2008), p. 113526.

[13] K De Keyser, C Van Bockstael, RL Van Meirhaeghe, C Detavernier, E Verleysen, H Bender, W Vandervorst, J Jordan-Sweet, and C Lavoie. "Phase formation and thermal stability of ultrathin nickel-silicides on Si (100)." In: *Applied Physics Letters* 96.17 (2010), p. 173503.

[14] Z Zhang, SL Zhang, B Yang, Y Zhu, S M Rossnagel, S Gaudet, A J Kellock, J Jordan-Sweet, and C Lavoie. "Morphological stability and specific resistivity of sub-10 nm silicide films of Ni Pt_x on Si substrate." In: *Applied Physics Letters* 96 (2010), p. 071915.

[15] J Luo, Z Qiu, C Zha, Z Zhang, D Wu, J Lu, J Åkerman, M Östling, L Hultman, and SL Zhang. "Surface-energy triggered phase formation and epitaxy in nanometer-thick $Ni_{1-x}Pt_x$ silicide films." In: *Applied Physics Letters* 96.3 (2010).

[16] RT Tung, JM Poate, JC Bean, JM Gibson, and DC Jacobson. "Epitaxial silicides." In: *Thin Solid Films* 93.1 (1982), pp. 77–90.

[17] RT Tung, JM Gibson, and JM Poate. "Formation of Ultrathin Single-Crystal Silicide Films on Si: Surface and Interfacial Stabilization of Si-$NiSi_2$ Epitaxial Structures." In: *Physical Review Letters* 50.6 (1983), p. 429.

[18] A Zur and TC McGill. "Lattice match: An application to heteroepitaxy." In: *Journal of Applied Physics* 55.2 (1984), pp. 378–386.

[19] A Zur, TC McGill, and M-A Nicolet. "Transition-metal silicides lattice-matched to silicon." In: *Journal of Applied Physics* 57.2 (1985), pp. 600–603.

[20] H Brahmi, S Ravipati, M Yarali, S Shervin, W Wang, JH Ryou, and A Mavrokefalos. "Electrical and optical properties of sub-10 nm nickel silicide films for silicon solar cells." In: *Journal of Physics D: Applied Physics* 50.3 (2016), p. 035102.

[21] A Mondon, D Wang, A Zuschlag, J Bartsch, M Glatthaar, and SW Glunz. "Nanoscale investigation of the interface situation of plated nickel and thermally formed nickel silicide for silicon solar cell metallization." In: *Applied Surface Science* 323 (2014), pp. 31–39.

REFERENCES FOR CHAPTER 3

[1] D Mangelinck, JY Dai, JS Pan, and SK Lahiri. "Enhancement of thermal stability of NiSi films on (100) Si and (111) Si by Pt addition." In: *Applied Physics Letters* 75.12 (1999), pp. 1736–1738.

[2] FM d'Heurle. "Nucleation of a new phase from the interaction of two adjacent phases: Some silicides." In: *Journal of Materials Research* 3.01 (1988), pp. 167–195.

[3] C Lavoie, C Detavernier, C Cabral, FM d'Heurle, AJ Kellock, J Jordan-Sweet, and JME Harper. "Effects of additive elements on the phase formation and morphological stability of nickel monosilicide films." In: *Microelectronic Engineering* 83.11 (2006), pp. 2042–2054.

[4] C Detavernier and C Lavoie. "Influence of Pt addition on the texture of NiSi on Si (001)." In: *Applied Physics Letters* 84.18 (2004), pp. 3549–3551.

[5] D Smeets, A Vantomme, K De Keyser, C Detavernier, and C Lavoie. "The role of lattice mismatch and kinetics in texture development: $Co_{1-x}Ni_xSi_2$ thin films on Si (100)." In: *Journal of Applied Physics* 103.6 (2008), p. 063506.

[6] B De Schutter, K De Keyser, C Lavoie, and C Detavernier. "Texture in thin film silicides and germanides: A review." In: *Applied Physics Reviews* 3.3 (2016), p. 031302.

[7] D Mangelinck, K Hoummada, F Panciera, M El Kousseifi, I Blum, M Descoins, M Bertoglio, A Portavoce, C Perrin, and M Putero. "Progress in the understanding of Ni silicide formation for advanced MOS structures." In: *Physica Status Solidi (a)* 211.1 (2014), pp. 152–165.

[8] D Deduytsche. "An in situ study of the stability of thin Ni-silicide layers." PhD thesis. Ghent University, 2006.

[9] C Detavernier, C Lavoie, and FM d'Heurle. "Thermal expansion of the isostructural PtSi and NiSi: Negative expansion coefficient in NiSi and stress effects in thin films." In: *Journal of Applied Physics* 93.5 (2003), pp. 2510–2515.

[10] KL Pey, PS Lee, and D Mangelinck. "Ni (Pt) alloy silicidation on (100) Si and polysilicon lines." In: *Thin Solid Films* 462 (2004), pp. 137–145.

[11] O Cojocaru-Mirédin, D Mangelinck, K Hoummada, E Cadel, D Blavette, B Deconihout, and C Perrin-Pellegrino. "Snowplow effect and reactive diffusion in the Pt doped Ni–Si system." In: *Scripta Materialia* 57.5 (2007), pp. 373–376.

[12] C Van Bockstael, K De Keyser, D Deduytsche, RL Van Meirhaeghe, C Detavernier, JL Jordan-Sweet, and C Lavoie. "Effect of Pt addition on growth stress and thermal stress of NiSi films." In: *Journal of Applied Physics* 104.5 (2008), p. 053510.

[13] J Demeulemeester, D Smeets, C Van Bockstael, C Detavernier, CM Comrie, NP Barradas, A Vieira, and A Vantomme. "Pt redistribution during Ni (Pt) silicide formation." In: *Applied Physics Letters* 93.26 (2008), p. 261912.

[14] Z Zhang, SL Zhang, B Yang, Y Zhu, S M Rossnagel, S Gaudet, A J Kellock, J Jordan-Sweet, and C Lavoie. "Morphological stability and specific resistivity of sub-10 nm silicide films of Ni Pt_x on Si substrate." In: *Applied Physics Letters* 96 (2010), p. 071915.

[15] Z Zhang, B Yang, Y Zhu, S Gaudet, S Rossnagel, A J Kellock, A Ozcan, C Murray, P Desjardins, SL Zhang, et al. "Exploitation of a self-limiting process for reproducible formation of ultrathin $Ni_{1-x}Pt_x$ silicide films." In: *Applied Physics Letters* 97.25 (2010), p. 252108.

[16] J Luo, Z Qiu, C Zha, Z Zhang, D Wu, J Lu, J Åkerman, M Östling, L Hultman, and SL Zhang. "Surface-energy triggered phase formation and epitaxy in nanometer-thick $Ni_{1-x}Pt_x$ silicide films." In: *Applied Physics Letters* 96.3 (2010).

[17] J Demeulemeester, D Smeets, CM Comrie, C Van Bockstael, W Knaepen, C Detavernier, K Temst, and A Vantomme. "The influence of Pt redistribution on $Ni_{1-x}Pt_xSi$ growth properties." In: *Journal of Applied Physics* 108.4 (2010), p. 043505.

[18] J Demeulemeester, D Smeets, CM Comrie, NP Barradas, A Vieira, C Van Bockstael, C Detavernier, K Temst, and A Vantomme. "On the growth kinetics of Ni (Pt) silicide thin films." In: *Journal of Applied Physics* 113.16 (2013), p. 163504.

[19] F Panciera, K Hoummada, M Gregoire, M Juhel, and D Mangelinck. "Pt redistribution in N-MOS transistors during Ni salicide process." In: *Microelectronic Engineering* 107 (2013), pp. 173–177.

[20] F Panciera, D Mangelinck, K Hoummada, M Texier, M Bertoglio, A De Luca, M Gregoire, and M Juhel. "Direct epitaxial growth of θ-Ni_2 Si by reaction of a thin Ni (10at.% Pt) film with Si (100) substrate." In: *Scripta Materialia* 78 (2014), pp. 9–12.

[21] M El Kousseifi, K Hoummada, M Bertoglio, and D Mangelinck. "Selection of the first Ni silicide phase by controlling the Pt incorporation in the intermixed layer." In: *Acta Materialia* 106 (2016), pp. 193–198.

[22] K Barmak and K Coffey. "Metallic films for electronic, optical and magnetic applications: Structure, processing and properties." In: Woodhead Publishing, 2014. Chap. Metal silicides in advanced complementary metal-oxide-semiconductor (CMOS) technology.

[23] FM d'Heurle, DD Anfiteatro, VR Deline, and TG Finstad. "Reaction of silicon with films of Co-Ni alloys: Phase separation of the monosilicides and nucleation of the disilicides." In: *Thin Solid Films* 128.1-2 (1985), pp. 107–124.

[24] FM d'Heurle, J Tersoff, TG Finstad, and A Cros. "Resistivity of the solid solutions (Co-Ni) Si2." In: *Journal of Applied Physics* 59.1 (1986), pp. 177–180.

[25] C Lavoie, C Cabral Jr, FM d'Heurle, JL Jordan-Sweet, and JME Harper. "Effects of alloying elements on cobalt silicide formation." In: *Journal of Electronic Materials* 31.6 (2002), pp. 597–609.

[26] A Lauwers, M De Potter, O Chamirian, R Lindsay, C Demeurisse, C Vrancken, and K Maex. "Silicides for the 100-nm node and beyond: Co-silicide, Co (Ni)-silicide and Ni-silicide." In: *Microelectronic Engineering* 64.1 (2002), pp. 131–142.

[27] RT Tung, JM Poate, JC Bean, JM Gibson, and DC Jacobson. "Epitaxial silicides." In: *Thin Solid Films* 93.1 (1982), pp. 77–90.

[28] A Zur, TC McGill, and M-A Nicolet. "Transition-metal silicides lattice-matched to silicon." In: *Journal of Applied Physics* 57.2 (1985), pp. 600–603.

[29] D Deduytsche, C Detavernier, RL Van Meirhaeghe, JL Jordan-Sweet, and C Lavoie. "Formation and stability of NiSi in the presence of Co and Fe alloying elements." In: *Journal of Vacuum Science & Technology B* 26.6 (2008), pp. 1971–1977.

[30] *Binary Alloy Phase Diagrams*. ASM international, 1996.

[31] D Mangelinck, P Gas, JM Gay, B Pichaud, and O Thomas. "Effect of Co, Pt, and Au additions on the stability and epitaxy of $NiSi_2$ films on (111) Si." In: *Journal of Applied Physics* 84 (1998), pp. 2583–2590.

[32] AS Özcan, K F Ludwig Jr, C Detavernier, C Lavoie, and JL Jordan-Sweet. "Axiotaxy of CoSi2 thin films on Si (100) substrates and the effects of Ti alloying." In: *Journal of Applied Physics* 95.12 (2004), pp. 8376–8381.

[33] D Smeets, J Demeulemeester, K De Keyser, D Deduytsche, C Detavernier, CM Comrie, CC Theron, C Lavoie, and A Vantomme. "Nucleation and diffusion during growth of ternary Co1- xNixSi2 thin films studied by complementary techniques in real time." In: *Journal of Applied Physics* 104.9 (2008), p. 093533.

[34] P Rodriguez, S Favier, F Nemouchi, C Sÿsÿ, F Deprat, C Fenouillet-Beranger, and P Gergaud. "Contacts for monolithic 3D architecture: Study of $Ni_{0.9}Co_{0.1}$ silicide formation." In: *Interconnect Technology Conference/Advanced Metallization Conference (IITC/AMC), 2016 IEEE International*. IEEE. 2016, pp. 72–74.

[35] F Deprat, F Nemouchi, C Fenouillet-Beranger, P Rodriguez, S Joblot, M Gregoire, D Barge, P Gergaud, N Rambal, P Batude, et al. "Technological enhancers effect on $Ni_{0.9}Co_{0.1}$ silicide stability for 3D sequential integration." In: *Physica Status Solidi (C)* 13.10–12 (2016), pp. 760–765.

[36] H Von Känel. "Growth and characterization of epitaxial Ni and Co silicides." In: *Materials Science Reports* 8.5 (1992), pp. 193–269.

[37] RT Tung. "Epitaxial $CoSi_2$ and $NiSi_2$ thin films." In: *Materials Chemistry and Physics* 32.2 (1992), pp. 107–133.

[38] KW Richter and K Hiebl. "$Ni_{1.74}Al_{0.26}$ and $NiSi_{1.83}Ga_{0.17}$: Two materials with perfect lattice match to Si." In: *Applied Physics Letters* 83 (2003).

[39] KW Richter and H Ipser. "The Al–Ni–Si phase diagram between 0 and 33.3 at.% Ni." In: *Intermetallics* 11.2 (2003), pp. 101–109.

[40] KW Richter, K Chandrasekaran, and H Ipser. "The Al–Ni–Si phase diagram. Part II: phase equilibria between 33.3 and 66.7 at.% Ni." In: *Intermetallics* 12.5 (2004), pp. 545–554.

[41] K Chandrasekaran, KW Richter, and H Ipser. "The Al–Ni–Si phase diagram Part III: Phase equilibria in the nickel rich part." In: *Intermetallics* 14.5 (2006), pp. 491–497.

[42] A Mogilatenko, G Beddies, M Falke, I Häusler, and W Neumann. "Microstructure analysis of novel ternary $NiSi_{2-x}Al_x$ silicide layers on Si (001) formed by solid-state reaction." In: *Journal of Applied Physics* 111.10 (2012), p. 103512.

[43] F Allenstein, L Budzinski, D Hirsch, A Mogilatenko, G Beddies, R Grötzschel, and HJ Hinneberg. "Influence of Al on the growth of $NiSi_2$ on Si (001)." In: *Microelectronic Engineering* 82.3 (2005), pp. 474–478.

[44] YF Huang, YL Jiang, GP Ru, and BZ Li. "Study of Ni/Si (100) solid-state reaction with Al addition." In: *Applied Surface Science* 254.17 (2008), pp. 5631–5634.

[45] AV Mogilatenko, F Allenstein, MA Schubert, M Falke, G Beddies, and W Neumann. "Structural Changes in Nickel Silicide Thin Films under the Presence of Al and Ga." In: *Materials Science Forum*. Vol. 638. Trans Tech Publ. 2010, pp. 2938–2943.

[46] SH Huang, SC Twan, SL Cheng, T Lee, JC Hu, LT Chen, and SW Lee. "Influence of Al addition on phase transformation and thermal stability of nickel silicides on Si (001)." In: *Journal of Alloys and Compounds* 586 (2014), S362–S367.

[47] C Detavernier, C Lavoie, FM d'Heurle, H Bender, and RL Van Meirhaeghe. "Low-temperature formation of $CoSi_2$ in the presence of Au." In: *Journal of Applied Physics* 95.10 (2004), pp. 5340–5346.

REFERENCES FOR CHAPTER 4

[1] SP Murarka. "Silicide thin films and their applications in microelectronics." In: *Intermetallics* 3.3 (1995), pp. 173–186.

[2] H Von Känel. "Growth and characterization of epitaxial Ni and Co silicides." In: *Materials Science Reports* 8.5 (1992), pp. 193–269.

[3] JA Knapp and ST Picraux. "Epitaxial growth of rare-earth silicides on (111) Si." In: *Applied Physics Letters* 48.7 (1986), pp. 466–468.

[4] RT Tung, JC Bean, JM Gibson, JM Poate, and DC Jacobson. "Growth of single-crystal $CoSi_2$ on Si (111)." In: *Applied Physics Letters* 40.8 (1982), pp. 684–686.

[5] LJ Chen, JW Mayer, and KN Tu. "Formation and structure of epitaxial $NiSi_2$ and $CoSi_2$." In: *Thin Solid Films* 93.1-2 (1982), pp. 135–141.

[6] RT Tung, JM Poate, JC Bean, JM Gibson, and DC Jacobson. "Epitaxial silicides." In: *Thin Solid Films* 93.1 (1982), pp. 77–90.

[7] F Allenstein, L Budzinski, D Hirsch, A Mogilatenko, G Beddies, R Grötzschel, and HJ Hinneberg. "Influence of Al on the growth of $NiSi_2$ on Si (001)." In: *Microelectronic Engineering* 82.3 (2005), pp. 474–478.

[8] M Sinha, EF Chor, and YC Yeo. "Tuning the Schottky barrier height of nickel silicide on p-silicon by aluminum segregation." In: *Applied Physics Letters* 92.22 (2008), p. 2114.

[9] A Mogilatenko, G Beddies, M Falke, I Häusler, and W Neumann. "Microstructure analysis of novel ternary $NiSi_{2-x}Al_x$ silicide layers on Si (001) formed by solid-state reaction." In: *Journal of Applied Physics* 111.10 (2012), p. 103512.

[10] SH Huang, SC Twan, SL Cheng, T Lee, JC Hu, LT Chen, and SW Lee. "Influence of Al addition on phase transformation and thermal stability of nickel silicides on Si (001)." In: *Journal of Alloys and Compounds* 586 (2014), S362–S367.

[11] KW Richter and H Ipser. "The Al–Ni–Si phase diagram between 0 and 33.3 at.% Ni." In: *Intermetallics* 11.2 (2003), pp. 101–109.

[12] AV Mogilatenko, F Allenstein, MA Schubert, M Falke, G Beddies, and W Neumann. "Structural Changes in Nickel Silicide Thin Films under the Presence of Al and Ga." In: *Materials Science Forum*. Vol. 638. Trans Tech Publ. 2010, pp. 2938–2943.

[13] L Goux, K Opsomer, R Degraeve, R Müller, C Detavernier, DJ Wouters, M Jurczak, L Altimime, and JA Kittl. "Influence of the Cu-Te composition and microstructure on the resistive switching of Cu-Te/Al2O3/Si cells." In: *Applied Physics Letters* 99.5 (2011), p. 053502.

[14] W Devulder, K Opsomer, A Franquet, J Meersschaut, A Belmonte, R Muller, B De Schutter, S Van Elshocht, M Jurczak, L Goux, and C Detavernier. "Influence of carbon content on the copper-telluride phase formation and on the resistive switching behavior of carbon alloyed Cu-Te conductive bridge random access memory cells." In: *Journal of Applied Physics* 115.5 (2014), p. 054501.

[15] W Devulder, K Opsomer, J Meersschaut, D Deduytsche, M Jurczak, L Goux, and C Detavernier. "Combinatorial Study of Ag-Te Thin Films and Their Application as Cation Supply Layer in CBRAM Cells." In: *ACS Combinatorial Science* 17.5 (2015), pp. 334–340.

[16] C Detavernier, J Jordan-Sweet, and C Lavoie. "Texture of NiSi films on Si (001),(111), and (110) substrates." In: *Journal of Applied Physics* 103.11 (2008), p. 113526.

[17] B De Schutter, K De Keyser, C Lavoie, and C Detavernier. "Texture in thin film silicides and germanides: A review." In: *Applied Physics Reviews* 3.3 (2016), p. 031302.

[18] A Vantomme. "50 years of ion channeling in materials science." In: *Nuclear Instruments and Methods in Physics Research Section B: Beam Interactions with Materials and Atoms* 371 (2016), pp. 12–26.

[19] D Deduytsche, C Detavernier, RL Van Meirhaeghe, and C Lavoie. "High-temperature degradation of NiSi films: Agglomeration versus $NiSi_2$ nucleation." In: *Journal of Applied Physics* 98.3 (2005), p. 033526.

[20] JA Kittl, MA Pawlak, C Torregiani, A Lauwers, C Demeurisse, C Vrancken, PP Absil, S Biesemans, C Coia, C Detavernier, J Jordan-Sweet, and C Lavoie. "Transient and end silicide phase formation in thin film Ni/polycrystalline-Si reactions for fully silicided gate applications." In: *Applied Physics Letters* 91.17 (2007), p. 172108.

[21] S Gaudet, C Coia, P Desjardins, and C Lavoie. "Metastable phase formation during the reaction of Ni films with Si (001): The role of texture inheritance." In: *Journal of Applied Physics* 107.9 (2010), p. 093515.

[22] KW Richter. "Crystal structure and phase relations of $Ni_{13\pm x}Al_y$ Si_{9-y}." In: *Journal of Alloys and Compounds* 338.1 (2002), pp. 43–50.

[23] KW Richter, K Chandrasekaran, and H Ipser. "The Al–Ni–Si phase diagram. Part II: phase equilibria between 33.3 and 66.7 at.% Ni." In: *Intermetallics* 12.5 (2004), pp. 545–554.

[24] K De Keyser, C Van Bockstael, C Detavernier, RL Van Meirhaeghe, J Jordan-Sweet, and C Lavoie. "Epitaxial formation of a metastable hexagonal nickel–silicide." In: *Electrochemical and Solid-State Letters* 11.9 (2008), H266–H268.

[25] C Detavernier, AS Ozcan, J Jordan-Sweet, EA Stach, J Tersoff, FM Ross, and C Lavoie. "An off-normal fibre-like texture in thin films on single-crystal substrates." In: *Nature* 426.6967 (2003), pp. 641–645.

[26] B De Schutter, K De Keyser, and C Detavernier. "Visualization and classification of epitaxial alignment at hetero-phase boundaries." In: *Thin Solid Films* 599 (2016), pp. 104–112.

[27] K De Keyser and C Detavernier. GUSTAV*: Ghent University Software for Texture Analysis and Visualisation*. `http://www.cocoon.ugent.be/content/gustav/`.

[28] K Chandrasekaran, KW Richter, and H Ipser. "The Al–Ni–Si phase diagram Part III: Phase equilibria in the nickel rich part." In: *Intermetallics* 14.5 (2006), pp. 491–497.

[29] AS Özcan, K F Ludwig Jr, C Detavernier, C Lavoie, and JL Jordan-Sweet. "Axiotaxy of CoSi2 thin films on Si (100) substrates and the effects of Ti alloying." In: *Journal of Applied Physics* 95.12 (2004), pp. 8376–8381.

[30] D Smeets, A Vantomme, K De Keyser, C Detavernier, and C Lavoie. "The role of lattice mismatch and kinetics in texture development: $Co_{1-x}Ni_xSi_2$ thin films on Si (100)." In: *Journal of Applied Physics* 103.6 (2008), p. 063506.

REFERENCES FOR CHAPTER 5

[1] SL Zhang and Ml Östling. "Metal silicides in CMOS technology: past, present, and future trends." In: *Critical Reviews in Solid State and Materials Sciences* 28.1 (2003), pp. 1–129.

[2] C Lavoie, FM d'Heurle, C Detavernier, and C Cabral. "Towards implementation of a nickel silicide process for CMOS technologies." In: *Microelectronic Engineering* 70.2 (2003), pp. 144–157.

[3] LJ Chen. *Silicide technology for integrated circuits*. Vol. 5. The Institution of Electrical Engineers, 2004.

[4] C Lavoie, C Detavernier, C Cabral, FM d'Heurle, AJ Kellock, J Jordan-Sweet, and JME Harper. "Effects of additive elements on the phase formation and morphological stability of nickel monosilicide films." In: *Microelectronic Engineering* 83.11 (2006), pp. 2042–2054.

[5] D Mangelinck, K Hoummada, and I Blum. "Kinetics of a transient silicide during the reaction of Ni thin film with (100) Si." In: *Applied Physics Letters* 95.18 (2009), p. 1902.

[6] S Gaudet, C Coia, P Desjardins, and C Lavoie. "Metastable phase formation during the reaction of Ni films with Si (001): The role of texture inheritance." In: *Journal of Applied Physics* 107.9 (2010), p. 093515.

[7] D Mangelinck, K Hoummada, F Panciera, M El Kousseifi, I Blum, M Descoins, M Bertoglio, A Portavoce, C Perrin, and M Putero. "Progress in the understanding of Ni silicide formation for advanced MOS structures." In: *Physica Status Solidi (a)* 211.1 (2014), pp. 152–165.

[8] K De Keyser, C Van Bockstael, RL Van Meirhaeghe, C Detavernier, E Verleysen, H Bender, W Vandervorst, J Jordan-Sweet, and C Lavoie. "Phase formation and thermal stability of ultrathin nickel-silicides on Si (100)." In: *Applied Physics Letters* 96.17 (2010), p. 173503.

[9] Z Zhang, SL Zhang, B Yang, Y Zhu, S M Rossnagel, S Gaudet, A J Kellock, J Jordan-Sweet, and C Lavoie. "Morphological stability and specific resistivity of sub-10 nm silicide films of Ni Pt_x on Si substrate." In: *Applied Physics Letters* 96 (2010), p. 071915.

[10] J Luo, Z Qiu, C Zha, Z Zhang, D Wu, J Lu, J Åkerman, M Östling, L Hultman, and SL Zhang. "Surface-energy triggered phase formation and epitaxy in nanometer-thick $Ni_{1-x}Pt_x$ silicide films." In: *Applied Physics Letters* 96.3 (2010).

[11] RT Tung, JM Poate, JC Bean, JM Gibson, and DC Jacobson. "Epitaxial silicides." In: *Thin Solid Films* 93.1 (1982), pp. 77–90.

[12] RT Tung, JM Gibson, and JM Poate. "Formation of Ultrathin Single-Crystal Silicide Films on Si: Surface and Interfacial Stabilization of Si-$NiSi_2$ Epitaxial Structures." In: *Physical Review Letters* 50.6 (1983), p. 429.

[13] A Mouroux, S-L Zhang, W Kaplan, S Nygren, M Östling, and CS Petersson. "Enhanced formation of the C54 phase of $TiSi_2$ by an interposed layer of molybdenum." In: *Applied Physics Letters* 69.7 (1996), pp. 975–977.

[14] D Mangelinck, P Gas, JM Gay, B Pichaud, and O Thomas. "Effect of Co, Pt, and Au additions on the stability and epitaxy of $NiSi_2$ films on (111) Si." In: *Journal of Applied Physics* 84 (1998), pp. 2583–2590.

[15] D Mangelinck, JY Dai, JS Pan, and SK Lahiri. "Enhancement of thermal stability of NiSi films on (100) Si and (111) Si by Pt addition." In: *Applied Physics Letters* 75.12 (1999), pp. 1736–1738.

[16] C Detavernier and C Lavoie. "Influence of Pt addition on the texture of NiSi on Si (001)." In: *Applied Physics Letters* 84.18 (2004), pp. 3549–3551.

[17] O Cojocaru-Mirédin, D Mangelinck, K Hoummada, E Cadel, D Blavette, B Deconihout, and C Perrin-Pellegrino. "Snowplow effect and reactive diffusion in the Pt doped Ni–Si system." In: *Scripta Materialia* 57.5 (2007), pp. 373–376.

[18] F Panciera, D Mangelinck, K Hoummada, M Texier, M Bertoglio, A De Luca, M Gregoire, and M Juhel. "Direct epitaxial growth of θ-Ni_2Si by reaction of a thin Ni (10at.% Pt) film with Si (100) substrate." In: *Scripta Materialia* 78 (2014), pp. 9–12.

[19] C Mocuta, MI Richard, J Fouet, S Stanescu, A Barbier, C Guichet, O Thomas, S Hustache, AV Zozulya, and D Thiaudiere. "Fast pole figure acquisition using area detectors at the DiffAbs beamline–Synchrotron SOLEIL." In: *Journal of Applied Crystallography* 46.6 (2013), pp. 1842–1853.

[20] P Pangaud, S Basolo, N Boudet, J-F Berar, B Chantepie, P Delpierre, B Dinkespiler, S Hustache, M Menouni, and C Morel. "XPAD3: A new photon counting chip for X-ray CT-scanner." In: *Nuclear Instruments and Methods in Physics Research Section A: Accelerators, Spectrometers, Detectors and Associated Equipment* 571.1 (2007), pp. 321–324.

[21] P Pangaud, S Basolo, N Boudet, J-F Berar, B Chantepie, J-C Clemens, P Delpierre, B Dinkespiler, K Medjoubi, S Hustache, et al. "XPAD3-S: A fast hybrid pixel readout chip for X-ray synchrotron facilities." In: *Nuclear Instruments and Methods in Physics Research Section A: Accelerators, Spectrometers, Detectors and Associated Equipment* 591.1 (2008), pp. 159–162.

[22] K Medjoubi, T Bucaille, S Hustache, J-F Bérar, N Boudet, J-C Clemens, P Delpierre, and B Dinkespiler. "Detective quantum efficiency, modulation transfer function and energy resolution comparison between CdTe and silicon sensors bump-bonded to XPAD3S." In: *Journal of Synchrotron Radiation* 17.4 (2010), pp. 486–495.

[23] K Medjoubi, A Thompson, J-F Bérar, J-C Clemens, P Delpierre, P Da Silva, B Dinkespiler, R Fourme, P Gourhant, B Guimaraes, et al. "Energy resolution of the CdTe-XPAD detector: calibration and potential for Laue diffraction measurements on protein crystals." In: *Journal of Synchrotron Radiation* 19.3 (2012), pp. 323–331.

[24] K De Keyser and C Detavernier. GUSTAV*: Ghent University Software for Texture Analysis and Visualisation*. `http://www.cocoon.ugent.be/content/gustav/`.

[25] E Verleysen. "Chemical analysis of thin films in electronic devices by analytical transmission electron microscopy methodologies." PhD thesis. KU Leuven, 2013.

[26] K De Keyser, C Van Bockstael, C Detavernier, RL Van Meirhaeghe, J Jordan-Sweet, and C Lavoie. "Epitaxial formation of a metastable hexagonal nickel–silicide." In: *Electrochemical and Solid-State Letters* 11.9 (2008), H266–H268.

[27] FA Geenen, K van Stiphout, M Minjauw, J Jordan-Sweet, A Vantomme, C Lavoie, and C Detavernier. "The influence of Al alloying on nickel silicide formation and texture." In: *to be submitted* (2017).

[28] KW Richter and H Ipser. "The Al–Ni–Si phase diagram between 0 and 33.3 at.% Ni." In: *Intermetallics* 11.2 (2003), pp. 101–109.

[29] KW Richter, K Chandrasekaran, and H Ipser. "The Al–Ni–Si phase diagram. Part II: phase equilibria between 33.3 and 66.7 at.% Ni." In: *Intermetallics* 12.5 (2004), pp. 545–554.

[30] K Chandrasekaran, KW Richter, and H Ipser. "The Al–Ni–Si phase diagram Part III: Phase equilibria in the nickel rich part." In: *Intermetallics* 14.5 (2006), pp. 491–497.

[31] C Detavernier, AS Ozcan, J Jordan-Sweet, EA Stach, J Tersoff, FM Ross, and C Lavoie. "An off-normal fibre-like texture in thin films on single-crystal substrates." In: *Nature* 426.6967 (2003), pp. 641–645.

[32] C Detavernier, J Jordan-Sweet, and C Lavoie. "Texture of NiSi films on Si (001),(111), and (110) substrates." In: *Journal of Applied Physics* 103.11 (2008), p. 113526.

[33] D Deduytsche, C Detavernier, RL Van Meirhaeghe, and C Lavoie. "High-temperature degradation of NiSi films: Agglomeration versus $NiSi_2$ nucleation." In: *Journal of Applied Physics* 98.3 (2005), p. 033526.

[34] X Gao, J Andersson, T Kubart, T Nyberg, U Smith, J Lu, L Hultman, A J Kellock, A Zhang, C Lavoie, et al. "Epitaxy of ultrathin $NiSi_2$ films with predetermined thickness." In: *Electrochemical and Solid-State Letters* 14.7 (2011), H268–H270.

[35] *Binary Alloy Phase Diagrams*. ASM international, 1996.

[36] M Ellner, S Heinrich, MK Bhargava, and K Schubert. "Einige strukturelle untersuchungen in der mischung NiSi." In: *Journal of the Less Common Metals* 66.2 (1979), pp. 163–173.

[37] H Von Känel. "Growth and characterization of epitaxial Ni and Co silicides." In: *Materials Science Reports* 8.5 (1992), pp. 193–269.

[38] JA Van Beek, PJTL Oberndorff, AA Kodentsov, and FJJ Van Loo. "Interactions in the Co–Ni–Si system at 800° C." In: *Journal of Alloys and Compounds* 297.1 (2000), pp. 137–143.

[39] F Panciera, K Hoummada, M Gregoire, M Juhel, and D Mangelinck. "Pt redistribution in N-MOS transistors during Ni salicide process." In: *Microelectronic Engineering* 107 (2013), pp. 173–177.

[40] A Schrauwen, J Demeulemeester, D Deduytsche, W Devulder, C Detavernier, CM Comrie, K Temst, and A Vantomme. "Ternary silicide formation from Ni-Pt, Ni-Pd and Pt-Pd alloys on Si (100): Nucleation and solid solubility of the monosilicides." In: *Acta Materialia* 130 (2017), pp. 19–27.

[41] M E Schlesinger. "Thermodynamics of solid transition-metal silicides." In: *Chemical Reviews* 90.4 (1990), pp. 607–628.

[42] FA Geenen, W Knaepen, F Moens, L Brondeel, A Leenaers, S Van den Berghe, and C Detavernier. "Anisotropic thermal expansion of Ni, Pd and Pt germanides and silicides." In: *Journal of Physics D: Applied Physics* 49.27 (2016), p. 275307.

[43] D Smeets, A Vantomme, K De Keyser, C Detavernier, and C Lavoie. "The role of lattice mismatch and kinetics in texture development: $Co_{1-x}Ni_xSi_2$ thin films on Si (100)." In: *Journal of Applied Physics* 103.6 (2008), p. 063506.

REFERENCES FOR CHAPTER 6

[1] C Lavoie, FM d'Heurle, C Detavernier, and C Cabral. "Towards implementation of a nickel silicide process for CMOS technologies." In: *Microelectronic Engineering* 70.2 (2003), pp. 144–157.

[2] A Lauwers, J A Kittl, M JH Van Dal, O Chamirian, M A Pawlak, M de Potter, R Lindsay, T Raymakers, X Pages, B Mebarki, et al. "Ni based silicides for 45nm CMOS and beyond." In: *Materials Science and Engineering: B* 114 (2004), pp. 29–41.

[3] D Deduytsche, C Detavernier, RL Van Meirhaeghe, and C Lavoie. "High-temperature degradation of NiSi films: Agglomeration versus $NiSi_2$ nucleation." In: *Journal of Applied Physics* 98.3 (2005), p. 033526.

[4] JA Kittl, K Opsomer, C Torregiani, C Demeurisse, S Mertens, DP Brunco, MJH Van Dal, and A Lauwers. "Silicides and germanides for nano-CMOS applications." In: *Materials Science and Engineering: B* 154 (2008), pp. 144–154.

[5] D Mangelinck, JY Dai, JS Pan, and SK Lahiri. "Enhancement of thermal stability of NiSi films on (100) Si and (111) Si by Pt addition." In: *Applied Physics Letters* 75.12 (1999), pp. 1736–1738.

[6] Z Zhang, SL Zhang, B Yang, Y Zhu, S M Rossnagel, S Gaudet, A J Kellock, J Jordan-Sweet, and C Lavoie. "Morphological stability and specific resistivity of sub-10 nm silicide films of Ni Pt_x on Si substrate." In: *Applied Physics Letters* 96 (2010), p. 071915.

[7] N Breil, C Lavoie, A Ozcan, F Baumann, N Klymko, K Nummy, B Sun, J Jordan-Sweet, J Yu, F Zhu, et al. "Challenges of nickel silicidation in CMOS technologies." In: *Microelectronic Engineering* 137 (2015), pp. 79–87.

[8] RT Tung, JM Poate, JC Bean, JM Gibson, and DC Jacobson. "Epitaxial silicides." In: *Thin Solid Films* 93.1 (1982), pp. 77–90.

[9] K De Keyser, C Van Bockstael, RL Van Meirhaeghe, C Detavernier, E Verleysen, H Bender, W Vandervorst, J Jordan-Sweet, and C Lavoie. "Phase formation and thermal stability of ultrathin nickel-silicides on Si (100)." In: *Applied Physics Letters* 96.17 (2010), p. 173503.

[10] Z Zhang, B Yang, Y Zhu, S Gaudet, S Rossnagel, A J Kellock, A Ozcan, C Murray, P Desjardins, SL Zhang, et al. "Exploitation of a self-limiting process for reproducible formation of ultrathin $Ni_{1-x}Pt_x$ silicide films." In: *Applied Physics Letters* 97.25 (2010), p. 252108.

[11] J Fouet, M Texier, M-I Richard, A Portavoce, D Mangelinck, C Guichet, N Boudet, and O Thomas. "Silicide formation during reaction between Ni ultra-thin films and Si (001) substrates." In: *Materials Letters* 116 (2014), pp. 139–142.

[12] L Knoll, QT Zhao, S Habicht, C Urban, B Ghyselen, and S Mantl. "Ultrathin Ni silicides with low contact resistance on strained and unstrained silicon." In: *IEEE Electron Device Letters* 31.4 (2010), pp. 350–352.

[13] L Knoll, QT Zhao, R Luptak, S Trellenkamp, KK Bourdelle, and S Mantl. "20nm Gate length Schottky MOSFETs with ultra-thin NiSi/epitaxial $NiSi_2$ source/drain." In: *Solid-State Electronics* 71 (2012), pp. 88–92.

[14] X Gao, J Andersson, T Kubart, T Nyberg, U Smith, J Lu, L Hultman, A J Kellock, A Zhang, C Lavoie, et al. "Epitaxy of ultrathin $NiSi_2$ films with predetermined thickness." In: *Electrochemical and Solid-State Letters* 14.7 (2011), H268–H270.

[15] C Detavernier, J Jordan-Sweet, and C Lavoie. "Texture of NiSi films on Si (001),(111), and (110) substrates." In: *Journal of Applied Physics* 103.11 (2008), p. 113526.

[16] B De Schutter, K De Keyser, and C Detavernier. "Visualization and classification of epitaxial alignment at hetero-phase boundaries." In: *Thin Solid Films* 599 (2016), pp. 104–112.

[17] B De Schutter, K De Keyser, C Lavoie, and C Detavernier. "Texture in thin film silicides and germanides: A review." In: *Applied Physics Reviews* 3.3 (2016), p. 031302.

[18] P Schlossmacher, DO Klenov, B Freitag, and HS Von Harrach. "Enhanced detection sensitivity with a new windowless XEDS system for AEM based on silicon drift detector technology." In: *Microscopy Today* 18.04 (2010), pp. 14–20.

[19] S Gaudet, C Coia, P Desjardins, and C Lavoie. "Metastable phase formation during the reaction of Ni films with Si (001): The role of texture inheritance." In: *Journal of Applied Physics* 107.9 (2010), p. 093515.

[20] F Allenstein, L Budzinski, D Hirsch, A Mogilatenko, G Beddies, R Grötzschel, and HJ Hinneberg. "Influence of Al on the growth of $NiSi_2$ on Si (001)." In: *Microelectronic Engineering* 82.3 (2005), pp. 474–478.

[21] J Luo, Z Qiu, C Zha, Z Zhang, D Wu, J Lu, J Åkerman, M Östling, L Hultman, and SL Zhang. "Surface-energy triggered phase formation and epitaxy in nanometer-thick $Ni_{1-x}Pt_x$ silicide films." In: *Applied Physics Letters* 96.3 (2010).

[22] M E Schlesinger. "Thermodynamics of solid transition-metal silicides." In: *Chemical Reviews* 90.4 (1990), pp. 607–628.

[23] C Detavernier, RL Van Meirhaeghe, Felix Cardon, and K Maex. "Influence of mixing entropy on the nucleation of $CoSi_2$." In: *Physical Review B* 62.18 (2000), p. 12045.

[24] A Lauwers, M De Potter, O Chamirian, R Lindsay, C Demeurisse, C Vrancken, and K Maex. "Silicides for the 100-nm node and beyond: Co-silicide, Co (Ni)-silicide and Ni-silicide." In: *Microelectronic Engineering* 64.1 (2002), pp. 131–142.

[25] C Lavoie, C Detavernier, C Cabral, FM d'Heurle, AJ Kellock, J Jordan-Sweet, and JME Harper. "Effects of additive elements on the phase formation and morphological stability of nickel monosilicide films." In: *Microelectronic Engineering* 83.11 (2006), pp. 2042–2054.

[26] J Demeulemeester, D Smeets, CM Comrie, NP Barradas, A Vieira, C Van Bockstael, C Detavernier, K Temst, and A Vantomme. "On the growth kinetics of Ni (Pt) silicide thin films." In: *Journal of Applied Physics* 113.16 (2013), p. 163504.

[27] JP Toinin, A Portavoce, M Texier, M Bertoglio, and K Hoummada. "First stages of Pd/Ge reaction: Mixing effects and dominant diffusing species." In: *Microelectronic Engineering* (2016).

[28] A Schrauwen, J Demeulemeester, D Deduytsche, W Devulder, C Detavernier, CM Comrie, K Temst, and A Vantomme. "Ternary silicide formation from Ni-Pt, Ni-Pd and Pt-Pd alloys on Si (100): Nucleation and solid solubility of the monosilicides." In: *Acta Materialia* 130 (2017), pp. 19–27.

[29] A Schrauwen, K Van Stiphout, J Demeulemeester, B De Schutter, W Devulder, CM Comrie, C Detavernier, K Temst, and A Vantomme. "The role of composition and microstructure in Ni-W silicide formation and low temperature epitaxial $NiSi_2$ growth by premixing Si." In: *Journal of Physics D: Applied Physics* 50.6 (2017), p. 065303.

[30] KW Richter, K Chandrasekaran, and H Ipser. "The Al–Ni–Si phase diagram. Part II: phase equilibria between 33.3 and 66.7 at.% Ni." In: *Intermetallics* 12.5 (2004), pp. 545–554.

[31] JA Van Beek, PJTL Oberndorff, AA Kodentsov, and FJJ Van Loo. "Interactions in the Co–Ni–Si system at 800° C." In: *Journal of Alloys and Compounds* 297.1 (2000), pp. 137–143.

[32] D Smeets, J Demeulemeester, K De Keyser, D Deduytsche, C Detavernier, CM Comrie, CC Theron, C Lavoie, and A Vantomme. "Nucleation and diffusion during growth of ternary Co1- xNixSi2 thin films studied by complementary techniques in real time." In: *Journal of Applied Physics* 104.9 (2008), p. 093533.

[33] D Smeets, G Vanhoyland, J D'Haen, and A Vantomme. "On the thermal expansion coefficient of CoSi2 and NiSi2." In: *Journal of Physics D: Applied Physics* 42.23 (2009), p. 235402.

[34] Y Okada and Y Tokumaru. "Precise determination of lattice parameter and thermal expansion coefficient of silicon between 300 and 1500 K." In: *Journal of Applied Physics* 56.2 (1984), pp. 314–320.

[35] D Deduytsche, C Detavernier, RL Van Meirhaeghe, JL Jordan-Sweet, and C Lavoie. "Formation and stability of NiSi in the presence of Co and Fe alloying elements." In: *Journal of Vacuum Science & Technology B* 26.6 (2008), pp. 1971–1977.

[36] TH Yang, G Luo, EY Chang, TY Yang, HC Tseng, and CY Chang. "Study of nickel silicide contact on $Si/Si_{1-x}\ Ge_x$." In: *IEEE Electron Device Letters* 24.9 (2003), pp. 544–546.

[37] PR Besser, P King, E Paton, and S Robie. "Ge effects on silicidation." In: *Microelectronic Engineering* 82.3 (2005), pp. 467–473.

REFERENCES FOR CHAPTER 7

[1] LJ Chen. *Silicide technology for integrated circuits*. Vol. 5. The Institution of Electrical Engineers, 2004.

[2] "Handbook of semiconductor manufacturing technology." In: CRC Press, 2007. Chap. Silicides.

[3] K Barmak and K Coffey. "Metallic films for electronic, optical and magnetic applications: Structure, processing and properties." In: Woodhead Publishing, 2014. Chap. Metal silicides in advanced complementary metal-oxide-semiconductor (CMOS) technology.

[4] T Skotnicki, JA Hutchby, TJ King, HSP Wong, and F Boeuf. "The end of CMOS scaling: toward the introduction of new materials and structural changes to improve MOSFET performance." In: *IEEE Circuits and Devices Magazine* 21.1 (2005), pp. 16–26.

[5] J-P Colinge. "Fully-depleted SOI CMOS for analog applications." In: *IEEE Transactions on Electron Devices* 45.5 (1998), pp. 1010–1016.

[6] Vishal P Trivedi and JG Fossum. "Nanoscale FD/SOI CMOS: Thick or thin box?" In: *IEEE electron device letters* 26.1 (2005), pp. 26–28.

[7] J Dick. *Leading Edge Silicon Devices*. Tech. rep. Chipworks, 2015.

[8] N Breil, C Lavoie, A Ozcan, F Baumann, N Klymko, K Nummy, B Sun, J Jordan-Sweet, J Yu, F Zhu, et al. "Challenges of nickel silicidation in CMOS technologies." In: *Microelectronic Engineering* 137 (2015), pp. 79–87.

[9] C Lavoie, A Praneet, AV Carr, JL Jordan-Sweet, AS Ozcan, E Levrau, N Breil, and E Alptekin. "Contacts in Advanced CMOS: History and Emerging Challenges." In: *ECS Transactions* (2017). accepted manuscript.

[10] P Adusumilli, E Alptekin, M Raymond, N Breil, F Chafik, C Lavoie, D Ferrer, S Jain, V Kamineni, A Ozcan, et al. "Ti and NiPt/Ti liner silicide contacts for advanced technologies." In: *VLSI Technology, 2016 IEEE Symposium on*. IEEE. 2016, pp. 1–2.

[11] A Das. "How finFETs ended the service contract of silicide process." In: *Solid State Technology* (2016).

[12] P Adusumilli, AV Carr, AS Ozcan, C Lavoie, J Jordan-Sweet, D Prater, N Breil, S Polvino, M Raymond, D Deniz, et al. "Formation and microstructure of thin Ti silicide films for advanced technologies." In: *2016 IEEE International Interconnect Technology Conference/Advanced Metallization Conference (IITC/AMC)*. IEEE. 2016, pp. 139–140.

[13] K Maex and M Van Rossum. *Properties of metal silicides*. 14. IET, 1995.

[14] ZH Yan, M Oehring, and R Bormann. "Metastable phase formation in mechanically alloyed and ball milled Ti–Si." In: *Journal of Applied Physics* 72.6 (1992), pp. 2478–2487.

[15] LH Allen, G Ramanath, SL Lai, Z Ma, S Lee, DDJ Allman, and KP Fuchs. "1 000 000° C/s thin film electrical heater: Insitu resistivity measurements of Al and Ti/Si thin films during ultra rapid thermal annealing." In: *Applied Physics Letters* 64.4 (1994), pp. 417–419.

[16] Z Ma and LH Allen. "Kinetic mechanisms of the C49-to-C54 polymorphic transformation in titanium disilicide thin films: A microstructure-scaled nucleation-mode transition." In: *Physical Review B* 49.19 (1994), p. 13501.

[17] V Svilan, KP Rodbell, LA Clevenger, C Cabral, RA Roy, C Lavoie, J Jordan-Sweet, and JME Harper. "Dependence of Crystallographic Texture of C54 $TiSi_2$ on Thickness and Linewidth In Submicron CMOS Structures." In: *MRS Proceedings*. Vol. 427. Cambridge Univ Press. 1996, p. 53.

[18] MS Fung, HC Cheng, and LJ Chen. "Localized epitaxial growth of C54 and C49 $TiSi_2$ on (111) Si." In: *Applied Physics Letters* 47.12 (1985), pp. 1312–1314.

[19] A Catana, PE Schmid, M Heintze, F Levy, P Stadelmann, and R Bonnet. "Atomic scale study of local $TiSi_2$/Si epitaxies." In: *Journal of Applied Physics* 67.4 (1990), pp. 1820–1825.

[20] IC Wu, JJ Chu, and LJ Chen. "Local epitaxy of $TiSi_2$ on (111) Si: Effects due to rapid thermal annealing and to the annealing atmosphere." In: *Journal of Applied Physics* 60.9 (1986), pp. 3172–3175.

[21] AS Özcan, KF Ludwig Jr, P Rebbi, C Lavoie, C Cabral Jr, and JME Harper. "Texture of $TiSi_2$ thin films on Si (001)." In: *Journal of Applied Physics* 92.9 (2002), pp. 5011–5018.

[22] C Detavernier, AS Ozcan, J Jordan-Sweet, EA Stach, J Tersoff, FM Ross, and C Lavoie. "An off-normal fibre-like texture in thin films on single-crystal substrates." In: *Nature* 426.6967 (2003), pp. 641–645.

[23] B De Schutter, K De Keyser, C Lavoie, and C Detavernier. "Texture in thin film silicides and germanides: A review." In: *Applied Physics Reviews* 3.3 (2016), p. 031302.

REFERENCES FOR CHAPTER 8

[1] SL Zhang and Ml Östling. "Metal silicides in CMOS technology: past, present, and future trends." In: *Critical Reviews in Solid State and Materials Sciences* 28.1 (2003), pp. 1–129.

[2] LJ Chen. *Silicide technology for integrated circuits*. Vol. 5. The Institution of Electrical Engineers, 2004.

[3] N Breil, C Lavoie, A Ozcan, F Baumann, N Klymko, K Nummy, B Sun, J Jordan-Sweet, J Yu, F Zhu, et al. "Challenges of nickel silicidation in CMOS technologies." In: *Microelectronic Engineering* 137 (2015), pp. 79–87.

[4] P Adusumilli, AV Carr, AS Ozcan, C Lavoie, J Jordan-Sweet, D Prater, N Breil, S Polvino, M Raymond, D Deniz, et al. "Formation and microstructure of thin Ti silicide films for advanced technologies." In: *2016 IEEE International Interconnect Technology Conference/Advanced Metallization Conference (IITC/AMC)*. IEEE. 2016, pp. 139–140.

[5] D Deduytsche, C Detavernier, RL Van Meirhaeghe, and C Lavoie. "High-temperature degradation of NiSi films: Agglomeration versus $NiSi_2$ nucleation." In: *Journal of Applied Physics* 98.3 (2005), p. 033526.

[6] C Detavernier, J Jordan-Sweet, and C Lavoie. "Texture of NiSi films on Si (001),(111), and (110) substrates." In: *Journal of Applied Physics* 103.11 (2008), p. 113526.

[7] RT Tung, JM Poate, JC Bean, JM Gibson, and DC Jacobson. "Epitaxial silicides." In: *Thin Solid Films* 93.1 (1982), pp. 77–90.

[8] B De Schutter, K De Keyser, C Lavoie, and C Detavernier. "Texture in thin film silicides and germanides: A review." In: *Applied Physics Reviews* 3.3 (2016), p. 031302.

[9] MS Fung, HC Cheng, and LJ Chen. "Localized epitaxial growth of C54 and C49 $TiSi_2$ on (111) Si." In: *Applied Physics Letters* 47.12 (1985), pp. 1312–1314.

[10] A Catana, PE Schmid, M Heintze, F Levy, P Stadelmann, and R Bonnet. "Atomic scale study of local $TiSi_2$/Si epitaxies." In: *Journal of Applied Physics* 67.4 (1990), pp. 1820–1825.

[11] IC Wu, JJ Chu, and LJ Chen. "Local epitaxy of $TiSi_2$ on (111) Si: Effects due to rapid thermal annealing and to the annealing atmosphere." In: *Journal of Applied Physics* 60.9 (1986), pp. 3172–3175.

[12] AS Özcan, KF Ludwig Jr, P Rebbi, C Lavoie, C Cabral Jr, and JME Harper. "Texture of $TiSi_2$ thin films on Si (001)." In: *Journal of Applied Physics* 92.9 (2002), pp. 5011–5018.

[13] V Svilan, KP Rodbell, LA Clevenger, C Cabral, RA Roy, C Lavoie, J Jordan-Sweet, and JME Harper. "Dependence of Crystallographic Texture of C54 $TiSi_2$ on Thickness and Linewidth In Submicron CMOS Structures." In: *MRS Proceedings*. Vol. 427. Cambridge Univ Press. 1996, p. 53.

[14] MX Zhang, D Qiu, and PM Kelly. "Crystallography of$TiSi_2$ (C54) epitaxy on (111) Si and (001) Si surfaces." In: *Thin Solid Films* 516.16 (2008), pp. 5498–5502.

[15] C Detavernier, AS Ozcan, J Jordan-Sweet, EA Stach, J Tersoff, FM Ross, and C Lavoie. "An off-normal fibre-like texture in thin films on single-crystal substrates." In: *Nature* 426.6967 (2003), pp. 641–645.

[16] VY Kolosov and AR Thölen. "Transmission electron microscopy studies of the specific structure of crystals formed by phase transition in iron oxide amorphous films." In: *Acta Materialia* 48.8 (2000), pp. 1829–1840.

[17] S Gaudet, K De Keyser, S Lambert-Milot, J Jordan-Sweet, C Detavernier, C Lavoie, and P Desjardins. "Three dimensional reciprocal space measurement by x-ray diffraction using linear and area detectors: Applications to texture and defects determination in oriented thin films and nanoprecipitates." In: *Journal of Vacuum Science & Technology A* 31.2 (2013), p. 021505.

[18] S Gaudet, P Desjardins, and C Lavoie. "The thermally-induced reaction of thin Ni films with Si: Effect of the substrate orientation." In: *Journal of Applied Physics* 110.11 (2011), p. 113524.

[19] K De Keyser and C Detavernier. GUSTAV*: Ghent University Software for Texture Analysis and Visualisation*. `http://www.cocoon.ugent.be/content/gustav/`.

[20] B De Schutter, K De Keyser, and C Detavernier. "Visualization and classification of epitaxial alignment at hetero-phase boundaries." In: *Thin Solid Films* 599 (2016), pp. 104–112.

REFERENCES FOR CHAPTER 9

[1] CL Hsin and YS Tsai. "Epitaxial silicides: the case of Fe, Ni, and Ti." In: *CrystEngComm* 18.42 (2016), pp. 8155–8158.

[2] M El Kousseifi, K Hoummada, T Epicier, and D Mangelinck. "Direct observation of NiSi lateral growth at the epitaxial θ-Ni_2 Si/Si (100) interface." In: *Acta Materialia* 99 (2015), pp. 1–6.

[3] Y Wu, J Xiang, C Yang, W Lu, and C M Lieber. "Single-crystal metallic nanowires and metal/semiconductor nanowire heterostructures." In: *Nature* 430.6995 (2004), pp. 61–65.

[4] K L Lin, S A Bojarski, C T Carver, M Chandhok, J S Chawla, J S Clarke, M Harmes, B Krist, H Lang, M Mayeh, et al. "Nickel silicide for interconnects." In: *2015 IEEE International Interconnect Technology Conference and 2015 IEEE Materials for Advanced Metallization Conference (IITC/MAM)*. IEEE. 2015, pp. 169–172.

REFERENCES FOR APPENDIX A

[1] A Steegen and K Maex. "Silicide-induced stress in Si: origin and consequences for MOS technologies." In: *Materials Science and Engineering: R: Reports* 38.1 (2002), pp. 1–53.

[2] TF Retajczyk and AK Sinha. "Elastic stiffness and thermal expansion coefficients of various refractory silicides and silicon nitride films." In: *Thin Solid Films* 70.2 (1980), pp. 241–247.

[3] D Smeets, G Vanhoyland, J D'Haen, and A Vantomme. "On the thermal expansion coefficient of CoSi2 and NiSi2." In: *Journal of Physics D: Applied Physics* 42.23 (2009), p. 235402.

[4] DF Wilson and OB Cavin. "Thermal expansion behavior of NiSi/NiSi 2." In: *Scripta Metallurgica et Materialia* 26.1 (1992), pp. 85–88.

[5] C Detavernier, C Lavoie, and FM d'Heurle. "Thermal expansion of the isostructural PtSi and NiSi: Negative expansion coefficient in NiSi and stress effects in thin films." In: *Journal of Applied Physics* 93.5 (2003), pp. 2510–2515.

[6] C Perrin, F Nemouchi, G Clugnet, and D Mangelinck. "Anisotropy of the thermal expansion of the Ni (Si1- xGex) phases investigated by high-temperature x-ray diffraction." In: *Journal of Applied Physics* 101.7 (2007), p. 073512.

[7] EJ Graeber, RJ Baughman, and B Morosin. "Crystal structure and linear thermal expansitivities of platinum silicide and platinum germanide." In: *Acta Crystallographica Section B: Structural Crystallography and Crystal Chemistry* 29.9 (1973), pp. 1991–1994.

[8] S Gaudet, C Detavernier, AJ Kellock, P Desjardins, and C Lavoie. "Thin film reaction of transition metals with germanium." In: *Journal of Vacuum Science & Technology A* 24.3 (2006), pp. 474–485.

[9] C Lavoie, FM d'Heurle, C Detavernier, and C Cabral. "Towards implementation of a nickel silicide process for CMOS technologies." In: *Microelectronic Engineering* 70.2 (2003), pp. 144–157.

[10] *Binary Alloy Phase Diagrams*. ASM international, 1996.

[11] KN Tu. "Thermal stability of Pd2Si and PdSi in thin film and in bulk diffusion couples." In: *Journal of Applied Physics* 53.1 (1982), pp. 428–432.

[12] Y Okada and Y Tokumaru. "Precise determination of lattice parameter and thermal expansion coefficient of silicon between 300 and 1500 K." In: *Journal of Applied Physics* 56.2 (1984), pp. 314–320.

[13] R R Reeber and K Wang. "Thermal expansion and lattice parameters of group IV semiconductors." In: *Materials Chemistry and Physics* 46.2 (1996), pp. 259–264.

[14] M-I Richard, J Fouet, C Guichet, C Mocuta, and O Thomas. "Exploring Pd–Si (001) and Pd–Si (111) thin-film reactions by simultaneous synchrotron X-ray diffraction and substrate curvature measurements." In: *Thin Solid Films* 530 (2013), pp. 100–104.

[15] K Selte and A Kjekshus. "Phase Transitions Between the MnP and NiAs Type Structures." In: *Acta Chemica Scandinavica* 27.9 (1973), pp. 3195–3206.

[16] HF Franzen, C Haas, and F Jellinek. "Phase transitions between NiAs-and MnP-type phases." In: *Physical Review B* 10.4 (1974), p. 1248.

[17] W Tremel, R Hoffmann, and J Silvestre. "Transitions between NiAs and MnP type phases: an electronically driven distortion of triangular (36) nets." In: *Journal of the American Chemical Society* 108.17 (1986), pp. 5174–5187.

[18] F Ishikawa, K Koyama, K Watanabe, T Asano, and H Wada. "First-order phase transition at the Curie temperature in MnAs and $MnAs_{0.9}Sb_{0.1}$." In: *Journal of the Physical Society of Japan* 75.8 (2006), p. 084604.

[19] D Connétable and O Thomas. "Comparative study of metallic silicide–germanide orthorhombic MnP systems." In: *Journal of Physics: Condensed Matter* 25.35 (2013), p. 355403.

REFERENCES FOR APPENDIX B

[1] S Gaudet, P Desjardins, and C Lavoie. "The thermally-induced reaction of thin Ni films with Si: Effect of the substrate orientation." In: *Journal of Applied Physics* 110.11 (2011), p. 113524.

[2] W Friedrich, P Knipping, and M Laue. "Interferenzerscheinungen bei Röntgenstrahlen." In: *Annalen der Physik* 346.10 (1913), pp. 971–988.

[3] B De Schutter, K De Keyser, C Lavoie, and C Detavernier. "Texture in thin film silicides and germanides: A review." In: *Applied Physics Reviews* 3.3 (2016), p. 031302.

[4] LG Schulz. "A direct method of determining preferred orientation of a flat reflection sample using a Geiger counter X-ray spectrometer." In: *Journal of Applied Physics* 20.11 (1949), pp. 1030–1033.

[5] S Gaudet, K De Keyser, S Lambert-Milot, J Jordan-Sweet, C Detavernier, C Lavoie, and P Desjardins. "Three dimensional reciprocal space measurement by x-ray diffraction using linear and area detectors: Applications to texture and defects determination in oriented thin films and nanoprecipitates." In: *Journal of Vacuum Science & Technology A* 31.2 (2013), p. 021505.

[6] B De Schutter, K Van Stiphout, NM Santos, E Bladt, J Jordan-Sweet, S Bals, C Lavoie, CM Comrie, A Vantomme, and C Detavernier. "Phase formation and texture of thin nickel germanides on Ge (001) and Ge (111)." In: *Journal of Applied Physics* 119.13 (2016), p. 135305.

[7] BB He. *Two-dimensional X-ray diffraction*. John Wiley & Sons, 2011.

[8] C Mocuta, MI Richard, J Fouet, S Stanescu, A Barbier, C Guichet, O Thomas, S Hustache, AV Zozulya, and D Thiaudiere. "Fast pole figure acquisition using area detectors at the DiffAbs beamline–Synchrotron SOLEIL." In: *Journal of Applied Crystallography* 46.6 (2013), pp. 1842–1853.

[9] P Pangaud, S Basolo, N Boudet, J-F Berar, B Chantepie, P Delpierre, B Dinkespiler, S Hustache, M Menouni, and C Morel. "XPAD3: A new photon counting chip for X-ray CT-scanner." In: *Nuclear Instruments and Methods in Physics Research Section A: Accelerators, Spectrometers, Detectors and Associated Equipment* 571.1 (2007), pp. 321–324.

[10] P Pangaud, S Basolo, N Boudet, J-F Berar, B Chantepie, J-C Clemens, P Delpierre, B Dinkespiler, K Medjoubi, S Hustache, et al. "XPAD3-S: A fast hybrid pixel readout chip for X-ray synchrotron facilities." In: *Nuclear Instruments and Methods in Physics Research Section A: Accelerators, Spectrometers, Detectors and Associated Equipment* 591.1 (2008), pp. 159–162.

[11] K Medjoubi, T Bucaille, S Hustache, J-F Bérar, N Boudet, J-C Clemens, P Delpierre, and B Dinkespiler. "Detective quantum efficiency, modulation transfer function and energy resolution comparison between CdTe and silicon sensors bump-bonded to XPAD3S." In: *Journal of Synchrotron Radiation* 17.4 (2010), pp. 486–495.

[12] K Medjoubi, A Thompson, J-F Bérar, J-C Clemens, P Delpierre, P Da Silva, B Dinkespiler, R Fourme, P Gourhant, B Guimaraes, et al. "Energy resolution of the CdTe-XPAD detector: calibration and potential for Laue diffraction measurements on protein crystals." In: *Journal of Synchrotron Radiation* 19.3 (2012), pp. 323–331.

[13] K De Keyser and C Detavernier. GUSTAV*: Ghent University Software for Texture Analysis and Visualisation*. `http://www.cocoon.ugent.be/content/gustav/`.

REFERENCES FOR APPENDIX C

[1] *Binary Alloy Phase Diagrams*. ASM international, 1996.

[2] O Fabrichnaya, G Beuers, C Bätzner, and HL Lukas. *Al-Ni-Si (Aluminium - Nickel - Silicon)*. Ed. by G Effenberg and S Ilyenko.

[3] P Villars and H Okamoto, eds. *Co-Ni-Si Isothermal Section of Ternary Phase Diagram*.

[4] P Villars and H Okamoto, eds. *Ni-Si-Ti Isothermal Section of Ternary Phase Diagram*.